Thermoelectric transport properties of thin metallic films, nanowires and novel Bi-based core/shell nanowires

Dissertation

zur Erlangung des akademischen Grades
doctor rerum naturalium
(Dr. rer. nat.)
im Fach Physik
Spezialisierung: Experimentalphysik

eingereicht an der
Mathematisch-Naturwissenschaftlichen Fakultät
der Humboldt-Universität zu Berlin

von
M. Sc. Maximilian Emil Kockert

Präsidentin der Humboldt-Universität zu Berlin:
Prof. Dr.-Ing. Dr. Sabine Kunst

Dekan der Mathematisch-Naturwissenschaftlichen Fakultät:
Prof. Dr. Elmar Kulke

Gutachter/innen:

1. Prof. Dr. Saskia F. Fischer
2. Prof. Christoph T. Koch, PhD
3. Prof. Dr. Kornelius Nielsch

Tag der mündlichen Prüfung: 17.06.2021

Integration of published content

Parts of this thesis are based on published scientific journal papers of which I am the first author.

- [1] **M. Kockert**, R. Mitdank, A. Zykov, S. Kowarik and S. F. Fischer. "Absolute Seebeck coefficient of thin platinum films." *Journal of Applied Physics*, **126**(10):105106, (2019). DOI: 10.1063/1.5101028
  https://aip.scitation.org/doi/10.1063/1.5101028
  Integrated in chapter 7 of this thesis, text fragments partially integrated into abstract, introduction, fundamentals and summary.

- [2] **M. Kockert**, D. Kojda, R. Mitdank, A. Mogilatenko, Z. Wang, J. Ruhhammer, M. Kroener, P. Woias and S. F. Fischer. "Nanometrology: Absolute Seebeck coefficient of individual silver nanowires." *Scientific Reports*, **9**(1):20265, (2019). DOI: 10.1038/s41598-019-56602-9
  https://www.nature.com/articles/s41598-019-56602-9
  Integrated in chapter 8 of this thesis, text fragments partially integrated into abstract, introduction, fundamentals and summary.

- [3] **M. Kockert**, R. Mitdank, H. Moon, J. Kim, A. Mogilatenko, S. H. Moosavi, M. Kroener, P. Woias, W. Lee and S. F. Fischer. "Semimetal to semiconductor transition in Bi/TiO_2 core/shell nanowires." *Nanoscale Advances*, **3**(1):263-271, (2020). DOI: 10.1039/D0NA00658K
  https://pubs.rsc.org/en/content/articlelanding/2021/NA/D0NA00658K
  Integrated in chapter 9 of this thesis, text fragments partially integrated into abstract, introduction, fundamentals and summary.

redistribute the material in any medium or format"[1] [2].

In addition, AIP Publishing LLC says that "Copyright to the Work remains with the Author(s)" and "Reprint the Version of Record (VOR) in print collections written by the Author, or in the Author's thesis or dissertation. It is understood and agreed that the thesis or dissertation may be made available electronically on the university's site or in its repository and that copies may be offered for sale on demand"[3].

[1] Creative Commons Attribution 4.0 International (CC BY 4.0) - https://creativecommons.org/licenses/by/4.0/

[2] Creative Commons Attribution 3.0 Unported (CC BY 3.0) - https://creativecommons.org/licenses/by/3.0/

[3] License to publish agreement for journals - AIP Publishing LLC - https://publishing.aip.org/wp-content/uploads/2019/10/AIPP-Author-License.pdf

Abstract

Thermoelectric phenomena can be strongly modified in nanomaterials. The determination of the electrical conductivity σ, the absolute Seebeck coefficient S and the thermal conductivity λ is a major challenge for metrology with respect to micro- and nanostructures because the transport properties of the bulk may change due to surface and confinement effects.

Within the scope of this thesis, the influence of size effects on the thermoelectric properties of thin platinum films is investigated and compared to the bulk material. For this reason, a measurement platform was developed as a standardized method to determine the absolute Seebeck coefficient of a thin film. Structural properties, like film thickness and grain size, are varied. The electron mean free path is correlated with the temperature dependence of σ and S of platinum. Boundary and surface scattering reduce the absolute Seebeck coefficient of the thin films to nearly 20 % of the bulk value at room temperature.

In addition, a method is demonstrated to determine S of individual metallic nanowires. For highly pure and single crystalline silver nanowires, the influence of nanopatterning on the temperature dependence of S is shown. A nanowire diameter below 200 nm suppresses S by 50 % compared to the bulk to less than $S = 1\,\mu\mathrm{VK}^{-1}$ at room temperature. This is attributed to the reduced electron mean free path.

A model allows the distinct decomposition of the temperature-dependent absolute Seebeck coefficient of platinum and silver into a thermodiffusion and phonon drag contribution. Size effects lead to a reduction of the thermodiffusion and phonon drag component.

Furthermore, the thermoelectric transport properties of individual bismuth-based (Bi) core/shell nanowires, which consist of a Bi core and different shell materials (tellurium (Te) and titanium dioxide (TiO_2)), are investigated and compared to the bulk material. A special measurement platform allows the temperature-dependent determination of σ, S and λ of an individual nanowire accompanied with structural investigations. The influence of the shell material and spatial dimension of the nanowire on the transport properties are discussed. Scattering at surfaces, indentations and interfaces between the core and the shell reduces σ to less than 5 % and λ to less than 25 % of the bulk value at room temperature. A compressive strain induced by the shell can lead to a band opening of bismuth increasing S by 10 % − 30 % compared to the bulk at room temperature. The core/shell system points towards a route to successfully tailor the thermoelectric properties of bismuth.

Kurzzusammenfassung

Thermoelektrische Phänomene können in Nanomaterialien stark modifiziert werden. Die Bestimmung der elektrischen Leitfähigkeit σ, des absoluten Seebeck-Koeffizienten S und der Wärmeleitfähigkeit λ ist eine wesentliche Herausforderung für die Messtechnik in Hinblick auf Mikro- und Nanostrukturen aufgrund dessen, dass die Transporteigenschaften vom Volumenmaterial sich durch Oberflächen- und Einschränkungseffekte verändern können.

Im Rahmen dieser Abschlussarbeit wird der Einfluss von Größeneffekten auf die thermoelektrischen Eigenschaften von dünnen Platinschichten untersucht und mit dem Volumenmaterial verglichen. Dafür wurde eine Messplattform als standardisierte Methode entwickelt, um den absoluten Seebeck-Koeffizienten einer dünnen Schicht zu bestimmen. Strukturelle Eigenschaften wie Schichtdicke und Korngröße werden variiert. Die mittlere freie Elektronenweglänge wird mit der Temperaturabhängigkeit von σ und S von Platin korreliert. Grenz- und Oberflächenstreuung reduzieren den absoluten Seebeck-Koeffizienten der dünnen Schichten auf etwa 20 % des Volumenmaterialwertes.

Außerdem wird eine Methode demonstriert um S von einzelnen metallischen Nanodrähten zu bestimmen. Für hochreine und einkristalline Silber-Nanodrähte wird der Einfluss von Nanostrukturierung auf die Temperaturabhängigkeit von S gezeigt. Ein Nanodrahtdurchmesser unter 200 nm unterdrückt S um 50 % im Vergleich zum Volumenmaterial auf weniger als $S = 1\,\mu\mathrm{VK}^{-1}$ bei Raumtemperatur. Dies wird der reduzierten mittleren freien Elektronenweglänge zugeschrieben.

Ein Modell ermöglicht die eindeutige Zerlegung des temperaturabhängigen absoluten Seebeck-Koeffizienten von Platin und Silber in einen Thermodiffusions- und Phononen-Drag-Anteil. Größeneffekte führen zur Reduktion der Thermodiffusions- und Phononen-Drag-Komponente.

Des Weiteren werden die Transporteigenschaften von einzelnen Bismut-basierenden (Bi) Kern/Hülle-Nanodrähten, welche aus einem Bi-Kern und unterschiedlichen Hüllenmaterialien (Tellur (Te) und Titandioxid (TiO_2)) bestehen untersucht und mit dem Volumenmaterial verglichen. Eine spezielle Messplattform erlaubt die temperaturabhängige Bestimmung von σ, S und λ eines einzelnen Nanodrahts im Zusammenhang mit strukturellen Untersuchungen. Der Einfluss des Hüllenmaterials und der räumlichen Dimension des Nanodrahts auf die Transporteigenschaften wird diskutiert. Streuung an Oberflächen, Einkerbungen und Grenzflächen zwischen dem Kern und der Hülle reduzieren σ auf weniger als 5 % und λ auf weniger als 25 % des Volumenmaterialwertes bei Raumtemperatur. Eine Druckverformung induziert durch die Hülle kann zu einer Bandöffnung bei Bismut führen, sodass S um 10 % − 30 % gegenüber dem Volumenmaterial bei Raumtemperatur gesteigert werden kann. Das Kern/Hülle-System zeigt in eine Richtung, um die thermoelektrischen Eigenschaften von Bismut erfolgreich anzupassen.

Contents

Chapter 1

Introduction

Miniaturization of electronic components has been a driving force in recent decades to advance the technological progress [4, 5]. This is an ongoing process and with every technical improvement comes the next downsizing step of components and materials. Along with the downsizing of materials, there is also a change in the transport properties, which are namely the electrical conductivity σ, the thermal conductivity λ and the absolute Seebeck coefficient S. Because, structure sizes can be compared with intrinsic lengths such as the mean free path of electrons or for even smaller structure dimensions with the Fermi wavelength. Miniaturization and the associated micro- and nanopatterning not only have an impact on technological developments, but also offer new research opportunities. The process of downsizing has created new and interesting micro- and nanostructures, such as thin films and nanowires. Thin films can be produced with the appropriate techniques to an atomic precision, thereby making it possible to tailor the transport properties [6–10]. Nanowires are characterized by a high surface-are-to-volume ratio and a high aspect ratio. Furthermore, nanowires can exhibit confined transport directions due to the small spatial dimension and the influence of the surface on the transport properties. These structural features make nanowires suitable for biochemical, sensory and thermoelectric applications [11–18].

However, these micro and nanostructures also pose new challenges and open questions for science and metrology. New reference standards and standardized measurement methods have to be developed and established so that a comparison of the transport properties of miniature structures is possible. Standardized model systems have to be found to investigate the influence of micro- and nanopatterning on the transport properties. Further possibilities, beyond miniaturization, have to be found to change the transport properties of a material in order to vary the transport properties on purpose. All of these challenges are the subject of this thesis and are tackled using three different materials.

One of those materials are thin platinum films. Platinum is the most commonly used thermoelectric reference material and is used with other materials, e.g. as commercially available bulk thermocouples [19]. In order to determine the thermoelectric transport properties of nanowires, measurements are usually performed relative to thin films [20–23]. For this purpose, microelectromechanical systems (MEMS) with thin platinum conduction lines of a few hundred nanometer thickness have been developed as measurement platforms [24–26]. However, thin metal films have a reduced absolute Seebeck coefficient compared to the bulk material [27–32]. Especially for metal-metal junctions, it is important to know the absolute Seebeck

coefficient of the reference material. Deviations in the single-digit microvolt per Kelvin range can easily lead to misinterpretations of the measurement results. For this reason, a standardized measurement platform that is suitable to investigate the temperature-dependent thermoelectric transport properties of thin metal films is presented in this thesis. Its usability is demonstrated by investigating platinum films with a thickness of 22 nm up to 197 nm. These platinum thin films will serve as a reference standard for thermoelectric characterizations.

Another material that is investigated in this work with respect to nanopatterning are silver nanowires. Bulk silver has the highest electrical and thermal conductivity of all metals [33] and well-known thermoelectric properties [34–38]. For this reason, it is a widely used metal in the electronics industry. In recent years, there has been a great interest in micro- and nanostructures of silver which are suitable for touch screens, solar cells and batteries [12, 39, 40]. For interconnects in low-noise electronics, a small absolute Seebeck coefficient is important. While the thermoelectric properties of metallic thin films have been studied [1, 28, 37, 41–45], it is very challenging to determine these of individual metallic nanowires [21, 46–49]. For this reason, the thermoelectric nanowire characterization platform is used in this thesis [2, 20, 21, 25]. This special measurements platform allows the determination of the electrical and thermal conductivity and of the Seebeck coefficient of an individual nanowire. In addition, structural and chemical investigations of the same nanowire can be performed with this platform. It has been shown that individual single crystalline silver nanowires are well suited to study size effects that influence the transport properties [21].

However, the absolute Seebeck coefficient of individual silver nanowires remains an open issue. In particular, the determination of the absolute Seebeck coefficient of an individual metallic nanowire requires the knowledge of the absolute Seebeck coefficient of the micro- and nanopatterned thermoelectric reference material. This issue can be solved in combination with the examined absolute Seebeck coefficient of the thin platinum films. As a result, high-purity and single crystalline nanowires can serve as a model system to investigate the influence of nanopatterning on the absolute Seebeck coefficient S. Thermodiffusion and phonon drag are the two main contributions to the absolute Seebeck coefficient [28, 41, 50]. The thermodiffusion of charge carriers in the material caused by a temperature difference can be described by Mott's formula [28, 41, 50, 51]. The phonon drag arises from the interaction between electrons and phonons [28, 41, 50, 52]. A high precision method to measure ultra-low absolute Seebeck coefficients of individual metallic nanowires is demonstrated in this thesis. Furthermore, a model for the temperature dependence of S is presented and the influence of the electron-phonon and phonon-phonon interaction on the absolute Seebeck coefficient of metallic thin films and nanowires is discussed.

The third material that is investigated in this thesis are bismuth-based nanowires. Bismuth (Bi) has been under investigations for a long time [53] due to its unique properties, e.g. its anisotropic transport properties, long charge carrier mean free path (up to a few hundred micrometers at 4 K), large Fermi wavelength (70 nm) and semimetal band structure [53–57]. But, for thermoelectric applications bulk Bi is not of interest due to its low thermoelectric performance [53, 58] that can be described by the figure of merit $ZT = \frac{\sigma S^2 T}{\lambda}$ at a certain bath temperature T. However, Dresselhaus *et al.* predicted theoretically an improvement of the thermoelectric efficiency due to quantum size effects for 1D quantum-wire-structures made of Bi [58]. The practical implementation of Bi nanowires with such small diameters into

applications can be challenging.

For this reason, Bi-based core/shell nanowires have raised attention in recent years because of their increased thermoelectric performance with relatively large diameters ($d > 300\,\mathrm{nm}$) [59–61]. An additional shell material, e.g. tellurium (Te), that is coated onto the Bi nanowire core can cause a semimetal to semiconductor transition due to the lattice mismatch of the Bi core and the Te shell [60, 61]. An increased Seebeck coefficient and a reduced thermal conductivity can be the result of such a heterostructure [60, 61]. However, the combined full thermoelectric characterization of individual pure Bi and Bi/Te core/shell nanowires, in which all transport parameters (σ, S and λ) were measured on one and the same nanowire remains an open issue. This is crucial in order to understand the thermoelectric behavior of a material. Furthermore, titanium dioxide (TiO_2) is presented as a new shell material for Bi-based nanowires. The TiO_2 shell has the advantage that it is electrical insulating compared to other shell materials [60–62]. In this work, the thermoelectric properties of individual Bi-based nanowires are investigated and the effects of the core/shell structure are discussed, allowing to vary the transport properties on purpose.

The outline of the thesis is as follows:

In the **2nd** chapter, the principles of the electrical, thermal and thermoelectric transport are presented. In the first part of the chapter, important characteristics of the electric transport of a metal, semimetal and semiconductor are introduced. The second part of the chapter deals with the principles of the thermal conductivity. The thermoelectric principles of a material are presented in the third part. In particular, the thermodiffusion and phonon drag contribution to the Seebeck coefficient are introduced. The last part of the chapter deals with the figure of merit that is a thermoelectric performance parameter.

An overview of the materials which are investigated in this thesis is given in the **3rd** chapter. Structural, transport and further material properties of platinum, silver and bismuth are presented. For each material, the current state of research is evaluated, This is namely the transition from bulk platinum to platinum thin films, the transition from bulk silver to silver nanowires and the transition from bulk bismuth to bismuth-based nanowires, in particular the concept of the core/shell nanowires is presented. The silver nanowires were prepared by the group of Prof. Dr. Peter Woias at the Laboratory for Design of Microsystems (IMTEK) from the University of Freiburg (Germany). The Bi-based nanowires were prepared by the group of Prof. Dr. Wooyoung Lee at the Department of Material Science and Engineering from the Yonsei University (Korea).

Chapter 4 shows different measurement devices and cryogenic techniques which are used in this thesis. Furthermore, the concepts of microlithography and electron beam-induced deposition (EBID) are introduced. In the last part of the chapter different methods for structural characterization are presented.

Chapter 5 deals with thermoelectric characterization platforms and contact preparation of individual nanowires. At first the thermoelectric micro lab is presented which allows the determination of the electrical conductivity and the Seebeck coefficient of a thin film. Then, two version of the thermoelectric nanowire charac-

terization platform (TNCP) which were designed at the Laboratory for Design of Microsystems (IMTEK) by the group of Prof. Dr. Peter Woias are presented. Both versions are discussed from a thermoelectric point of view. A nanowire manipulation method and the subsequent preparation of EBID contacts is shown. In addition, a discussion of different EBID precursor materials based on platinum and tungsten is given.

Chapter 6 deals with preparatory measurements of metallic microwires. This chapter shows the determination of the electrical conductivity, the relative and absolute Seebeck coefficient and the thermal conductivity in detail. The results of the investigations prove the reliability of the measurement principles which are later applied on thin films and nanowires.

The thermoelectric and structural properties of thin platinum films are presented in **chapter 7**. A new self-developed measurement platform for thin films is used to determine the thermoelectric transport properties. X-ray and atomic force microscopy investigations are correlated with the electron mean free path and give information about the influence of size effects on the electrical conductivity and the absolute Seebeck coefficient of the thin films.

Chapter 8 deals with the structural and thermoelectric properties of individual silver nanowires. The thermoelectric properties of the silver nanowires are measured on the thermoelectric nanowire characterization platform. The influence of nanopatterning on the thermodiffusion and phonon drag contribution and the related electron-phonon and phonon-phonon interaction of the absolute Seebeck coefficient is discussed.

The structural and thermoelectric properties of individual Bi-based core/shell nanowires are presented in **chapter 9**. The electrical conductivity, the thermal conductivity and the absolute Seebeck coefficient of pure Bi, Bi/Te and Bi/TiO_2 nanowires are determined. The influence of the different shell materials on the thermoelectric transport properties is discussed.

Chapter 10 gives a summary of all results and the according interpretations.

Chapter 11 concludes this thesis and shows further investigation possibilities.

Chapter 2

Electrical, thermal and thermoelectric principles and parameters

2.1 Electrical transport

In general, metals, semimetals and semiconductors can be distinguished from one another on the basis of the position of the Fermi energy (E_F) in the band diagram and on the basis of the occupation of the different bands. This is sketched in Fig. 2.1.

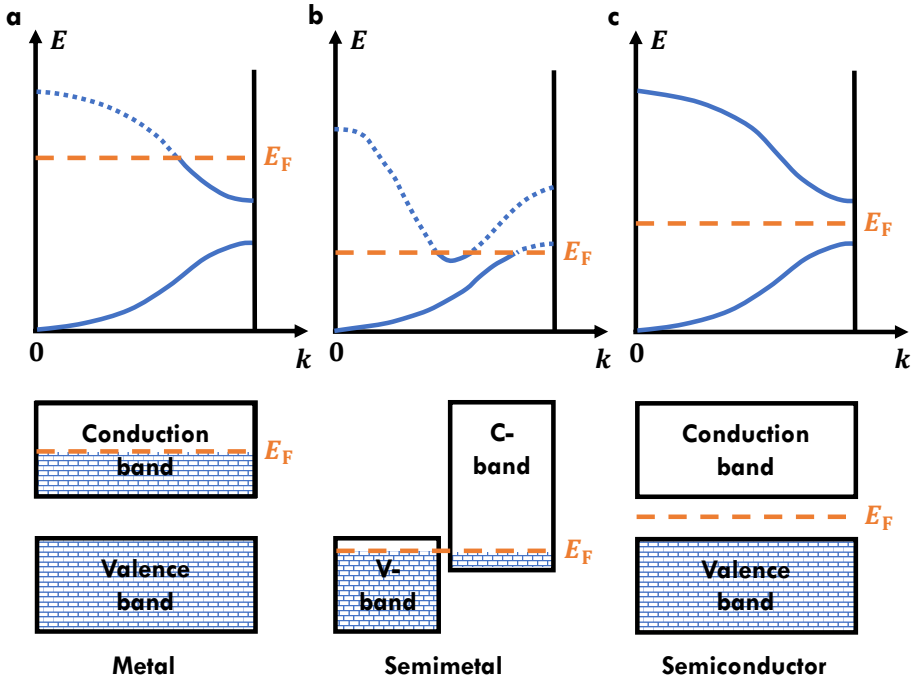

Figure 2.1: **Position of the Fermi energy (E_F) in a band diagram ($E(k)$). a**, For a metal, the Fermi energy is situated in the partly filled conduction band. **b**, For a semimetal, the Fermi energy is situated both in the conduction band and in the valence band. This is the result of a band overlap. **c**, For an intrinsic semiconductor, the Fermi energy is situated between the valence and conduction band in the band gap. Sketch after Ref. [63][p. 346].

The conduction band edge and the valence band edge are depicted in a diagram of the energy E as a function of the reciprocal lattice vector k. For metals, the Fermi energy (or the chemical potential if the temperature is not 0 K) is within a band that is not completely filled with free charge carriers. In the case of semimetals, there is a band overlap, so that the Fermi energy is partly in the valence band and partly in the conduction band. This means that both holes and electrons contribute to the charge transport. For intrinsic semiconductors, the Fermi energy is in the band gap between the valence and conduction band. The resulting electrical transport properties of a material are presented in the following.

Metal and semimetal

The well-known ohmic law is given by [63, p. 508]

$$\vec{j} = \sigma \vec{E}. \tag{2.1}$$

$\vec{j}$ is the current density, $\vec{E}$ is the applied electrical field and σ is the electrical conductivity of the material. A representation of Ohm's law in measurement parameters is given by $R = \frac{U}{I}$. R is the electrical resistance, I is the current applied to the device under test and U is the measured voltage. The combination of both equations for Ohm's law provides the material-specific electrical conductivity under the assumption that the charge transport is isotropic

$$\sigma = \frac{1}{\rho} = \frac{l}{AR}. \tag{2.2}$$

ρ is the inverse electrical conductivity which is known as the resistivity. A is the cross-sectional area and l is the length of the measurement object. Furthermore, the electrical conductivity according to Drude's model is given by [63, p. 282], [64, p. 250]

$$\sigma = \frac{1}{\rho} = \frac{ne^2\tau}{m} = ne\mu. \tag{2.3}$$

n is the concentration of the free electrons, e is the elementary charge, τ is the relaxation time of the charge carriers and thus the mean scattering time of the electrons between two collisions. μ is the mobility of the electrons. Metals and semimetals differ in their electrical conductivity because not only electrons but also holes contribute to the charge transport. The total resistivity is given by the sum of several independent partial resistances which are a result of different scattering processes. The resistivity is proportional to the inverse scattering time, the so-called scattering rate. The total scattering rate $\frac{1}{\tau_{\mathrm{Ges}}}$ is the sum of the individual rates (Matthiessen's rule) [63, p. 284], [64, p. 254]

$$\frac{1}{\tau_{\mathrm{Ges}}} = \sum_{n=0}^{N}. \tag{2.4}$$

The individual scattering rates can result from the scattering at impurities, phonons, electrons or lattice atoms. Different scattering events influence the temperature-dependent resistivity of a metal. At high temperatures ($T \gg \Theta_{\mathrm{D}}$, Θ_{D} is the Debye temperature), the electron-phonon scattering dominates. This results in a linear temperature dependence of the resistance. At low temperatures ($T \ll \Theta_{\mathrm{D}}$), the

resistance shows a T^5 dependency due to the decreasing contributions from phonon scattering. At even lower temperatures ($T \to 0\,\mathrm{K}$), a constant residual resistance remains that is mainly caused by the scattering of defects. The temperature dependence of the resistivity of a metal can be described using the Bloch-Grüneisen formula [63, p. 284-286], [64, p. 254]

$$\rho = \rho_0 + A \left(\frac{T}{\Theta_\mathrm{D}}\right)^5 \int_0^{\frac{\theta_\mathrm{D}}{T}} \frac{x^5}{(\exp(x)-1)(1-\exp(-x))} \mathrm{d}x. \tag{2.5}$$

ρ_0 is the temperature-dependent residual resistivity. A is a prefactor that contains the Fermi energy, the Boltzmanm constant and other natural constants and material parameters. A Bloch-Grüneisen fit (BGE) of bulk platinum (Pt) is given in Fig. 2.2. Θ_D can be determined from the BGE-fit. The Debye temperature for platinum is $\Theta_\mathrm{D} = 240\,\mathrm{K}$.

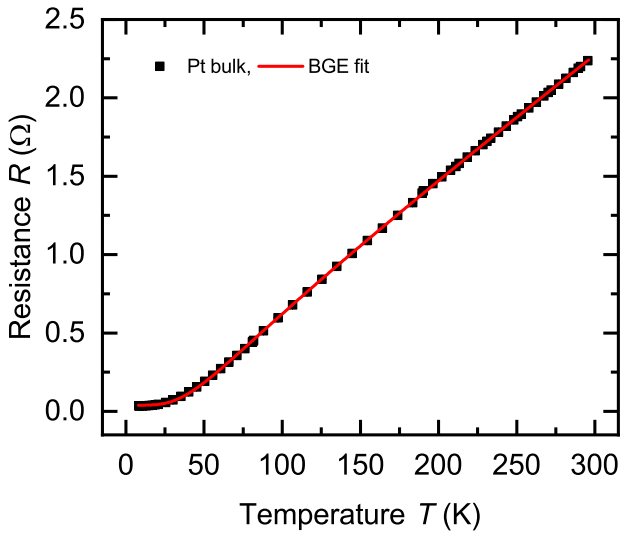

Figure 2.2: **Bloch-Grüneisen fit of bulk platinum.** Resistance R as a function of the bath temperature T. A Bloch-Grüneisen fit (BGE) of bulk platinum (Pt) yields the Debye temperature for platinum to $\Theta_\mathrm{D} = 240\,\mathrm{K}$.

The relationship between resistance and temperature is characterized by the temperature coefficient of resistance α [65,66]. The temperature coefficient depends on the material and is given by

$$\alpha = \frac{1}{\rho}\frac{\partial \rho(T)}{\partial T}. \tag{2.6}$$

A positive temperature coefficient means that the resistance increases with increasing temperature, as is the case with metals.

Another material parameter is the residual resistance ratio RRR [63, p. 286]. This is the ratio of the resistance at a certain temperature (usually room temperature (RT)) to the residual resistance ρ_0. It is given by

$$RRR = \frac{\rho_\mathrm{RT}}{\rho_0}. \tag{2.7}$$

The residual resistance ratio is a measure of the crystal quality of a material because ρ_0 is determined by impurities and crystal defects [67–69].

Semiconductor

In intrinsic semiconductors, a band gap separates the conduction band edge and the valence band edge from one another and the Fermi energy lies in this gap. Electrons and holes contribute to the electrical conductivity σ of a semiconductor. The electrical conductivity can be written as [63, p. 508], [64, p. 422]

$$\sigma = |q|(n\mu_{\mathrm{n}} + p\mu_{\mathrm{p}}), \tag{2.8}$$

where q is the elementary charge, μ_{n} is the electron mobility, μ_{p} is the hole mobility, n is the electron charge carrier concentration and p is the hole charge carrier concentration [70, p. 419-423]. The electrical conductivity of a semiconductor (Eq. 2.8) differs from a metal (Eq. 2.3) not only due to the additional contribution of holes to the electrical conductivity, but also in the temperature dependence of the charge carrier concentration and mobility.

Charge carriers can be excited by thermal energy. As a result, several temperature ranges for the charge carrier concentration in a semiconductor can be distinguished. At high temperatures, there is enough thermal energy to bring charge carriers from the valence band into the conduction band. This is the so-called intrinsic area. If the temperature deceases, there is not enough thermal energy anymore to overcome the band gap. However, all charge carriers from impurity levels are excited and the charge carrier concentration stays on a constant level. This is the saturation range. If the temperature decreases further, the charge carrier concentration begins to decrease because there is not enough thermal energy to generate charge carriers from impurity levels. At $T = 0\,\mathrm{K}$, all charge carriers are frozen out, so that there is no electrical conductivity [63, p. 504-508], [64, p. 418-421].

The mobility exhibits a temperature dependence, which is a result of different scattering processes. At low temperatures, most scattering events are due to ionized impurities. At high temperatures, scattering events occur due to phonons [63, p. 509], [64, p. 423]. In general, the mobility of a semiconductor is given by the following equation [63, p. 509], [64, p. 423]

$$\mu = \frac{|\vec{v}_{\mathrm{D}}|}{|\vec{E}|} = |q|\frac{\tau}{m^*}, \tag{2.9}$$

where $\vec{v}_{\mathrm{D}}$ is the drift velocity of the charge carriers with the elementary charge q and $\vec{E}$ is the applied electrical field. Scattering mechanisms influence the mobility. The mobility increases for a large relaxation time τ between two scattering processes and a small effective mass m^* of the charge carriers. As a result of the temperature dependence of the charge carrier concentration and of the mobility, the electrical conductivity of a semiconductor can exhibit exponential behavior over a wide temperature range.

More information about the electrical transport properties of solids can be found in the following references Ref. [63, 64, 71].

2.2 Thermal transport

Principles of thermal conductivity

Heat is mostly transmitted in solids via charge carriers (electrons or holes) or lattice vibrations (phonons). The total thermal conductivity of a solid is given by the sum

of individual thermal conductivities. In metals, the heat transport is dominated by charge carriers and in insulators, lattice vibrations mainly contribute to the heat transfer [72, p. 1-2]. The thermal conductivity is determined by the Fourier equation [63, p. 246], [64, p. 123], [72, p. 2]

$$\vec{Q} = -\lambda \vec{\nabla} T, \tag{2.10}$$

where $\vec{Q}$ is the heat flux and $\vec{\nabla} T$ is the temperature gradient. The proportionality factor is the thermal conductivity λ. In order to determine an expression for the thermal conductivity, it is assumed that a particle with the heat capacity c travels with the velocity $\vec{v}$ due to the temperature gradient [72, p. 2]. The resulting energy change rate is given by [72, p. 2]

$$\frac{\delta E}{\delta t} = c\vec{v}\vec{\nabla} T. \tag{2.11}$$

Assuming an average velocity over all particles with the concentration n and a relaxation time τ between scattering events lead to an expression of the heat flux [72, p. 2]

$$\vec{Q} = -\frac{1}{3} nc\tau v^2 \vec{\nabla} T. \tag{2.12}$$

The thermal conductivity can be written as [72, p. 2]

$$\lambda = \frac{1}{3} nc\tau v^2 = \frac{1}{3} Cv\Lambda, \tag{2.13}$$

where $C = nc$ is the total heat capacity and $\Lambda = v\tau$ is the mean free path of a particle. In general, the thermal conductivity for different kinds of excitations α is given by [72, p. 2]

$$\lambda = \frac{1}{3} \sum_{\alpha} C_\alpha v_\alpha \Lambda_\alpha. \tag{2.14}$$

For most solids, it is sufficient to describe the heat transport by the sum of the thermal conductivities of the electrons λ_e and the phonons λ_ph, so that [72, p. 22]

$$\lambda = \lambda_\mathrm{e} + \lambda_\mathrm{ph}. \tag{2.15}$$

The thermal conductivity of the electrons [72, p. 26]

$$\lambda_\mathrm{e} = \frac{1}{3} C_\mathrm{e} v_\mathrm{e} \Lambda_\mathrm{e} \tag{2.16}$$

is determined by the heat capacity within the free electron model [63, p. 275]

$$C_\mathrm{e} = \frac{\pi^2}{2} \frac{n k_\mathrm{B}^2}{E_\mathrm{F}} T. \tag{2.17}$$

The mean free path of the electrons Λ_e depends on the interaction between electrons and phonons. For temperatures above the Debye temperature ($T \gg \Theta_\mathrm{D}$), Λ_e is determined by electron-phonon scattering. As a result, $\lambda_\mathrm{e} \propto$ const. Scattering at defects and impurities lead to a temperature-independent mean free path of the electrons at very low temperatures. Thus, $\lambda_\mathrm{e} \propto T$ [63, p. 289-290].

As presented in the last section, the electrical conductivity of a metal is given by

$$\sigma = \frac{ne^2\Lambda_\mathrm{e}}{mv_\mathrm{e}}. \tag{2.18}$$

The ratio of the electrical conductivity (Eq. 2.18) and the thermal conductivity of the electrons (Eq. 2.16) yields the well-known Wiedemann-Franz relation [63, p. 287], [64, p. 260], [72, p. 27]

$$\frac{\lambda_\mathrm{e}}{\sigma} = \frac{\pi^2}{3}\left(\frac{k_\mathrm{B}}{e}\right)^2 T = LT. \tag{2.19}$$

The proportionality constant L is known as the Lorenz number [63, p. 287], [64, p. 260], [72, p. 27]

$$L = \frac{\lambda_\mathrm{e}}{\sigma T} = 2.44 \cdot 10^{-8}\,\frac{\mathrm{W\Omega}}{\mathrm{K}^2}. \tag{2.20}$$

The Wiedemann-Franz relation holds for a wide temperature range for bulk metals. There are deviations for nanopatterned materials [21, 49].

In order to describe the thermal conductivity of the lattice λ_ph, the phonon heat capacity has to be taken into account [41, 50, 73], [64, p. 117]

$$C_\mathrm{ph} = 9nk_\mathrm{B}\left(\frac{T}{\Theta_\mathrm{D}}\right)^3 \int_0^{\frac{\theta_\mathrm{D}}{T}} \frac{x^4 \exp(x)}{(\exp(x)-1)^2}\mathrm{d}x, \tag{2.21}$$

with the number of charge carriers per volume n. $x = \frac{\hbar\omega_\mathrm{D}}{k_\mathrm{B}T}$ is given by the reduced Planck constant $\hbar$ and by the Debye frequency ω_D. Interface scattering dominates the mean free path of the phonons Λ_ph at low temperatures, so that Λ_ph is constant. Thus, the thermal conductivity of the lattice λ_ph is determined by the phonon heat capacity C_ph, so that $\lambda_\mathrm{ph} \propto T^3$. At high temperatures, phonon-Umklapp processes determine λ_ph [63][p. 249f.].

More information about the thermal transport properties of solids can be found in the following references Ref. [63, 64, 71, 72].

Thermal conductivity of nanowires

The measurement of the thermal conductivity λ of a nanowire is the most critical step in order to determine the thermoelectric transport properties. A method to determine the thermal conductivity of a nanowire, which was introduced by Völklein *et al.* [49], is presented in the following. The idea of the method is to directly apply a heating current at the nanowire. Great care has to be taken not to destroy the nanowire during the measurement. The applied heating current leads to a temperature increase ΔT of the nanowire which results also in a resistance change r. The mean temperature increase of the nanowire is given by

$$\Delta T_\mathrm{m} = \frac{r}{m}, \tag{2.22}$$

where m is the slope from the resistance R as a function of the temperature T. Furthermore, ΔT_m is a function of the thermal conductivity. Solving the thermal heat equation leads to an expression that contains λ and ΔT_m. Fig. 2.3 shows a sketch of a suspended nanowire. The ends of the nanowire lying on top of metallic conduction lines. These conduction lines serve as heat sinks with a constant arbitrary temperature T_0. Most heating power during the measurement is dissipated in the

suspended part of the nanowire [49]. The experimental setup requires that the measurements have to be carried out in vacuum. For this reason, the convective heat loss through the nanowire can be neglected [49]. As a result of the long aspect ratio of a nanowire (length $\gg$ diameter), the heat transport can be described by a one-dimensional model in a volume element $\mathrm{d}V = A\mathrm{d}x$, where the Joule heat is given by [49]

$$Q_{\mathrm{J}} = \frac{I^2\rho}{A}\mathrm{d}x. \tag{2.23}$$

A is the cross-sectional area and ρ is the resistivity of a nanowire. A radiation term, derived from the Stefan-Boltzmann law, describes the dissipated heat to the ambient [49]

$$Q_{\mathrm{R}} = 4\epsilon\sigma_{\mathrm{B}}T_0^3\Delta T(x)2\pi r\mathrm{d}x, \tag{2.24}$$

with ϵ as the emissivity and σ_{B} as the Stefan-Boltzmann constant. The thermal power loss term describes the dissipated heat by thermal conduction through the nanowire [49]

$$Q_{\mathrm{C}} = -\lambda A\frac{\mathrm{d}^2\Delta T(x)}{\mathrm{d}x^2}\mathrm{d}x. \tag{2.25}$$

The heat balance is given by [49]

$$Q_{\mathrm{J}} = Q_{\mathrm{R}} + Q_{\mathrm{C}}. \tag{2.26}$$

The following differential equation results from Eq. 2.26

$$\frac{I^2\rho}{A}\mathrm{d}x = 4\epsilon\sigma_{\mathrm{B}}T_0^3\Delta T(x)2\pi r\mathrm{d}x - \lambda A\frac{\mathrm{d}^2\Delta T(x)}{\mathrm{d}x^2}\mathrm{d}x. \tag{2.27}$$

For nanowires, it was shown that the heat loss due to radiation can be neglected. As a result, the expression

$$\Delta T_{\mathrm{m}} = \frac{I^2Rl}{12\lambda A}, \tag{2.28}$$

is a solution of the differential equation Eq. 2.27. The combination of Eq. 2.22 and Eq. 2.28 gives the thermal conductivity [49]

$$\lambda = \frac{mI^2Rl}{12Ar}. \tag{2.29}$$

The equation for the thermal conductivity, which is used within the scope of this thesis is given by

$$\lambda = \frac{1}{12}\frac{\alpha lR}{A}\frac{\mathrm{d}P}{\mathrm{d}r(P)}, \tag{2.30}$$

where α is the temperature coefficient of the resistance of the nanowire, R is the four-terminal resistance, r is the resistance change, l is the length, P is the heating power and A is the cross-sectional area of the nanowire.

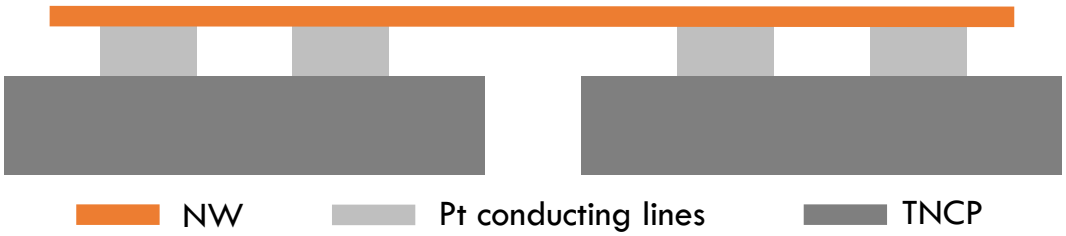

Figure 2.3: **Sketch of a suspended nanowire on a measurement platform.** Sketch of a suspended nanowire on top of metallic conduction lines which serve as a heat sink at constant arbitrary temperature T_0.

2.3 Thermoelectric transport

In the field of thermoelectricity there are three main effects, which are based on a correlation between electrical energy and temperature differences. The first effect was discovered in 1821 by Thomas Johann Seebeck [74]. Seebeck observed that a magnetic needle is deflected by the presence of a metallic conductor loop. The contacts of the conductor were at different temperatures. The reason for the deflection of the needle is a current flow within the conductor loop due to the temperature difference along the two materials from which the conductor loop is made. This thermoelectric effect is known today as the Seebeck effect.

In 1835, Jean Peltier discovered the reverse effect to the Seebeck effect, the so called Peltier effect [75]. This effect says that the contacts of two different materials, which are soldered together, can be cooled or heated by a current flow.

The third thermoelectric effect was named after William Thomson (Lord Kelvin) and describes that a material with an applied current and under the influence of a temperature difference can emit or absorb heat [76, p. 48]. Thomson predicted that the Seebeck effect, the Peltier effect and the Thomson effect are related to each other. This relation was proved by Lars Onsager in 1931 [77]. The focus of this thesis is on the investigation of the temperature-dependent Seebeck coefficient of different materials.

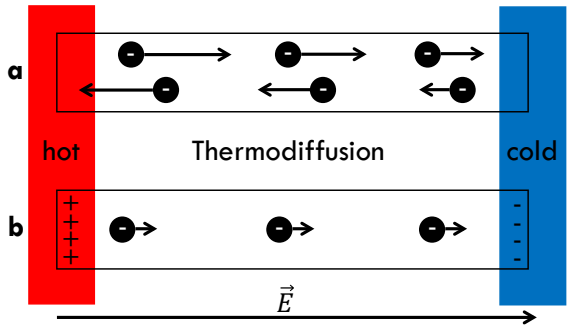

Figure 2.4: **Sketch of thermodiffusion in an electrical conductor.** **a**, The temperature difference in the conductor leads to a temperature-dependent velocity distribution of the charge carriers. **b**, The resulting thermodiffusion current leads to the formation of an electric field $\vec{E}$ with the thermovoltage U_S. Sketch after Ref. [78].

In an electrical conductor, the charge carriers have a temperature-dependent velocity distribution. If there is a temperature difference along the material, the electrons on the hot side have a higher energy and thus a higher average velocity

than charge carriers on the cold side. For this reason, there is a net flow of charge carriers towards the cold side of the material. This is known as thermodiffusion. Due to thermodiffusion, more and more electrons accumulate on the cold side of the material. This results in an electric field $\vec{E}$, which compensates the diffusion current. The resulting voltage is referred to as thermovoltage U_S [63, p. 290-292], [64, p. 256-259]. U_S can between a few microvolts (metals) up to millivolts (semiconductors).

This thermovoltage can be measured using a thermocouple [64, p. 259]. A thermocouple consists of two different electrical conductors A and B, which are linked with each other. The contacts of both materials are at different temperatures. This temperature difference along the materials enables a measurement of the thermovoltage between both materials in order to determine the relative Seebeck coefficient $S_\mathrm{A,B}$. The Seebeck coefficient S is a material and temperature-dependent thermoelectric parameter with the unit of measure $[\mathrm{S}] = \mathrm{VK}^{-1}$.

The thermovoltage of a thermocouple can be determined by the integral over the circuit and according to Fig. 2.5 it is given by

$$U_{\mathrm{S_{A,B}}} = -\left(\int_{T_0}^{T_\mathrm{cold}} S_\mathrm{B}\mathrm{dT} + \int_{T_\mathrm{cold}}^{T_\mathrm{hot}} S_\mathrm{A}\mathrm{dT} + \int_{T_\mathrm{hot}}^{T_0} S_\mathrm{B}\mathrm{dT}\right), \tag{2.31}$$

$$U_{\mathrm{S_{A,B}}} = -\left(S_\mathrm{B}T_\mathrm{cold} - S_\mathrm{B}T_0 + S_\mathrm{A}T_\mathrm{hot} - S_\mathrm{A}T_\mathrm{cold} + S_\mathrm{B}T_0 - S_\mathrm{B}T_\mathrm{hot}\right), \tag{2.32}$$

$$U_{\mathrm{S_{A,B}}} = -\left(S_\mathrm{A} - S_\mathrm{B}\right)\left(T_\mathrm{hot} - T_\mathrm{cold}\right) = -S_\mathrm{A,B}\left(T_\mathrm{hot} - T_\mathrm{cold}\right). \tag{2.33}$$

$S_\mathrm{A,B}$ is the relative Seebeck coefficient of material A relative to material B, where S_A and S_B are the absolute Seebeck coefficients. The sign is negative because the cold side of the thermocouple is identified with the low potential of the thermovoltage measurement. For sufficiently small temperature differences δT, the relative Seebeck coefficient is given by

$$S_\mathrm{A,B} = -\frac{U_{\mathrm{S_{A,B}}}}{T_\mathrm{hot} - T_\mathrm{cold}} = -\frac{dU_{\mathrm{S_{A,B}}}}{d\delta T}. \tag{2.34}$$

In general, it is very challenging experimentally to determine the absolute Seebeck coefficient of a material. There are essentially three options to determine the absolute Seebeck coefficient. The first option uses a thermocouple with two different materials. The absolute Seebeck coefficient of one material has to be known in order to determine the absolute Seebeck coefficient of the other material. This option is the usual procedure to determine absolute Seebeck coefficients. The second option also uses a thermocouple with one material being a superconductor. Below the critical transition temperature, the absolute Seebeck coefficient of the superconductor becomes zero [73, 79]. Then, the absolute Seebeck coefficient of the other material can be determined directly. The disadvantage of this method is that the absolute Seebeck coefficient can only be determined in a small temperature range (up to the critical temperature). The third method is based on the determination of the Thomson coefficient μ [73, 79]

$$S(T) = \int_0^T \frac{\mu(T^*)}{T^*}\mathrm{d}T^*. \tag{2.35}$$

Since the determination of the Thomson coefficient is very difficult, there are only a few materials that have been intensively investigated. Lead is a material that was

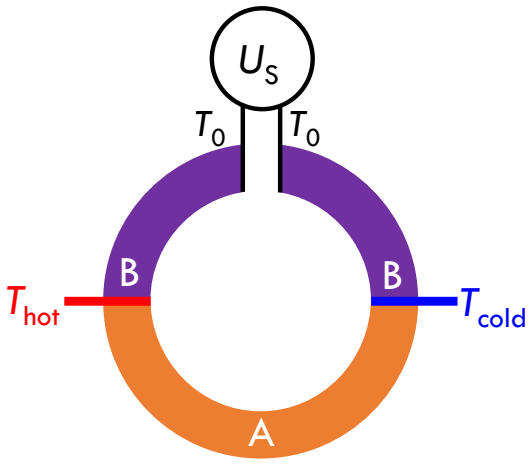

Figure 2.5: **Sketch of a thermocouple.** Thermocouple that consists of two different electrical conductors A and B that are connected with each other. The junctions of the two materials are at different temperatures. This leads to a thermovoltage U_S. U_S can be measured at an intermediate temperature T_0. Sketch after Ref. [78], [64, p. 259].

established as a Seebeck reference material [73,80]. From the investigated Thomson coefficient of lead, the absolute Seebeck coefficient was then determined according to Eq. 2.35. For this reason, lead is a reference material for the determinination of the absolute Seebeck coefficient of other materials.

Thermodiffusion and phonon drag contribution to the Seebeck coefficient

In general, the Seebeck coefficient is the sum of two parts. The thermodiffusion part and the phonon drag part [28, 41, 50]:

$$S = S_{\text{diff}} + S_{\text{ph}}. \tag{2.36}$$

S_{diff} is the contribution due to the thermodiffusion of the charge carriers in metals as described by Mott's formula [28, 41, 51, 81]:

$$S_{\text{diff}} = \frac{\pi^2 k_B^2 T}{3e} \left(\frac{\partial \ln \rho(E)}{\partial E} \right) \Bigg|_{E_F} \tag{2.37}$$

where k_B is the Boltzmann constant, T is the bath temperature, e is the elementary charge and $\frac{\partial \ln \rho(E)}{\partial E}\Big|_{E_F}$ is the derivative of the resistivity according to the energy at the Fermi energy.

S_{ph} is the contribution due to the phonon drag effect. The phonon drag effect is based on the electron-phonon interaction. A momentum transfer from phonons to electrons leads to a change of the Seebeck coefficient [50, 73]. The phonon drag part of the Seebeck coefficient is connected with the specific heat of the phonons [41,50,73]

$$C_{\text{ph}(T)} = 9nk_B \left(\frac{T}{\Theta_D} \right)^3 \int_0^{\frac{\theta_D}{T}} \frac{x^4 \exp(x)}{(\exp(x) - 1)^2} \mathrm{d}x \tag{2.38}$$

with the number of charge carriers per volume n. $x = \frac{\hbar \omega_D}{k_B T}$ is given by the reduced Planck constant $\hbar$ and by the Debye frequency ω_D.

The phonon drag effect is a phenomenon that occurs mostly at low temperatures ($T \ll \Theta_\mathrm{D}$, Θ_D is the Debye temperature). For this reason, the phonon drag contribution of the Seebeck coefficient can be described by $S_\mathrm{ph} = \frac{C_\mathrm{ph}}{3ne}$ [50, 73]. According to the Debye model, the specific heat is $C_\mathrm{ph} \propto T^3$ with $T \to 0$. Therefore, $S_\mathrm{ph} \propto T^3$ [50, 73]. The resulting Seebeck coefficient at low temperatures can be written as $S_\mathrm{low} = S_\mathrm{diff} + S_\mathrm{ph} = aT + bT^3$. a and b are variables. At high temperatures, the phonon drag effect vanishes [50, 73]. The Debye model predicts a constant specific heat ($C_\mathrm{ph} \approx 3nk_\mathrm{B}$) for temperatures above the Debye temperature and due to phonon-phonon Umklapp scattering $S_\mathrm{ph} \propto \frac{1}{T}$ [50]. This results in $S_\mathrm{high} = S_\mathrm{diff} + S_\mathrm{ph} = cT + d\frac{1}{T}$. c and d are variables.

The combination of the low temperature approach, the high temperature approach and additionally a characterization of the intermediate regime gives

$$S_\mathrm{ph} = \frac{C_\mathrm{ph}(T)}{3ne}\gamma = \frac{C_\mathrm{ph}(T)}{3ne}\frac{\tau_\mathrm{pp}}{\tau_\mathrm{pp} + \tau_\mathrm{ep}} \quad [41, 50], \tag{2.39}$$

hence

$$S_\mathrm{ph} = \frac{C_\mathrm{ph}(T)}{3ne}\frac{1}{1 + \frac{\tau_\mathrm{ep}}{\tau_\mathrm{pp}}} = \frac{C_\mathrm{ph}(T)}{3ne}\frac{1}{1 + F_\tau T \exp\left(-\frac{\Theta_\mathrm{D}}{T}\right)}. \tag{2.40}$$

The relation $\frac{\tau_\mathrm{ep}}{\tau_\mathrm{pp}} = F_\tau T \exp\left(-\frac{\Theta_\mathrm{D}}{T}\right)$ was suggested by and adapted from Ref. [41, 82]. This equation assumes that the phonon-phonon interaction becomes dominant at high temperatures [41, 82]. This results in the γ-factor

$$\gamma = \frac{1}{1 + \frac{\tau_\mathrm{ep}}{\tau_\mathrm{pp}}} = \frac{1}{1 + F_\tau T \exp\left(-\frac{\Theta_\mathrm{D}}{T}\right)}. \tag{2.41}$$

Finally, the approach of the phonon drag part with the specific heat of the phonons and the thermodiffusion part $S_\mathrm{diff} = F_\mathrm{diff}\frac{T}{\Theta_D}$ are combined to the formula that describes the Seebeck coefficient over a wide temperature range

$$S = F_\mathrm{diff}\frac{T}{\Theta_\mathrm{D}} + \frac{F_\mathrm{ph}\left(\frac{T}{\Theta_\mathrm{D}}\right)^3 \int_0^{\frac{\theta_\mathrm{D}}{T}} \frac{x^4 \exp(x)}{(\exp(x)-1)^2}\mathrm{d}x}{1 + F_\tau T \exp\left(-\frac{\Theta_\mathrm{D}}{T}\right)}. \tag{2.42}$$

This formula provides different parameters to describe the temperature dependence of the absolute Seebeck coefficient. The thermodiffusion contribution is described by the fit parameter F_diff. F_ph estimates the strength of the phonon drag on the absolute Seebeck coefficient. F_τ gives the ratio of the scattering time of the electron-phonon and phonon-phonon interaction.

Fig. 2.6 shows the absolute Seebeck coefficient S_Au of bulk gold as a function of the bath temperature T. The expected linear temperature-dependence (see Eq. 2.37) of the thermodiffusion contribution to the absolute Seebeck coefficient is depicted as a black dotted line if there was no phonon drag effect. The influence of the phonon drag becomes significant below 100 K and leads to an increase of the absolute Seebeck coefficient.

The sign of the absolute Seebeck coefficient can provide information about the dominant charge carrier type in the material [63][p. 514]. A positive sign of the Seebek coefficient indicates that holes are the dominant charge carrier type. A negative sign can indicate electrons as the dominant type. These assumptions are mostly correct for semiconductors. In general, metals are electron conductors. But

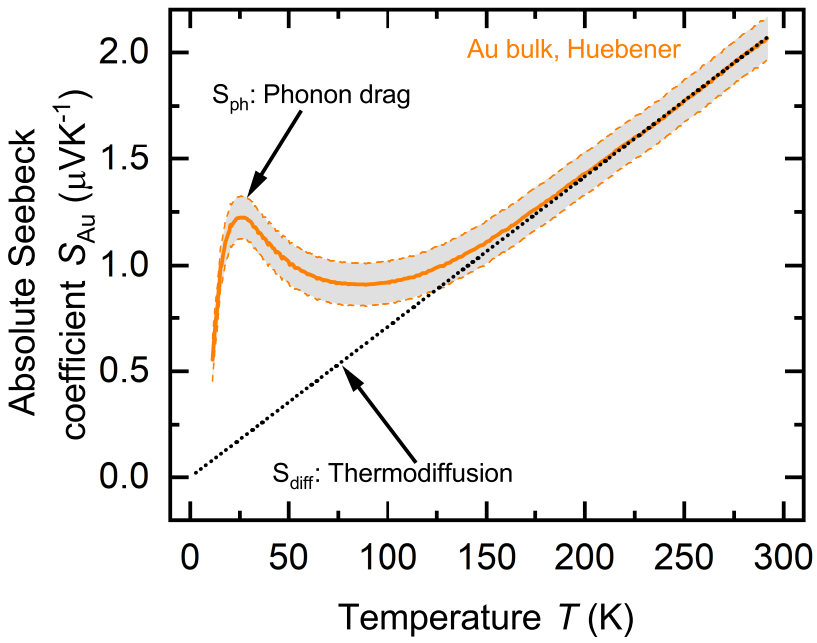

Figure 2.6: **Absolute Seebeck coefficient of gold (Au).** Absolute Seebeck coefficient S_{Au} of bulk gold as a function of the bath temperature T taken from Ref. [45]. The thick dashed orange line indicates the absolute Seebeck coefficient of bulk gold. The gray shaded area marks the uncertainty of the Seebeck coefficient. The black dotted line describes the expected amount of the thermodiffusion contribution to the Seebeck coefficient if there was no phonon drag effect. The influence of the phonon drag becomes significant below 100 K.

not all metals have a negative Seebeck sign. Fig. 2.7 shows the absolute Seebeck coefficient for various metals as a function of the temperature. There are three main variations for Seebeck signs in metals. Metals that have a negative Seebeck coefficient over a wide temperature range, such as aluminum (Al). Metals that have a positive Seebeck coefficient over a wide temperature range, such as gold (Au) and silver (Ag). Metals with a sign change, such as platinum (Pt).

The sign of the Seebeck coefficient of metals depends on the shape of the Fermi surface, the phonon spectrum together with electron-phonon interaction and the sign of the quantity $\frac{\partial \ln \rho(E)}{\partial E}\Big|_{E_F}$ [73]. For the thermodiffusion contribution, Eq. 2.37 has to be taken into account which can also be written as [73]

$$S_{\mathrm{diff}} = -\frac{\pi^2 k_{\mathrm{B}}^2 T}{3e}\left(\frac{\partial \ln \Lambda(E)}{\partial E} + \frac{\partial \ln A(E)}{\partial E}\right)\Bigg|_{E_F}. \tag{2.43}$$

Λ is the mean free path of the electrons and A denotes the Fermi surface area.

Aluminum has a negative Seebeck coefficient. This can can be attributed to the Fermi surface which is nearly a sphere [83]. For this reason, the free electron model predicts a negative sign for the thermodiffusion and phonon drag contributions [73]. Gold and silver are noble metals with a positive Seebeck sign. The positive sign can be attributed to a mechanism based on electron-electron scattering [73, 84] or it can be explained by a nearly free electron model if the electron-ion interaction is taken into account [73, 85]. The transition metal platinum has a negative thermodiffusion contribution which can be understood according to Eq. 2.37. The positive phonon drag contribution is a result of phonon-induced s-d scattering [73, 86].

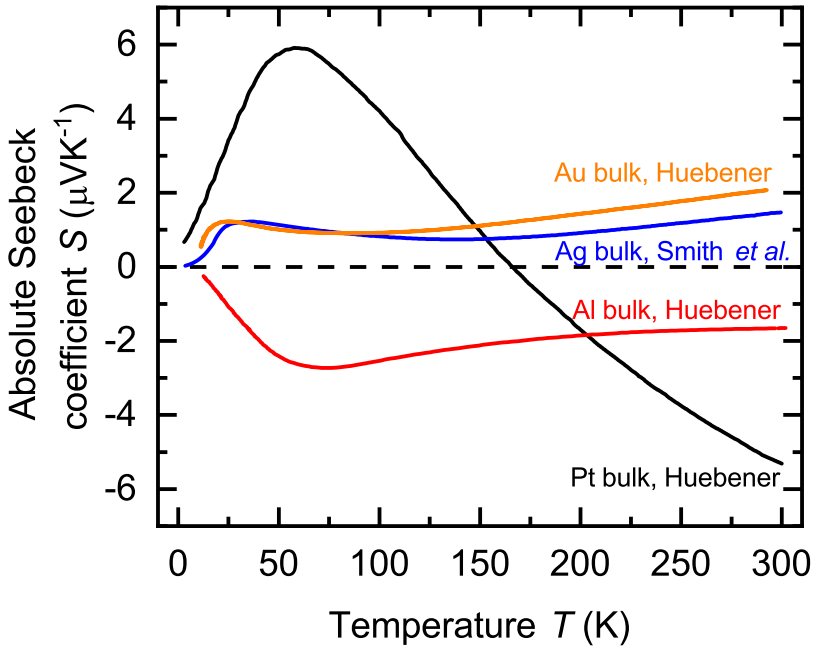

Figure 2.7: **Absolute Seebeck coefficient of different metals.** Absolute Seebeck coefficient of bulk gold (Au), silver (Ag), aluminum (Al) and platinum (Pt) as a function of the bath temperature T. Al has a negative sign of the Seebeck coefficient over the temperature range. Au and Ag have a positive Seebeck sign. The sign of Pt changes within the temperature range. Values of Al taken form Ref. [83], Ag from Ref. [38], Au from Ref. [45] and Pt from Ref. [28, 41]

.

2.4 Figure of merit

The thermoelectric performance of a material is described by the dimensionless quantity [87]

$$ZT = \frac{\sigma S^2}{\lambda} T. \tag{2.44}$$

This quantity is called figure of merit. The figure of merit combines all the relevant transport properties of a material at a certain temperature T. That is the electrical conductivity σ, the thermal conductivity λ and the absolute Seebeck coefficient S. This makes it easy to compare thermoelectrics materials with each other. The actual efficiency of a thermoelectric generator is given by [87]

$$\eta = \frac{T_{\text{hot}} - T_{\text{cold}}}{T_{\text{hot}}} \frac{\sqrt{1+ZT}-1}{\sqrt{1+ZT}+\frac{T_{\text{cold}}}{T_{\text{hot}}}}, \tag{2.45}$$

where T_{hot} is the temperature of the hot side and T_{cold} is the temperature of the cold side. T is the mean temperature $T = \frac{T_{\text{hot}}+T_{\text{cold}}}{2}$. A high value of the figure of merit leads to a high thermoelectric efficiency in order to obtain as much electrical energy as possible from a temperature difference. S and σ have to be large but at the same time $\lambda = \lambda_{\text{e}} + \lambda_{\text{ph}}$ has to be small to maximize ZT. The difficulty is that the transport properties are interconnected with each other. For metals and degenerate semiconductors, λ_{e} and σ are linked via the Wiedemann-Franz relation [63, p. 287], [64, p. 260], [72, p. 27].

Chapter 3

Materials - structural and transport properties

3.1 Bulk platinum and thin platinum films

Structural and transport properties

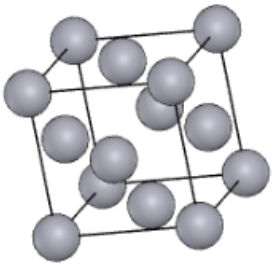

Figure 3.1: **Crystal structure of platinum.** Face-centered cubic crystal structure of platinum. Image taken from Ref. [88].

Bulk platinum (Pt) is a transition metal with an electron configuration of $4f^{14}5d^{8}6s^{2}$ [63]. The Debye temperature is about 240 K [89]. It crystallizes in a face-centered cubic structure [63]. The crystal structure is given in Fig. 3.1.

At 300 K, the electrical conductivity of Pt bulk is $\sigma = 9.2 \cdot 10^{6}\,\Omega^{-1}\mathrm{m}^{-1}$ [90], the absolute Seebeck coefficient is $S = -5.3\,\mu\mathrm{VK}^{-1}$ [28,41] and the thermal conductivity is $\lambda = 71.4\,\mathrm{Wm}^{-1}\mathrm{K}^{-1}$ [91, p. 269].

Fig. 3.2 a shows the electrical conductivity σ as a function of the bath temperature T. σ is increasing with decreasing temperature. At high bath temperatures ($T \gg \Theta_{\mathrm{D}}$), the electrical conductivity is mainly limited by electron-phonon scattering. At low temperatures ($T \ll \Theta_{\mathrm{D}}$), σ is determined by the residual resistance.

The absolute Seebeck coefficient S of Pt, which is given in Fig. 3.2 b as a function of T, is for temperatures above 150 K negative and for temperatures below 150 K positive. The negative sign can be explained by Mott's equation [28, 41, 51, 81] and the positive sign can be attributed to the positive phonon drag contribution that is a result of phonon-induced s-d scattering [73, 86].

The thermal conductivity λ is presented in Fig. 3.2 c. In Metals, the heat transport is dominated by charge carriers. This leads to the increase of λ with decreasing bath temperatures.

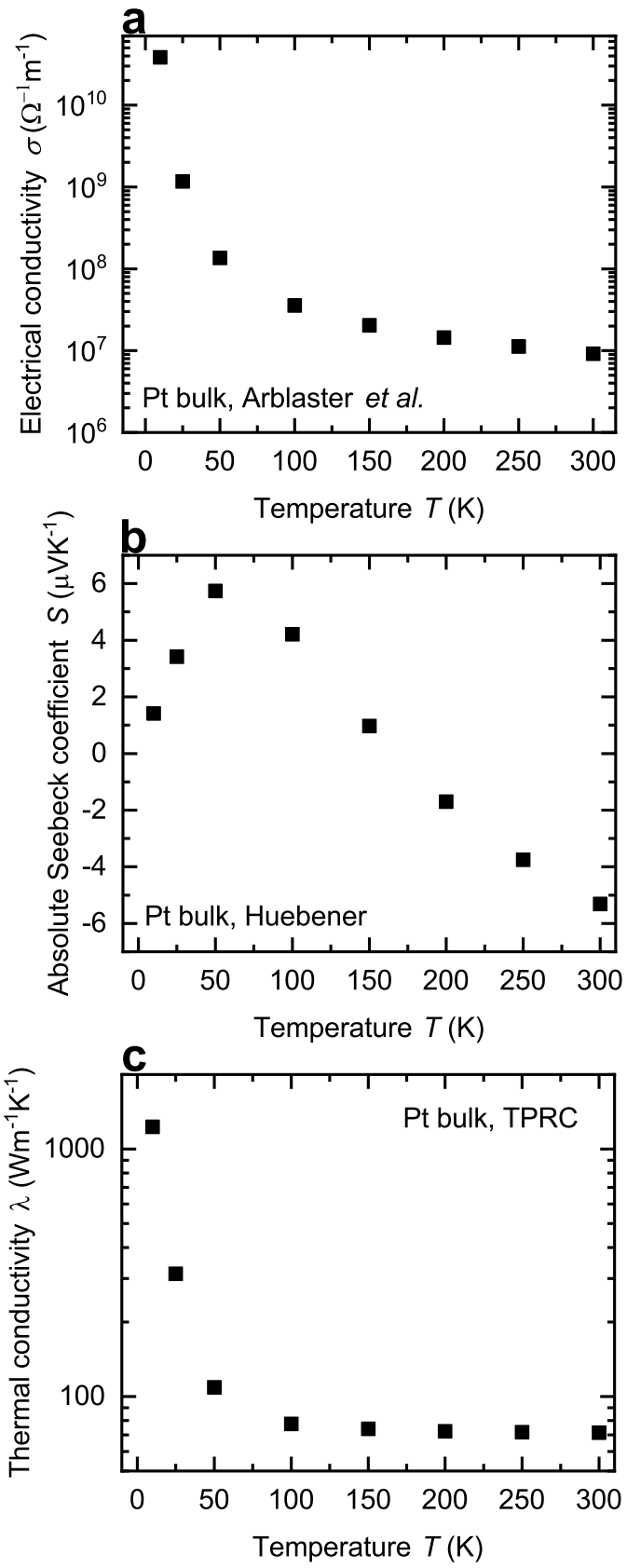

Figure 3.2: **Temperature-dependent transport properties of bulk platinum.** **a**, Electrical conductivity σ. **b**, Absolute Seebeck coefficient S. **c**, Thermal conductivity λ. The values are taken from Ref. [90] (σ), Ref. [28, 41] (S), Ref. [91, p. 269] (λ).

Current state of research: Changes of the transport properties of thin films compared to the bulk material

The transport properties of platinum as a bulk material are well-known [28,41,90,91]. However, the transport properties will change if the structure size of platinum is reduced from bulk to thin films or nanowires [1, 28, 41, 92].

In general, there are publications that examine the electrical and thermal properties of thin platinum films and platinum nanowires [92–95] . In contrast, there are only a few studies that investigate the Seebeck coefficient of micro- or nanopatterned platinum [28, 41, 96]. This is interesting, because platinum is an important Seebeck reference material both as a bulk material and as a micro- and nanopatterned material [19,24–26]. In the following, a selection of articles of various authors is presented that investigate the transport properties of thin platinum films and platinum nanowires.

In 1980, the electrical conductivity of ultra thin platinum films with a thickness of less than a 1 nm was investigated in Ref. [93]. σ is significantly reduced due to the very small thickness and the resulting size effects [93].

Over the next few years, not only the electrical properties were examined, but also the thermal properties. Q. Zhang *et al.* investigated the thermal conductivity of Pt films with a thickness ranging from 15 nm up to 63 nm [94]. They showed that λ is reduced compared to the bulk mainly caused by grain boundary scattering [94].

X. Zhang *et al.* even showed that the thermal conductivity is less than half of the bulk value [95].

In 2009, Vöklein *et al.* determined the electrical and thermal conductivity of polycrystalline Pt nanowires with a diameter of about 100 nm [92]. They showed that σ is reduced by a factor of 2.5 and λ is reduced by a factor of 3.4 compared to the bulk material at room temperature due to boundary and surface scattering [92].

Seebeck measurements of thin platinum films or nanowires are rare. Salvadori *et al.* used a thermocouple consisting of thin platinum and gold films for thermoelectric measurements in 2006 [96]. The thickness of the Pt films varied between 2.2 nm and 166 nm while the thickness of Au was kept constant at 144 nm [96]. They investigated the thickness dependence of the relative Seebeck coefficient of this thermocouple and they showed that with decreasing thickness the relative Seebeck coefficient also decreases [96]. However, the absolute Seebeck coefficient of the platinum and gold films was not determined. But this is crucial in order to determine the transport properties of a material correctly.

Very important research on the absolute Seebeck coefficient of platinum was done by Huebener [28, 41]. He investigated the temperature dependence of Pt foils with a thickness from 1.58 μm up to 8.03 μm [28, 41]. He showed that the absolute Seebeck coefficient is reduced compared to the bulk value which was attributed to the influence of size effects [28, 41]. However, due to the relatively thick foils, the difference between the absolute Seebeck coefficient of the foils and of the bulk materials is between 0.01 $\mu\mathrm{VK}^{-1}$ and 0.1 $\mu\mathrm{VK}^{-1}$ in the temperature range between 20 K and 300 K [28,41]. This thesis closes an important gap in the field of thermoelectric characterization of thin platinum films. Here, the absolute Seebeck coefficient of thin platinum films in the range from 22 nm to 197 nm is given.

3.2 Bulk silver and silver nanowires

Structural and transport properties

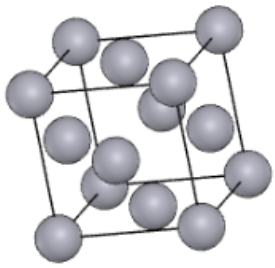

Figure 3.3: **Crystal structure of silver.** Face-centered cubic crystal structure of silver. Image taken from Ref. [97].

Bulk silver (Ag) is a noble metal with an electron configuration of $4d^{10}5s^1$ [63]. The Debye temperature is about 215 K [63]. It crystallizes in a face-centered cubic structure [63]. The crystal structure is given in Fig. 3.3.

At 300 K, the electrical conductivity of Ag bulk is $\sigma = 61 \cdot 10^6\,\Omega^{-1}\mathrm{m}^{-1}$ [98], the absolute Seebeck coefficient is $S = 1.5\,\mu\mathrm{VK}^{-1}$ [38] and the thermal conductivity is $\lambda = 427\,\mathrm{Wm}^{-1}\mathrm{K}^{-1}$ [91, p. 269].

Fig. 3.4 a shows the electrical conductivity σ of bulk silver versus bath temperature T. σ is increasing with decreasing temperature. Silver is the metal with the highest electrical conductivity of all metals [33].

The temperature-dependent absolute Seebeck coefficient S of Ag is depicted in Fig. 3.4 b. The sign of S is positive over the entire temperature range. This can be attributed to a mechanism based on electron-electron scattering [73, 84]. The Seebeck coefficient decreases with decreasing bath temperature. Above 150 K, the temperature dependence of S is linear which can be attributed to the thermodiffusion contribution. The phonon drag peak can be observed at 30 K.

The thermal conductivity λ increases with decreasing bath temperature. This is shown in Fig. 3.4 c. The increase can be explained by Wiedemann-Franz relation. Electrons are the dominant heat carrier type and the high σ leads also to a high λ. Silver is the metal with the highest thermal conductivity of all metals [33].

Current state of research: Changes of the transport properties of nanowires compared to the bulk

Bulk silver has the highest electrical and thermal conductivity of all metals [33]. For this reason, there has been a great interest in micro- and nanostructures of silver [12,39,40]. While the transport properties of bulk silver are well-known [34–38], they will change if the structure size is reduced. A selection of papers is presented in the following which investigate the transport properties of thin silver films and silver nanowires [21, 37, 42, 43, 48].

Yu *et al.* investigated the resistivity and the Seebeck coefficient of thin silver films with a thickness ranging from 71.2 nm to 270 nm at room temperature in 1973 [43]. They found that the resistivity increases with decreasing film thickness and that a decrease of the thickness leads to an increase of the difference between

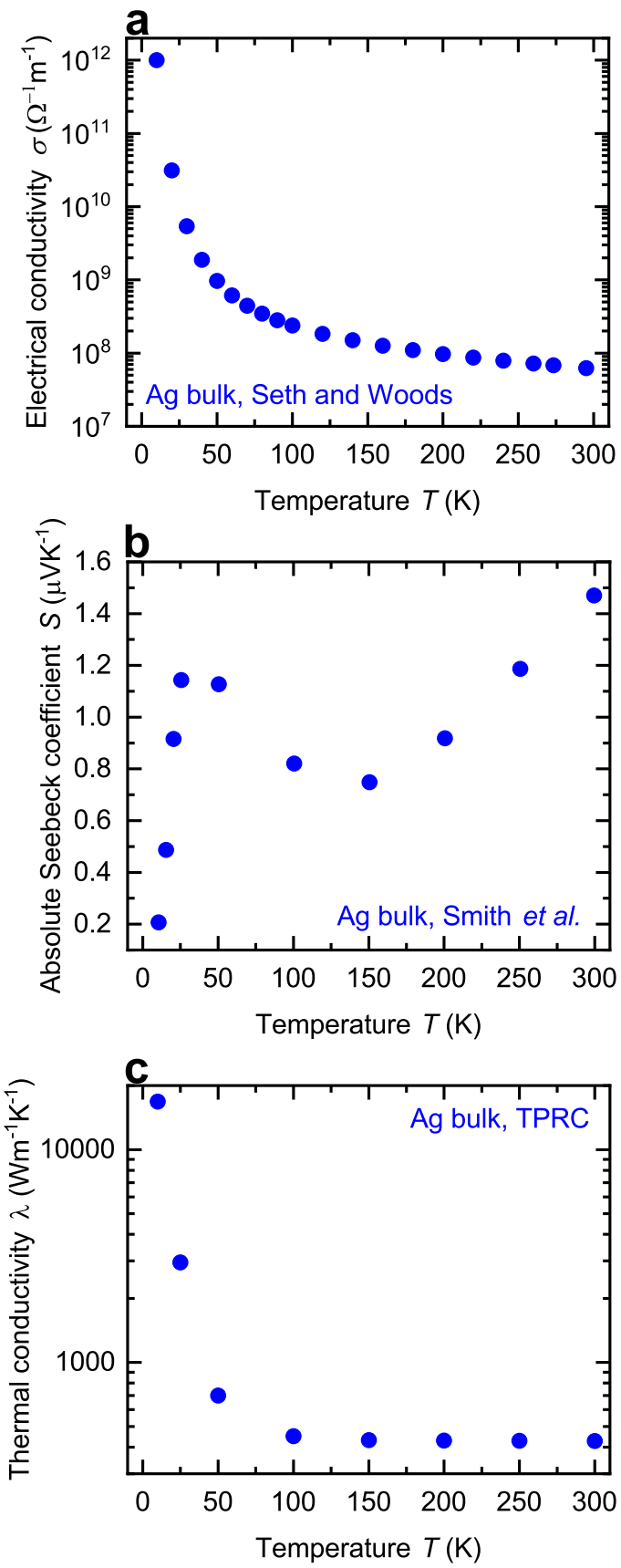

Figure 3.4: **Temperature-dependent transport properties of bulk silver. a** Electrical conductivity σ. **b** Absolute Seebeck coefficient S. **c** Thermal conductivity λ. The values are taken from Ref. [98] (σ), Ref. [38] (S), Ref. [91, p. 348] (λ).

the absolute Seebeck coefficient of the thin film and the bulk material [43]. The thickness dependency was also proven by Rao *et al.* [37].

Zhu *et al.* determined the Seebeck coefficient of nanostructured silver and investigated the influence of heat treatment on the thermoelectric properties [42]. They showed that heat treatment leads to an increase of the grain size from 10 nm to 11 nm after 200 °C annealing [42]. Increasing the annealing temperature to 500 °C leads to a further increase of the grain size to 44 nm due to the recrystallization process [42]. As a result, the growth of the grain size leads to an increase of the Seebeck coefficient [42].

There are two important works about the transport properties of silver nanowires. The first is from Cheng *et al.* [48]. They investigated the temperature-dependent electrical and thermal transport in an individual polycrystalline silver nanowire [48]. They showed that the electrical and thermal conductivity are reduced compared to the bulk material [48]. λ is reduced by 55 % compared to the bulk value at room temperature [48]. The reduction of the transport properties was attributed to the fact that the electrical and thermal mean free paths are comparable with the crystal size [48]. However, only one silver nanowire was investigated and Seebeck measurements are missing.

In contrast to Cheng *et al.*, Kojda *et al.* investigated the electrical and thermal conductivity and in addition also the relative Seebeck coefficient of single crystalline silver nanowires [21]. The silver nanowires used in Ref. [21] are from the same batch as used in this thesis. A reduction of the electrical and thermal conductivity with respect to the bulk material was found, this was attributed to surface scattering [21]. However, the absolute Seebeck coefficient of individual silver nanowires was not covered in this paper.

Here, in this thesis, the absolute Seebeck coefficient of silver nanowires is provided. This is important in order to understand the complete influence of nanopatterning on the transport properties.

3.3 Bulk bismuth and bismuth-based nanowires

Structural and transport properties

Bulk bismuth (Bi) is a semimetal with an electron configuration of $4f^{14}5d^{10}6s^{2}6p^{3}$ [63]. The Debye temperature is about 120 K [63]. The anisotropic transport properties that arise from the extraordinary crystal structure of Bi can be described in several ways. This was already proposed by Abrikosov and Fal'kovskiĭ under the expression of "deformation theory" in 1962 [99–101]. The crystal structure can be described by a rhombohedral lattice with two atoms per unit cell [53, 102], see Fig. 3.5 a (red arrows). Furthermore, a hexagonal lattice system with the lattice parameters a and c can also be used in order to describe the crystal structure of Bi, see Fig. 3.5 a (blue arrows). In addition, the crystal structure can be represented by a Cartesian coordinate system with the trigonal axis, binary axis and bisectrix axis, see Fig. 3.5 a (black arrows) [102]. The trigonal and binary axes have multiple rotational symmetry with the corresponding axes in the hexagonal lattice [102]. In order to understand the anisotropic transport properties of Bi, the crystal structure can be translated into a pseudo-cubic lattice as given in Fig. 3.5 b [102]. The pseudocubic lattice representation can be achieved by incorporating two interpenetrating face-centered cubic sub-lattices that are displaced and stretched along the

trigonal axis [102]. The trigonal axis corresponds to the T-point (hole pocket) of the Brillouin zone, see Fig. 3.6, in momentum space and the other axes are denoted as L-points (electron pockets) [102]. As a result of the distortion along the trigonal axis, energy splitting occurs between the T- and L-points, see Fig. 3.10 a. This is the origin of the band overlap between the valence band at the T-point and the conduction band at the L-point and that leads to the semimetallic band structure of Bi [102]. The band overlap is shown in Fig. 3.10 a.

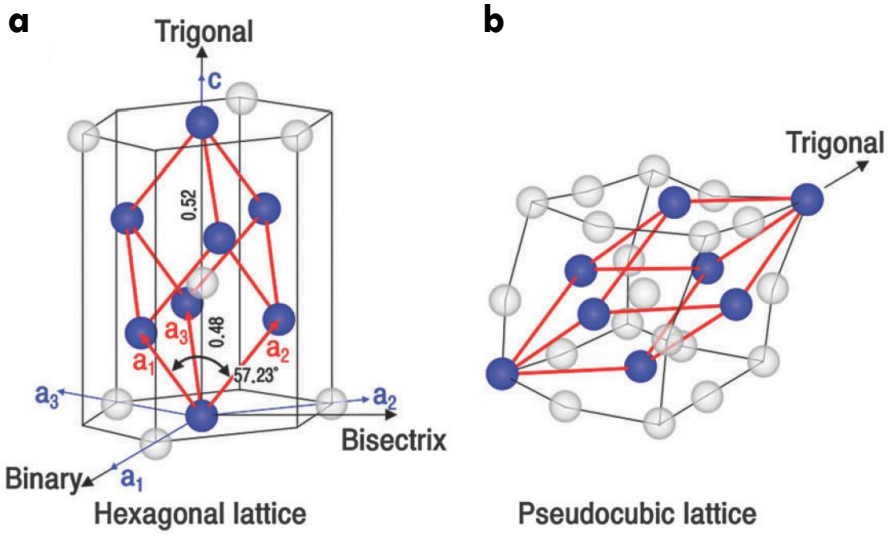

Figure 3.5: **Crystal structure of bismuth.** **a**, Crystal structure described by a rhombohedral lattice (red arrows), by a hexagonal lattice (blue arrows) and in Cartesian coordinate system (black arrows). **b**, Representation of the crystal structure by a pseudo-cubic lattice. Figure from Ref. [102].

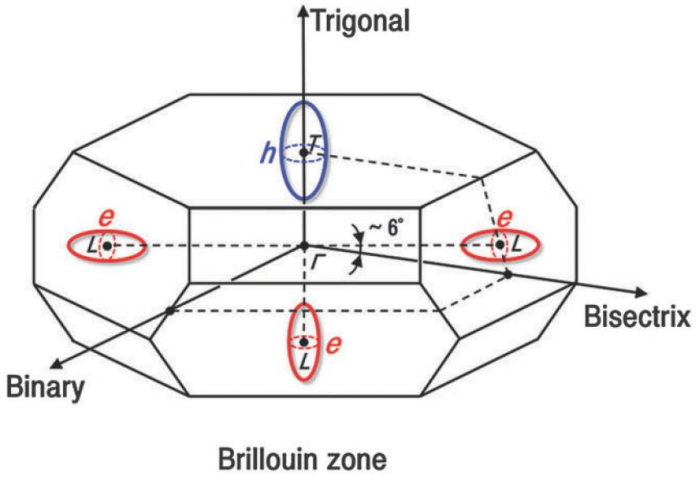

Figure 3.6: **Brillouin zone of bismuth.** Brillouin zone of bulk Bi in momentum space. The trigonal axis corresponds to the T-point (hole pocket). The binary and bisectrix axes are denoted as L-points (electron pockets). Figure from Ref. [102].

Due to the anisotropic transport properties of Bi, in the following the transport properties of Bi bulk are given perpendicular to the trigonal axis because the transport properties of the Bi-based nanowires correspond also to this direction.

The values of the electrical conductivity, the absolute Seebeck coefficient and the thermal conductivity are taken from [53]. At 300 K, the electrical conductivity of Bi bulk is $\sigma = 0.9 \cdot 10^6\,\Omega^{-1}\mathrm{m}^{-1}$ [53], the absolute Seebeck coefficient is $S = -51\,\mu\mathrm{VK}^{-1}$ [53] and the thermal conductivity is $\lambda = 9.9\,\mathrm{Wm}^{-1}\mathrm{K}^{-1}$ [53].

Fig. 3.7 a shows the electrical conductivity σ as a function of the bath temperature T. Bi exhibits a semimetallic-like electrical conductivity. Decreasing bath temperatures lead to an increase of σ. The overall electrical conductivity of Bi is significantly reduced compared to "real" metals like platinum and silver.

The temperature-dependent absolute Seebeck coefficient S of Bi bulk is given in Fig. 3.7 b. The absolute Seebeck coefficient is negative. This means electrons are the dominant contribution to S. In general, the total Seebeck coefficient S_{tot} is determined by a partial contribution of holes and electrons. Theoretical studies revealed that each partial Seebeck coefficient can be larger than S_{tot} [58, 103] but due to the opposite sign of both contributions due to the band overlap, they cancel each other out.

Fig. 3.7 c shows the thermal conductivity λ as a function of the bath temperature T. Decreasing bath temperatures lead to an increase of λ. For bulk Bi it has been shown that phonons are the dominant heat carrier source at low temperatures [53, 104]. As the bath temperatures rises, the charge carrier contribution becomes the dominant part [53, 104].

Concept of core/shell nanowires

In order to make bismuth (Bi) nanowires more interesting for thermoelectric applications, the concept of a core/shell structure, see Fig. 3.8, was applied to Bi nanowires [59–61]. The idea behind this concept is that the additional shell leads to structural changes in the core which in turn change the transport properties of the core [60, 61]. This concept is opposed to other options for changing the thermoelectric properties, such as low dimensional and quantum size effects [58, 105–108]. Quantum size effects have disadvantages, such as an increase in the effective carrier mass due to electron-hole interaction, a significant reduction of the mean free path due to the reduced structure sizes and arising of surface state effects [61,103,109,110].

The core/shell concept approaches band engineering for thermoelectric materials in a new way without a significant reduction of the sample size compared to the quantum size approach. The first successful implementation of the core/shell concept was demonstrated with bismuth/tellurium (Bi/Te) nanowires [59–61]. Tellurium is a seminconductor with a direct band gap of $E_{\mathrm{g}} = 0.33\,\mathrm{eV}$ [111, p.150], electrical conductivity of $\sigma = 185\,\Omega^{-1}\mathrm{m}^{-1}$ [112], an absolute Seebeck coefficient of $400 - 500\,\mu\mathrm{VK}^{-1}$ [113, 114] and a thermal conductivity of about $\lambda = 2\,\mathrm{Wm}^{-1}\mathrm{K}^{-1}$ [113]. Tellurium is suitable as a shell material due to its hexagonal lattice [111, p. 6] and the corresponding lattice parameters. The lattice parameters of Te are $a_{\mathrm{Te}} = 0.4457\,\mathrm{nm}$ and $c_{\mathrm{Te}} = 0.5929\,\mathrm{nm}$ [61], [111, p. 14]. The lattice parameters of Bi are $a_{\mathrm{Bi}} = 0.4546\,\mathrm{nm}$ and $c_{\mathrm{Bi}} = 1.1862\,\mathrm{nm}$ [61]. This difference leads to a lattice mismatch-induced compressive strain that yields a reduction in the unit cell length along the trigonal axis of the Bi core [60, 61], see Fig. 3.9. As a result the crystal anisotropy is decreased and thus the band overlap by the energy splitting between T- and L-points is also decreased [60,61], see Fig. 3.10. This can induce the semimetal-to-semiconductor transition [60, 61]. This transition can lead to a reduction of the compensation of the partial Seebeck coefficients of electrons and holes, so that the

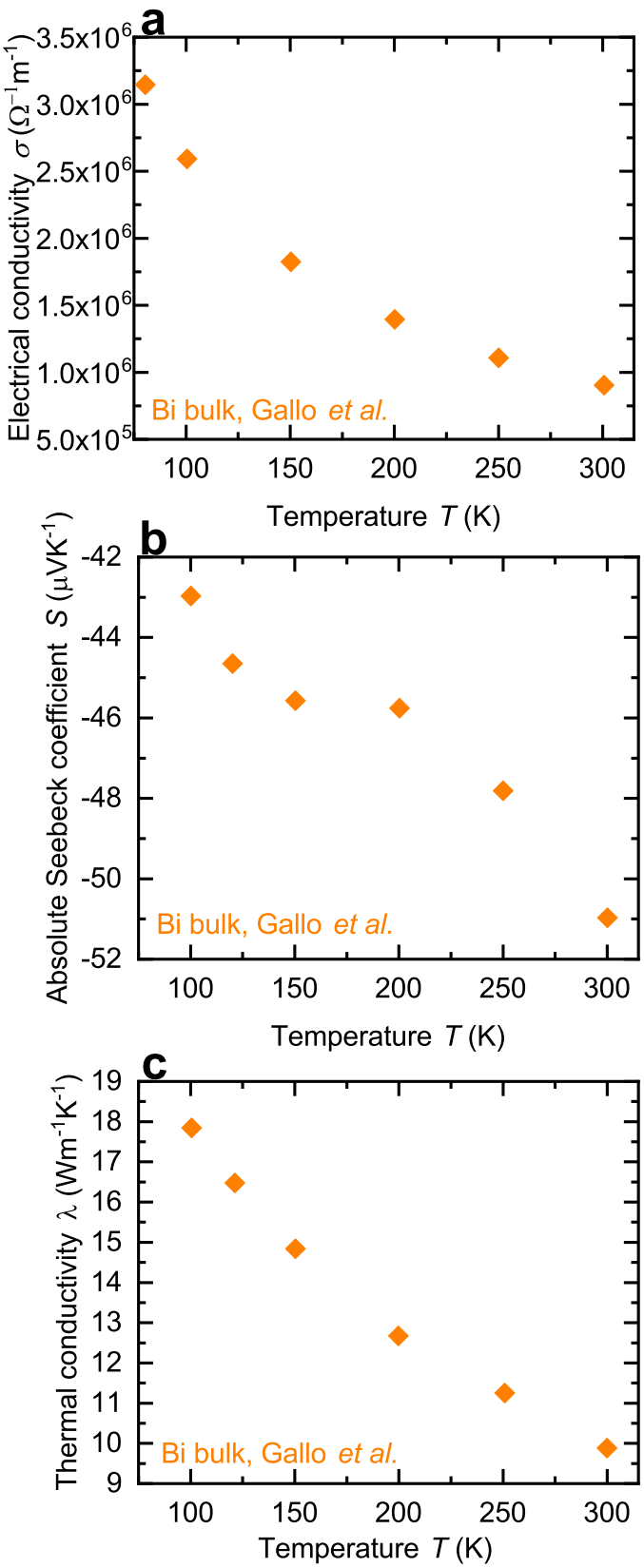

Figure 3.7: **Temperature-dependent transport properties of bulk bismuth (perpendicular to the trigonal axis). a**, Electrical conductivity σ. **b**, Absolute Seebeck coefficient S. **c**, Thermal conductivity λ. The values are taken from Ref. [53].

resulting Seebeck coefficient can be increased [60, 61]. Furthermore, the core/shell structure has another advantage. The thermal conductivity of the Bi core is reduced because of the rough interface between the core and the shell material which leads to more phonon scattering events [59–61].

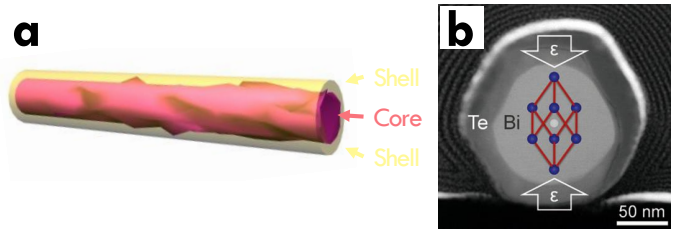

Figure 3.8: **Core/shell nanowire.** **a**, Sketch of a core/shell nanowire. The shell covers the core of the nanowire over the entire length. Figure from Ref. [59]. **a**, Cross-sectional transmission electron microscopy image of a core/shell nanowire with a bismuth (Bi) core and a tellurium (Te) shell. The strain ϵ is along the trigonal axis. Figure from Ref. [61].

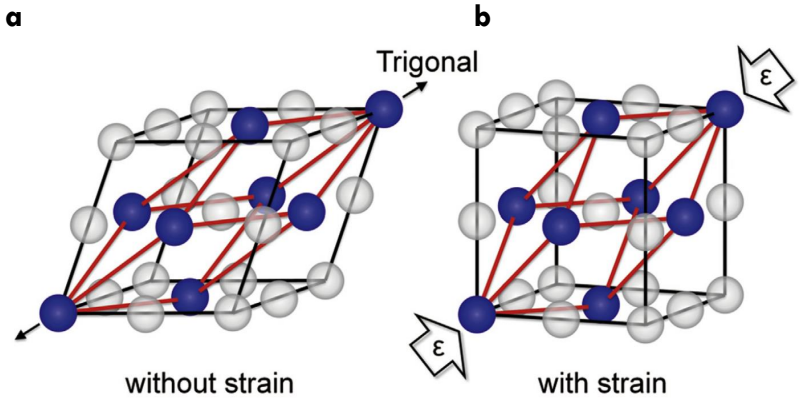

Figure 3.9: **Bismuth crystal structure with and without strain.** **a**, Bi crystal structure without strain. **b**, Transition to a near-cubic structure with strain ϵ along the trigonal axis. Figure from Ref. [61].

Current state of research: Changes of the transport properties of core/shell nanowires compared to the bulk

Due to its highly anisotropic Fermi surfaces and thus the crystal direction-dependent transport properties, bismuth is under investigation for years [53, 58, 99, 101, 115]. Bismuth has a large mean free path of the electrons (100 nm at 300 K up to a few hundred micrometers at 4 K) and a large Fermi wavelength (70 nm) [56,103,116,117], [118, p. 273]. For this reason, finite size and quantum size effects are expected to occur in Bi nanowires with relatively large diameters ($\approx$ 100 nm). This makes them to a subject of interest. In the following, an overview of scientific work is presented that deals with the transport properties of bulk bismuth and bismuth nanowires.

Two very important works on the transport properties of Bi bulk were done by Chandrasekhar and Gallo *et al.* Chandrasekhar determined the absolute Seebeck coefficient of bismuth single crystals in 1959 [115]. Four years later, Gallo

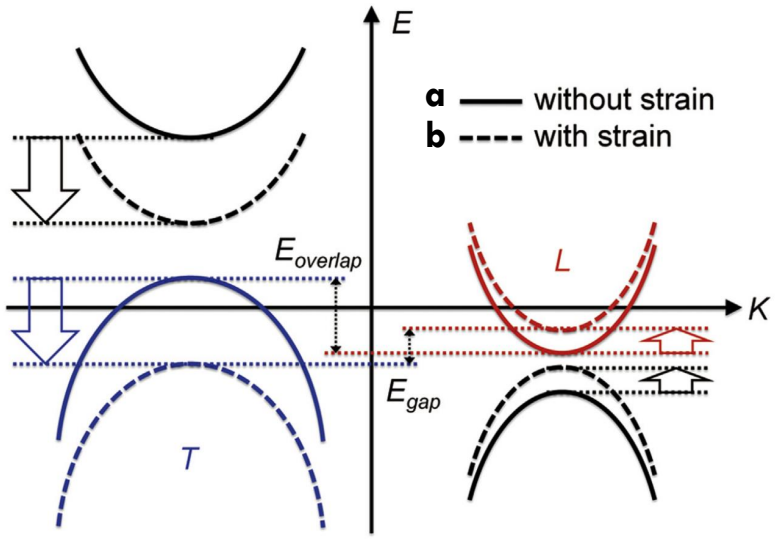

Figure 3.10: **Energy E diagram of the bismuth electronic band structure with and without strain as a function of the K-vector in momentum space at the T- and L- points. a**, Without strain (solid lines): Energy overlap E_{overlap} between the valence band edge at the T-point and the conduction band edge at L-point. **b**, With strain (dashed lines): Compressive strain leads to a band gap opening E_{gap}. Figure from Ref. [61].

et al. made important investigations concerning the electrical and thermal conductivity and the absolute Seebeck coefficient of Bi bulk [53]. They connected the temperature-dependent transport properties with investigation of the band overlap and the resulting influence of electrons and holes and they investigated the transport properties as a function of the crystal directions parallel and perpendicular to the trigonal axis [53].

Years later, Heremans and Thrush presented thermoelectric measurements of an 200 nm Bi nanowire array [119]. They observed a lower Seebeck coefficient compared to the bulk material and attributed this to the compensation between the negative contribution of electrons and the positive contribution of holes [119].

For a better understanding of the transport properties of Bi nanowires, individual nanowires are preferred over arrays of nanowires. For this reason, methods to grow individual nanowires are needed. Ham, Shim *et al.* developed a new growth method for single crystalline nanowires in 2009 and demonstrated the feasibility of this method with Bi_2Te_3 nanowires [120]. They called this method *On-Film Formation of Nanowires (OFF-ON)* [120]. This growth method was also used for the Bi-based nanowires which are used in this thesis. Moreover, another review article about Bi nanowires showed the influence of the different growth methods on the transport properties [102].

Various investigations about the transport properties of pure Bi nanowires have been released in the last couple of years. Roh, Hippalgaonkar *et al.* observed an anisotropy in the thermal conductivity of individual single-crystalline bismuth nanowires [121]. A four-fold difference of λ between different growth directions was determined [121]. The difference was attributed to a change of the mobility that arises from a change of the band effective mass [121].

The anisotropy of the transport properties was also confirmed by theoretical calculations of Murata *et al.* [122]. They determined the electrical resistivity and

the absolute Seebeck coefficient as a function of the bath temperature, the nanowire diameter and the transport direction along the binary, bisectrix and trigonal axes [122]. A significant variation of S along the different directions was calculated [122].

A full thermoelectric review of Bi nanowires was published in 2015 [103]. The authors investigated the diameter-dependent resistivity, Seebeck coefficient and thermal conductivity [103]. However, the resistivity and the relative Seebeck coefficient were determined with one measurement platform of the same nanowire and the thermal conductivity on another platform and another nanowire. The measurement results of nanowires with comparable diameters were used to determine the figure of merit ZT. A maximum increase of ZT to 0.28 at a diameter of 109 nm was observed [103]. This was attributed to the reduced thermal conductivity of the Bi nanowires [103].

In 2011, Kang, Roh *et al.* presented for the first time the possibility to reduce the thermal conductivity of Bi nanowires with a new approach by sputtering a shell material (tellurium) onto the Bi core [59]. They showed that these core/shell nanowires have a rough interface between the Bi core and Te shell and can reduce λ due to an additional scattering phase [59].

These core/shell nanowires raised more interest in the following years because of the possibility to increase the figure of merit. Kim *et al.* showed in two articles that Bi/Te core/shell nanowires can indeed improve ZT [60, 61]. They measured the electrical and thermal conductivity and the relative Seebeck coefficient. The strain-engineered Bi/Te core/shell nanowires exhibit a reduction of the anisotropy of the Bi core [60, 61]. This leads to an improvement of the transport properties of the Bi core related to an increase of the figure of merit. In detail, the electrical conductivity is slightly decreased compared to pure Bi nanowires, but the Seebeck coefficient is significantly increased [60, 61]. Moreover, the thermal conductivity is decreased compared to pure Bi nanowires at room temperature [60, 61]. However, σ and S were determined from the same Bi/Te nanowires with one measurement setup and the thermal conductivity with a different setup and different nanowires.

A recent work by Moon, Kim *et al.* reports about the electrical conductivity and the Seebeck coefficient of Bi/Sn and Bi/Sb core/shell nanowires [62]. They showed a reduction of the Seebeck coefficient compared to pure Bi nanowires that is attributed to a doping effect of the shell material [62].

Despite the great interest in Bi-based nanowires, it has so far not been possible to carry out a complete thermoelectric characterization on one and the same nanowire. However, this is very important for a comprehensive understanding of the transport properties. This gap is closed within the scope of this thesis.

Chapter 4

Experimental methods

4.1 Measurement devices and cryostats

Measurement devices

A Keithley 2401 Low Voltage SourceMeter, a Keithley 6221 Current Source, a Keithley 2182 Nanovoltmeter and a Keithley 7001 Switch/Control Mainframe with two 7012-C Matrix cards have been used in this work for all transport measurements. The Keithley 2401 serves as a direct current or direct voltage source and it was mainly used to apply a heating current at the heaters for the Seebeck measurements. The Keithley 6221 and Keithley 2182 are a combination of a precise direct and alternating current source and a low-noise nanovoltmeter, respectively. This device combinations has been used for all two-terminal and four-terminal measurements and to the measure the thermovoltage. The Keithley 7001 Switch/Control Mainframe can switch between up to 16 contact combinations. All devices were controlled manually or via the GPIB computer interface. LabVIEW (National Instruments) programs were used to automate the measurements. Additional measurement instructions are given in the appendix.

Cryostats

In this thesis, two cryostats have been used in order to perform the temperature-dependent thermoelectrical measurements. The KONTI-IT (CryoVac GmbH & Co KG) flow cryostat and ARS DE-202A-DMX-20 (Advanced Research Systems, Inc.) closed cycled cryostat. The KONTI-IT allows measurements in a temperature range between $T = 1.3\,\mathrm{K}$ and $T = 320\,\mathrm{K}$ and it consists of a multi-walled stainless steel container with a central sample chamber, integrated reservoirs for liquid nitrogen (LN_2) and liquid helium (LHe) and a chamber for a thermal insulating vacuum. The sample is located at the lower end of a measuring rod in a sample holder. The sample chamber is filled with helium gas. Since it is necessary to measure the thermal conductivity in a vacuum, the sample chamber can also be evacuated. The temperature of the sample chamber is stabilized by an electric heater, which is controlled by a temperature controller.

The ARS DE-202A-DMX-20 allows measurements in a temperature range between $T = 12\,\mathrm{K}$ and $T = 450\,\mathrm{K}$ and works on a different cooling principle. Compressed He-4 gas is pumped into the upper part of the cryostat. This gas reaches the cold finger through a rotary valve. Thus, the cooled helium gas is exchanged

with heated up gas, which gets to the reprocessing system in order to be compressed again. Two regenerators are arranged so that the lowest temperature prevails at the lowest point of the cryostat. The sample holder, which consists of a copper block is located at this point and it is in thermal contact with the cold finger. The sample chamber is in a vacuum environment. The temperature of the sample chamber is stabilized by an electric heater, which is controlled by a temperature controller.

4.2 Microlithography and sputtering

Lithography plays an important role in semiconductor and microsystem technology. The process allows the transfer of a computer-aided design on a substrate or a sample by means of exposure of photoresist with an electromagnetic radiation of a defined wavelength and subsequent development [123][p. 1-6]. The minimum structure size that can be patterned is determined by the wavelength of the applied radiation. For the preparation of microstructures visible light or UV radiation is used. For the preparation of nanostructures smaller wavelengths are required. This can be realized with electron beam lithography.

Different resists based on organic polymers are available depending on the process that is used. These can be roughly divided into positive and negative resists. A positive resist changes its chemical structure through exposure so that it becomes soluble in the developer fluid. Negative resist shows the opposite behavior. It is soluble in developer fluid and becomes insoluble when exposed to light.

The photolithography process, which has been used in this work, can be divided into several steps. The first step includes the cleansing of the substrate from dust, water and organic residuals with ultrasonic baths and solvents like acetone and isopropyl. After that, a thin photoresist film (typically $0.1 - 2\,\mu$m [123][p. 2]) is applied to the substrate using a spin coater. The coated substrate is then heated (soft bake) to compress the resist film and allow the excess solvent to evaporate. This is followed by the exposure of the substrate. The polymer chains are broken for the positive resist. After exposure, the sample is placed in the developer fluid which leads to the dissolution of the exposed resist.

The remaining resist on the substrate can be further processed in the sputter coater by performing the metalization. For this, an argon plasma is generated in the sputter coater. The argon ions are accelerated towards the target material in the sputter coater and thus release atoms from the target. As a result, a thin film is gradually formed on the substrate.

In the next step during the the lift-off, the excess sputtering material is removed from the substrate by dissolving the remaining resist and only the patterned area remains on the substrate.

In this work, the DMO MicroWriter ML3 has been used for the exposure step of the samples. It has a laser with a wavelength of 405 nm that can reach a resolution of about $1\,\mu$m. The sputter coater Q300T D from Quorum Technologies was used for the metalization process. A sketch of the lithography process is presented in Fig. 4.1.

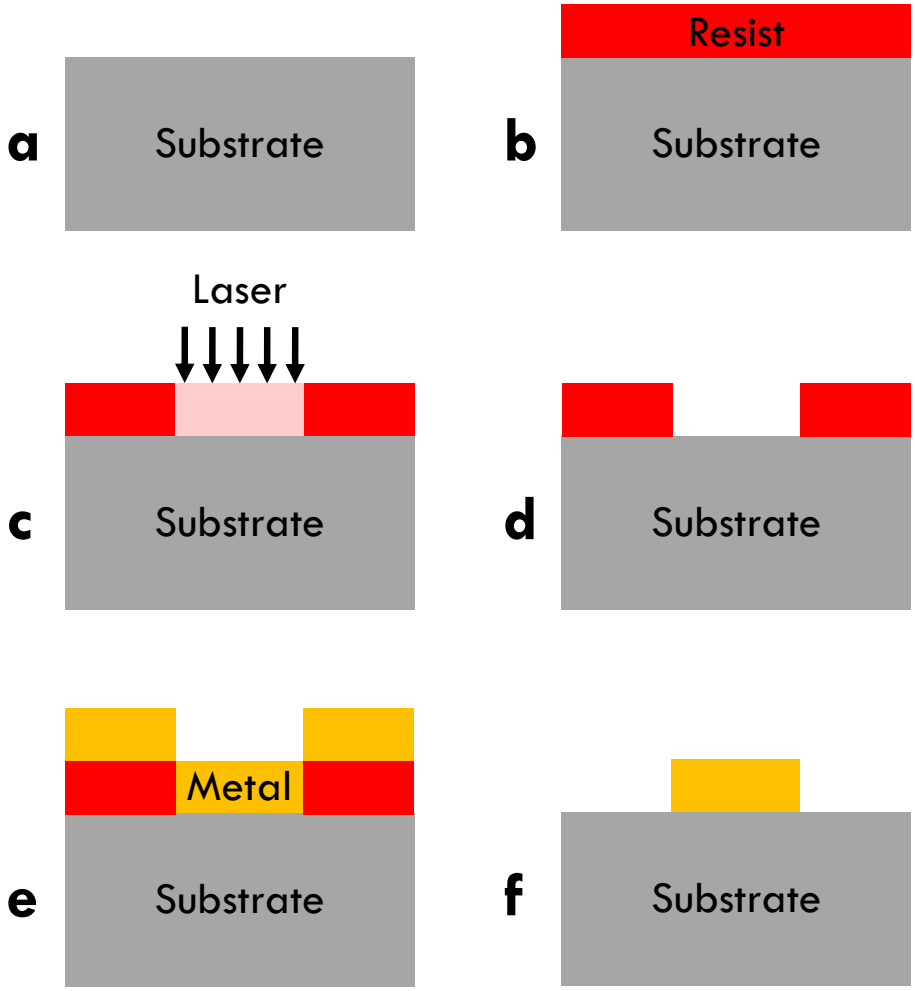

Figure 4.1: **Sketch of the lithography process.** **a**, Cleaning process of the substrate. **b**, Resist is applied on the substrate by a spin coating process. **c**, Transfer of a computer-aided design on the substrate by laser exposure of the resist. **d**, Dissolution of the exposed resist in the developer fluid. **e**, Metalization process by means of sputtering. **f**, Lift-off process removes the excess sputtering material.

4.3 Electron beam-induced deposition (EBID)

Electron beam-induced deposition (EBID) is a technique based on the local dissociation of precursors by an electron beam of a scanning electron microscope (SEM) [124–126]. In order to prepare the mechanical and electrical connection of nanowires, a solid precursor has to be heated, so that it becomes gaseous. A gas injection system (GIS) provides the gaseous precursor at the substrate. There, the precursor adsorbed to the surface of the substrate. When the electron beam of the SEM comes into the vicinity of the adsorbed gas molecules, they become dissociated and the contact material is deposited [124–126]. The volatile components of the gaseous precursor are removed. In general, structures made by EBID are characterized both by the flexibility of the shapes to be written and by their local resolution [124]. The writing process is mainly influenced by parameters such as the accelerating voltage and beam current, the time that the electron beam stays at one point (dwell time), the distance of the electron beam between consecutive points in the target area (line spacing and step size) and the number of repetitions of the writing process (loops). Within the scope of this thesis three different precursor materials have been used in order to prepare the EBID contacts. Two precursors are based on platinum ($(CH_3)_3\,Pt\,(CpCH_3)$ and $C_9H_{16}Pt$). One precursor is based on tungsten ($W(CO)_6$). A detailed discussion of the precursor material and other influences are discussed in the next chapter.

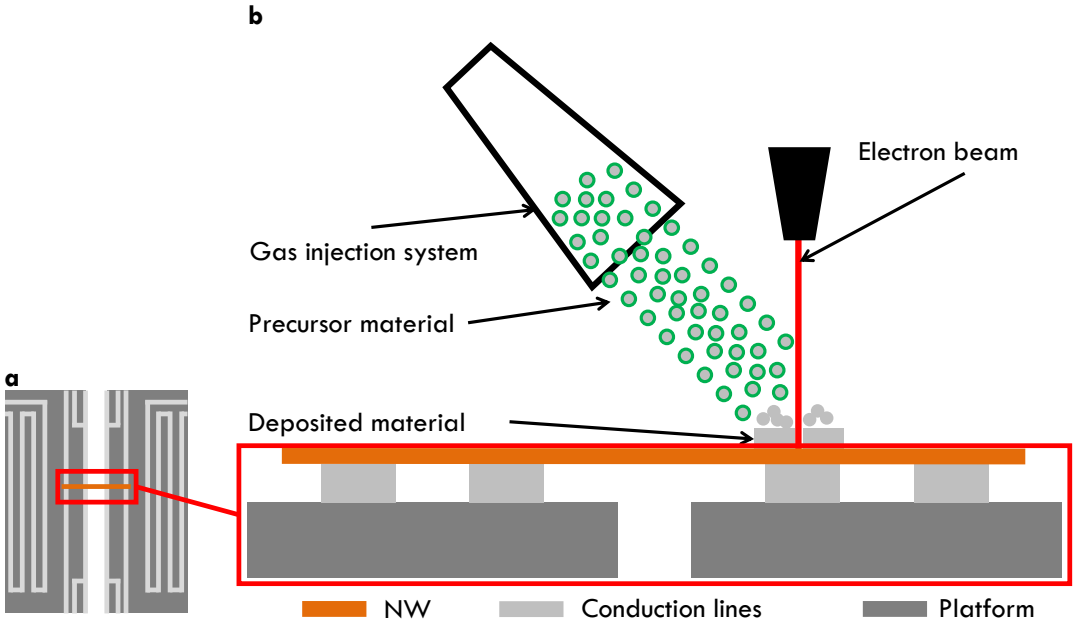

Figure 4.2: **Sketch of the electron beam-induced deposition (EBID). a**, Top-view of a nanowire lying on a measurement platform. **b**, Cross-sectional view of a nanowire lying on a measurement platform. The gas injection system provides the gaseous precursor at the substrate. The electron beam of the scanning electron microscope dissociates the gas molecules and the contact material is deposited. Figure after Ref. [124].

4.4 Methods for structural characterization

Atomic force microscopy

An atomic force microscope (AFM) allows to map the morphology of a sample surface with a high resolution. The AFM consists of a cantilever with a nanoscopic fine tip. When measuring with the AFM, this tip is scanned over the sample and atomic forces (e.g. van der Waals) between the sample surface and the tip cause a deflection of the cantilever. A laser beam, which is directed on the back of the cantilever, and a photodiode are used to detect the deflection of the cantilever. The change of position or bending of the cantilever is converted by a computer program into a three-dimensional surface topography [127]. A sketch of an AFM is given in Fig. 4.3.

An atomic force microscope can be operated in two different modes. These can be determined according to the forces, which are acting between the tip and the surface. In contact mode, the tip is in contact with the surface and the repulsive force is measured. For the non-contact mode, the cantilever oscillates with a defined vibration frequency over the surface of the sample and deviations from this frequency are being measured [127].

In this thesis an AFM of the manufacteur Nanosurf was used to determine the thickness of thin platinum films. The measurements were carried out both in contact mode and in non-contact mode.

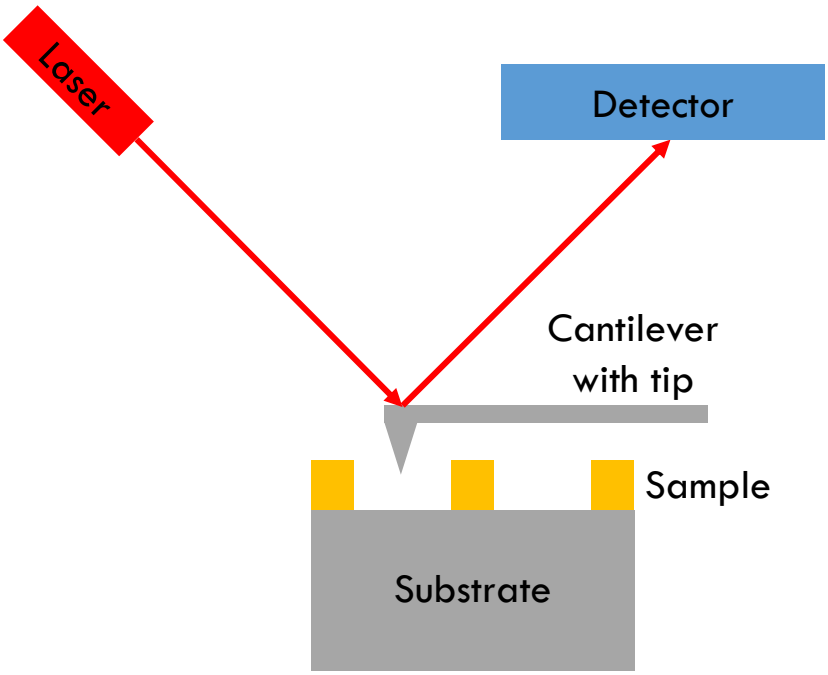

Figure 4.3: **Sketch of an atomic force microscope (AFM).** An AFM consists of a cantilever with a fine tip. This tip is scanned over the sample and atomic forces between the sample surface and the tip cause a deflection of the cantilever. A laser beam, which is directed on the back of the cantilever, and a photodiode are used to detect the deflection of the cantilever. Figure after Ref. [127].

Optical microscopy

A classical optical microscope consists of an objective lens or lenses, an ocular and a light source with a condenser. The objective lens creates an inverted, real and magnified intermediate image in the focal plane of the sample. This image is magnified with the ocular and can be viewed [128, p. 6]. Conventional light microscopes can separate two distinct objects from each other with the minimum distance $x_{\min}$ if the Abbe criterion is fulfilled. $x_{\min}$ is given by

$$x_{\min} = 1.22 \frac{\lambda}{2n \sin(\alpha)}, \tag{4.1}$$

where $n \sin(\alpha)$ is the numerical aperture of the microscope. Thus, the resolution is mainly limited by the wavelength of visible light [129, p. 354-355].

In this thesis, two digital microscopes (PLu neox Optical Profiler from Sensofar and the VHX-6000 from Keyence) were used for imaging nanowires, thin films and measurement platforms. Furthermore, the microscopes have been used to transfer and position nanowires on a thermoelectric nanowire characterization platform.

Scanning electron microscopy

The basic principle of a scanning electron microscope (SEM) for imaging is to use the interaction between the incident primary electron beam and the atoms of the sample surface [130, p. 1-12]. Electrons are released by thermal emission or field emission from a cathode. After the emission, the electrons between the cathode and anode are accelerated by an applied electrical field. The primary electron beam is parallelized by condenser lenses and focused by objective lenses. After focusing through the objective lens, the electron beam hits the sample and interacts with the surface atoms. The interaction area is called the excitation volume. The range R of the electrons in the sample depends on the electron energy and on the density or thickness of the sample and is in the range from a few nanometers to micrometers. Depending on the range, X-rays, Auger, back-scattered and secondary electrons can be generated. This relationship is shown schematically in Fig. 4.4. Backscatter and secondary electrons are generally used for imaging. These electrons are registered by the detector. The signal is then amplified and displayed on the screen. A high vacuum in the sample chamber is required in order to reduce interactions between electrons and other particles, so that the primary electron beam can reach the sample.

In this thesis, the PIONEER Two scanning electron microscope from Raith Nanofabrication has been used for imaging different nanowires and for the preparation of the electron beam-induced deposition (EBID) contacts with precursors based on platinum ($C_9H_{16}Pt$) and tungsten ($W(CO)_6$). Furthermore, the Nova 600 NovaLab Dual Beam Focused Ion Beam Scanning Electron Microscope of the Leibniz Institute for Crystal Growth (IKZ) in Berlin was used to perform EBID of a platinum-based precursor ($(CH_3)_3 Pt (CpCH_3)$) on silver nanowires and Bi/Te core/shell nanowires.

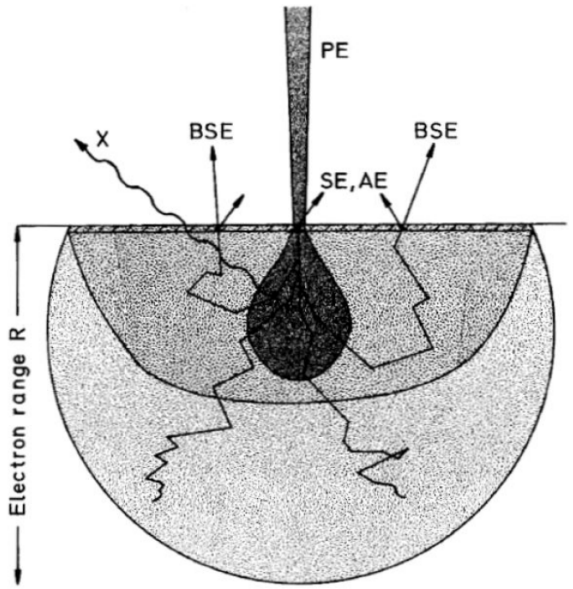

Figure 4.4: **Sketch of the excitation volume.** Representation of the excitation volume with the electron range R, with the incident primary electron beam (PE) and the origin and depth of information of secondary electrons (SE), backscattered electrons (BSE), Auger electrons (AE) and X-rays (X) [130, p. 5].

Transmission electron microscopy

As for the SEM, electrons are generated by thermal emission or field emission and accelerated by a high voltage (e.g. 200 kV) in a transmission electron microscope (TEM). The electron beam is focused on the optical axis of the TEM using multiple condenser lenses and after that impinges the sample. The main difference between a SEM and a TEM is that the electron beam passes through the sample. For this reason, TEM samples have to be very thin (< 100 nm). The electrons are scattered according to the atomic structure of the sample and can therefore provide information from inside the sample [131]. Transmission electron microscopy distinguishes between elastic (interaction between beam electrons and sample atoms) and inelastic (interaction between beam electrons and sample electrons) scattering processes [131]. Elastically scattered electrons are used for image generation in conventional transmission electron microscopy. Inelastically scattered electrons lose energy on their way through the sample and thus carry element-specific information with them [131]. Magnifications that allow the lattice imaging of a crystalline sample are referred to as high-resolution transmission electron microscopy (HRTEM) which is based on the coherence of the electron wave and the phase differences of the electron waves. High-angle annular dark-field scanning transmission electron microscopy (HAADF-STEM) is a method in which the electron beam is scanned very finely over the sample in order to investigate the local structure of a sample on the atomic scale. Selected area electron diffraction (SAED) refers to a mode that reveals the electron diffraction pattern, which is the Fourier transform of the crystal lattice. SAED can be used to determine the crystal structure and orientation of the sample. Information about the chemical elements and their spatial distribution in the sample can be obtained by energy-dispersive X-ray spectroscopy (EDX). The electron beam can excite electrons of the inner shell of the sample. If electrons have been excited this way, electrons from higher energy states are able to drop into

the lower states under the emission of characteristic X-rays from the sample. This radiation can be identified by a detector.

In this thesis, the JEM 2200FS transmission electron microscope from JEOL has been used for imaging and analysis of different nanowires.

X-ray diffraction

X-ray diffraction (XRD) is a method to determine the structural properties of a sample. Monochromatic X-rays can be regarded as a plane wave with the wavelength λ that strikes a crystal at an angle of incidence θ to the crystal plane. Constructive interference of the scattered waves occurs, if the Bragg condition is fulfilled [63, p. 66],

$$n\lambda = 2d\sin(\theta). \tag{4.2}$$

Where d is the lattice plane distance of the crystalline material and n is an integer. Apart from information regarding the crystal structure of a sample, X-ray diffraction is used to determine the average crystallographic grain size D_{S} of thin platinum films. D_{S} can be estimated by the Scherrer equation [132, 133]

$$D_{\mathrm{S}} = \frac{K\lambda}{\Delta(2\theta)\cos(\theta)}. \tag{4.3}$$

K is a dimensionless shape factor with a value of 0.9, $\lambda = 0.154\,\mathrm{nm}$ is the X-ray wavelength. X-ray experiments have been conducted with a lab-based diffractometer, with a Cu-K_α rotating anode source with a wavelength of $\lambda = 0.154\,\mathrm{nm}$.

Chapter 5

Thermoelectric characterization platforms and contact preparation of individual nanowires

5.1 Thermoelectric micro lab (TML)

Overview and preparation of the TML

A measurement platform has been designed, fabricated and tested within the scope of this thesis in order to investigate the temperature-dependent thermoelectric transport properties of thin metallic films. The usability and feasibility is demonstrated by investigating thin platinum films.

The so called thermoelectric micro lab (TML) was designed with lithography on a 5 mm x 9 mm glass substrate and it is shown in Fig. 5.1.

The general steps of a lithography process are explained in the last chapter. The specific recipe to prepare the TML is given in the following. At first, the substrate has to be cleaned 5 min in an ultrasonic bath with acetone. After that, 5 min in isopropyl. Afterwards, the substrate is rinsed with deionized water. The excess liquid is removed with a dry nitrogen gas flow. Subsequently, 30 s baking on a heat plate at 120 °C. The drying process at the end of the cleaning process leads to the evaporation of any residual liquid and is crucial for a good resist adhesion on the substrate.

After the cleaning process, the resist is applied by spin coating. For this, the positive resist AZ ECI 3007 from Microchemicals is used. With a microliter pipette, a few drops of the resist are dropped onto the substrate. A rotation frequency of 3000 rpm, an acceleration of 1000 rpm^{-s} and a process time of 40 s have proven to create a uniform resist film. Immediately after this step, the coated substrate is soft baked at 120 °C for one minute.

The micropatterning is done in the next step. For this, the structure of the TML was created with the CleWin 4 layout editor. First, the focus of the laser is adjusted to the sample surface. The focus for glass substrates is approximately 1250 μm. The coordinate origin is set and the layout is loaded into the software of the microwriter. The energy dose of the exposure is 170 $\frac{\mathrm{mJ}}{\mathrm{cm}^2}$. The process time is about 60 min.

After the exposure of the resist in the microwriter, the development of the structure is the next step. The developper AZ 326MIF from Microchemicals is used. The development time is 30 s. The subsequent swirling in deionized water ends the

development process.

During the metallization process, a platinum thin film is sputtered on the TML at a current of 30 mA. For the lift-off process, dimethyl sulfoxide (DMSO) is used to dissolve the unexposed areas of the resist. The dwell time in the solution is about 15 min. The excess platinum is then removed using a fine needle.

At the end of preparation process, the TML is visually checked with a microscope. The TML is then glued into a chip carrier with a low temperature adhesive. A wire bonder is used to create an electrical connection between the chip carrier and the TML. Recommend parameters for the wire bonder are given in Tab. 5.1. After the last step, the TML is ready for measurements.

Working principle of the TML

The TML involves a thermocouple, which consists of a thin sputtered platinum film (sputter target: 99,99 % platinum, LOT-QuantumDesign) and a bonded bulk gold wire (diameter: 25 μm, purity: 99.99 %, Heraeus). This bulk gold wire creates a thermoelectric connection between the upper and lower part of the platinum film. A platinum line heater is used to generate a temperature difference δT between the hot (temperature T_1, red) and cold (temperature T_2, blue) contacts. Glass as substrate material is used in order to serve as electric insulating material and to increase δT due to the low thermal conductivity of glass. The temperatures at the hot contact and cold contact are determined by four-terminal resistance thermometers. The resulting temperature difference along both materials due to the different junction temperatures ($T_1 > T_2$) produces a thermovoltage U_S. The relative Seebeck coefficient between the bulk gold wire and the thin platinum film with respect to the cold side is given by

$$S_\mathrm{Au,Pt} = -\frac{\mathrm{d}U_{\mathrm{S}_\mathrm{Au,Pt}}}{\mathrm{d}\delta T}. \tag{5.1}$$

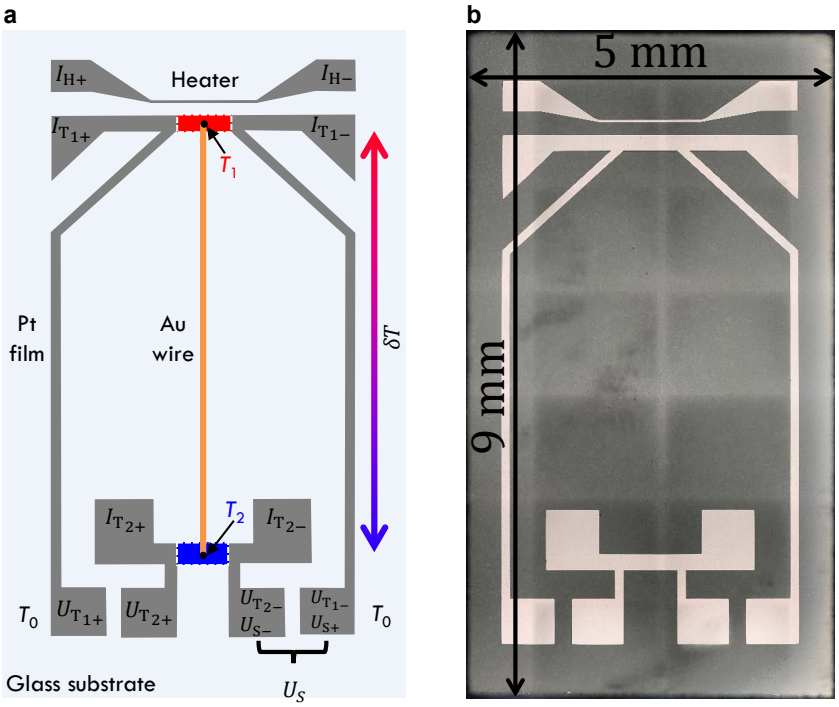

Figure 5.1: **Thermoelectric micro lab (TML). a**, Sketch of the thermoelectric micro lab. Platinum (Pt) was sputtered on a (5×9) mm^2 glass substrate. A line heater creates a temperature difference $\delta T = T_1 - T_2$ between the hot (temperature T_1, red) and cold (temperature T_2, blue) contacts by applying a current at the contacts $I_{\mathrm{H}+}$ and $I_{\mathrm{H}-}$. A bulk gold (Au) wire (diameter $d = 25\,\mu$m) was bonded at the hot and cold four-terminal resistance thermometers indicated by the corresponding current contacts ($I_{\mathrm{T}_1,\mathrm{T}_2}$) and voltage contacts ($U_{\mathrm{T}_1,\mathrm{T}_2}$). The thermovoltage U_{S} was measured at the Pt pads with respect to the cold side of the sample. The Pt pads were kept at the same temperature T_0 in order to minimize parasitic thermovoltages. **b**, Optical microscope image of the thermoelectric micro lab.

5.2 Thermoelectric nanowire characterization platform (TNCP)

Overview of the TNCP

In this thesis a thermoelectric nanowire characterization platform (TNCP) was used to perform full investigations of the temperature-dependent transport properties of individual nanowires. This means the determination of the electrical conductivity, the Seebeck coefficient and the thermal conductivity. Furthermore, structural characterizations of the same nanowires can be performed by means of transmission and scanning electron microscopy.

Within the scope of this thesis, two versions of the TNCP (TNCP A and TNCP B) are used with different nanowires. An optical microscope image of TNCP A is given in Fig. 5.2 a and a scanning electron microscopy image of TNCP B is given Fig 5.3 a. Both version were developed and fabricated at the Laboratory for Design of Microsystems (IMTEK) at the University of Freiburg in Germany under the supervision of Prof. Dr. Peter Woias. Dr. Zhi Wang and Dr. Michael Kroener were responsible for TNCP A. Dr. S. Hoda Moosavi and Dr. Michael Kroener were responsible for TNCP B.

The measurement area of the platforms is divided by an electron transparent gap into two sides. The electron transparent gap serves as thermal insulation of the suspended nanowire and enables an investigation of the specimen by scanning (SEM) and transmission electron microscopy (TEM). Both TNCPs consists of an insulating silicon dioxide surface. On top of that surface, 200 nm platinum electrodes were prepared by radio frequency sputtering. A sketch of the measurement area of TNCP A is given in Fig. 5.2b and in Fig. 5.2b for TNCP B.

The measurement area of TNCP A is situated on two freestanding cantilevers. This has the advantage that both cantilevers are thermally well insulated from each other. For this reason, Seebeck measurements can be well performed on this type of TNCP. The disadvantage of the cantilevers is that the whole inner structure is very fragile. In order to reduce parasitic thermovoltages to a minimum, all measurement contacts are placed on the same side of the TNCP, so that there is no additional temperature difference between the bond pads. The disadvantage of this layout is that all bond pads have to be very small (about $90\,\mu\text{m} \times 90\,\mu\text{m}$) in order to fit on the platform. As a result, the bonding process is very difficult. Furthermore, in order to fit into a normal TEM holder, TNCP A needs to be mechanically prepared.

On the other hand, TNCP B fits without further adjustments into to a TEM holder due to size of the platform of $2\,\text{mm} \times 2\,\text{mm}$. Furthermore, TNCP B has much larger bonds pads that leads to a much more easily bonding process. Another advantage that arises from these large bonds pads is that TNCP B is rebondable. A disadvantage of these large bond pads is that they have to be placed on both sides of the TNCP B. As a consequence, parasitic thermovoltages occur due to an additional temperature difference between the bond pads, which leads to an error of the determined Seebeck coefficient. This is negligible for large Seebeck coefficients but for small Seebeck coefficients (e.g. for metals) this can be crucial. A detailed discussion is given at the end of this chapter. More information about TNCP A and TNCP B is given in Ref. [135, 136].

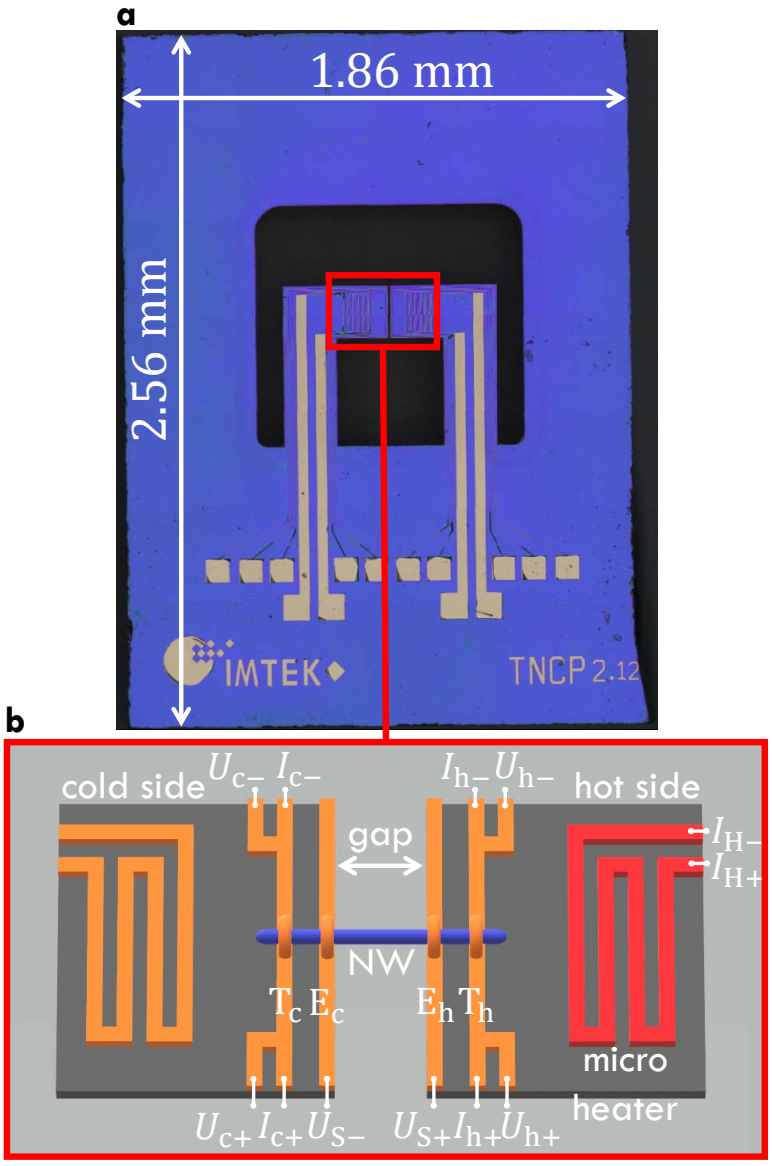

Figure 5.2: **Thermoelectric nanowire characterization platform (TNCP) A.** **a**, Opitcal microscopy image of the thermoelectric nanowire characterization platform. Image taken from my Master thesis, Ref. [134]. **b**, Sketch of the measurement area of the platform. An electron transparent gap divides the measurement area into two sides. In order to measure the thermovoltage of a nanowire (NW) (blue) relative to platinum conduction lines E_c and E_h (orange). A heating current I_H is applied at the micro heater (red), which creates a temperature difference along the nanowire that can be calculated by four-terminal resistance measurements of the thermometers T_c and T_h (orange) for the cold and hot side, respectively.

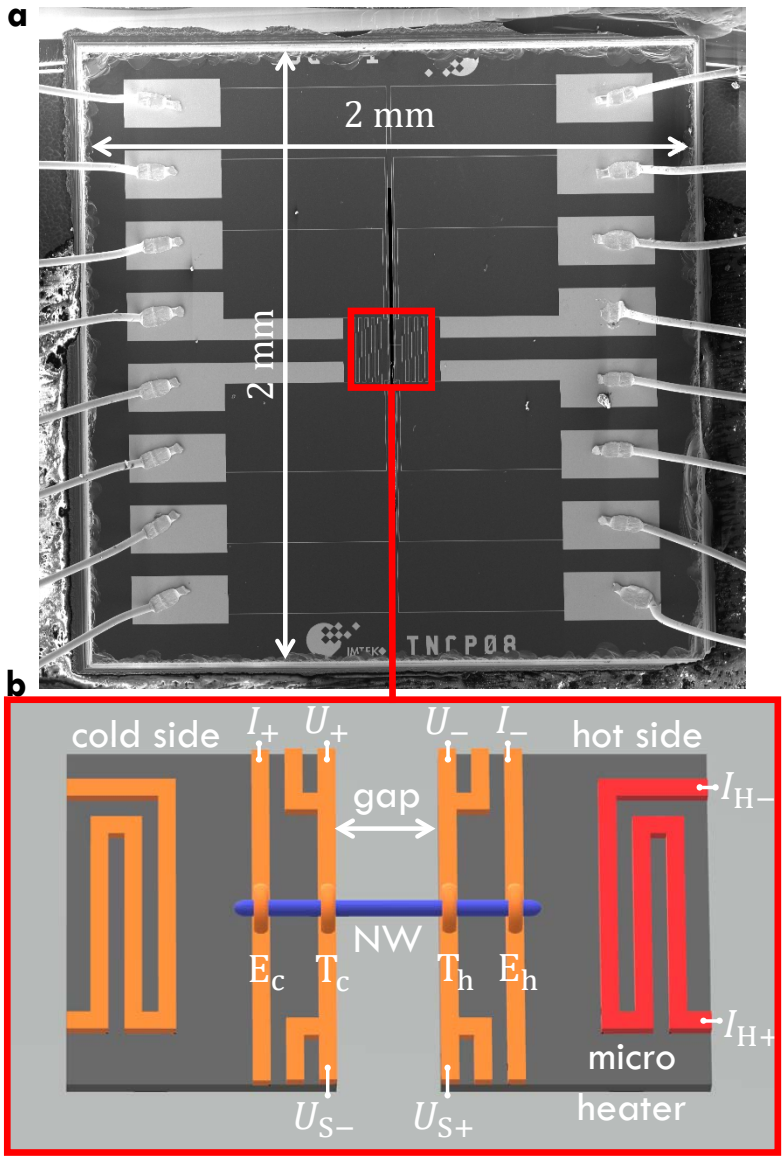

Figure 5.3: **Thermoelectric nanowire characterization platform (TNCP) B.** **a**, Scanning electron microscopy image of the thermoelectric nanowire characterization platform. **b**, Sketch of the measurement area of the platform. An electron transparent gap divides the measurement area into two sides. The determination of the four-terminal resistance of a nanowire (NW) (blue) can be performed by applying a current I at the outer platinum conduction lines E_c and E_h (orange) and measuring the voltage U at inner conduction lines. The thermovoltage U_S of a nanowire relative to the platinum conduction lines can be measured by applying a heating current I_H at the micro heater (red). This creates a temperature difference along the nanowire that can be calculated by four-terminal resistance thermometers T_c and T_h (orange) for the cold and hot side, respectively.

Mechanical and electrical preparation of the TNCP

Due to size restrictions of a TEM holder, TNCP A had to be ground at the top corners in order to fit into a holder. The diameter of the TNCP should be less than 3 mm. For this, an aluminum disk with a piece of Crystalbond 509 (thermoplastic polymer from Plano GmbH) was placed on a hot plate (180 °C) in order to melt the thermoplastic polymer. The TNCP A has to be brought into the melt. It should be completely covered by the Crystalbond. In the next step, the platform was moved to the edge of the disc, so that a corner of the platform reaches over the edge of the disc. After the Crystalbond has been cooled down, the exposed corner was ground off with fine sandpaper (grain size $< 30\,\mu$m) and cleaned with deionized water. This process was repeated for the other corner. Finally, the platform was cleaned with acetone, isopropanol and deionized water.

After the mechanical preparation of TNCP A (TNCP B is just ready from the start), follows the electrical preparation. A piece of a silicon wafer is glued with silver conductive paint (SPI Supplies) into the chip carrier (Kyocera). The silicon wafer serves as a spacer. Then, the TNCP is glued with a very thin film of the silver paint on the silicon wafer. After the sample has dried, the electrical connection between the TNCP and the chip carrier can be made. For this, the half automatic Wire Bonder HB16 from TPT Wire Bonder GmbH and Co. KG is used. Gold, aluminum-silicon and platinum wires are the preferred bond material. Recommend parameters for the wire bonder are given in Tab. 5.1. After all electrical connections have been made, safety bonds have to be placed between the chip carrier and the TNCP in order to short circuit the TNCP. This is necessary because the electron beam of the SEM can lead to electrostatic charging of the insulating substrate of the measurement platform. The grounding of all conduction lines of the TNCP prevents a possible discharge that may destroy the nanowire.

Bonding parameter	TML	TNCP A and B
Ultra sonic 1 (mW)	350	400
Time 1 (ms)	250	250
Force 1 (μN)	350	400
Ultra sonic 2 (mW)	400	400
Time 2 (ms)	500	500
Force 2 (μN)	400	400

Table 5.1: **Recommend parameters for the wire bonder.** Overview of the recommend parameters for the wire bonder that can be used to prepare the electrical connection between the chip carrier and the thermoelectric micro lab (TML) or between the thermoelectric nanowire characterization platform (TNCP) and the chip carrier. For the TML, the first bond is placed on the chip carrier and the second bond on the TML. For both TNCPs, the first bond is placed on the TNCP and the second bond on the chip carrier. The stated parameters are recommend for gold bond wires.

Working principle of the TNCP

Both versions of the TNCP work on the same principle when it comes to the determination of the thermoelectric properties of individual nanowires. The measurement

area of the platforms is divided by an electron transparent gap into two sides. The electron transparent gap serves as thermal insulation of the suspended nanowire and enables an investigation of the specimen by scanning (SEM) and transmission electron microscopy (TEM). A sketch of the measurement area of TNCP A is given in Fig. 5.2 b and in Fig. 5.3 b for TNCP B. Both TNCPs consists of an insulating silicon dioxide surface. On top of that surface, 200 nm platinum electrodes were prepared by radio frequency sputtering. A four-terminal configuration of the platinum electrodes E_c, E_h, T_c and T_h can be used to measure the resistance R of individual nanowires. SEM and TEM investigation can be performed to determine the geometry parameters. These geometry parameters are used to calculate the electrical conductivity σ and thermal conductivity λ. In order to determine the relative Seebeck coefficient of a nanowire, the thermovoltage U_S was measured by applying a heating current I_H at one of the micro heaters. The resulting temperature difference δT along the nanowires was determined by the two resistance thermometers T_c and T_h at certain stabilized bath temperatures T. The thermal conductivity λ of a nanowire can be determined by the change of the resistance of the nanowire due to self-heating [92]. Therefore, a gradually increasing current was applied at the outer electrodes. A complete thermoelectric characterization of a microwire is presented in the next chapter. The measurement process of the microwires can be completely transferred to the measurement process of the nanowires. Additional information on the measurement process is given in the appendix.

5.3 Nanowire manipulation and preparation of EBID contacts

Nanowire manipulation

There are existing methods which enable the manipulation of nanowires, e.g. methods with high frequency electrical fields [137] or the use of nanotweezers [138]. Within the scope of this thesis, a mechanical method is used to harvest, transfer and position individual nanowires. The idea of this method is based on Ref. [139]. The setup consists of a three axes manipulator (MBT616D/M, Thorlabs GmbH) with a movable arm (article 100715 Cascade Microtech GmbH). This arm can hold needles with a very fine manipulation tip. Tungsten tips Picoprobe T-4-10 (GGB Industries Inc.) with a tip radius less than 0.1 μm have been used in this work. The nanowire manipulation buildup is supported by an optical light microscope (PLu neox Sensofar or Keyence VHX-6000) with a large working distance (several millimeters). The substrate with the nanowires has to be placed under the microscope next to the measurement platform (e.g. TNCP). Next, the manipulator needle is slowly guided to the nanowire until it finally comes to an adhesive contact between the nanowire and the manipulator tip. Finally, the nanowire is placed down on the TNCP over the four conduction lines. The harvesting, transferring and positioning of a Bi-based nanowire is exemplary shown in figure 5.5a and b.

Preparation of EBID contacts on individual nanowires

In this section, the contacting procedure by means of electron beam-induced deposition (EBID) is explained using the Pioneer Two from Raith. After an individual

nanowire has been placed on the measurement platform, EBID can be done in order to prepare the electrical connection between the nanowire and the measurement platform. To do this, the chip carrier with the TNCP and the nanowire are loaded into the scanning electron microscope (SEM). Then, a vacuum with 10^{-7} mbar is established. Next, the gas injection system (GIS) has to be outgased in order to clean the capillary of the GIS. Then, the heater of the GIS has to be activated to bring the precursor into a gaseous phase. After that, the working distance (10 mm) is adjusted and the electron beam of the SEM has to be roughly aligned (focus, axial astigmatism etc.). For this, a part of the platinum conduction line near the nanowire, but not the nanowire itself, is used. The nanowire should be imaged as little as possible before the electrical measurements because carbon (C) can be deposited. The next step is to measure the electron current using an integrated Faraday cup. After that, the GIS is loaded into the sample chamber of the SEM. For this, the field of view is centered at the nanowire. Then, the working distance has to be increased from 10 mm to 13 mm. This is the safety distance for the GIS. Now, the GIS is loaded. The laoded GIS is shown in Fig. 5.4. Next, the working distance has to be manually adjusted via joystick back to 10 mm. Then, the fine alignment of the electron beam can be made. After the alignment, the area for the first EBID contact is marked. The inflow through the GIS for the gaseous precursor can then be opened. The pressure in the sample chamber will then deteriorate. As soon as the pressure no longer changes significantly, the writing process can be started. After all EBID contacts have been created, images of the nanowire can be taken, after several minutes of waiting time. Fig. 5.5 c and d show a SEM image of a Bi-based nanowire before and after the EBID process, respectively. Recommend writing parameters are given in Tab. 5.2. Additional information on the EBID process is given in the appendix.

EBID parameter	
Aperture	30 μm or 60 μm
Accelerating voltage	3 kV
Working distance	10 mm
Process type	Deposition
Fill mode	Direction
Line spacing	0.02 μm
Step size	0.02 μm
Loops	50000
Dwell time	0.01 ms
Loop mode	Area
Direction mode	Parallel
Scan direction	U
Vector mode	Meander
Line movement	Down

Table 5.2: **Recommend parameters for electron beam-induced deposition (EBID).** Overview of the recommend parameters for electron beam-induced deposition (EBID) of nanowire contacts using the Pioneer Two (Raith) with tungsten or platinum-based precursors.

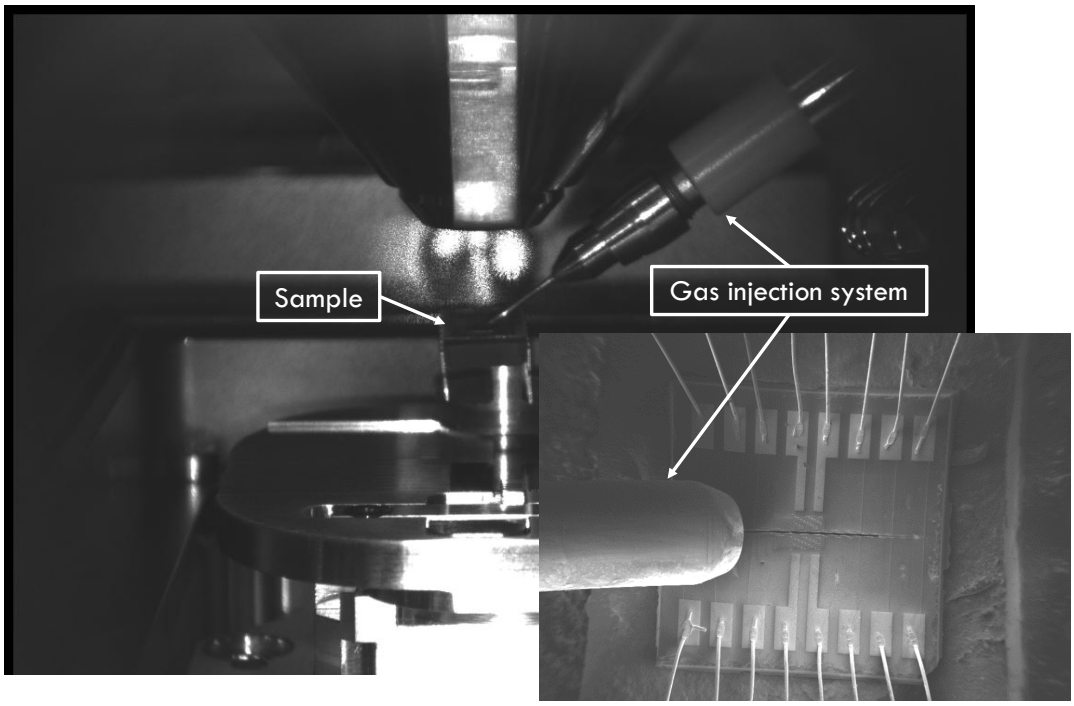

Figure 5.4: **Gas injection system (GIS). a**, Image of the sample chamber of the scanning electron microcope (SEM) Pioneer Two from Raith. The chip carrier with the measurement platform and the loaded gas injection system (GIS) is shown. **b**, The inset shows a SEM image of the measurement platform with the loaded GIS.

5.4 Discussion: Comparison of platforms

In this section, the differences between TNCP A and TNCP B are discussed from a thermoelectrical point of view. In order to be able to carry out this comparison, silver nanowires have been selected as reference material due to the high purity, single crystalline structure and very small absolute Seebeck coefficient, see Ch. 8. For these reasons, they are very suitable for comparing the two measurement platforms, because even the smallest differences in the Seebeck coefficient can be detected. All silver nanowires used for this investigation have a comparable diameter. Four individual silver nanowires were examined on the TNCP A. The relative Seebeck coefficient, which was determined with the TNCP A, can be seen as the "real" values. The values, which were determined with the TNCP B, deviate from the values determined by TNCP A. This is shown in Fig. 5.6.

In order to investigate this in more detail, various bond wires were used on the TNCP B. The TNCP B bonded with gold (Au) wires shows the smallest relative Seebeck coefficient. This can be attributed to the design of TNCP B. Because, when one of the micro heaters is used, both sides of the measurement area (hot and cold side) are heated. This is not the case with TNCP A. Furthermore, the contact area for the bond wires on TNCP B are distributed on both sides of the platform, so that an additional temperature difference along the platinum conduction lines and between the bond pads leads to an additional parasitic Seebeck coefficient. The additional parasitic Seebeck coefficient can be reduced by using platinum (Pt) bond wires instead of Au bond wires. The difference ΔS between the relative Seebeck coefficient between TNCP A and TNCP B (with Pt bond wires) can be reduced to $\Delta S_{\mathrm{Pt}} \approx 2\,\mu\mathrm{VK}^{-1}$ instead of $\Delta S_{\mathrm{Au}} \approx 3\,\mu\mathrm{VK}^{-1}$ with the Au bond wires. The

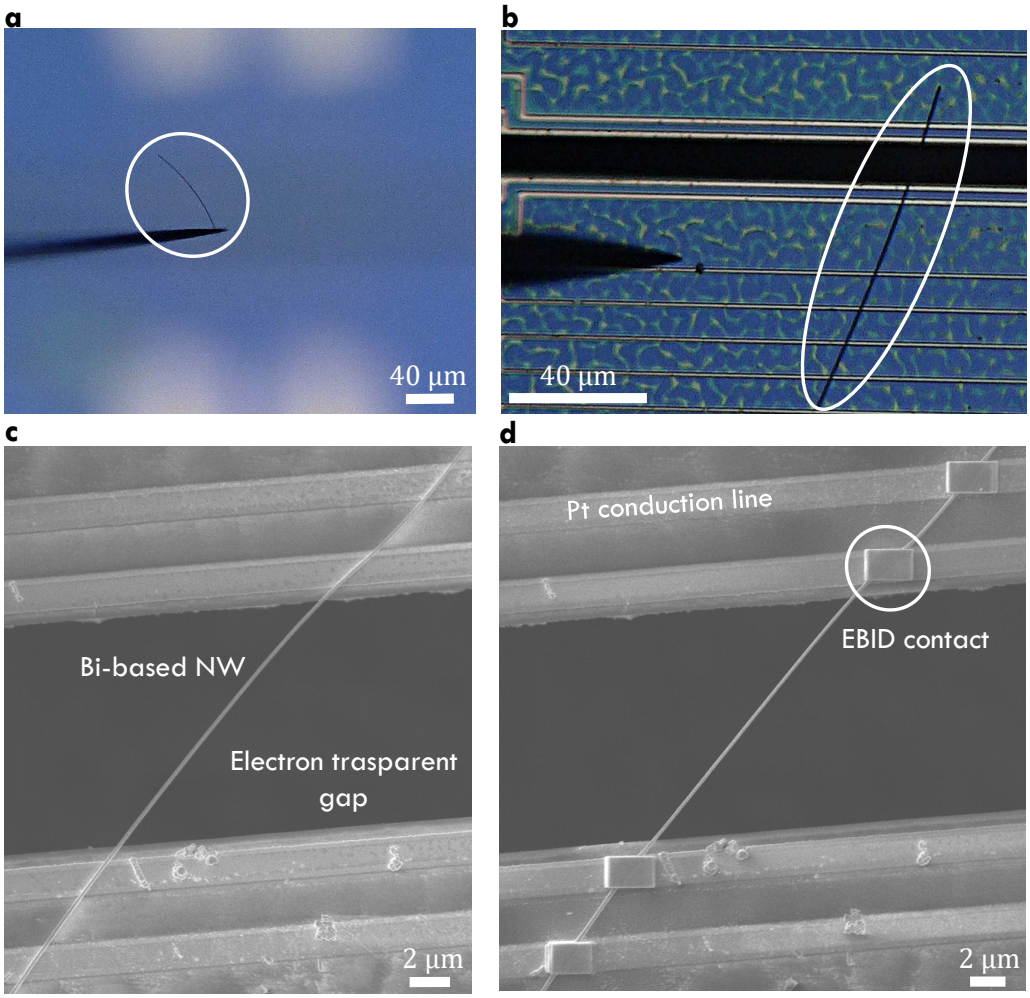

Figure 5.5: **Nanowire manipulation and EBID contacts.** **a**, Optical microscopy image of a Bi-based nanowire hanging at the tip of a very fine tungsten needle above the thermoeletric nanowire characterization platform (TNCP). **b**, Image of a Bi-based nanowire transferred to the TNCP and lying on the platinum conduction lines in the measurement area. **c**, Scanning electron microcopy (SEM) image of a Bi-based nanowire lying on the platinum conduction lines before the EBID procedure. **d**, SEM image after the EBID procedure.

reduction of ΔS can be explained by the fact that the difference between the absolute Seebeck coefficient of a thin platinum film and bulk gold is significantly larger than the difference between a thin platinum film and bulk platinum, see Ch. 7.

Nevertheless, there is still a difference between TNCP B with the Pt bond wire compared to TNCP A. This can be explained by the fact that TNCP A and TNCP B both have thin platinum films as Seebeck reference material with a thickness of 200 nm. However, these differ in their material quality. Tab. 5.3 shows the mean values of the temperature coefficients α of the resistance and the residual resistance ratio RRR of the thin platinum films of both versions of the TNCP. The Pt film of TNCP A has a higher crystal quality than that of TNCP B. This can probably be explained by the different heat treatments of the conduction lines during the manufacturing process [135, 136]. The different quality of the platinum conduction lines also leads to different absolute Seebeck coefficients, see Chap. 7.

In summary, it can be said that both TNCPs are suitable for carrying out thermoelectric measurements. However, if materials are examined that have a very small absolute Seebeck coefficient, for example metals, then TNCP A is preferable to TNCP B because no parasitic Seebeck coefficients occur on TNCP A. For materials with a large absolute Seebeck coefficient, for example semiconductors, then both TNCPs can be used because the deviation due to the parasitic Seebeck coefficients of TNCP B are negligible. Further information on the temperature distribution on the TNCP B can be found in Ref. [25].

TNCP version	Temperature coefficient $\alpha\,(\cdot 10^{-3}\,\mathrm{K}^{-1})$	RRR
TNCP A	3.1 ± 0.2	7.8 ± 0.3
TNCP B	2.2 ± 0.1	2.8 ± 0.1

Table 5.3: **Comparison between TNCP A and TNCP B.** Overview of temperature coefficient of the resistance α at room temperature and residual resistance ratio RRR as a mean value determined from several TNCPs. The residual resistance ratio RRR was determined as the ratio of the resistance at 290 K divided by the resistance of 20 K. Larger values indicate a higher material quality.

5.5 Discussion: Quality of EBID contacts

In this section, the quality of EBID contacts and methods to improve the electrical properties of the contacts are discussed. Good (ohmic) electrical contacts are important in order to be able to determine the transport properties of nanowires and other measuring objects. In order to examine individual nanowires, the flexibility of EBID contacts is an important advantage. Fig. 5.7 a and b show scanning electron microscopy (SEM) images of EBID structures based on different precursor materials. Fig. 5.7 a presents an EBID contact made of a platinum-based precursor ($C_9H_{16}Pt$). Fig. 5.7 b shows a tungsten-based contact ($W(CO)_6$). The deposited contact material is connected with thin platinum conduction lines, so that electrical two-terminal measurement can be carried out.

The resulting resistance R of these measurements is given in Fig. 5.8 a as a function of the bath temperature T. The geometry parameters of the EBID contacts were estimated from SEM images. The determined resistivity ρ is shown in Fig. 5.8 b. At room temperature, the two-terminal resistivity of the platinum-based

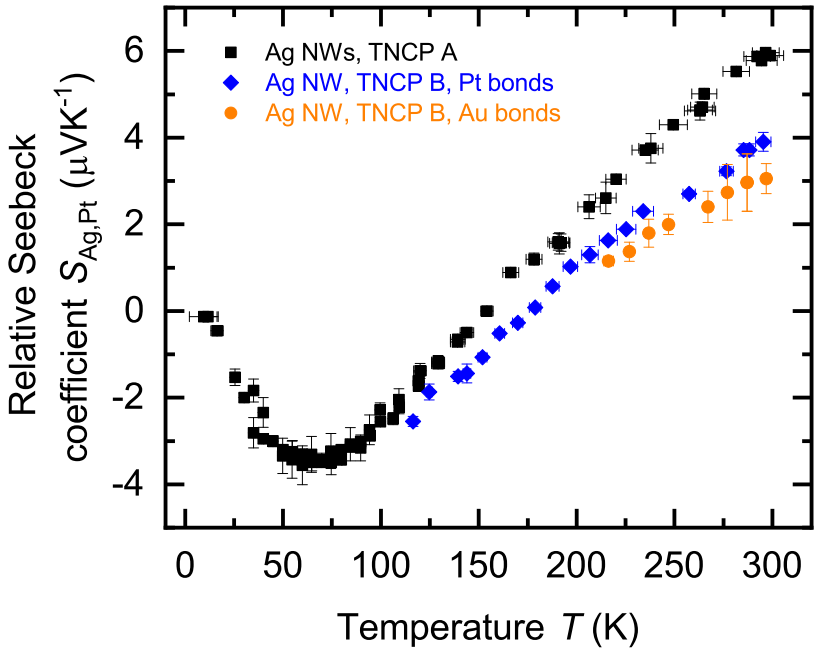

Figure 5.6: **Comparison between TNCP A and TNCP B.** Relative Seebeck coefficient $S_{\mathrm{Ag,Pt}}$ of silver nanowires as a function of the bath temperature T for different TNCPs and bond wires. Parasitic Seebeck coefficients of TNCP B lead to a change of the relative Seebeck coefficient compared to TNCP A.

precursor is about 8 times larger than the resistivity of the tungsten-based precursor. The difference increases at a temperature of $T = 130\,\mathrm{K}$ to a factor of 108. The difference of the resistivity between the two materials can be attributed to the composition of the precursor deposition. The platinum-based deposition contains a much larger amount of carbon (atomic percent) than the precursor deposition based on tungsten. The distribution of the elements is shown in Tab. 5.4. Overall, it can be said that the tungsten-based EBID contacts should be preferred because they have a lower resistivity. This leads to better electrical contacts so that the transport properties can be determined over a wide temperature range.

Elemental composition (at %) from Ref. [140]	$C_9H_{16}Pt$	$W(CO)_6$
Platinum (Pt)	21	0
Tungsten (W)	0	37
Carbon (C)	79	36
Oxygen (O)	0	27

Table 5.4: **Elemental composition $C_9H_{16}Pt$ and $W(CO)_6$.** Distribution of the elemental composition of two EBID depositions. Based on platinum ($C_9H_{16}Pt$) and based on tungsten ($W(CO)_6$) in at %. The platinum-based precursor exhibits a much larger amount of carbon (C) than the tungsten-based precursor. The values have been taken from Ref. [140].

Furthermore, it was examined how EBID contacts, which are based on platinum, can be improved. The influence of the dwell time during the EBID process, the influence of the electron beam power and the influence of a subsequent heat treatment of the EBID contacts were investigated. The manual of the Pioneer TWO (Raith) suggests that the electrical conductivity of the EBID contacts can be improved by

increasing the dwell time of the electron beam. This could not be confirmed within this thesis. However, increasing the dwell time leads to a detachment of individual layers from the EBID structure, which is shown in Fig. 5.7 c. Therefore, an increase of the dwell time cannot be recommended.

Botman *et al.* propose to increase the power of the electron beam in order to improve the electrical properties [141]. An increase of the beam power is intended to reduce the carbon content in the deposited EBID material, so that the relative platinum content increases [141]. The power of the electron beam can be increased by increasing the aperture and increasing the acceleration voltage of the SEM. In order to investigate the effect of the beam power increase on the electrical resistance of the nanowires and the EBID contacts, a Bi-based nanowire was contacted with the recommended parameters as given in Tab. 5.2.

Electrical two-terminal and four-terminal measurements were carried out on this nanowire. The results are shown in Fig. 5.9. The same nanowire was then reinserted into the SEM and the EBID contacting was again carried out at the same contact points with increased beam power. Then, the electrical measurements were carried out again with the same contact configuration. All three investigated contact configurations showed an improvement of the electrical measurements after the contact preparation with the increased beam power. This means that the resistance between the outer contacts of the nanowire could be more than halved. An ohmic characteristic was determined between the inner contacts. However, this can maybe attributed to the halo effect. In the four-terminal measurement, the *U-I* curve has improved by reducing the noise of the measured values. However, the four-terminal resistance has increased from 1.9 kΩ to 16 kΩ. This is probably due to an increased amount of carbon, which was deposit on the nanowire because of the longtime investigation in the SEM. This carbon can lead to increased resistance.

Despite the improvements due to the increase of the beam power, a recommendation for EBID contacting on nanowires cannot be made. Due to the large beam power, an unnecessarily large amount of carbon was deposited on the nanowire, which can lead to a misinterpretation of the measurement results. Moreover, the halo effect, which is a side effect of EBID, can be increased by an increased beam power. This results in the deposition of material around the actual main deposit and can lead to undesired short circuits.

Furthermore, the influence of subsequent heat treatment of the EBID contacts was examined. A Bi-based nanowire was contacted by EBID. A *U-I* curve of the nanowire was then taken at the outer contacts. A two-terminal resistance of 240 kΩ at a bath temperature of 295 K was obtained. Thereafter, a heat treatment was carried out at a temperature of 100 degrees Celsius for ten minutes in vacuum. After the heat treatment, a two-terminal resistance of 31 kΩ was determined. The subsequent heat treatment has significantly reduced the contact resistance. This can be explained by the fact that the relative platinum content in the EBID contact material could be increased by the heat treatment and at the same time the relative carbon content was reduced [141, 142]. Subsequent heat treatment can only be recommended under certain conditions. A disadvantage is that not only the contacts are treated, but the entire measurement object (in this case a nanowire). Therefore, the structural properties of the measurement object could also be changed by the heat treatment, which can lead to a misinterpretation of the measurement results.

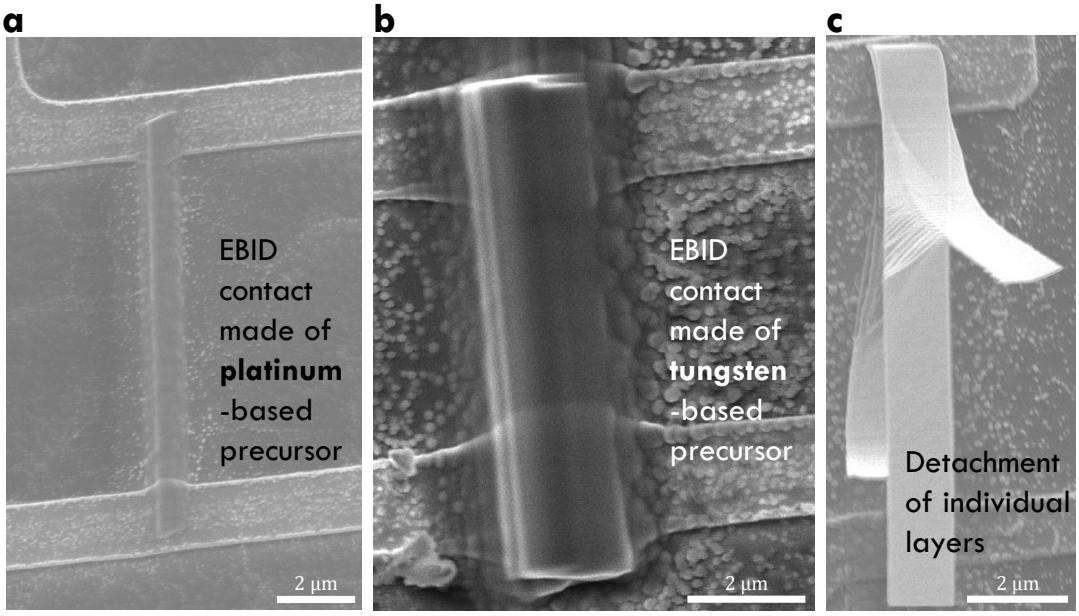

Figure 5.7: **Scanning electron microscopy (SEM) images of different EBID structures between two platinum conduction lines.** **a**, EBID contact made of platinum-based precursor ($C_9H_{16}Pt$). **b**, EBID contact made of tungsten-based precursor ($W(CO)_6$). The materials were deposited between two platinum conduction lines in order to perform electrical measurements. The results are given in Fig. 5.8. **c**, EBID contact prepared with increased dwell time of the electron beam. This leads to detaching of individual layers from the EBID structure.

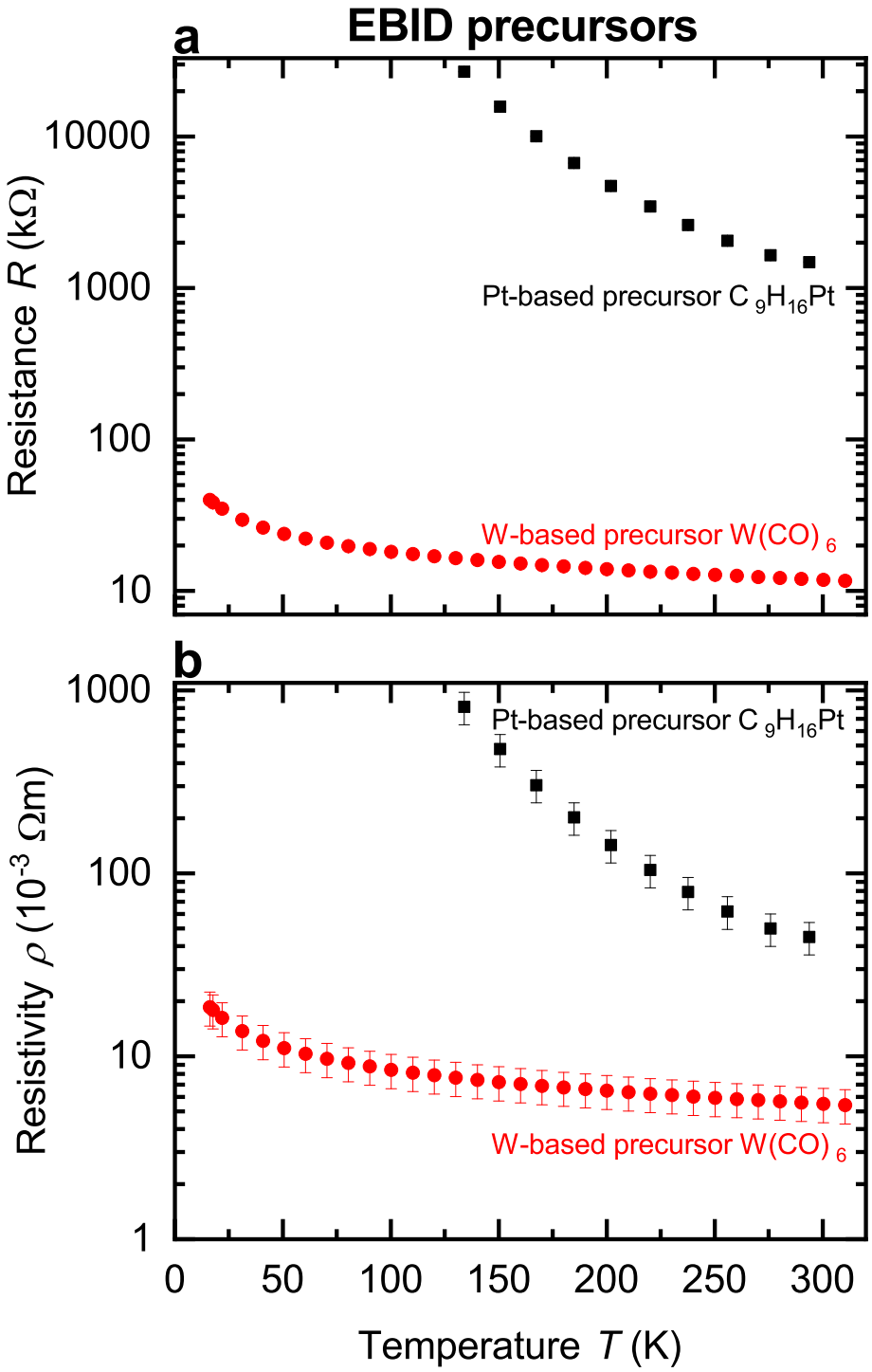

Figure 5.8: **Electrical properties of EBID structures made of different precursor materials.** **a**, Two-terminal resistance R of the platinum-based precursors ($C_9H_{16}Pt$) and of the tungsten-based precursor ($W(CO)_6$) as a function of the bath temperature T. **b**, Two-terminal resistivity ρ of both EBID structures. The tungsten-based precursor shows a significant lower resistivity than the platinum-based precursor.

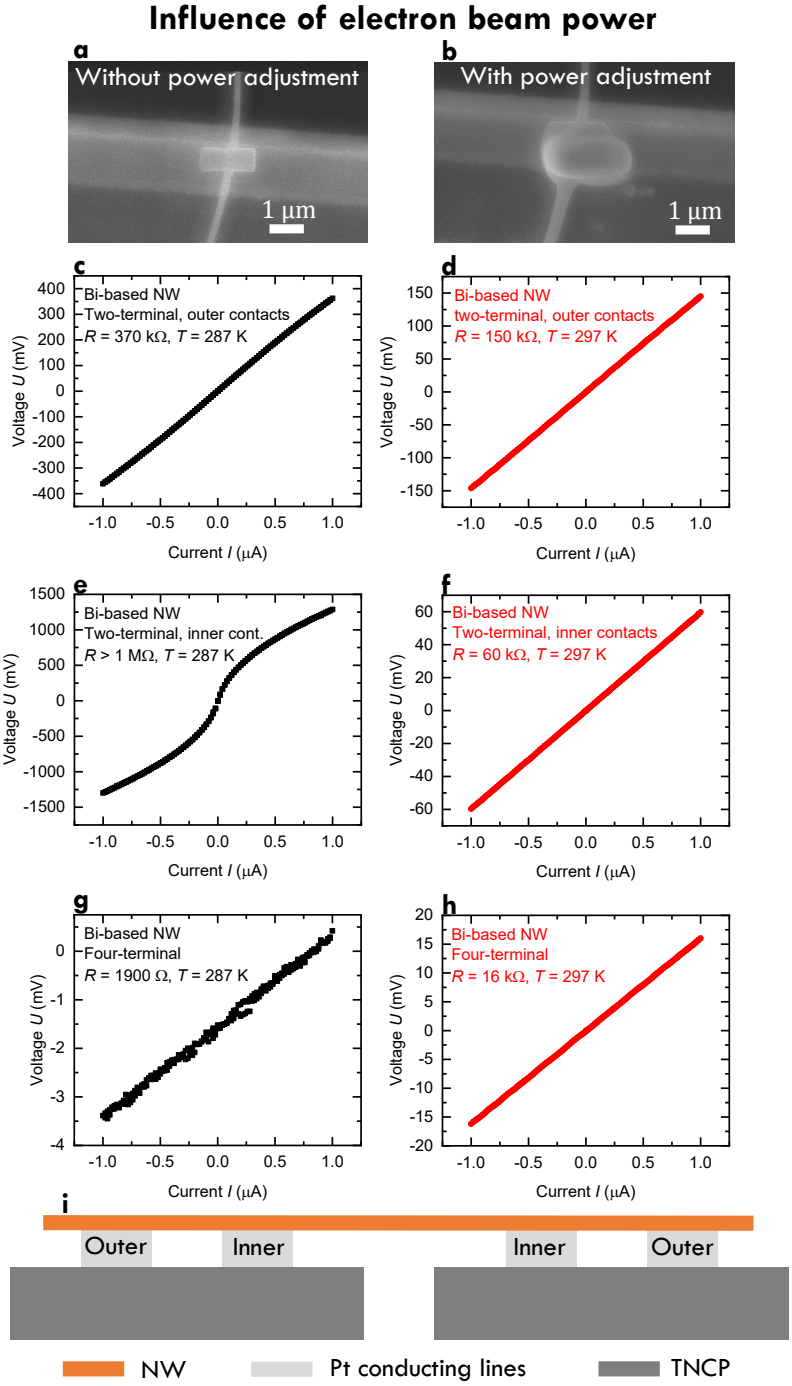

Figure 5.9: **Influence of electron beam power on the quality of EBID contacts.** **a**, SEM image of one contact of a Bi-based nanowire lying on the platinum conduction line. The image shows a EBID contact without power adjustment of the electron beam. **b**, SEM image after a second EBID contact has been created with power adjustment. **c**, Voltage U as a function of the current I (U-I-curve) without power adjustment at the two outer contacts. Resistance R was determined from U-I-curve at a given bath temperature T. **d**, U-I-curve with power adjustment at the two outer contacts. **e**, U-I-curve without power adjustment at the two inner contacts. **f**, U-I-curve with power adjustment at the two inner contacts. **g**, U-I-curve without power adjustment in a four-terminal configuration. **h**, U-I-curve with power adjustment in a four-terminal configuration. **i**, Cross-sectional sketch of a nanowire lying on top of the platinum conduction lines of the TNCP. *Outer* and *Inner* are indicating the outer and inner contacts that are used for the two-terminal and four-terminal measurements.

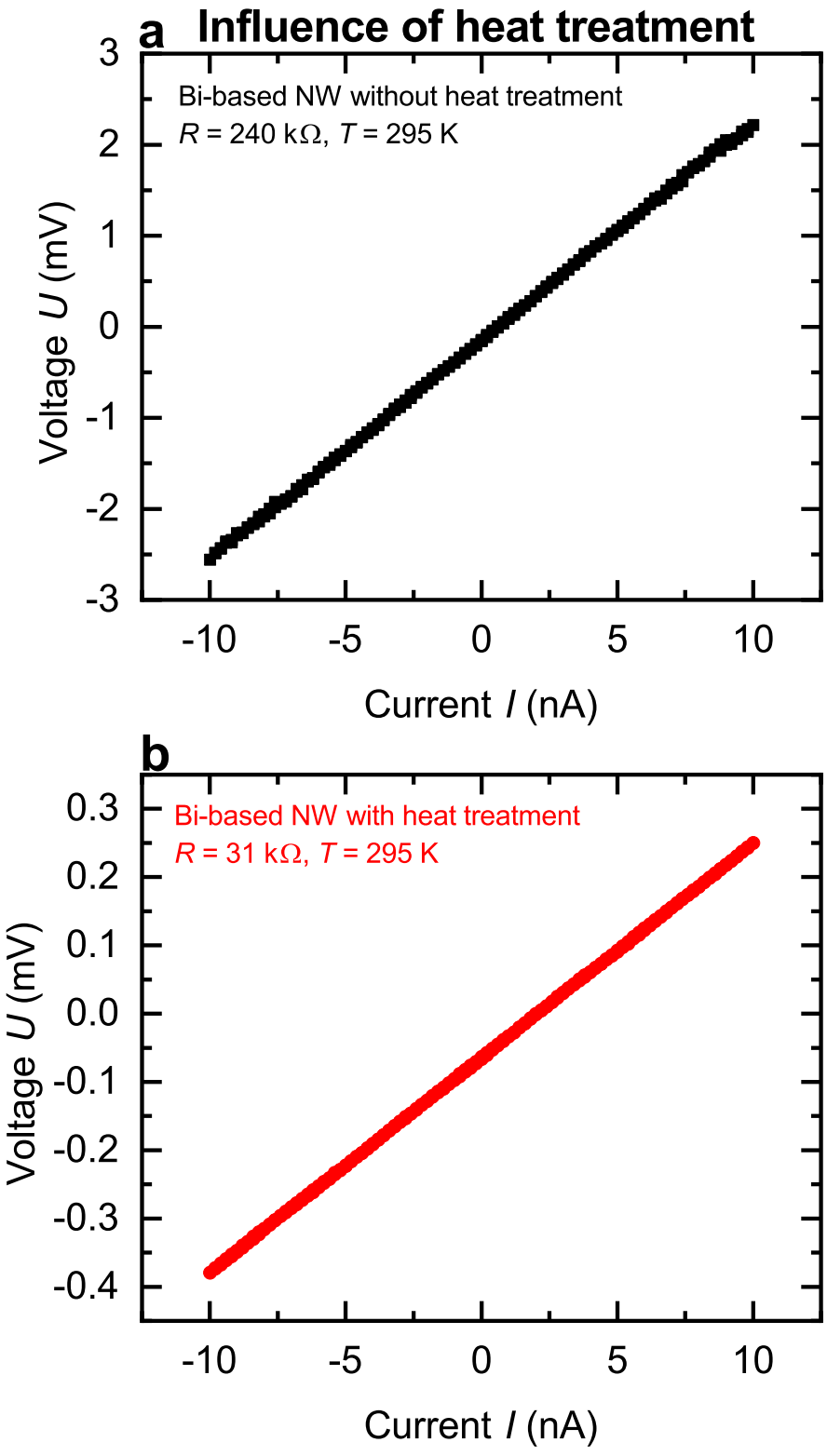

Figure 5.10: **Influence of heat treatment on the quality of EBID contacts.** **a**, Measured voltage U as a function of the applied current I (U-I-curve) without heat treatment of a Bi-based nanowire at a bath temperature of $T = 295\,\mathrm{K}$. The slope of the curve yields a two-terminal resistance of $R = 240\,\mathrm{k\Omega}$. **b**, U-I-curve after the heat treatment (100 °C for 10 min in vacuum). The slope of the curve yields a two-terminal resistance of $R = 31\,\mathrm{k\Omega}$. The heat treatment leads to a significant reduction of the resistance.

Chapter 6

Preparatory measurements of metallic microwires

Preparatory measurements of the transport properties of three metallic microwires are shown in this chapter in order to set the scene of the thermoelectric characterization and to prove the reliability of the measurement principles that are later applied on thin films and nanowires.

6.1 Measurement setup

Fig. 6.1 a shows a sketch of a chip carrier in top view. Three microwires, see Tab. 6.1, were anchored at the contact areas by wire bonding between both sides of a chip carrier in order to determine their electrical σ and thermal λ conductivity. A large gap is situated between those two contact areas which can be seen in the cross-sectional view of Fig. 6.1 b. This makes sure that an electrical connection is only available at the contact area and no thermal leakage is possible. For the electrical and thermal measurements, a current is applied at the outer contacts I_+ and I_-. The voltage drop is measured at the inner contacts U_+ and U_-. This four-terminal configuration was used to measure the resistance R of the microwires. Optical microscopy was performed to determine the length l of wires. The diameter d was given by the manufacturers, see Tab. 6.1. These geometry parameters were used to calculate σ and λ. In addition, the thermal conductivity was determined by the change of the resistance of the microwires due to self-heating [92]. Therefore, a gradually increasing current was applied at the outer contacts I_+ and I_-.

Fig. 6.2 a shows a sketch of the measurement setup in top view that was used to determine the relative Seebeck coefficient of the microwires. The setup consists of two separate measurement areas. The left measurement area consists of a glass substrate and on top of that there is a measurement platform. The right measurement area consists of a glass substrate and on top of that there is a heat plate (PT1000 sensor). The measurement platform on the right side is placed on the heat plate. Both measurement areas are connected with a gold (Au) microwire with known absolute Seebeck coefficient. The left side (cold side) of the measurement area is connected with some other microwire (here: platinum (Pt)) to the contact area of the chip carrier at U_{S-}. The right side (hot side) of the measurement area is connected to the contact area of the chip carrier at U_{S+}.

The electrical connection on each measurement platform between both microwires is prepared by a thin platinum film. However, this thin film is not contributing to

the Seebeck coefficient of the microwires because there is no temperature gradient along the measurement platform. In order to determine the relative Seebeck coefficient of a microwire, the thermovoltage U_S was measured between the contacts U_{S+} and U_{S-} by applying a heating current at the heat plate. The resulting temperature difference δT along the microwires was determined by the two resistance thermometers at certain stabilized bath temperatures T. Fig. 6.2 b shows the cross-sectional view of the measurement setup.

In the experiments, the four-terminal resistance of the microwires was measured by a Keithley 6221 AC and DC Current Source and Keithley 2182A Nanovoltmeter. For Seebeck measurements, the heat plate power was controlled by a Keithley SourceMeter 2401. The thermometer resistances were determined by four-terminal measurements performed by a Keithley 6221 and 2182A devices. The thermovoltage was measured by a Keithley 2182A Nanovoltmeter. The measurement configurations were changed by a Keithley 7001 switch matrix system. The electrical and thermal measurements were performed in a closed cycle cryocooler in vacuum. All Seebeck measurements were performed in a flow cryostat in helium atmosphere at ambient pressure.

Sample	Manufacturer	Diameter d (μm)	Length l (mm)	Composition
Pt wire	Alfa Aesar	25	10.5 ± 0.5	99.95 % Pt
Au wire	Heraeus	25	11.5 ± 0.5	99.99 % Au
AlSi wire	Heraeus	33	10.5 ± 0.5	99 % Al, 1 % Si

Table 6.1: **Manufacturer details of a platinum, gold and aluminum-silicon microwire.** Overview of the manufacturer, diameter d, length l and composition of each sample.

6.2 Electrical conductivity

The electrical conductivity σ of the three metallic microwires with a circular cross-sectional area can be determined by

$$\sigma = \frac{4l}{R\pi d_c^2}, \tag{6.1}$$

where R is the four-terminal resistance of the wire, l is the length and d is diameter. The uncertainty of the electrical conductivity σ mainly comes from the determination of the wire length and is about 0.5 mm. The four-terminal resistance R was determined by linear fits of corresponding U-I curve. The relative uncertainty of R is less than 1 %.

Fig. 6.3 a shows voltage U versus current I curves of a platinum (Pt), gold (Au) and aluminum-silicon (AlSi) wire at room temperature. The electrical conductivity σ of those wires is given in Tab. 6.2 and compared to the data reported in literature. σ of a platinum bulk wire as a function of the bath temperature T is given in Fig. 6.3 b. In addition, the thick dashed blue line indicates the literature data of bulk platinum taken from [143]. The gray shaded area marks the uncertainty due to different available data [90, 143]. The electrical conductivity is increasing with decreasing bath temperature and both the experimental and literature data are in agreement with each other.

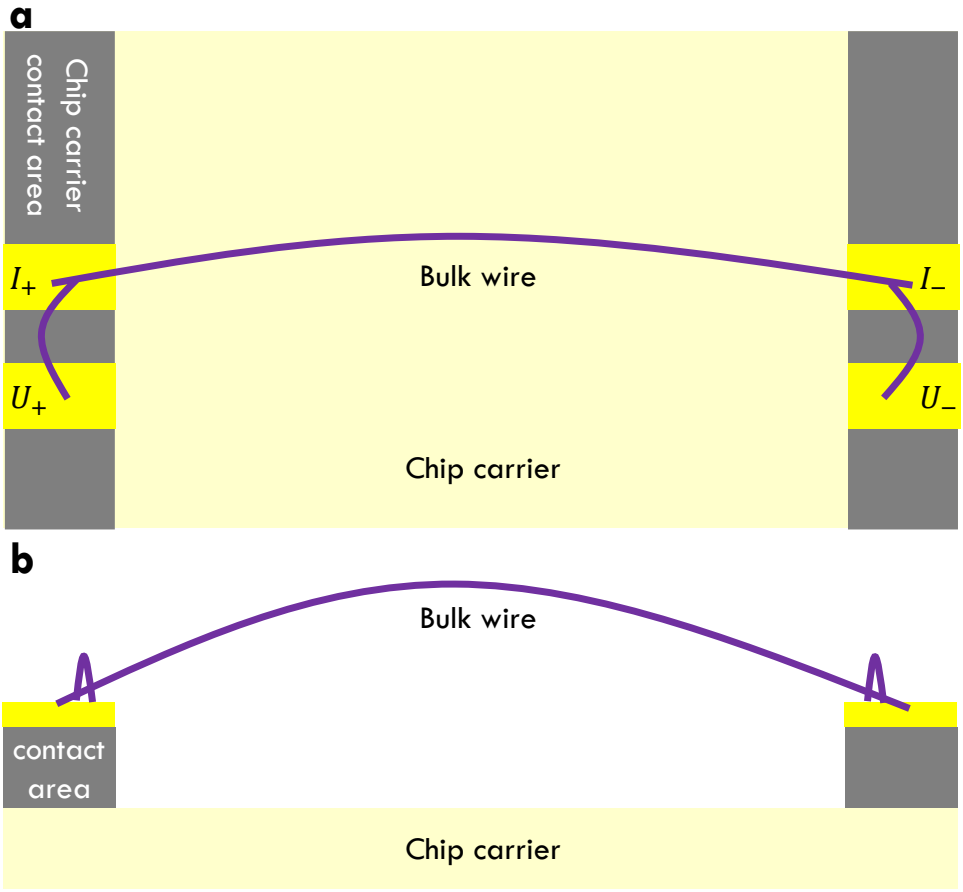

Figure 6.1: **Sketch of the measurement setup to determine the electrical and thermal conductivity of a microwire. a**, Top view sketch of a chip carrier including the measurement setup in order to determine electrical and thermal conductivity of a microwire. For the electrical and thermal measurements, a current is applied at the outer contacts (I_+ and I_-) and the voltage drop is measured at the inner contacts (U_+ and U_-) at the chip carrier contact area, respectively. **b**, Cross-sectional view sketch of a chip carrier showing the large gap between the two contact areas of the chip carrier. Both sides are connected with a bulk wire.

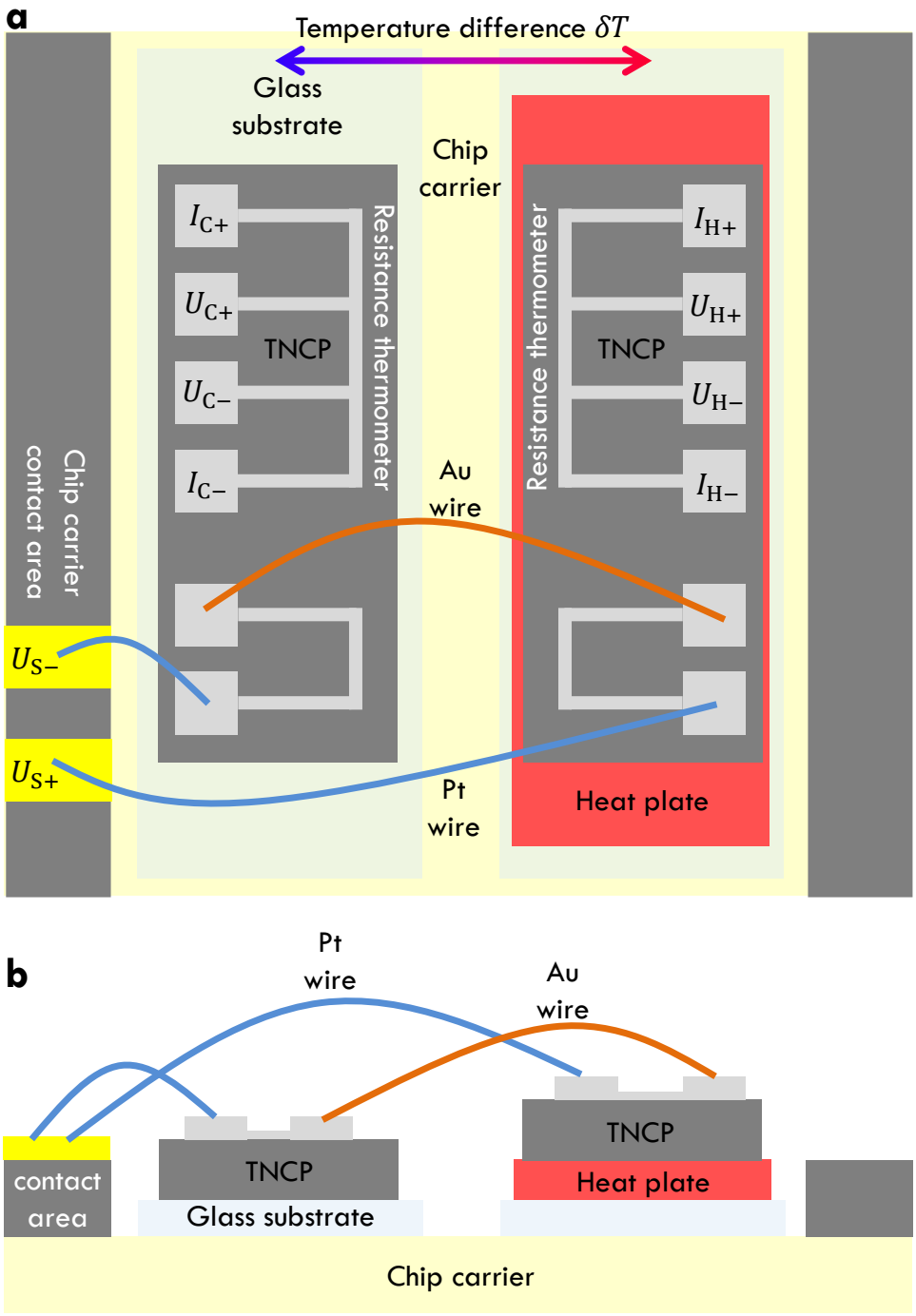

Figure 6.2: **Sketch of the measurement setup to determine the relative Seebeck coefficient of a microwire. a**, Top view sketch of a chip carrier including the measurement setup. On the left side, there is measurement area, which consists of a glass substrate and on top of that there is a measurement platform. The measurement area on the right side consists of a glass substrate, a heat plate (PT1000 sensor) and a measurement platform. Both measurement areas are connected with a gold (Au) microwire. The left side (cold side) of the measurement area is connected with platinum (Pt) microwire to the contact area of the chip carrier at U_{S-}. The right side (hot side) is connected to U_{S+}. The electrical connection on each measurement platform between both wires and the resistance thermometers are made of thin platinum films. A temperature difference δT between the wires can be created by the using the heat plate. **b**, Cross-sectional view sketch of a chip carrier showing Seebeck measurement setup.

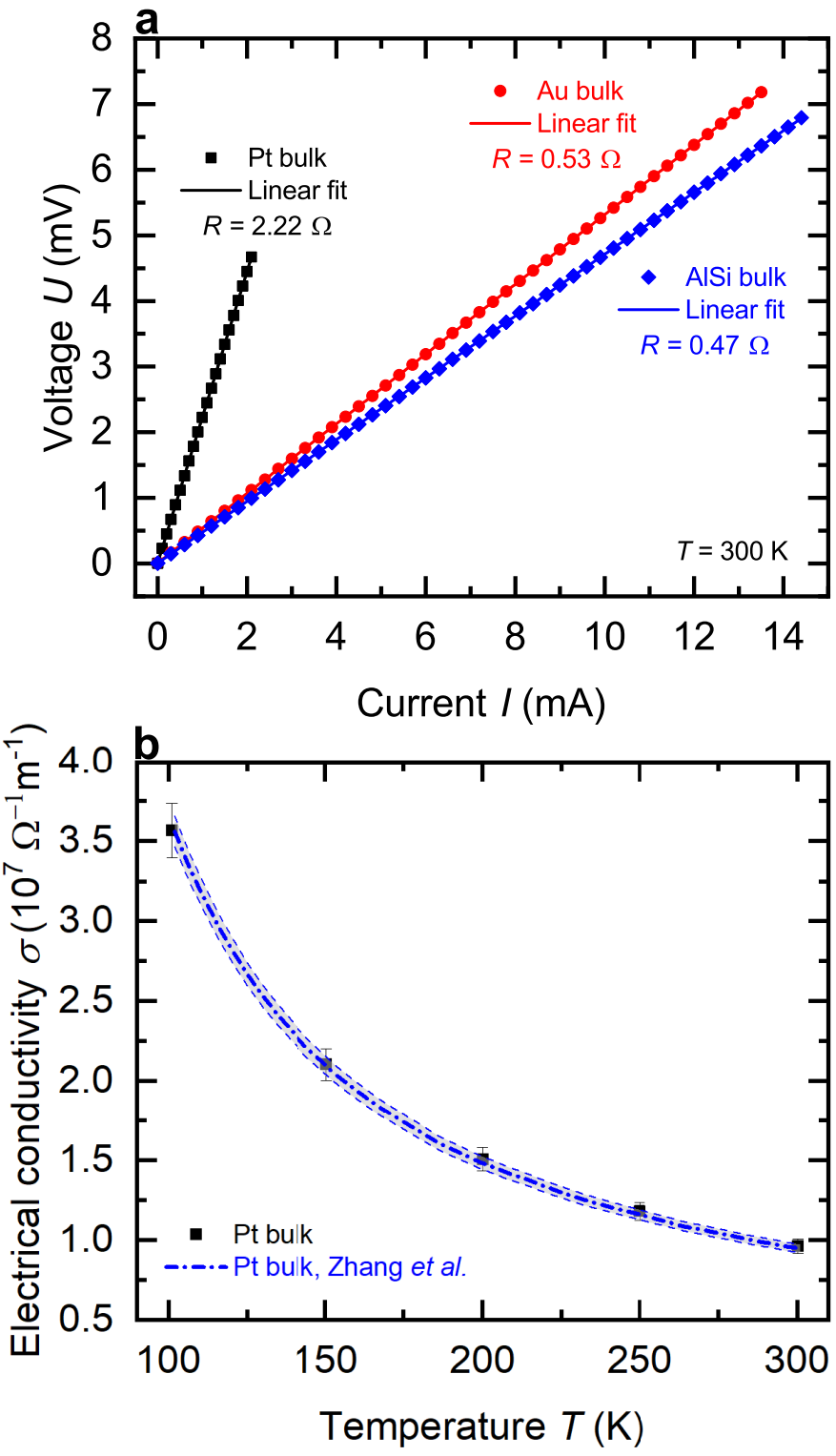

Figure 6.3: **Electrical transport properties of a platinum, gold and aluminum-silicon microwire.** **a**, Measured voltage U as a function of the applied current I of a platinum (Pt), gold (Au) and aluminum-silicon (AlSi) microwire at $T = 300\,\mathrm{K}$. The thick lines are linear fits of the corresponding data yielding the four-terminal resistances. **b**, Temperature-dependent electrical conductivity σ of a platinum microwire. The thick dashed blue line indicates the literature data of platinum taken from Ref. [143]. The gray shaded area marks the uncertainty due to different available data Ref. [90, 143].

6.3 Relative and absolute Seebeck coefficient

The relative thermovoltage U_S of a platinum (Pt), gold (Au) and aluminum-silicon (AlSi) microwire relative to a reference bulk wire was measured between bath temperatures of 11 K and 286 K for the Pt wire and at room temperature for the Au and AlSi wire. The temperature difference δT between the hot and the cold side of measurement areas was calculated by the change of four-terminal-resistance thermometers due to the variation of the power of the heat plate by increasing the applied heating current I_H from zero to $-I_{H,max}$ and from zero to $+I_{H,max}$ stepwise in equidistant steps.

Fig. 6.4 shows the temperature-dependent resistance thermometers of the measurement platforms. In general, the resistance $R(T+\Delta T,P)$ of the thermometers at a certain bath temperature T plus the temperature increase ΔT due to the power P of the heater is given by

$$R(T+\Delta T,P) = R(T,P=0) + \alpha \cdot \Delta T \cdot R(T,P=0), \tag{6.2}$$

where α is the temperature coefficient of the resistance. With the temperature coefficient

$$\alpha = \frac{1}{R(T,P=0)} \frac{\partial R(T,P=0)}{\partial T} \tag{6.3}$$

and Eq. 6.2, the temperature increase $\Delta T = T(P) - T(P=0)$ of a resistance thermometer can be determined by the resistance increase ΔR. The temperature increase is given by

$$\Delta T = \frac{\Delta R}{\alpha R(T,P=0)} = \frac{R(T,P) - R(T,P=0)}{\alpha R(T,P=0)} = \frac{R(T,P) - R(T,P=0)}{\frac{\partial R(T,P=0)}{\partial T}}. \tag{6.4}$$

According to this equation, the temperature increase on the hot side is

$$\Delta T_{hot} = \frac{R_{hot}(P) - R_{hot}(P=0)}{\frac{\partial R_{hot}(P=0)}{\partial T}} \tag{6.5}$$

and on the cold is

$$\Delta T_{cold} = \frac{R_{cold}(P) - R_{cold}(P=0)}{\frac{\partial R_{cold}(P=0)}{\partial T}}. \tag{6.6}$$

The temperature difference δT is then given by

$$\delta T = \Delta T_{hot} - \Delta T_{cold}. \tag{6.7}$$

The slope of the function $U_S(\delta T)$ gives the relative Seebeck coefficient. Here, $S_{Au,Pt}$ of the Pt wire with respect to the Au wire is given by

$$S_{Au,Pt} = S_{Au} - S_{Pt} = -\frac{dU_{S\text{-}Au,Pt}}{d\delta T}. \tag{6.8}$$

S_{Pt} is the absolute Seebeck coefficient of the Pt wire. S_{Au} is the absolute Seebeck coefficient of the gold wire that serve as the reference material. The temperature-dependent Seebeck coefficient $S_{Au,Pt}$ of a Au wire relative to Pt wire is presented in Fig. 6.5 a. The absolute Seebeck coefficient of a Pt wire is given by

$$S = S_{Pt} = S_{Au} - S_{Au,Pt}. \tag{6.9}$$

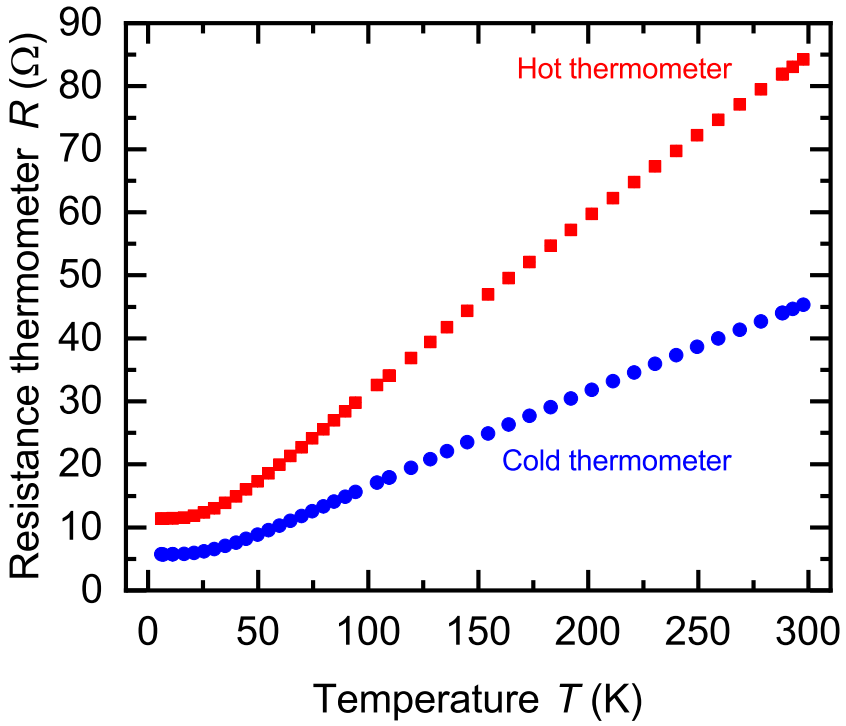

Figure 6.4: **Exemplary resistance thermometers.** Resistance R of the thermometers of the hot side and of the cold side of the measurement setup as a function of the bath temperature T. The slope $\frac{\partial R_{\mathrm{hot,cold}}(P=0)}{\partial T}$ of the temperature-dependent resistance is required in order to determine the temperature difference δT between the hot and cold side of the measurement setup. The slope has to be determined in regimes where $R(T)$ is linear.

The uncertainty of the thermovoltage is given by the confidence interval of the thermovoltage, which was measured ten times at each step of the applied heating current and then arithmetically averaged. The uncertainty of the relative Seebeck coefficient is determined by the modulus of the largest deviation of the mean value of different fit lines due to applied heating current I_{H}, which was varied from zero to $-I_{\mathrm{H,max}}$ and from zero to $+I_{\mathrm{H,max}}$. The uncertainty of the absolute Seebeck coefficient was determined by propagation of uncertainty.

Fig. 6.5 b shows the absolute Seebeck coefficient S of the experimental data of the Pt wire S_{Pt} in comparison with data reported in literature [28,41], which is represented by the thick dashed blue line. The gray shaded area marks the uncertainty due to different available data [28,41] and deviations due to plot digitization. Experimental data and reference data are in agreement with each other. Furthermore, the absolute Seebeck coefficient of gold S_{Au} from Ref. [45], which was used to determine the absolute Seebeck coefficient of platinum S_{Pt}, is given as a thick dashed orange line. In addition the absolute Seebeck coefficients of all investigated wires are given in Tab. 6.2 at room temperature. S_{Au}, S_{Pt} and S_{AlSi} are in agreement with the reference data.

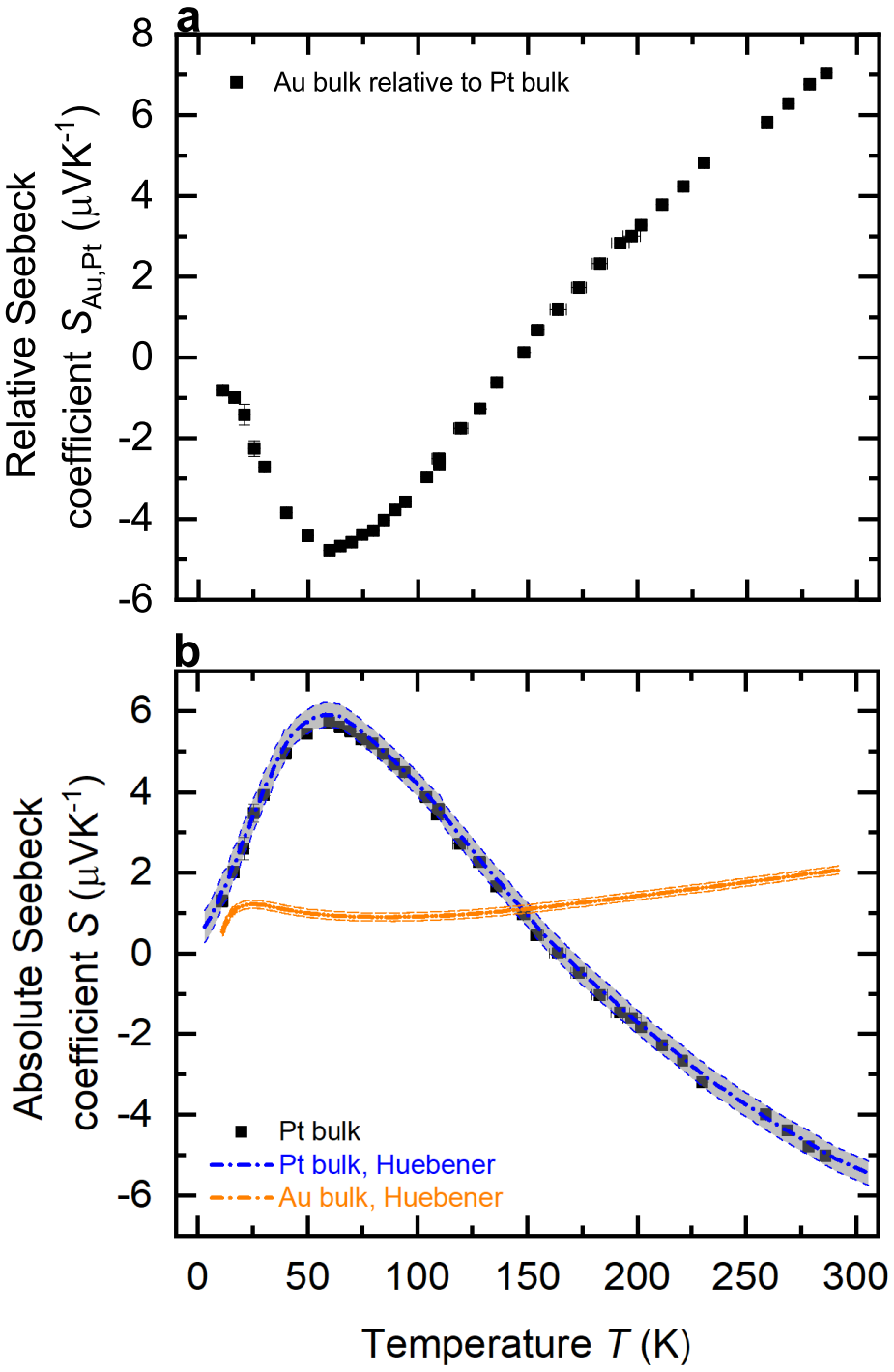

Figure 6.5: **Relative and absolute Seebeck coefficient of a platinum microwire. a**, Temperature-dependent Seebeck coefficient $S_{\mathrm{Au,Pt}}$ of a gold (Au) wire relative to platinum (Pt) wire. **b**, Absolute Seebeck coefficient S_{Pt} of a bulk platinum (Pt) wire as a function of the bath temperature T. The thick dashed blue line indicates the literature data of platinum taken from [28, 41]. The thick dashed orange line indicates the literature data of gold taken from [45]. The gray shaded area marks the uncertainty due to different available data [28, 41] and deviations due to plot digitization. The absolute Seebeck coefficient of gold S_{Au} from [45] was used in order to determine the absolute Seebeck coefficient of platinum S_{Pt}.

6.4 Thermal conductivity

The thermal conductivity λ of a platinum (Pt), gold (Au) and aluminum-silicon (AlSi) microwire was determined by the increase of the resistance of the wire due to self-heating. A current was applied at the outer contacts I_+ and I_- and gradually increased. λ is given by

$$\lambda = \frac{1}{12}\frac{\alpha l R}{A}\frac{\mathrm{d}P}{\mathrm{d}r(P)}. \tag{6.10}$$

α is the temperature coefficient of the resistance of the nanowire, R is the four-terminal resistance, l is the length, A is the cross-sectional area of the wire, P is the resulting power in the wire based on the voltage drop due to the applied current and r is the resistance of the wire at a certain power.

Fig. 6.6 a shows the resistance change r as a function of the power P in the wire due to the applied current of a platinum (Pt), gold (Au) and aluminum-silicon (AlSi) microwire at room temperature. The slope of the corresponding curves yields the relation between r and P that is necessary in order to determine the thermal conductivity. λ of a platinum wire as a function of the bath temperature T is given in Fig. 6.6 b. In addition, the thick dashed blue line indicates the literature data of bulk platinum taken from Ref. [143]. The gray shaded area marks the uncertainty due to deviations of the plot digitization and due to different available data [143], [91, p. 269]. The thermal conductivity of the experimental data is agreement with the literature data.

Transport properties	This work	Literature	Reference
$\sigma_{\mathrm{Pt}}\,(10^7 \cdot \Omega^{-1}m^{-1})$	0.96 ± 0.05	0.95	Ref. [143]
$S_{\mathrm{Pt}}\,(\mu\mathrm{V^{-1}K^{-1}})$	-5.0 ± 0.2	-4.9	Ref. [28, 41]
$\lambda_{\mathrm{Pt}}\,(\mathrm{Wm^{-1}K^{-1}})$	73 ± 11	71	Ref. [143]
$\sigma_{\mathrm{Au}}\,(10^7 \cdot \Omega^{-1}m^{-1})$	4.41 ± 0.19	4.42	Ref. [144]
$S_{\mathrm{Au}}\,(\mu\mathrm{V^{-1}K^{-1}})$	2.1 ± 0.3	2.0	Ref. [45]
$\lambda_{\mathrm{Au}}\,(\mathrm{Wm^{-1}K^{-1}})$	323 ± 20	315	Ref. [91, p. 137]
$\sigma_{\mathrm{AlSi}}\,(10^7 \cdot \Omega^{-1}m^{-1})$	2.61 ± 0.12	2.60 (AlSi $\mathrm{Si}_{5\,\%}$)	Ref. [145]
$S_{\mathrm{AlSi}}\,(\mu\mathrm{V^{-1}K^{-1}})$	-1.2 ± 0.5	-1.65 (pure Al)	Ref. [83]
$\lambda_{\mathrm{AlSi}}\,(\mathrm{Wm^{-1}K^{-1}})$	208 ± 11	190 (AlSi $\mathrm{Si}_{5\,\%}$)	Ref. [145]

Table 6.2: **Transport properties of a platinum, gold and aluminum-silicon microwire.** Overview of the electrical conductivity σ, absolute Seebeck coefficient S and thermal conductivity λ of a platinum (Pt), gold (Au) and aluminum-silicon (AlSi) bulk sample at 300 K. Except for S_{Pt} and S_{Au} which are given at 286 K.

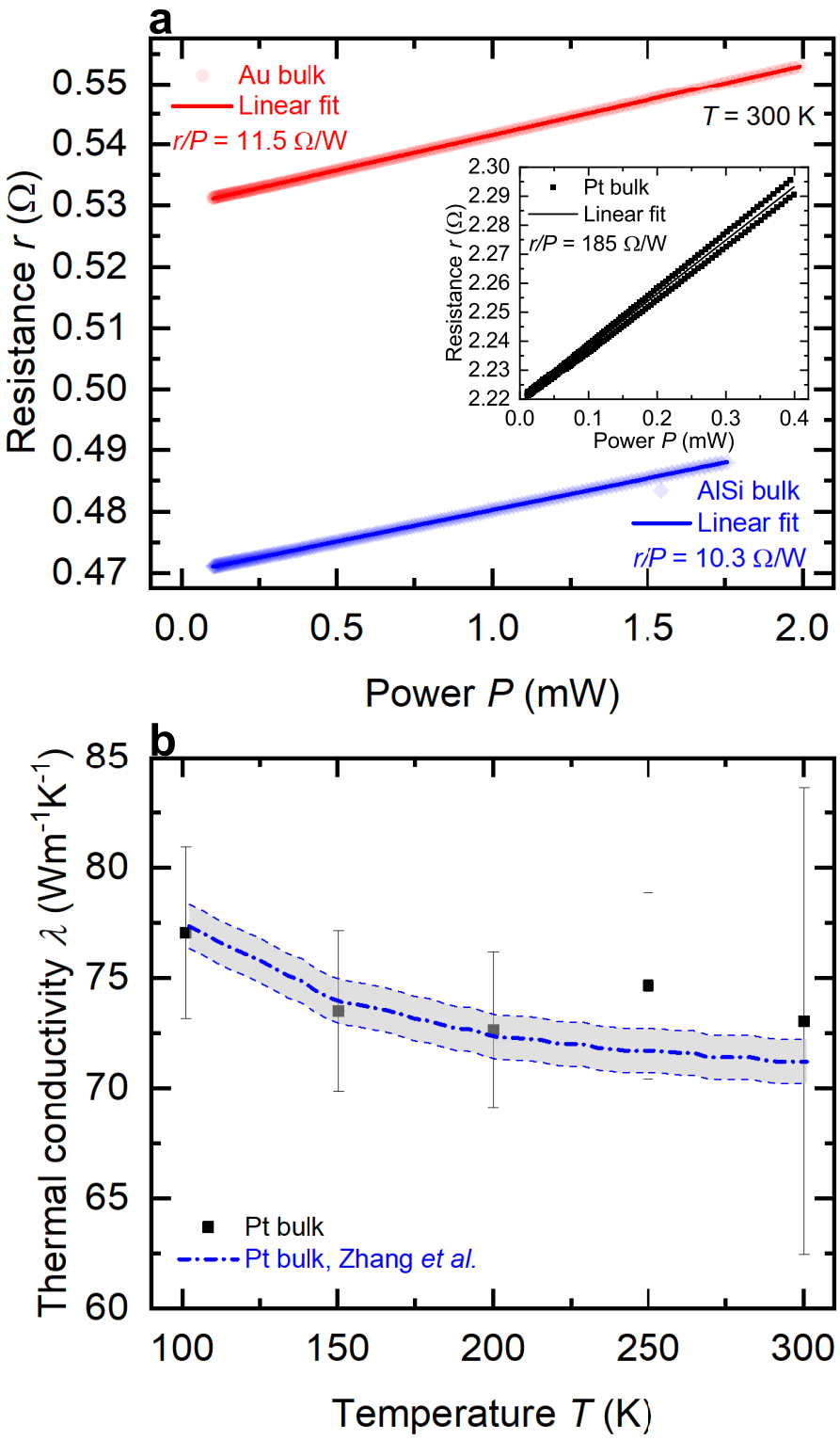

Figure 6.6: **Thermal transport properties of a platinum, gold and aluminum-silicon microwire. a**, Resistance change r as a function of the power P of the wire due to the applied current of a platinum (Pt) (in the inset), gold (Au) and aluminum-silicon (AlSi) wire at $T = 300\,\mathrm{K}$. The thick lines are linear fits that yield the relation between r and P. **b**, Temperature-dependent thermal conductivity λ of a platinum wire. The thick dashed blue line indicates the literature data of platinum taken from Ref. [143]. The gray shaded area marks the uncertainty due to deviations of the plot digitization and due to different available data [143], [91, p. 269].

Chapter 7

Structural and thermoelectric properties of thin platinum films

A new designed and fabricated measurement platform is presented in this chapter. For this purpose, thin platinum films were prepared in order to investigate the influence of size effects on the temperature-dependent thermoelectric transport properties.

7.1 Sample preparation

The thermoelectric micro lab (TML) was designed with microlithography on a 5 mm x 9 mm glass substrate as described in Ch. 5 and it is shown in Fig. 7.1. The TML involves a thermocouple, which consists of a thin sputtered platinum film (sputter target: 99,99 % platinum) and an attached bulk gold wire (diameter: 25 μm, purity: 99.99 %). Here, platinum films with a thickness of 22 nm, 134 nm and 197 nm were prepared as described in Ch. 5. After the thermoelectric characterization of the samples, a heat treatment was performed on the same samples with a thickness of 134 nm and 197 nm. The heat treatment was carried out in a rapid thermal annealer (Ulvac-Riko Mila-5000) in vacuum. The temperature of the annealer was gradually increased from 115 °C to 250 °C and finally to a maximum of 400 °C. The temperature plateaus were held for two minutes each. A thermoelectric characterization of the same samples was performed after the heat treatment. For the X-ray investigations, 10 mm x 10 mm large samples were prepared according to the same procedure with a thickness of 139 nm and 203 nm.

7.2 Experimental details

The thermoelectric characterization of the samples was performed in a flow cryostat in helium atmosphere at ambient pressure. The bulk gold wire creates a thermoelectric connection between the upper and lower part of the platinum film. A platinum line heater is used to generate a temperature difference δT between the hot (temperature T_1, red) and cold (temperature T_2, blue) contacts. The temperatures at the hot contact and cold contact are determined by four-terminal resistance thermometers. For exemplary *I-U* curves, see Fig. 7.3. The resulting temperature difference along both materials due to the different junction temperatures ($T_1 > T_2$) produces a thermovoltage U_S. For further information about the working principle of the

Sample	t (nm)	$T_{\max}$ (°C)	RRR
Pt 0	22 ± 2	–	1.59 ± 0.01
Pt 1	134 ± 5	–	–
Pt 2	134 ± 5	400	8.45 ± 0.01
Pt 3	197 ± 5	–	3.00 ± 0.01
Pt 4	197 ± 5	400	8.26 ± 0.01

Table 7.1: **Thickness, heat treatment parameters and residual resistance ratio of thin platinum films.** Overview of thickness t, maximum heat treatment temperature $T_{\max}$ and residual resistance ratio RRR of four thin platinum films. The thickness was determined by atomic force microscopy. The residual resistance ratio RRR was determined as the ratio of the resistance at 290 K divided by the resistance of 20 K.

TML, see Ch. 5. In the experiments, the heater power is controlled by a Keithley SourceMeter 2401. The thermometer resistances are determined by four terminal measurements performed by a Keithley 6221 and 2182A. The thermovoltage is measured by a Keithley 2182A Nanovoltmeter. The measurement configurations are changed by a Keithley 7001 switch matrix system. The thickness of all samples was determined by atomic force microscopy. X-ray experiments have been conducted with a lab-based diffractometer, with a Cu-K_α rotating anode source with a wavelength of $\lambda = 0.154$ nm. All X-ray experiments were carried out by Dr. Anton Zykov and Prof. Dr. Stefan Kowarik at the Humboldt-Universität zu Berlin.

7.3 X-ray investigations

X-ray measurements of polycrystalline platinum films with thicknesses of 139 nm and 203 nm exhibit four Bragg peaks corresponding to the platinum (111), (200), (220) and (311) reflections. The most intense Bragg peak of the 203 nm thin film is the (111) reflection (see Fig. 7.2 a), indicating a preferential orientation of the crystallites with a surface parallel (111) plane. Additional heat treatment and increased temperature of the heat treatment lead to an increase in the peak intensity and a shift of the peak position to larger detector angles. The position of the Bragg reflection at (111) of the annealed platinum films is in agreement with literature [146]. The average crystallographic grain size D_S of the crystallites with a (111) orientation was estimated by the Scherrer equation [132, 133]

$$D_S \geq \frac{K\lambda}{\Delta(2\theta)\cos(\theta)}. \tag{7.1}$$

K is a dimensionless shape factor with a value of 0.9, $\lambda = 0.154$ nm is the X-ray wavelength. The broadening $\Delta(2\theta)$ is given by the full-width at half-maximum FWHM of the X-ray diffraction peak shown in Fig. 7.2 a and θ is the Bragg angle. D_S of 139 nm and 203 nm from as sputtered thin platinum films are $D_{S,139nm} \geq (33 \pm 2)$ nm and $D_{S,203nm} \geq (35 \pm 2)$ nm, respectively. This size increases with heat treatment at 400 °C to $D_{S,139nm,400C} \geq (41 \pm 1)$ nm and $D_{S,203nm,400C} \geq (41 \pm 1)$ nm, respectively.

Furthermore, the mosaicity Γ, which is a measure of the spread of crystal plane orientations, was determined for the (111) Bragg reflection. Fig. 7.2 b shows a rocking scan where the sample angle ω is varied for a fixed detector angle 2θ. As the

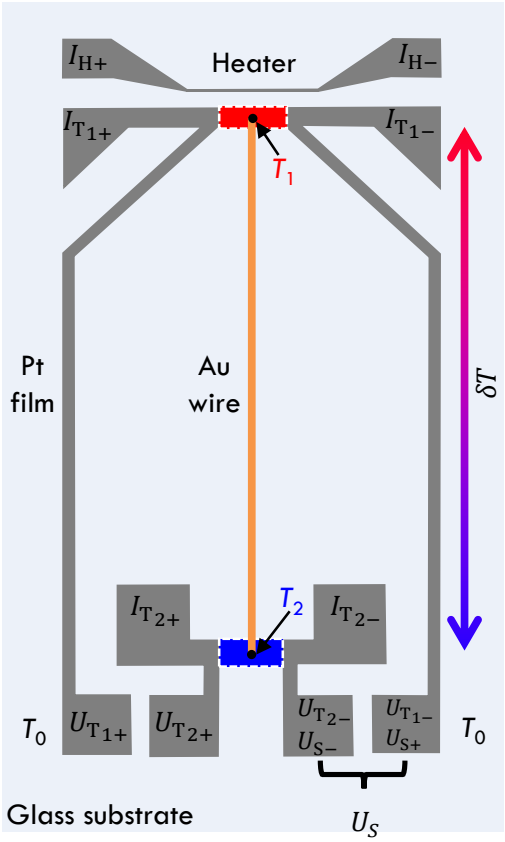

Figure 7.1: **Thermoelectric micro lab (TML).** Platinum (Pt) was sputtered on a $(5\,\mathrm{x}\,9)$ mm^2 glass substrate. A line heater creates a temperature difference $\delta T = T_1 - T_2$ between the hot (temperature T_1, red) and cold (temperature T_2, blue) contacts by applying a current at the contacts $I_{\mathrm{H}+}$ and $I_{\mathrm{H}-}$. A bulk gold (Au) wire (diameter $d = 25\,\mu$m) was bonded at the hot and cold four-terminal resistance thermometers indicated by the corresponding current contacts ($I_{\mathrm{T}_1,\mathrm{T}_2}$) and voltage contacts ($U_{\mathrm{T}_1,\mathrm{T}_2}$). The thermovoltage U_{S} was measured at the Pt pads with respect to the cold side of the sample. The Pt pads were kept at the same temperature T_0 in order to minimize parasitic thermovoltages.

(111) lattice planes are not all perfectly parallel to the substrate surface, intensity is found within an angular distribution of FWHM Γ. Γ of 139 nm and 203 nm as sputtered thin platinum films are $\Gamma_{139\mathrm{nm}} = (11.0 \pm 0.4)^\circ$ and $\Gamma_{203\mathrm{nm}} = (8.9 \pm 0.2)^\circ$, respectively. Thicker platinum films therefore have a more perfect texture corresponding to a narrower distribution of crystallite tilt angles. The tilt decreases and so the crystal quality increases with heat treatment at 400 °C to $\Gamma_{139\mathrm{nm,400C}} = (9.5 \pm 0.2)^\circ$ and $\Gamma_{203\mathrm{nm,400C}} = (7.7 \pm 0.2)^\circ$, respectively.

7.4 Electric transport properties

The Bloch-Grüneisen equation was used to fit the temperature-dependent resistance of the platinum films, which shows the expected metallic behavior given in Fig. 7.4 a, in order to determine the Debye temperature Θ_D of the material. All platinum films with heat treatment and the bulk material (wire diameter $d = 25\,\mu$m) agree with the literature value of $\Theta_\mathrm{D} = 240\,\mathrm{K}$ [89]. Pt 0 (22 nm) and Pt 3 (197 nm, without heat treatment) exhibit a reduced Debye temperature $\Theta_\mathrm{D} \approx 190\,\mathrm{K}$ compared to the literature. This can be attributed to the microstructure.

Furthermore, the residual resistance ratio RRR was determined as the ratio of the resistance at 290 K divided by the resistance of 20 K in order to compare the quality of the sputtered platinum films and the influence of the heat treatment. In general, RRR is a crystal quality characteristic that summarizes the influence of the defect density and impurities on the lattice and it is commonly used to ensure the crystal quality [67–69]. Bulk platinum has the highest residual resistance ratio $RRR_\mathrm{bulk} = 50.3 \pm 0.1$. Thin films have a reduced residual resistance ratio compared to the bulk given in Tab. 7.1. The electrical measurements and X-ray investigations give a sufficient overview about the structural properties of the thin platinum films.

Fig. 7.4 b shows the temperature coefficient α of resistance of platinum. The temperature coefficient of resistance is given by the derivative of the resistivity of platinum to the temperature [65, 66, 147]

$$\alpha = \frac{1}{\rho}\frac{\mathrm{d}\rho}{\mathrm{d}T}. \tag{7.2}$$

For thin films, α depends on the thickness of the platinum films. Larger film thickness and additional heat treatment lead to an increase of the temperature coefficient.

The four-terminal resistance of the cold thermometer was used to determine the electrical conductivity σ of the thin platinum films shown in Fig. 7.5 a. The electrical conductivity of the platinum bulk wire σ_bulk is larger than σ_film. σ_film depends on the film thickness, can be increased by heat treatment and reaches a maximum at low bath temperatures.

Fig. 7.5 b features the electron mean free path Λ_el of the thin films and of the bulk. The electron mean free path of the thin films is reduced compared to the bulk and increases with increasing film thickness and can be further increased by heat treatment. At low bath temperatures, the mean free path reaches a maximum limited by the film thickness and the structural properties.

The uncertainty of the electrical properties of the thin platinum films primarily comes from the determination of the geometry parameters. The thickness t of the thin platinum films was measured by an atomic force microscope (AFM) at several

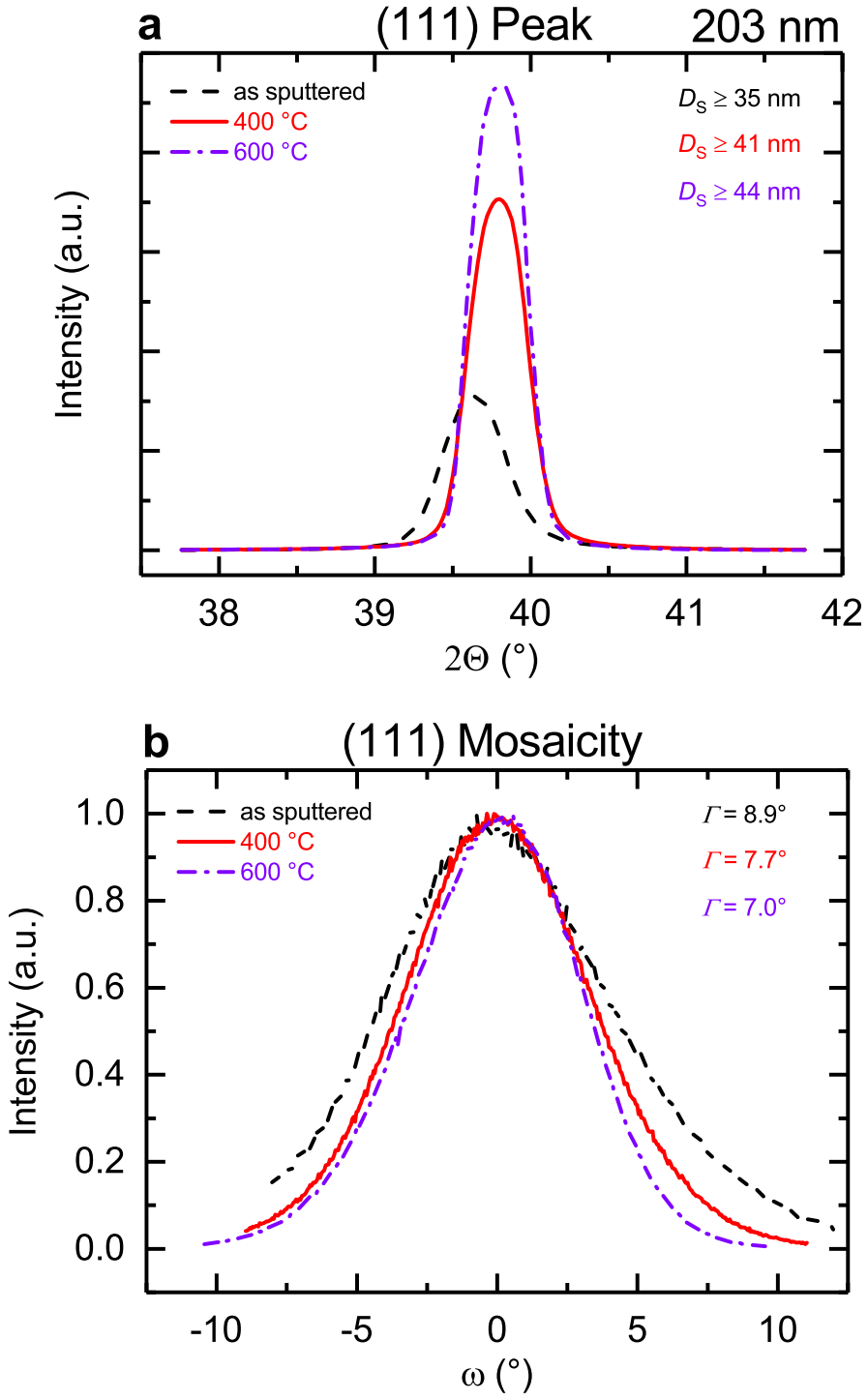

Figure 7.2: **X-ray diffractometry of a thin platinum film with a thickness of 203 nm as sputtered and with additional heat treatment. a**, Intensity of the (111) Bragg reflection as a function of detector angle 2Θ as sputtered, with heat treatment at a maximum temperature of 400 °C and 600 °C. The average crystallographic grain size D_S was determined by the Scherrer equation. **b**, Intensity of the (111) Bragg peak as a function of the rocking angle variation ω as sputtered, with heat treatment at a maximum temperature of 400 °C and 600 °C. The mosaicity Γ of the platinum crystallites with a (111) texture is given by the full width at half maximum of the peak.

points along each sample. The uncertainty of the thickness results from the resolution limitation of the AFM investigations and from the film thickness variation and it is between 2 nm and 5 nm. The size of the resistance thermometer is about $(740 \pm 5)\,\mu\mathrm{m}\,\mathrm{x}\,(200 \pm 5)\,\mu\mathrm{m}$. The four-terminal resistance R was determined by linear fits of corresponding I-U curves. The relative uncertainty of R is less than 1 %. The resulting uncertainty of σ, α and RRR was determined by propagation of uncertainty.

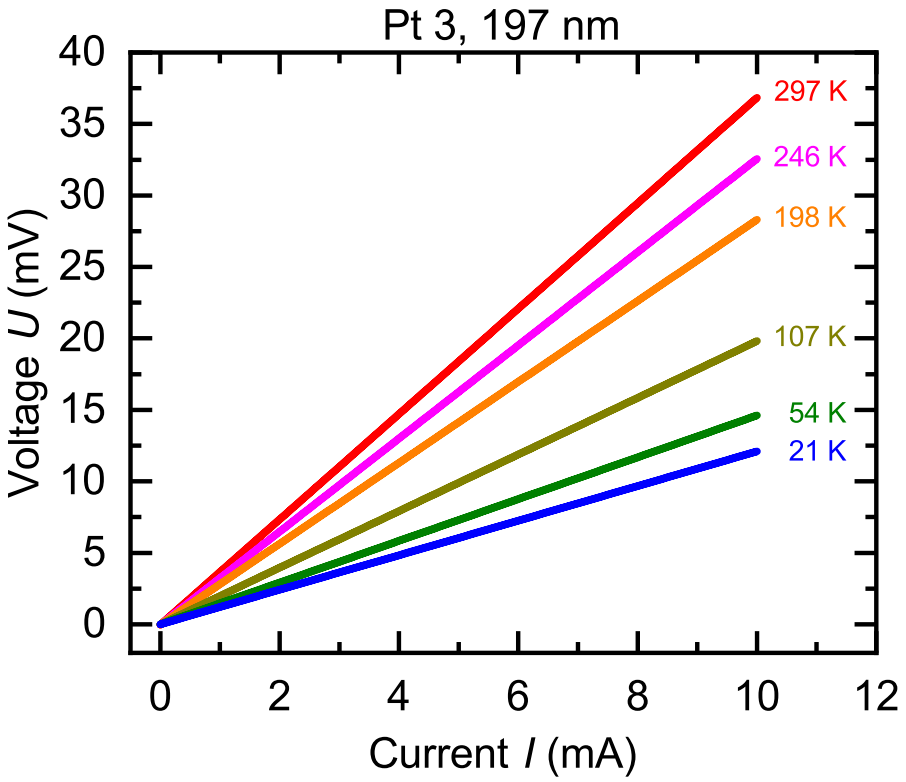

Figure 7.3: **Exemplary four-terminal I-U curves of Pt 3, 197 nm at different bath temperatures.** Voltage U as a function of the current I of the cold thermometer.

7.5 Determination of the Seebeck coefficient

In addition to the electrical characterization, the temperature-dependent Seebeck coefficient of thin platinum films and bulk platinum relative to a bulk gold wire (wire diameter $d = 25\,\mu\mathrm{m}$) was determined by measuring the thermovoltage U_S as a function of the heater current of the line heater. Fig. 7.6 shows the parabolic behavior of the thermovoltage indicating the thermoelectric effect. The temperature difference δT was determined by four-terminal resistance measurements of the thermometers at the hot and cold side of the measurement platform. The slope of the function $U_\mathrm{S}(\delta T)$ gives the relative Seebeck coefficient

$$S_\mathrm{Au,Pt} = S_\mathrm{Au} - S_\mathrm{Pt} = -\frac{\mathrm{d}U_{\mathrm{S_{Au,Pt}}}}{\mathrm{d}\delta T}. \tag{7.3}$$

The temperature difference was increased stepwise by applying a heating current I_H from zero to $-I_\mathrm{H,max}$ and from zero to $+I_\mathrm{H,max}$ in equidistant steps. At each step,

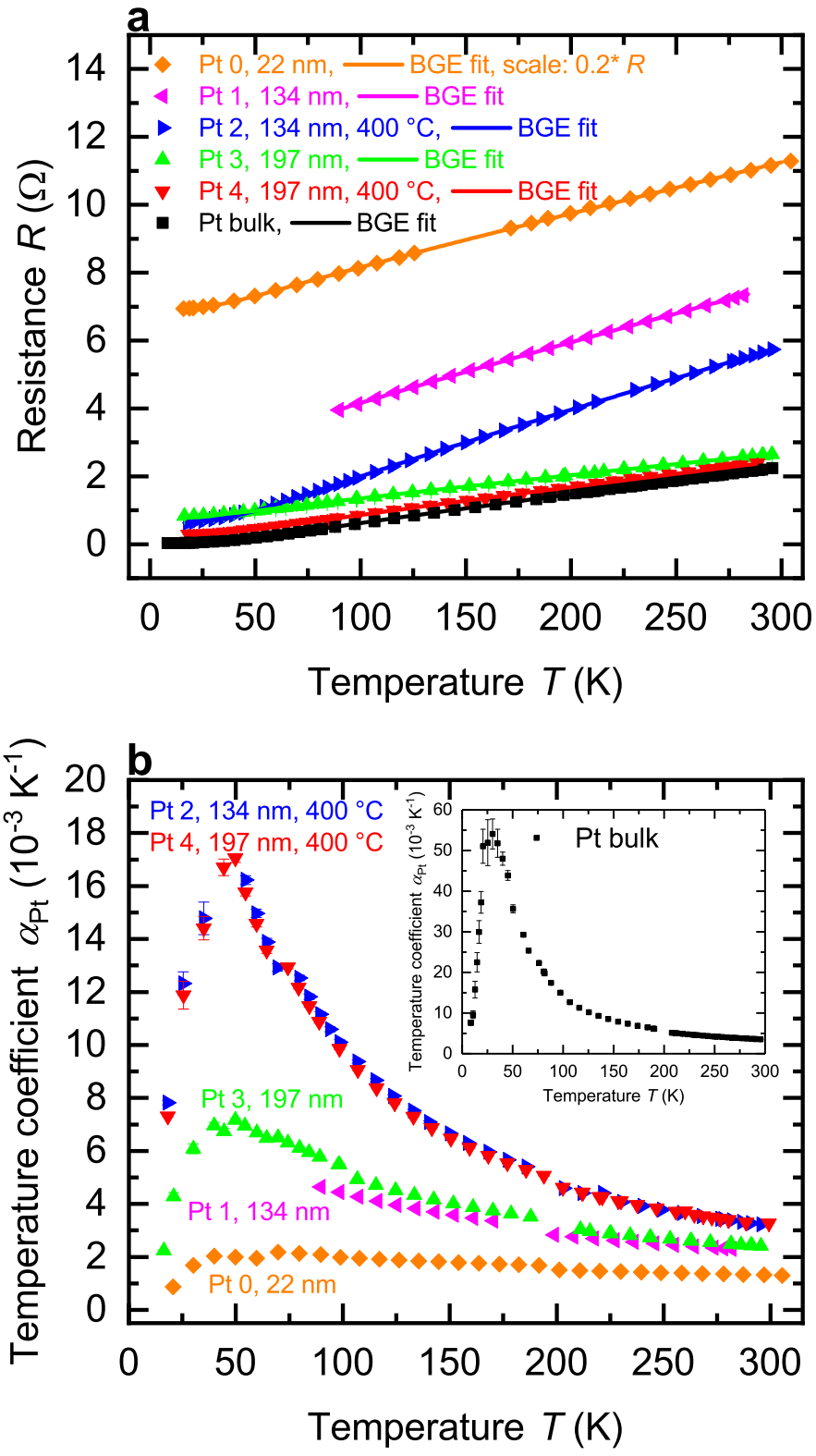

Figure 7.4: **Four-terminal resistance and temperature coefficient of thin platinum films as-sputtered and with heat treatment.** **a**, Four-terminal resistance R as a function of the bath temperature T. The Bloch-Grüneisen equation (BGE) was fitted to the data in order to determine the temperature dependence of the resistance and to calculate the Debye temperature. **b**, Temperature coefficient α_{Pt} of the resistance as a function of the bath temperature T. The inset shows temperature coefficient of the bulk material.

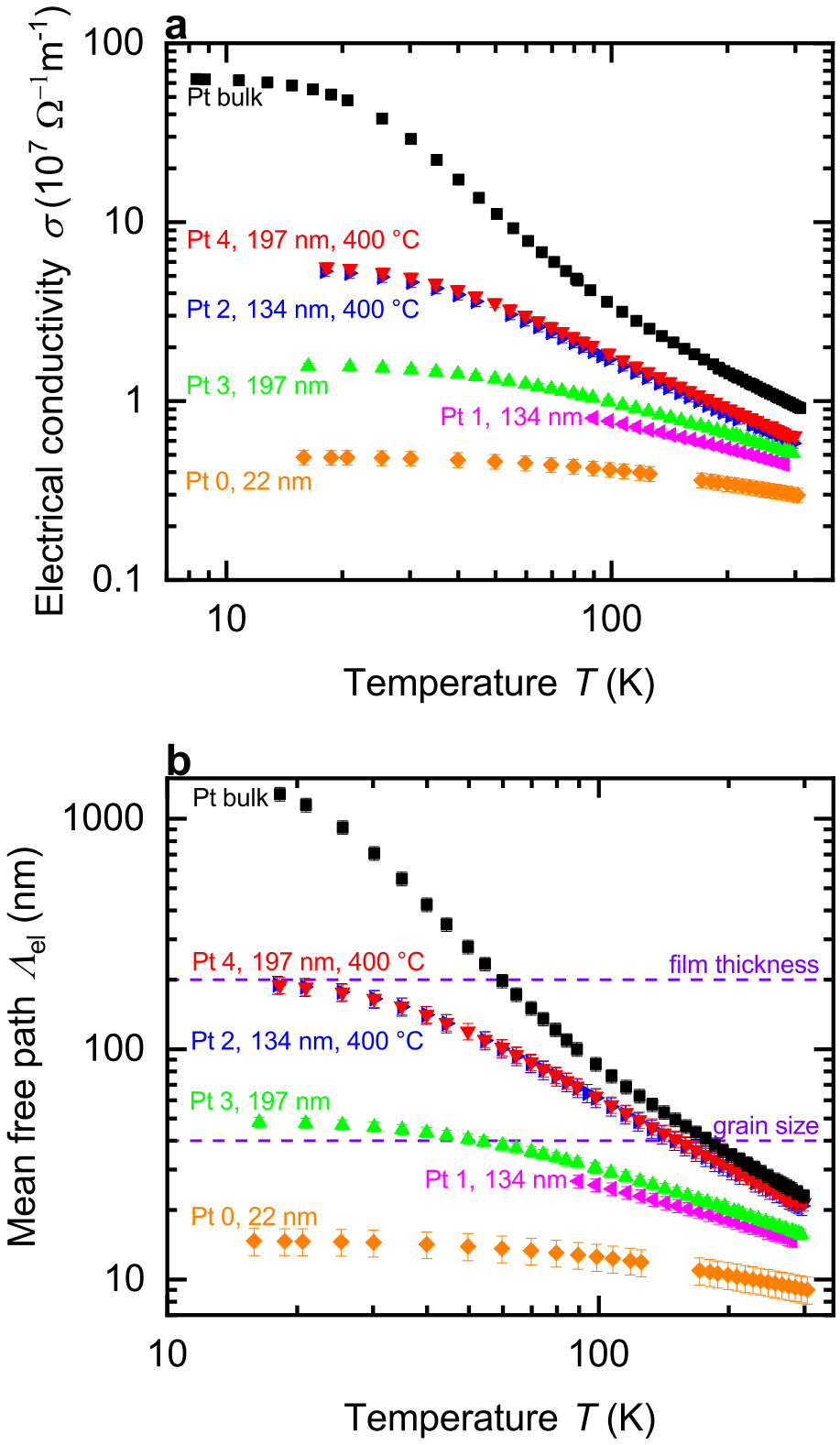

Figure 7.5: **Electrical conductivity and mean free path of thin platinum films as-sputtered and with heat treatment. a**, Electrical conductivity σ as a function of the bath temperature T. **b**, Mean free path of the electrons Λ_{el} as a function of the bath temperature T. The mean free path of as sputtered thin platinum films is mainly limited by grain boundaries at low temperatures. The mean free path of thin platinum films with heat treatment is mainly limited by the film thickness.

the thermovoltage was measured ten times and then arithmetically averaged. The uncertainty of the thermovoltage is given by the confidence interval of the measurement results. The relative Seebeck coefficient is given by the mean of the three slopes of the fit lines to the $U_{\text{S-Au,Pt}}(-I_{\text{H,max}})$ versus $\delta T(-I_{\text{H,max}})$, $U_{\text{S-Au,Pt}}(+I_{\text{H,max}})$ versus $\delta T(+I_{\text{H,max}})$ and $U_{\text{S-Au,Pt}}(-,+I_{\text{H,max}})$ versus $\delta T(-,+I_{\text{H,max}})$ plots, respectively. The uncertainty of the relative Seebeck coefficient is determined by the modulus of the largest deviation of the mean value. The average temperature increase by the micro heater determines the uncertainty of the bath temperature T of the temperature-dependent relative Seebeck coefficient $S_{\text{Au,Pt}}(T)$, which is typically less than 5 % of the bath temperature.

The relative Seebeck coefficient of the thin films and the bulk material is decreasing with decreasing bath temperature as depicted in Fig. 7.7 a. In order to determine the absolute Seebeck coefficient of platinum S_{Pt}, which is given by

$$S_{\text{Pt}} = S_{\text{Au}} - S_{\text{Au,Pt}}, \tag{7.4}$$

the absolute Seebeck coefficient of bulk gold S_{Au} was taken from Ref. [45]. S_{Pt} is given in Fig. 7.7 b. The resulting uncertainty of the absolute Seebeck coefficient was determined by propagation of uncertainty.

7.6 Discussion: Influence of size effects on the thermoelectric transport properties

Structural and electrical characterization

X-ray diffraction analysis gives the average crystallographic grain size D_{S} that was determined by the Scherrer equation [132, 133] from the (111) Bragg reflections of Fig. 7.2 a. The determined values indicate only a lower limit for the crystallographic grain size. The actual grain size can be larger. Furthermore, the X-ray measurements only provide information about the grain size in the growth direction. The in-plane grain size can be significantly larger than the grain size in the growth direction. In addition to the average crystallographic grain size, the morphological grain size is discussed in literature [148–150]. It was proposed that the morphological grains, which were determined by scanning tunneling microscopy, are agglomerates of crystallographic grains and that the morphological grain size is increasing with increasing film thickness much further than the crystallographic grain size [148,149]. Overall, X-ray diffraction analysis clearly exhibits that heat treatment increases the crystal quality of the thin platinum films.

In addition to structural investigations, the residual resistance ratio RRR is an indicator of the crystal quality [67–69]. The RRR is increased after the heat treatment of thin platinum films confirming the improved crystal quality compared to thin films without heat treatment. Furthermore, the reduced electrical conductivity and the reduced temperature coefficient of the platinum thin films compared to the bulk are comparable with results reported in [65, 95].

The structural properties like film thickness and grain size are linked with the mean free path of the electrons in order to investigate the transport properties of the thin platinum films. The electron mean free path Λ_{el} was determined from the change of the electrical conductivity of the thin films under the assumption that

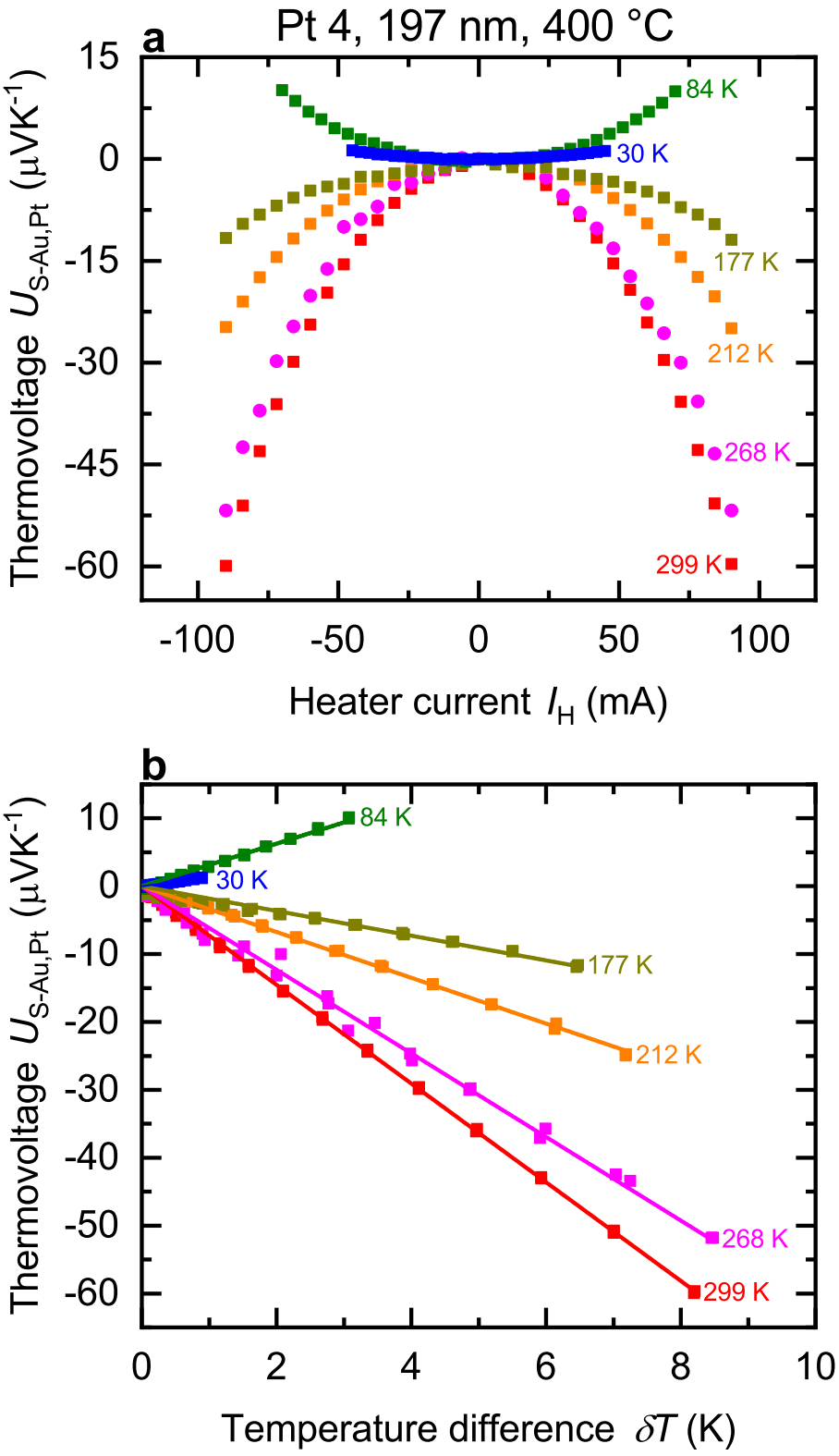

Figure 7.6: **Thermovoltage as a function of the heater current and temperature difference of Pt 4.** **a**, Thermovoltage U_S as a function of heater current I_H at different bath temperatures T. The sign of the thermovoltage changes below $T \approx 150\,\mathrm{K}$. **b** Thermovoltage U_S as a function of temperature difference δT at different bath temperatures T. The slope of the fitted solid lines gives the relative Seebeck coefficient between the thin platinum films and the bulk gold wire.

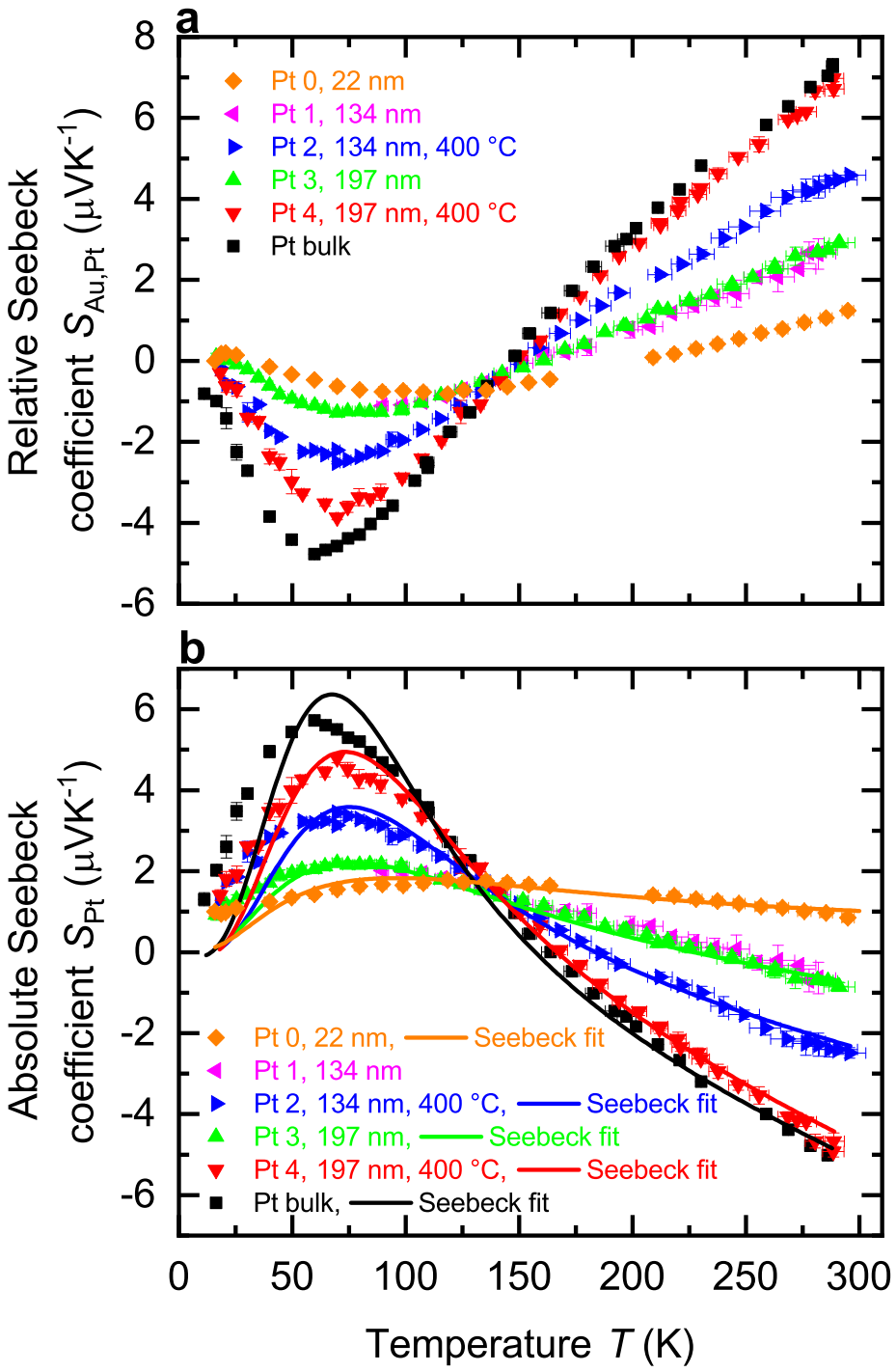

Figure 7.7: **Relative and absolute Seebeck coefficient of thin platinum films as sputtered and with heat treatment. a**, Relative Seebeck coefficient $S_{\mathrm{Au,Pt}}$ of platinum relative to a bulk gold wire with a diameter of 25 μm as a function of the bath temperature T. **b**, Absolute Seebeck coefficient S_{Pt} of platinum as a function of the bath temperature T. The corresponding solid lines represent the Seebeck fit of the data. Absolute Seebeck coefficient of bulk gold S_{Au} was taken from Ref. [45].

scattering events reduce this length. This reduction of the electron mean free path can be described and related to Matthiessen rule [21].

$$\Lambda_{\mathrm{el,f}}(T)^{-1} = \Lambda_{\mathrm{el,b}}(T)^{-1} + \Lambda_{\mathrm{el,s,gb}}^{-1} \tag{7.5}$$

is the inverse thin film electron mean free path, $\Lambda_{\mathrm{el,b}}(T)^{-1}$ is the inverse mean free path of the bulk and $\Lambda_{\mathrm{el,s,gb}}^{-1}$ is the inverse temperature-independent scattering length of the electrons due to surface and grain boundary scattering [21]. The electrical conductivity is proportional to the mean free path and changes of the electrical conductivity affect the electron mean free path,

$$\sigma = en\mu = \frac{ne^2\tau}{m} = \frac{ne^2}{mv}\Lambda. \tag{7.6}$$

e is the elementary charge, n is the charge carrier density, μ is the mobility, τ is the mean free time, m is the electron mass and v is the Fermi velocity.

$$\Lambda_{\mathrm{el,f}}(T) = \frac{\sigma_{\mathrm{f}}(T)}{\sigma_{\mathrm{f}}(\mathrm{RT})}\Lambda_{\mathrm{el,f}}(\mathrm{RT}) \tag{7.7}$$

and

$$\Lambda_{\mathrm{el,b}}(T) = \frac{\sigma_{\mathrm{b}}(T)}{\sigma_{\mathrm{b}}(\mathrm{RT})}\Lambda_{\mathrm{el,b}}(\mathrm{RT}) \tag{7.8}$$

are the electron mean free paths of the thin films and of the bulk material, respectively [21]. In order to determine $\Lambda_{\mathrm{el,f}}(T)$, Eq. 7.7 and Eq. 7.8 have to be combined with Eq. 7.5 [21]. These relative changes of the electrical conductivities are fitted and yield the parameters $\Lambda_{\mathrm{el,f}}(\mathrm{RT})$ and $\Lambda_{\mathrm{el,s,gb}}$ [21]. The electron mean free path of bulk platinum at room temperature $\Lambda_{\mathrm{el,b}}(\mathrm{RT}) = 23\,\mathrm{nm}$ is given in Ref. [89] and has to be considered for the calculation.

Fig. 7.5b shows the electron mean free path as a function of the bath temperature. Tab. 7.2 shows the electron mean free path at room temperature and the temperature-independent scattering length of the electrons. Pt 0 (22 nm) exhibits the lowest electron mean free path of all investigated platinum thin films. Pt 1 (197 nm, without heat treatment) and Pt 3 (197 nm, without heat treatment) have larger mean free paths that saturate at lower bath temperatures compared to Pt 0 (22 nm). Pt 2 (134 nm, with heat treatment) and Pt 4 (197 nm, with heat treatment) have nearly the same temperature dependence of the electron mean free path, which is in the order of magnitude of the film thickness. Heat treatment increases the mean free path.

From the structural properties, it can be concluded that the electron mean free path at low bath temperatures is mainly limited by grain boundaries for thin films without heat treatment. For thin films with heat treatment, the main limitation is set by the film thickness.

Seebeck coefficient

In general, the Seebeck coefficient is the sum of two parts. The thermodiffusion part and the phonon drag part [28, 41, 50]:

$$S = S_{\mathrm{diff}} + S_{\mathrm{ph}}. \tag{7.9}$$

Sample	t (nm)	$T_{\max}$ (°C)	$\Lambda_{\mathrm{el,f}}(\mathrm{RT})$ (nm)	$\Lambda_{\mathrm{el,s,gb}}$ (nm)
Pt 0	22	-	9 ± 1	15 ± 1
Pt 1	134	-	14 ± 1	36 ± 1
Pt 2	134	400	21 ± 2	212 ± 2
Pt 3	197	-	16 ± 1	48 ± 1
Pt 4	197	400	22 ± 2	219 ± 2

Table 7.2: **Electron mean free path.** Mean free path of the samples with thickness t and maximum heat treatment temperature $T_{\max}$. $\Lambda_{\mathrm{el,f}}(\mathrm{RT})$ is the electron mean free path of the thin films at room temperature and $\Lambda_{\mathrm{el,s,gb}}$ is the temperature-independent mean free path of the electrons due to surface and grain boundary scattering. $\Lambda_{\mathrm{el,b}}(\mathrm{RT}) = 23\,\mathrm{nm}$ of bulk is given in literature at room temperature [89].

as explained in detail in Ch. 2.3. As a brief recap, some important formulas are given in the following. S_{diff} is the contribution due to the thermodiffusion of the charge carriers as described by Mott's formula [28, 41, 51]:

$$S_{\mathrm{diff}} = \frac{\pi^2 k_{\mathrm{B}}^2 T}{3e} \left(\frac{\partial \ln \sigma(\epsilon)}{\partial \epsilon} \right) \Bigg|_{\epsilon_F}. \tag{7.10}$$

S_{ph} is the contribution due to the phonon drag effect. The phonon drag effect is based on the electron-phonon interaction and is given by

$$S_{\mathrm{ph}} = \frac{C_{\mathrm{ph}}(T)}{3ne}\gamma = \frac{C_{\mathrm{ph}}(T)}{3ne}\frac{\tau_{\mathrm{pp}}}{\tau_{\mathrm{pp}} + \tau_{\mathrm{ep}}} \quad [41, 50]. \tag{7.11}$$

The γ-factor is given by

$$\gamma = \frac{1}{1 + \frac{\tau_{\mathrm{ep}}}{\tau_{\mathrm{pp}}}} = \frac{1}{1 + F_\tau T \exp\left(-\frac{\Theta_{\mathrm{D}}}{T}\right)}. \tag{7.12}$$

The formula that describes the Seebeck coefficient over a wide temperature range is given by

$$S = F_{\mathrm{diff}} \frac{T}{\Theta_{\mathrm{D}}} + \frac{F_{\mathrm{ph}} \left(\frac{T}{\Theta_{\mathrm{D}}}\right)^3 \int_0^{\frac{\theta_{\mathrm{D}}}{T}} \frac{x^4 \exp(x)}{(\exp(x)-1)^2} \mathrm{d}x}{1 + F_\tau T \exp\left(-\frac{\Theta_{\mathrm{D}}}{T}\right)}. \tag{7.13}$$

The Seebeck fit and measurement results are given in Fig. 7.7 b. The phonon drag peak appears between bath temperatures of 65 K and 75 K. A possible reason for the deviation of the Seebeck fit from the measurement results below 50 K is that the phonon drag part is very sensitive to impurities [28, 45, 151]. The Seebeck fit provides different parameters that are given in table 7.3.

The thermodiffusion contribution is described by the fit parameter F_{diff}. The platinum films without heat treatment have the smallest thermodiffusion contribution to the absolute Seebeck coefficient which can be attributed to an increased scattering rate at grain boundaries. The fit parameter of the thermodiffusion part of Pt 2 (134 nm, with heat treatment) is $F_{\mathrm{diff,Pt\ 2}} = (-2.6 \pm 0.1)\,\mu\mathrm{VK}^{-1}$ and of Pt 4 (197 nm, with heat treatment) is $F_{\mathrm{diff,Pt\ 4}} = (-4.7 \pm 0.1)\,\mu\mathrm{VK}^{-1}$. This difference can be explained by increased size effects like surface scattering in Pt 2. The thermodiffusion part of Pt 4 and bulk have nearly the same temperature dependence and magnitude and it seems that Pt 4 reaches the upper limit of the thermodiffusion

part that is provided by the bulk material. For Pt 0 (22 nm), the thermodiffusion contribution is positive ($F_{\mathrm{diff,Pt\ 0}} = (0.09 \pm 0.02)\,\mu\mathrm{VK}^{-1}$). This can be attributed to a strong reduction of the thermodiffusion contribution. As a result, the phonon drag contribution dominates the absolute Seebeck coefficient already at room temperature.

All platinum thin films exhibit a vanishing of the phonon drag part at high bath temperatures. F_{ph} estimates the strength of the phonon drag on the absolute Seebeck coefficient. Pt 0 (22 nm) has the lowest value of the fit parameter $F_{\mathrm{ph,Pt\ 0}} = (7.4 \pm 0.4)\,\mu\mathrm{VK}^{-1}$ due to the influence of the microstructure and surface that leads to an increase of charge carrier scattering. This value increases with increasing film thickness and with additional heat treatment and reaches its maximum for the bulk material with $F_{\mathrm{ph,bulk}} = (47 \pm 2)\,\mu\mathrm{VK}^{-1}$ due to a decrease of charge carrier scattering.

$|F_{\mathrm{ph}}/F_{\mathrm{diff}}|$ gives the modulus ratio between the fit parameter of the thermodiffusion part and phonon drag part. The ratio $|F_{\mathrm{ph}}/F_{\mathrm{diff}}|$ of bulk and of the thin films (Pt 2, Pt 3, Pt 4) is approximately 10. This ratio indicates that the thermodiffusion and phonon drag part are reduced by nearly the same factor, when the film thickness is reduced. To further illustrate that the thermodiffusion and the phonon drag part are related to each other, F_τ, which gives the ratio of the scattering time of the electron-phonon and phonon-phonon interaction, is introduced. It determines the γ-factor. The γ-factor, see Eq. 7.12, is a number between 0 and 1 that depends on the interaction between phonons and electrons. For $T \ll \Theta_{\mathrm{D}}$, $\gamma \approx 1$, means electron-phonon interaction is dominant compared to phonon-phonon interaction. Phonon-phonon interaction is dominant compared to electron-phonon for $\gamma \approx 0$.

The γ-factor as a function of temperature for thin films and bulk is given in Fig. 7.8. For all temperatures applies: $\gamma_{\mathrm{film}} > \gamma_{\mathrm{bulk}}$. This means that there is an increased amount of electron-phonon interaction compared to phonon-phonon interaction in the thin films than in the bulk. The influence of the phonon drag part on the absolute Seebeck coefficient dominates in thin films compared to the bulk. For example, the thermodiffusion part of Pt 3 is reduced by 77 % towards bulk, resulting in a significant effect of the phonon drag part even at room temperature. This difference can be explained by the inner and outer interfaces of the the thin films and the resulting grain boundary scattering.

Decreasing temperatures lead to an increase of γ_{film} and γ_{bulk}. This indicates that the electron-phonon interaction is becoming more dominant compared to phonon-phonon interaction. At temperatures below 50 K, the thermodiffusion part tends to 0 and the γ-factor tends to 1. The reason for this behavior can be attributed to the phonon-phonon interaction which is negligible compared to the electron-phonon interaction.

Pt 2 (134 nm, with heat treatment) and Pt 4 (197 nm, with heat treatment) have the same γ-factor but different absolute Seebeck coefficients, indicating that the ratio of electron-phonon interaction compared to the phonon-phonon interaction is the same but the absolute amount of electron-phonon and phonon-phonon interaction is larger in thicker platinum films with heat treatment, because the essential limitation is no longer caused by grain boundaries, but by the film thickness.

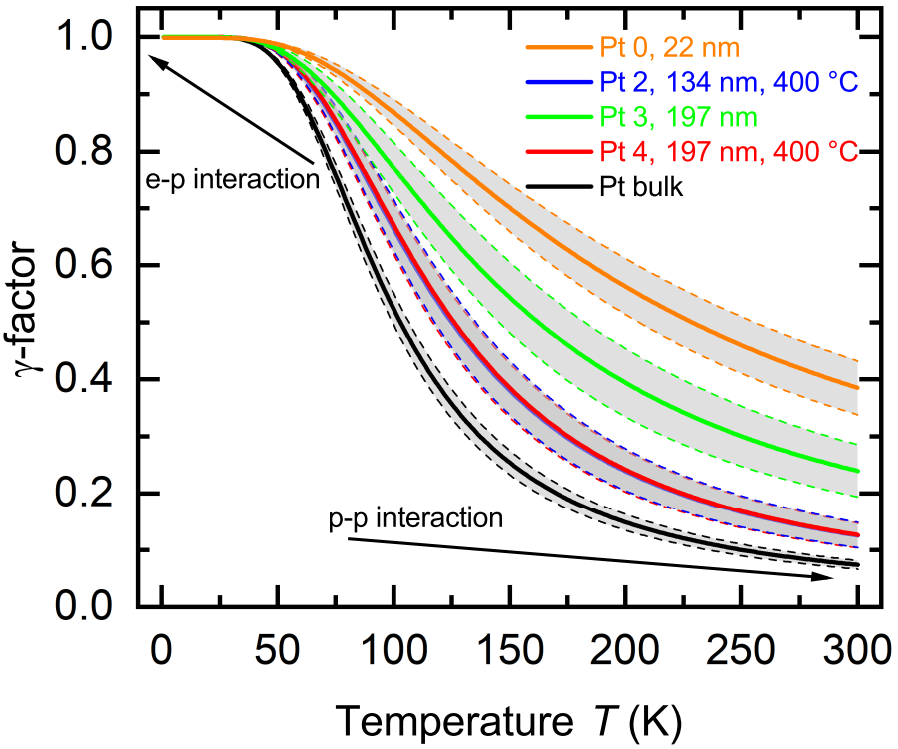

Figure 7.8: **γ-factor.** The panel shows the γ-factor of the thin platinum films as sputtered and with heat treatment as a function of temperature T. The γ-factor is determined by the electron-phonon (e-p) and phonon-phonon (p-p) interaction. The gray shaded area around the solid lines marks the uncertainty. $\gamma = 1$ means that the electron-phonon interaction compared to the phonon-phonon interaction is dominant. $\gamma = 0$ means that the phonon-phonon interaction compared to the electron-phonon interaction is dominant. The curves of Pt 2 and Pt 4 have a similar temperature dependence and are lying on top of each other.

Sample	t (nm)	$T_{\max}$ (°C)	F_{ph} (μVK^{-1})	F_τ (K^{-1})	F_{diff} (μVK^{-1})
Pt 0	22	-	7.4 ± 0.4	0.010 ± 0.002	0.09 ± 0.02
Pt 1	134	-	-	-	-
Pt 2	134	400	24 ± 2	0.05 ± 0.01	-2.6 ± 0.1
Pt 3	197	-	12 ± 1	0.020 ± 0.005	-1.1 ± 0.1
Pt 4	197	400	35 ± 2	0.05 ± 0.01	-4.7 ± 0.1
Bulk	-	-	47 ± 2	0.09 ± 0.01	-4.8 ± 0.1

Table 7.3: **Seebeck fit parameters.** Parameters of the Seebeck fit for each sample with thickness t and maximum heat treatment temperature $T_{\max}$. F_{ph} is the parameter that describes the intensity of the phonon drag part. F_τ gives the ratio of the scattering time of the electron-phonon interaction and of the phonon-phonon interaction. F_{diff} describes the intensity of the thermodiffusion contribution. Due to the lack of low temperature data, the fit parameters of Pt 1 (197 nm, without heat treatment) are not given.

Short summary

A comparison with the measurement data of metallic microwires from the previous chapter clearly shows the influence of the microstructure and the surface on the thermoelectric transport properties. In the case of thin films, the electrical conductivity compared to the bulk can be reduced by several orders of magnitude. This can be explained by the fact that the mean free path of the charge carriers is in the order of magnitude of the film thickness and thus additional scattering events occur at the surface. The reduction of σ can be further increased if the mean free path is in the order of magnitude of the grain size. The influence of the microstructure and the surface can also be observed for the absolute Seebeck coefficient. Here, a reduction of the film thickness leads also to a reduction of the absolute Seebeck coefficient due to an increase of scattering events. The change in the thermoelectric transport properties during the transition from bulk to thin films can not only be observed in the case of platinum, but it can also be transferred to other metals. This should be taken into account when making reference measurements with intermetallic connections.

Chapter 8

Structural and thermoelectric properties of individual silver nanowires

In this chapter, a special measurement platform was used in to order to investigate the temperature-dependent thermoelectric transport properties of individual single crystalline silver nanowires. The influence of nanopatterning on the thermodiffusion and phonon drag contribution of the absolute Seebeck coefficient is discussed.

8.1 Sample preparation

Highly pure and single crystalline silver nanowires were synthesized by the reduction of silver nitrate (purity: 99.9999 %) with ethylene glycol in presence of copper dichloride dihydrate and polyvinylpyrrolidone. Dr. Johannes Bourbon (neé Ruhhammer) and Prof. Dr. Peter Woias from the Laboratory for Design of Microsystems (IMTEK) of the University of Freiburg synthesized the silver nanowires. The nanowire suspension was immersed to a grooved silicon wafer.

Individual nanowires were lifted from the wafer and assembled on the thermoelectric nanowire characterization platform (TNCP A) by a mechanical transfer method. TNCP A was developed and fabricated at the Laboratory for Design of Microsystems (IMTEK) of the University of Freiburg by Dr. Zhi Wang, Dr. Michael Kroener and Prof. Dr. Peter Woias.

The electrical and mechanical connection between the nanowires and the TNCP was performed by electron beam-induced deposition (EBID) of a platinum-based precursor ($(CH_3)_3\,Pt\,(CpCH_3)$) as described in Ch. 4. This process was assisted by Dr. Toni Markurt and Dr. Martin Albrecht from the Leibniz Institute for Crystal Growth (IKZ) in Berlin.

8.2 Experimental details

The Seebeck coefficients of four individual silver nanowires were measured relative to the Seebeck coefficient of platinum conduction lines with a thickness of 200 nm in a flow cryostat in the temperature range between 16 K and room temperature in an ambient helium atmosphere. A temperature difference along the nanowires was applied by one of the micro heaters of the TNCP at certain stabilized bath

temperatures T. The thermovoltage $U_{\text{S-Ag,Pt}}$ was measured with respect to the cold side of the nanowires for different heater powers. The temperature difference δT between the hot side and the cold side of the nanowires was determined by the measured four-terminal resistance change of the calibrated thermometer lines T_h and T_c, see Fig. 8.2. For further information about the working principle of the TNCP A, see Ch. 5. Dr. Danny Kojda performed the relative Seebeck coefficient measurements of nanowire 4 at the Humboldt-Universität zu Berlin.

In the experiments, the heater power is controlled by a Keithley SourceMeter 2401. The thermometer resistances are determined by four terminal measurements performed by a Keithley 6221 and 2182A. The thermovoltage is measured by a Keithley 2182A Nanovoltmeter. The measurement configurations are changed by a Keithley 7001 switch matrix system.

Scanning (SEM) and transmission electron microscopy (TEM) were performed to investigate the structure of the silver nanowires as described in Ch. 4. Dr. Anna Mogilatenko conducted the structural investigations of the silver nanowires using TEM at the Humboldt-Universität zu Berlin.

8.3 Transmission and scanning electron microscopy investigations

The crystallinity of individual silver nanowires was confirmed by transmission electron microscopy. Fig. 8.1 a shows a silver nanowire placed on a lacey carbon film. The growth direction is along [110]. Selected area electron diffraction analysis and high-resolution transmission electron microscopy confirm the face centered cubic structure as given in Fig. 8.1 b and 8.1 c, respectively. A scanning transmission electron microscopy image of a complete silver nanowire can be seen in Fig. 8.1 d. The geometry parameters determined from scanning electron microscopy images are given in Tab. 8.1. A typical example of a silver nanowire on the measurement platform (TNCP A) is given in Fig. 8.2a.

Sample	$l\,(\mu\text{m})$	$d\,(\text{nm})$	$\sigma\,(10^7\Omega^{-1}\text{m}^{-1})$
NW 1	18.9 ± 0.4	190 ± 10	3.3 ± 0.4
NW 2	18.1 ± 0.8	180 ± 5	4.9 ± 0.4
NW 3	16.0 ± 0.7	120 ± 10	4.0 ± 0.7
NW 4	15.0 ± 1.0	120 ± 20	–

Table 8.1: **Geometry parameters and electrical conductivity.** Overview of length l and diameter d of each silver nanowire determined by scanning and transmission electron microscopy. The electrical conductivity σ is given at room temperature.

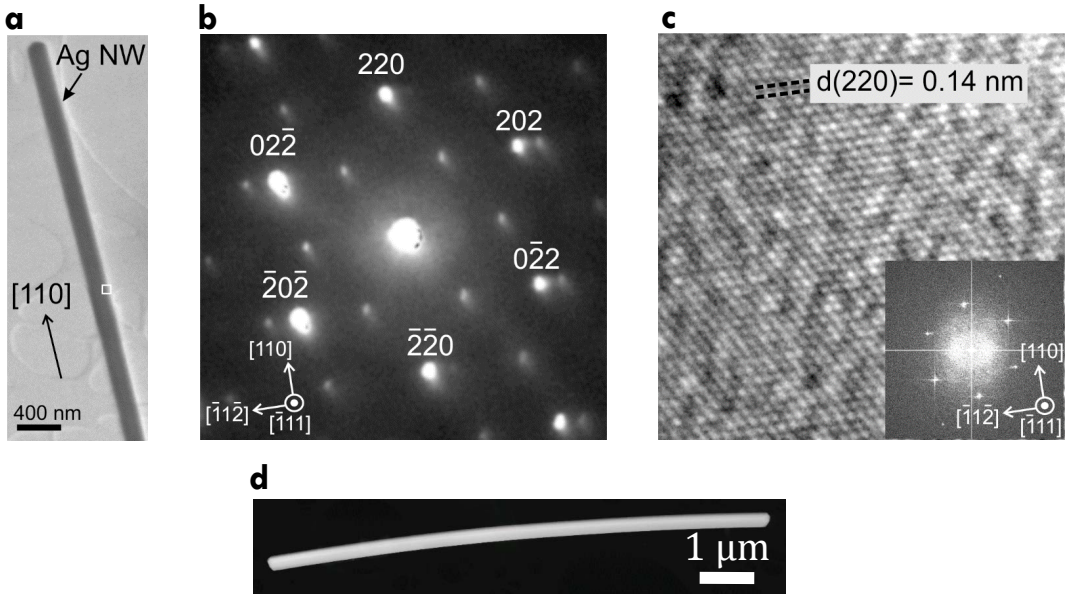

Figure 8.1: **Transmission electron microscopy (TEM) and selected area electron diffraction (SAED) images of a silver nanowire.** **a**, Transmission electron microscopy image of a silver nanowire placed on a carbon film showing the growth direction of the nanowire. **b**, Selected area electron diffraction confirms the face centered cubic structure of the silver nanowire viewed along one of the <111> directions. Additional diffraction spots, which are not indexed in the image correspond to a <110> direction and appear due to the presence of a twin in the nanowire [21]. **c**, High-resolution transmission electron microscopy image showing atomic planes. The inset shows the fast Fourier transformation. **d**, Scanning transmission electron microscopy image of a silver nanowire.

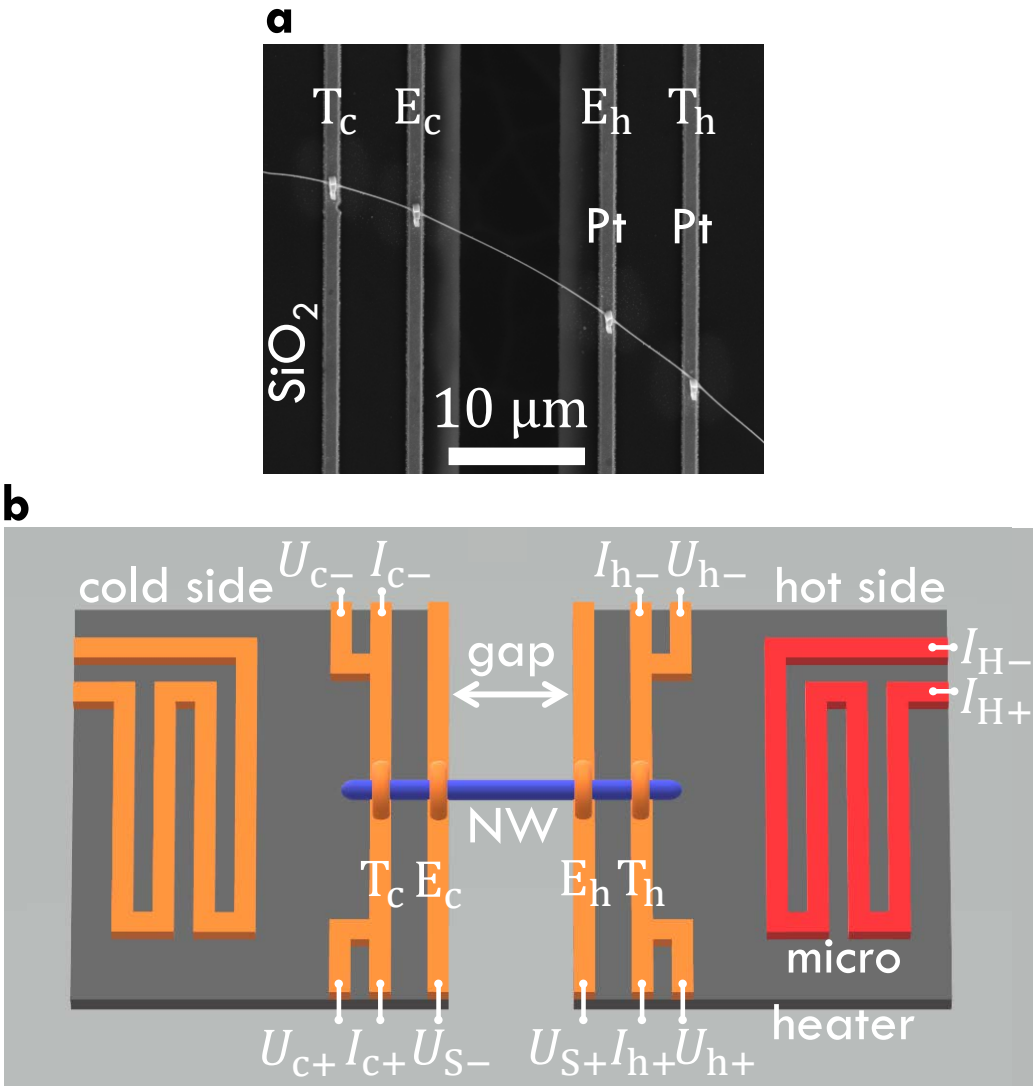

Figure 8.2: **Thermoelectric nanowire characterization platform (TNCP A).** **a**, Scanning electron microscopy (SEM) image of a silver nanowire (NW 3) contacted on platinum (Pt) conduction lines of the thermoelectric nanowire characterization platform (TNCP A) by electron beam-induced deposition. **b**, Sketch of the measurement area of the platform. An electron transparent gap divides the measurement area into two sides. The determination of the four-terminal resistance of a nanowire (NW) (blue) can be performed by applying a current I at the outer platinum conduction lines (orange) and measuring the voltage U at the inner conduction lines E_c and E_h. The thermovoltage U_S of a nanowire relative to the platinum conduction lines can be measured by applying a heating current I_H at the micro heater (red). This creates a temperature difference along the nanowire that can be calculated by four-terminal resistance thermometers T_c and T_h (orange) for the cold and hot side, respectively.

8.4 Electric transport properties

The thermoelectric nanowire characterization platform (TNCP A) was used in order to determine the electrical conductivity and the Seebeck coefficient of the silver nanowires. Electron beam-induced deposition contacts were prepared to improve the electrical and mechanical connection between the nanowire and the measurement platform. A scanning electron microscopy image of a silver nanowire (NW 3) on top of the platinum conduction lines of the TNCP is depicted in Fig. 8.2 a. A schematic of the measurement setup is given in Fig. 8.2 b. Geometry parameters determined by scanning and transmission electron microscopy and as well as the electrical conductivity σ determined from four-terminal resistance measurements at room temperature are given in Tab. 8.1.

The electrical conductivity of the silver nanowires is reduced compared to the bulk material, see Fig. 8.4 a. This can be attributed to size effects that reduce the electron mean free path in the silver nanowires as shown in Fig. 8.4 b. The results of the electrical measurements are in agreement with Ref. [21]. The uncertainty of the electrical conductivity σ of the silver nanowires primarily comes from the determination of the geometry parameters. The diameter d of the silver nanowires was measured by scanning electron microscopy (SEM) at several points along each nanowire. The uncertainty of the diameter results from the resolution limitation of the SEM investigations and from the nanowire diameter variation and it is between 5 nm and 20 nm. The length l of the silver nanowires was measured by SEM. The uncertainty of the length l mainly comes from the size of contact area that is defined by the electron beam-induced deposition contacts. The uncertainty of the length varies between 0.4 μm and 1.0 μm. The four-terminal resistance R was determined by linear fits of corresponding I-V curves, see Fig. 8.3. The relative uncertainty of R is less than 1 %. Overall, the average relative uncertainty of σ at room temperature is about 12.5 %.

8.5 Determination of the Seebeck coefficient

The temperature-dependent Seebeck coefficient $S_{\mathrm{Ag,Pt}}$ of individual silver nanowires relative to 200 nm thick platinum conduction lines was measured between bath temperatures of 16 K and room temperature. The thermovoltage $U_{\mathrm{S\text{-}Ag,Pt}}$ as a function of the micro heater current I_{H} is presented for a selection of bath temperatures in Fig. 8.5 a. The parabolic behavior confirms the presence of the thermoelectric effect. Fig 8.5 b shows the thermovoltage as a function of the temperature difference. The temperature difference δT between the hot and the cold side of the silver nanowires was calculated by the change of four-terminal-resistance thermometers due to the variation of the power of the micro heater.

The temperature difference was increased stepwise by applying a heating current I_{H} from zero to $-I_{\mathrm{H,max}}$ and from zero to $+I_{\mathrm{H,max}}$ in equidistant steps. At each step, the thermovoltage was measured ten times and then arithmetically averaged. The uncertainty of the thermovoltage is given by the confidence interval of the measurement results. The relative Seebeck coefficient is given by the mean of the three slopes of the fit lines to the $U_{\mathrm{S\text{-}Ag,Pt}}(-I_{\mathrm{H,max}})$ versus $\delta T(-I_{\mathrm{H,max}})$, $U_{\mathrm{S\text{-}Ag,Pt}}(+I_{\mathrm{H,max}})$ versus $\delta T(+I_{\mathrm{H,max}})$ and $U_{\mathrm{S\text{-}Ag,Pt}}(-,+I_{\mathrm{H,max}})$ versus $\delta T(-,+I_{\mathrm{H,max}})$ plots, respectively. The uncertainty of the relative Seebeck coefficient is determined by the modulus of the largest deviation of the mean value. The average temperature increase by the micro

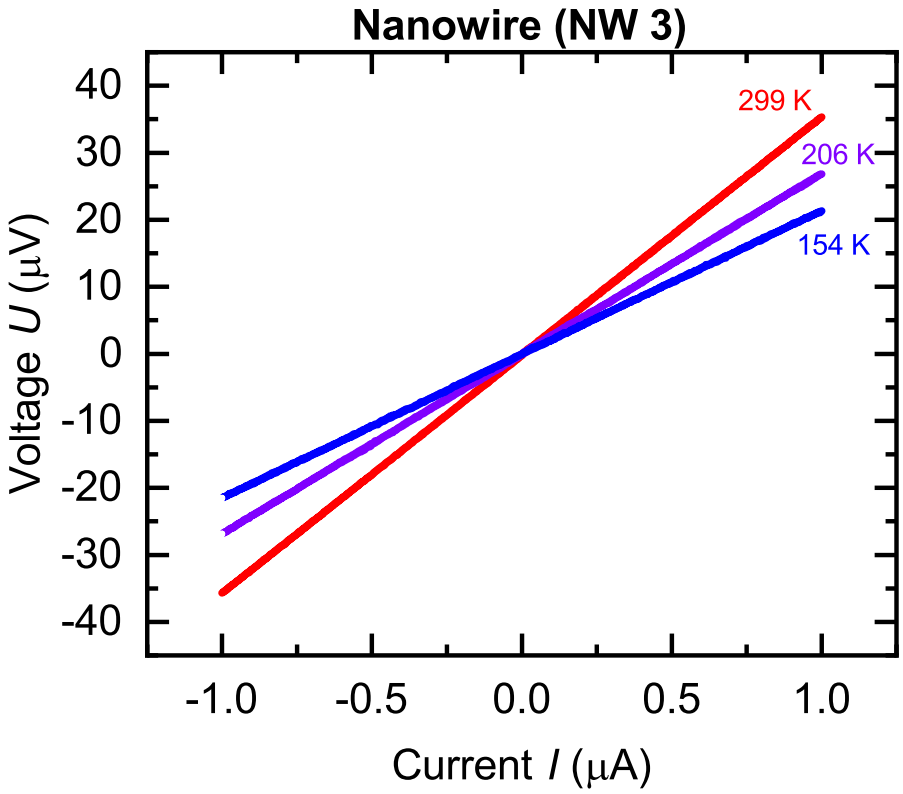

Figure 8.3: **Exemplary four-terminal I-U curves of nanowire (NW 3) at different bath temperatures.** Offset corrected voltage U as a function of the current I.

heater determines the uncertainty of the bath temperature T of the temperature-dependent relative Seebeck coefficient $S_{\mathrm{Ag,Pt}}(T)$, which is typically less than 5 % of the bath temperature. The relative Seebeck coefficient is given by

$$S_{\mathrm{Ag,Pt}} = S_{\mathrm{Ag}} - S_{\mathrm{Pt}} = -\frac{\mathrm{d}U_{\mathrm{S\text{-}Ag,Pt}}}{\mathrm{d}\delta T} \tag{8.1}$$

The temperature dependence of the relative Seebeck coefficient, see Fig. 8.7 a, agrees well for different individual silver nanowires. $S_{\mathrm{Ag,Pt}}$ is decreasing with decreasing bath temperature, a sign reversal occurs at 150 K. Below 50 K, the relative Seebeck coefficient tends to zero with decreasing bath temperature.

In order to obtain the absolute Seebeck coefficient of a silver nanowire, which is given by

$$S_{\mathrm{Ag}} = S_{\mathrm{Ag,Pt}} + S_{\mathrm{Pt}}, \tag{8.2}$$

the absolute Seebeck coefficient of the platinum conduction line S_{Pt} is required. S_{Pt} of the conduction line was determined in the last chapter. The relative and absolute Seebeck coefficients of the reference platinum film are given in Fig. 8.6 a and 8.6 b. The relative and absolute Seebeck coefficients of the silver nanowires versus bath temperature are given in Fig. 8.7 a and Fig. 8.7 b, respectively. Only data points of $S_{\mathrm{Ag,Pt}}$ and S_{Pt} at equal bath temperatures (no interpolation) were used to calculate S_{Ag}. The resulting uncertainty of the absolute Seebeck coefficient was determined by propagation of uncertainty. The reference value of the absolute Seebeck coefficient of bulk silver [35, 38] is plotted as a blue line in Fig. 8.7 b.

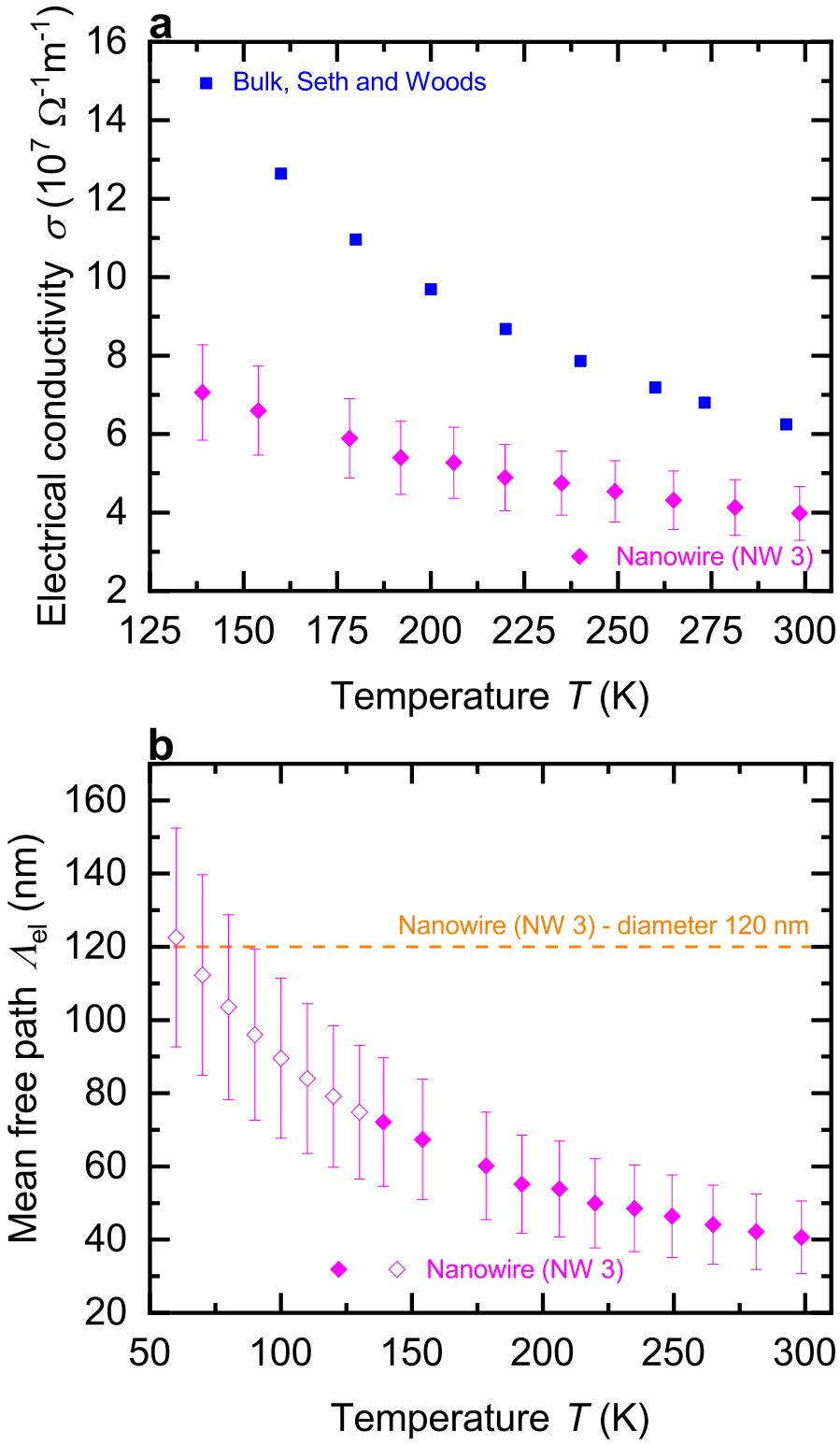

Figure 8.4: **Electrical conductivity and electron mean free path of a silver nanowire. a**, Temperature-dependent electrical conductivity σ of a silver nanowire (NW 3) and bulk silver [98]. **b**, Electron mean free path Λ_{el} as a function of the bath temperature T. The orange dashed line represents the diameter of a silver nanowire (NW 3). At low bath temperatures, the electron mean free path is mainly limited by the diameter of the nanowire. For $T > 130\,\mathrm{K}$, the electron mean free path (filled symbols) was calculated from the measured electrical conductivity. For $T \leq 130\,\mathrm{K}$, the electron mean free path (open symbols) was calculated from the extrapolated electrical resistance (electrical conductivity) that has been determined by the Bloch-Grüneisen formula.

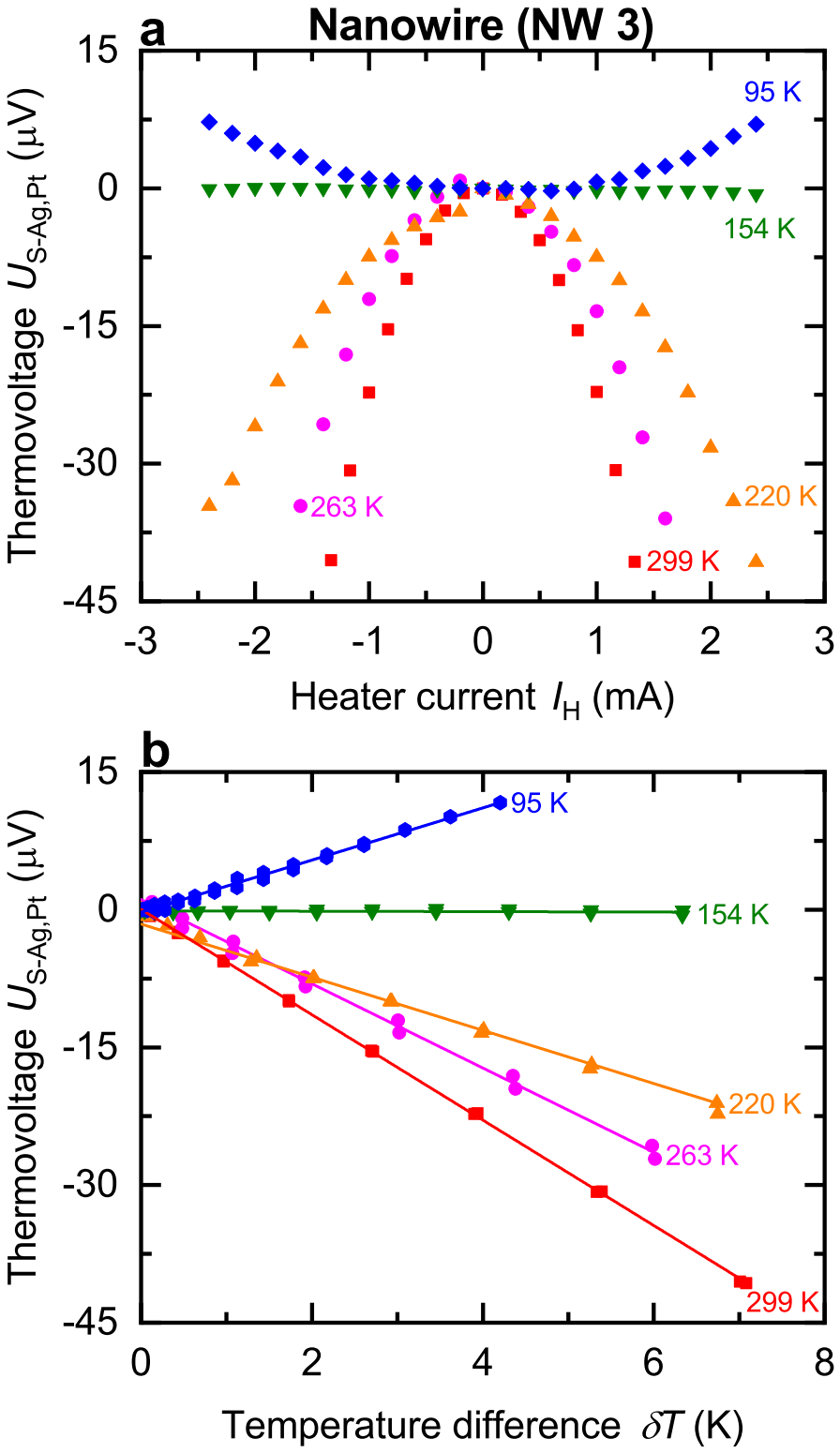

Figure 8.5: **Thermovoltage as a function of the heater current and temperature difference of a silver nanowire. a**, Thermovoltage $U_{\text{S-Ag,Pt}}$ of a silver nanowire (NW 3) as a function of the heater current I_{H}. **b**, Thermovoltage $U_{\text{S-Ag,Pt}}$ of the silver nanowire versus temperature difference δT. The slope of the fitted solid lines yields the relative Seebeck coefficient.

The gray shaded area around the blue line defines the uncertainty of the Seebeck coefficient due to several data given in the literature [34–36, 38].

The results show that the absolute Seebeck coefficient of the silver nanowires is reduced compared to the bulk material and exhibits only a weak temperature dependence in the temperature range from 200 K up to 300 K. In this regime, the absolute Seebeck coefficient of bulk silver exhibits a linear temperature dependence. In the temperature range from 200 K down to 100 K, the absolute Seebeck coefficient of the silver nanowires is increasing with decreasing bath temperature and reaches the maximum at 88 K. From 150 K down to 100 K the Seebeck coefficient of the silver nanowires is larger than the corresponding bulk Seebeck coefficient. The maximum Seebeck coefficient of bulk silver can be observed at 35 K. The phonon drag peak of the silver nanowires is shifted towards higher bath temperatures compared to the bulk material. The absolute Seebeck coefficient of the silver nanowires and of bulk silver tend to zero with decreasing bath temperature after reaching their maximum value.

8.6 Discussion: Influence of nanopatterning on the absolute Seebeck coefficient

The electron mean free path Λ_{el} was determined from the change of the electrical conductivity of the nanowire compared to the bulk material. Under the assumption that scattering events reduce the mean free path, it can be described and related to Matthiessen rule [1, 21].

$$\Lambda_{\mathrm{el,nw}}(T)^{-1} = \Lambda_{\mathrm{el,b}}(T)^{-1} + \Lambda_{\mathrm{el,s}}^{-1} \tag{8.3}$$

is the inverse nanowire electron mean free path, $\Lambda_{\mathrm{el,b}}(T)^{-1}$ is the inverse mean free path of the bulk material and $\Lambda_{\mathrm{el,s}}^{-1}$ is the inverse temperature-independent scattering length of the electrons due to surface scattering.

$$\Lambda_{\mathrm{el,nw}}(T) = \frac{\sigma_{\mathrm{nw}}(T)}{\sigma_{\mathrm{nw}}(\mathrm{RT})}\Lambda_{\mathrm{el,nw}}(\mathrm{RT}) \tag{8.4}$$

and

$$\Lambda_{\mathrm{el,b}}(T) = \frac{\sigma_{\mathrm{b}}(T)}{\sigma_{\mathrm{b}}(\mathrm{RT})}\Lambda_{\mathrm{el,b}}(\mathrm{RT}) \tag{8.5}$$

are the electron mean free paths of the nanowire and of the bulk material, respectively. For bulk silver, a value of $\Lambda_{\mathrm{el,b}}(\mathrm{RT}) = 53\,\mathrm{nm}$ is reported at room temperature [89].

For the silver nanowire 3 (NW 3), the electron mean free path was determined from the measured electrical resistance (electrical conductivity) in the temperature range from room temperature down to $T = 140\,\mathrm{K}$. Below $T = 140\,\mathrm{K}$, the contact resistance at outer contacts increased significantly. Thus, for $T \leq 130\,\mathrm{K}$, the electron mean free path was calculated from the extrapolated electrical resistance (electrical conductivity) that have been determined by the Bloch-Grüneisen formula for $T \leq 130\,\mathrm{K}$. The uncertainty of the electron mean free path Λ of the silver nanowire (NW 3) is mainly set by the uncertainty of the electrical conductivities coming from the silver nanowire and from bulk silver. The relative uncertainty of Λ is about 24 %. Fig 8.4 b shows the electron mean free path (NW 3) as a function of the bath temperature. It is in the order of the diameter of the nanowire. Therefore, the

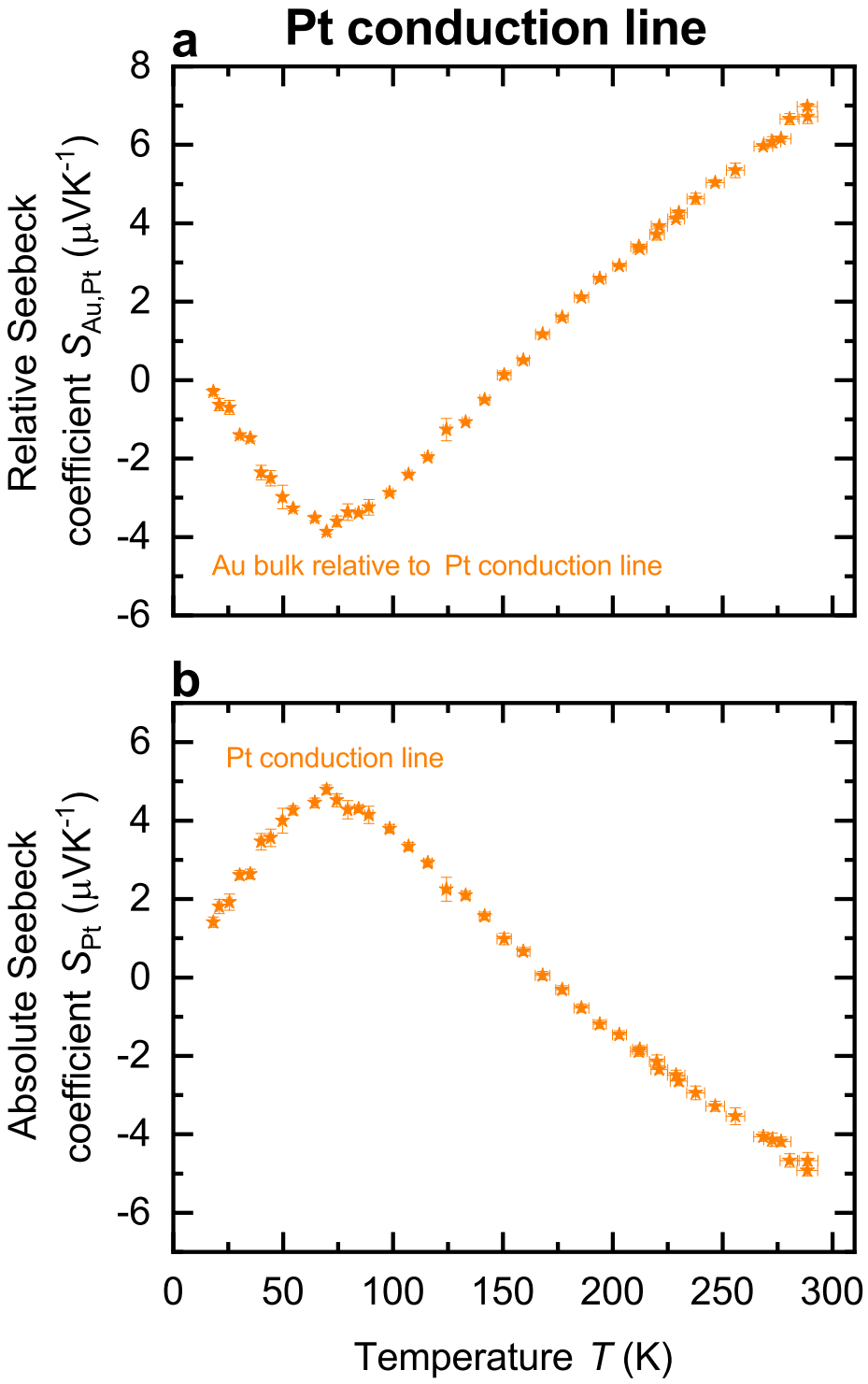

Figure 8.6: **Relative and absolute Seebeck coefficient of a platinum conduction line. a**, Seebeck coefficient $S_{\mathrm{Au,Pt}}$ of a bulk gold (Au) wire relative to a thin platinum (Pt) conduction line as a function of the bath temperature T. **b**, Absolute Seebeck coefficient S_{Pt} of the platinum conduction line versus bath temperature T, which was used in order to determine the absolute Seebeck coefficient of the silver nanowires.

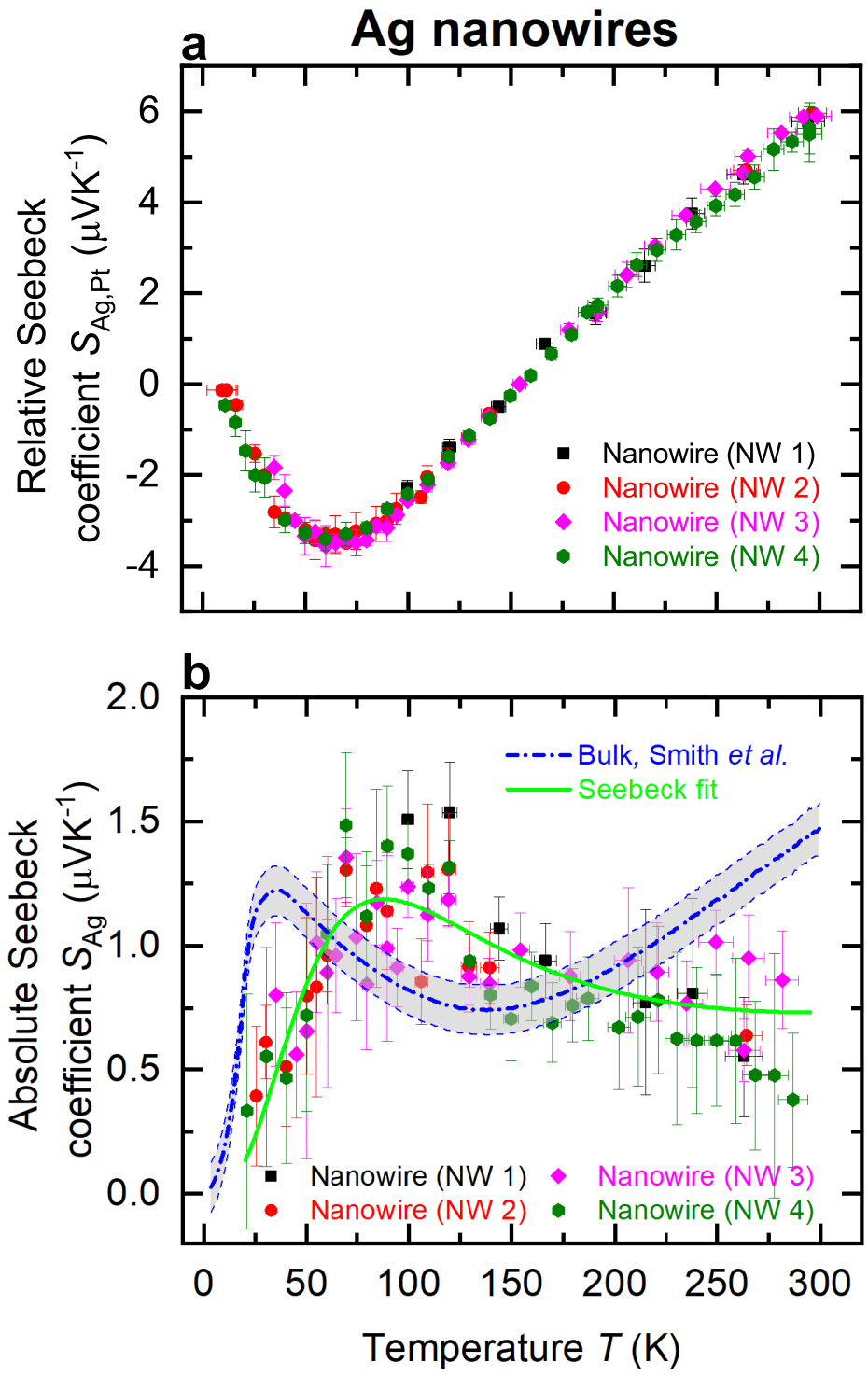

Figure 8.7: **Relative and absolute Seebeck coefficient of the silver nanowires. a**, Relative Seebeck coefficient $S_{\mathrm{Ag,Pt}}$ of four individual silver nanowires (NW 1, NW 2, NW 3 and NW 4) relative to the platinum conduction lines as a function of bath temperature T. **b**, Absolute Seebeck coefficient S_{Ag} of the silver nanowires versus bath temperature T. The thick dash-dotted blue line indicates the absolute Seebeck coefficient of bulk silver. The gray shaded area marks the uncertainty of the bulk Seebeck coefficient. Temperature-dependent fit (see equation 8.6) of S_{Ag} of the silver nanowires is depicted as a solid green line.

enhanced surface scattering leads to a reduced electrical conductivity of the silver nanowires compared to the bulk material [21].

The absolute Seebeck coefficient of the investigated silver nanowires in this work are comparable with each other. The similar Seebeck coefficients of the silver nanowires despite the different diameters can be explained by the similar surface-area-to-volume ratio A/V. Considering the ratio A/V of a nanowire to the typical A/V of a bulk material gives $\frac{(A/V_{\mathrm{NW}})}{(A/V_{\mathrm{Bulk}})} = 100$ up to $\frac{(A/V_{\mathrm{NW}})}{(A/V_{\mathrm{Bulk}})} = 10000$ or even larger. However, the ratio of nanowire NW3 A/V_{NW3} compared to nanowire NW1 A/V_{NW1} is only $\frac{(A/V_{\mathrm{NW3}})}{(A/V_{\mathrm{NW1}})} = 1.6$. Therefore, the difference is too small for a significant change of the absolute Seebeck coefficient. A further pronounced reduction of the Seebeck coefficient is expected if the diameter of the silver nanowires is less than 50 nm. Furthermore, the expected difference due to the reduced nanowire diameter (from 190 nm to 120 nm) is smaller than the distribution of the measurement data including their uncertainty.

In general, the absolute Seebeck coefficient S is the sum of the thermodiffusion S_{diff} and the phonon drag S_{ph} contributions [28, 41, 50], $S = S_{\mathrm{diff}} + S_{\mathrm{ph}}$ as described in Ch. 2.3 and in the previous chapter. The formula that describes the temperature dependence of the absolute Seebeck coefficient of a metal is given by

$$S(T) = F_{\mathrm{diff}} \frac{T}{\Theta_{\mathrm{D}}} + \frac{F_{\mathrm{ph}} \left(\frac{T}{\Theta_{\mathrm{D}}}\right)^3 \int_0^{\frac{\theta_{\mathrm{D}}}{T}} \frac{x^4 \exp(x)}{(\exp(x)-1)^2} \mathrm{d}x}{1 + F_\tau T \exp\left(-\frac{\Theta_{\mathrm{D}}}{T}\right)}. \tag{8.6}$$

The parameters F_{diff}, F_{ph} and F_τ include the size effects on behalf of nanopatterning. A best, a maximum and a minimum fit line to the measurement data was used to determine the arithmetic mean of each parameter. The uncertainty was derived from the largest deviation of the mean value. The parameters of the silver nanowires and of the bulk material are given in Tab. 8.2 and are discussed below.

Fit parameter	Silver nanowires	Bulk silver
$F_{\mathrm{diff}}\,(\mu\mathrm{VK}^{-1})$	0.3 ± 0.1	1.0 ± 0.1
$F_{\mathrm{ph}}\,(\mu\mathrm{VK}^{-1})$	5.2 ± 0.4	12 ± 2
$F_\tau\,(\mathrm{K}^{-1})$	0.03 ± 0.01	1.2 ± 0.3

Table 8.2: **Fit parameters.** Overview of the fit parameters of the thermodiffusion contribution F_{diff}, the phonon drag contribution F_{ph} and the ratio of the scattering times F_τ.

The thermodiffusion of charge carriers due to a temperature difference along the silver nanowires is described by the parameter F_{diff}. Applying $S(T)$ from Eq. 8.6 on the measurement data yields $F_{\mathrm{diff,NWs}} = (0.3 \pm 0.1)\,\mu\mathrm{VK}^{-1}$ and $F_{\mathrm{diff,bulk}} = (1.0 \pm 0.1)\,\mu\mathrm{VK}^{-1}$. The parameter F_{diff} of the silver nanowires is reduced compared to the bulk value. This can be attributed to the electron mean free path that is in the order of the nanowire diameter and leads to more surface scattering events compared to the bulk material. Bulk silver exhibits a linear temperature dependence of the Seeebeck coefficient (see Fig. 8.8) above the Debye temperature ($\Theta_{\mathrm{D,Ag,bulk}} = 215\,\mathrm{K}$). This is not observed for the silver nanowires in the investigated temperature range.

The phonon drag contribution is described by the parameter F_{ph}. The fit parameters of bulk silver $F_{\mathrm{ph,bulk}} = (12 \pm 2)\,\mu\mathrm{VK}^{-1}$ and of the silver nanowires $F_{\mathrm{ph,NWs}} = (5.2 \pm 0.4)\,\mu\mathrm{VK}^{-1}$ scale the influence of the phonon drag on the Seebeck coefficient. $F_{\mathrm{ph,NWs}}$ is reduced compared to $F_{\mathrm{ph,bulk}}$. The temperature profile

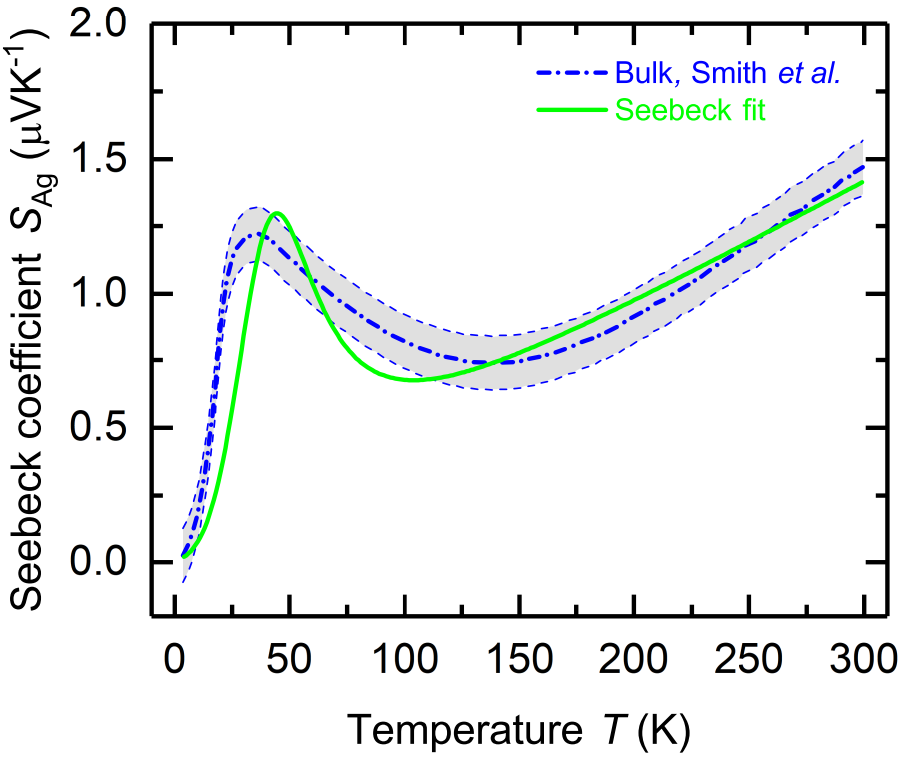

Figure 8.8: **Absolute Seebeck coefficient of bulk silver.** Absolute Seebeck coefficient S_{Ag} of bulk silver versus bath temperature T taken from Ref. [38]. The thick dash-dotted blue line indicates the absolute Seebeck coefficient of bulk silver. The gray shaded area marks the uncertainty of the bulk Seebeck coefficient. Temperature-dependent fit of S_{Ag} is depicted as a solid green line.

of the phonon drag contribution to the Seebeck coefficient of the silver nanowires is broadened compared to the bulk material. Furthermore, a shift of the phonon drag peak towards higher bath temperatures compared to the bulk material is observed. For temperatures $T > 300\,\mathrm{K}$, the absolute Seebeck coefficient of the silver nanowires is expected to increase linear with increasing bath temperatures according to thermodiffusion contribution.

The electron-phonon vs. phonon-phonon interaction is as follows. The parameter F_τ ($F_{\tau,\mathrm{bulk}} = (1.2 \pm 0.3)\,\mathrm{K}^{-1}$, $F_{\tau,\mathrm{NWs}} = (0.03 \pm 0.01)\,\mathrm{K}^{-1}$) gives the ratio of the scattering time of the electron-phonon interaction and of the phonon-phonon interaction and determines the γ-factor. $F_{\tau,\mathrm{NWs}}$ is reduced compared to the bulk material.

Fig. 8.9 shows the γ-factor of the silver nanowires and bulk silver as a function of the temperature. The γ-factor is a number between 0 and 1 that depends on the interaction between phonons and electrons. At low temperatures $T \ll \Theta_\mathrm{D}$, $\gamma \approx 1$. This means that the temperature dependence of the phonon drag is determined by the specific heat that results in $S_\mathrm{ph} \propto T^3$. Phonon-phonon interaction is dominant for $\gamma \approx 0$. This behavior occurs at temperatures $T > \Theta_\mathrm{D}$, so $S_\mathrm{ph} \propto \frac{1}{T}$.

In general, the difference between the γ-factor of the silver nanowires (γ_NWs) and of the bulk material (γ_bulk) can be explained by the small diameter of the nanowires and the much larger surface-area-to-volume ratio of the silver nanowires compared to bulk silver.

γ_NWs is larger than γ_bulk at room temperature. This can be attributed to a stronger reduction of the thermodiffusion contribution compared to the phonon drag contribution to the absolute Seebeck coefficient of the silver nanowires. For this reason, it can be derived that the electron-phonon interaction has already an influence on the absolute Seebeck coefficient of the silver nanowires at 300 K. Whereas, γ_bulk is dominated by the phonon-phonon interaction. This is expressed in a significant amount of the thermodiffusion contribution compared to the phonon drag contribution to the absolute Seebeck coefficient of bulk silver.

γ_NWs and γ_bulk increase with decreasing temperatures. Below 80 K, the increase of γ_NWs is less than the increase of γ_bulk because the influence of the phonon drag on the absolute Seebeck coefficient of the silver nanowires is decreasing. In contrast to the silver nanowires, the influence of the phonon drag on the absolute Seebeck coefficient of bulk silver is increasing in this temperature range.

Comparison of the change of the absolute Seebeck coefficient between platinum and silver

A comparison between the two fit parameters F_diff and F_ph shows the influence of micro- and nanopattering on the absolute Seebeck coefficient of platinum and silver. The factor that describes the intensity of the change between the thermodiffusion contribution between a platinum film with a thickness of 197 nm and the corresponding bulk contribution is determined to $f_\mathrm{diff,Pt,197nm} = F_\mathrm{diff,Pt,bulk}/F_\mathrm{diff,Pt,197nm} = 4.3$. This is larger than change between silver nanowires and the corresponding bulk material $f_\mathrm{diff,Ag,NWs} = F_\mathrm{diff,Ag,bulk}/F_\mathrm{diff,Ag,NWs} = 3.3$. For the phonon drag contribution, the following relations are determined. $f_\mathrm{ph,Pt,197nm} = F_\mathrm{ph,Pt,bulk}/F_\mathrm{ph,Pt,197nm} = 3.9$ and $f_\mathrm{ph,Ag,NWs} = F_\mathrm{ph,Ag,bulk}/F_\mathrm{ph,Ag,NWs} = 2.3$.

The change in the thermodiffusion component and phonon drag component is

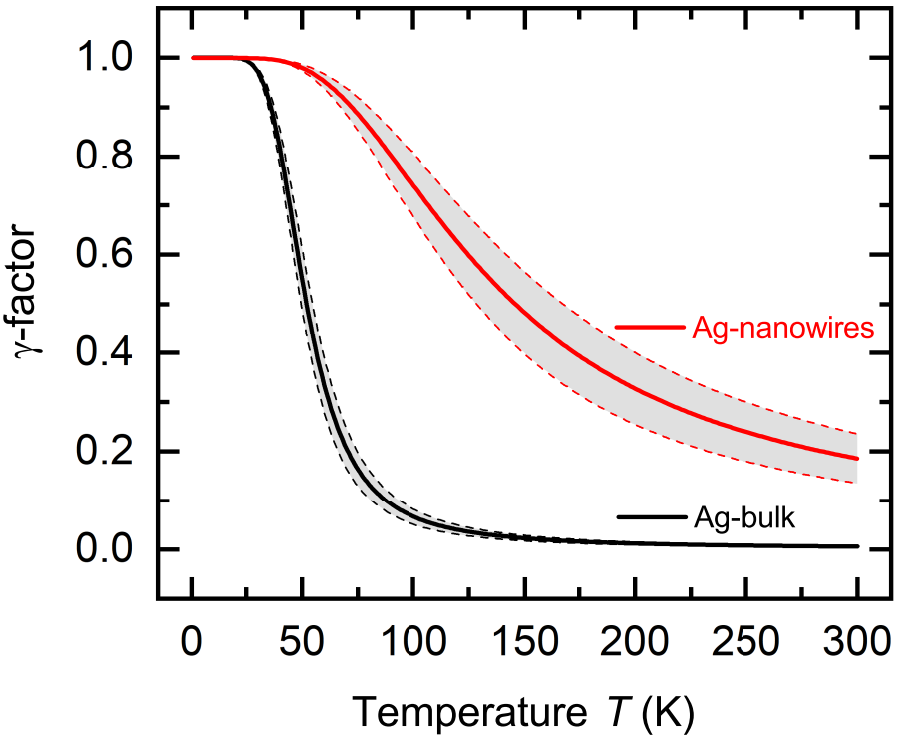

Figure 8.9: **γ-factor of silver nanowires and bulk silver.** The panel shows the γ-factor versus temperature T. The γ-factor is a function of the electron-phonon and phonon-phonon interaction of the silver nanowires (red line) and bulk silver (black line), respectively. The gray shaded area marks the uncertainty. $\gamma = 1$ means that the electron-phonon interaction compared to the phonon-phonon interaction is dominant. $\gamma = 0$ means that the phonon-phonon interaction compared to the electron-phonon interaction is dominant.

larger for thin platinum films than for silver nanowires. There are two main reasons for this. On the one hand there is a limitation of the charge transport by the surface of the thin films and on the other hand additional scattering events at grains lead to a further reduction of the thermodiffusion contribution. Due to the single crystalline structure of the silver nanowires, the influence of interfaces on the absolute Seebeck coefficient is lesser for silver compared to the polycrystalline structure of the thin platinum films. This becomes particularly clear for platinum when the film thickness is reduced to 22 nm, so that the influence of the microstructure leads to a significant reduction of the thermodiffusion component ($f_{\mathrm{diff,Pt,22nm}} = F_{\mathrm{diff,Pt,bulk}}/F_{\mathrm{diff,Pt,22nm}} = 53$ and $f_{\mathrm{ph,Pt,22nm}} = F_{\mathrm{ph,Pt,bulk}}/F_{\mathrm{ph,Pt,22nm}} = 6.4$)

A comparison between the γ-factors of platinum and silver is shown in Fig. 8.10. The Seebeck coefficient of bulk silver is clearly dominated by the phonon-phonon interaction in the temperature range between 150 K and 300 K. In the same temperature range, platinum shows an increasing influence of the electron-phonon interaction with decreasing temperature. For this reason, it can be concluded that the influence of the phonon drag effect compared to the thermodiffusion on the absolute Seebeck coefficient is larger for bulk platinum than for bulk silver in this temperature range. For temperatures below 150 K, the γ-factor increases faster with decreasing temperature for bulk silver than for bulk platinum. This can be explained by the fact that for the silver nanowires the phonon drag contribution dominates over the thermodiffusion part in this temperature regime.

The transition from bulk to the thin films and nanowires leads to an increase of γ-factor at room temperature compared to the bulk. This means that the amount of electron-phonon interaction compared to the phonon-phonon interaction has increased compared to the bulk. The change is comparable for both materials at 300 K. The difference of the γ-factors between the silver nanowires and bulk silver is given by $\Delta_{\gamma,\mathrm{Ag}} = \gamma_{\mathrm{Ag,NWs}} - \gamma_{\mathrm{Ag,bulk}} = 0.18$. The difference of the γ-factors between the thin platinum films and bulk platinum is given by $\Delta_{\gamma,\mathrm{Pt,197nm}} = \gamma_{\mathrm{Pt,197nm}} - \gamma_{\mathrm{Pt,bulk}} = 0.17$. Both differences increase with decreasing temperature. However, the difference between the γ-factors of the silver nanowires and bulk silver increases faster with decreasing temperature than that of platinum. At 150 K, the differences are $\Delta_{\gamma,\mathrm{Ag}} = \gamma_{\mathrm{Ag,NWs}} - \gamma_{\mathrm{Ag,bulk}} = 0.46$ and $\Delta_{\gamma,\mathrm{Pt,197nm}} = \gamma_{\mathrm{Pt,197nm}} - \gamma_{\mathrm{Pt,bulk}} = 0.29$. This can be explained by the fact that the phonon drag effect of the silver nanowires is shifted to higher bath temperatures compared to the bulk silver. Thus, the amount of the electron-phonon interaction is already significant at higher temperatures. This shift of the phonon drag peak is not as pronounced with platinum. As a result, the change of the γ-factor between thin platinum films and bulk platinum is not as large as for the silver nanowires and bulk silver. A larger change in the γ-factor can only be achieved if the film thickness is further reduced.

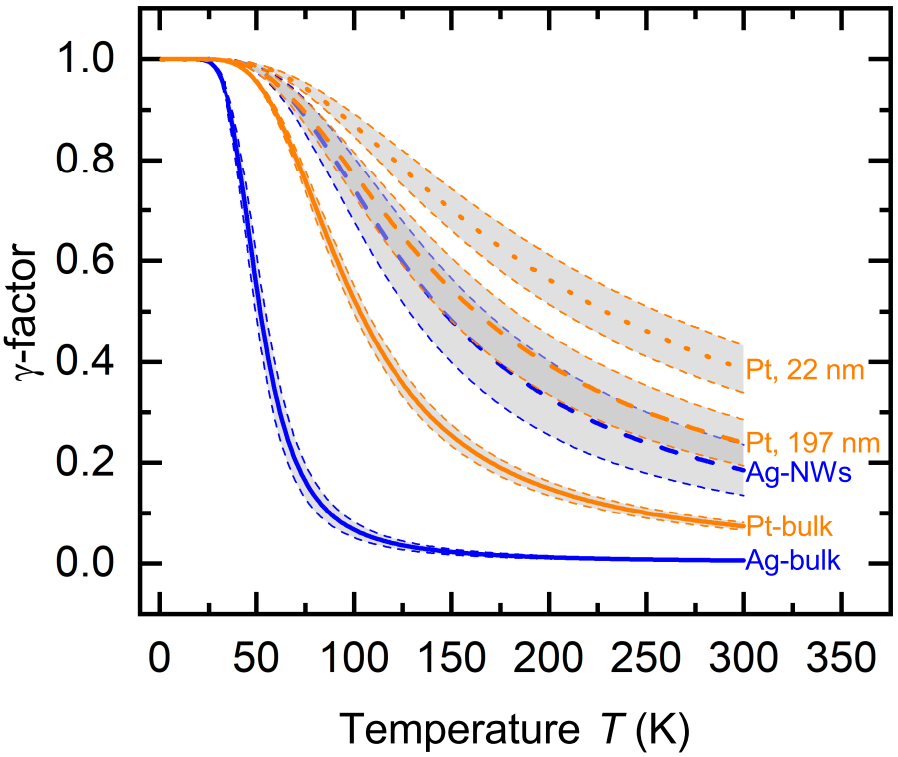

Figure 8.10: **γ-factors of platinum and silver.** The panel shows the γ-factor versus temperature T of bulk silver (Ag-bulk), silver nanowires (Ag-NWs), bulk platinum (Pt-bulk) and thin platinum films (Pt,197 nm and Pt,22 nm). The transition from bulk to the thin films and nanowires leads to an increase of the γ-factor that is a result of the micro- and nanopatterning. The increase of the γ-factor means that the amount of electron-phonon interaction compared to the phonon-phonon interaction is increased for the thin films and nanowires compared to the bulk in the same temperature range.

Reliability of the determination of the absolute Seebeck coefficient

It was ensured that the platinum conduction lines of TNCP A were equivalent to the platinum conduction lines, which were used as a reference material, by using the same purity (99.99 %) of the sputtering material, by the same measure of the thickness (200 nm), by the same heat treatment (max. 400 °C), by the same residual resistance ratio (approx. 8) and by the same temperature coefficient of the resistance (see Fig. 8.11). For these reasons, the platinum conduction lines that were used in the present work as Seebeck reference material for the silver nanowires can be seen as identical from a thermoelectric point of view.

Fig. 8.11 shows the temperature coefficient of the resistance of the platinum conduction lines α_{Pt} that were used for the relative Seebeck measurements of the silver nanowires (samples NW 1 - NW 3) as a function of the bath temperature T. Furthermore, the temperature coefficient of the reference platinum conduction line, whose absolute Seebeck coefficient was used to determine the absolute Seebeck coefficient of the silver nanowires, is given. These temperature coefficients are all in agreement with each other. In addition, the temperature coefficient of a platinum thin film with the same thickness but without additional heat treatment is added. The lack of the heat treatment leads to a temperature coefficient that is clearly reduced compared to the reference platinum conduction line. This in turn leads to a reduced absolute Seebeck coefficient compared to the thin film with heat treatment.

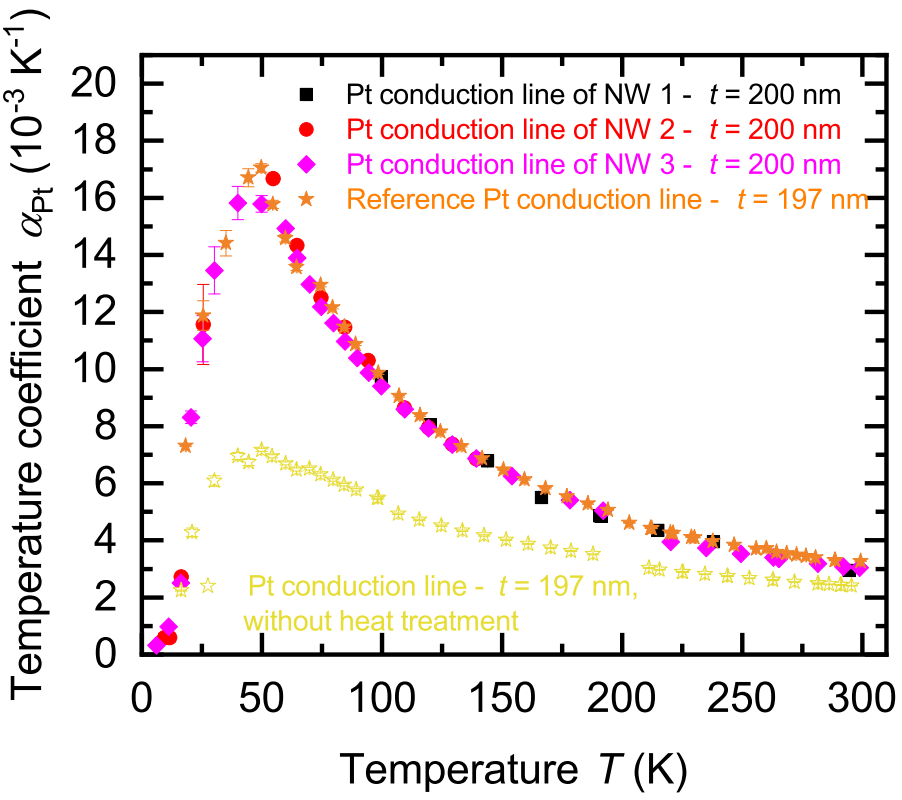

Figure 8.11: **Temperature coefficient of platinum conduction lines.** Temperature coefficient of the resistance of platinum conduction lines α_{Pt} versus bath temperature T.

Short summary

The absolute Seebeck coefficient of individual single crystalline silver nanowires is reduced compared to bulk silver. This can be attributed to the influence of the nanowire surface which lead to a reduction of the thermodiffusion contribution. In contrast to the thin platinum films, for the silver nanowires the phonon drag component is not as large reduced compared to bulk silver as the phonon drag effect in thin platinum films compared to bulk platinum. This can be attributed to the single crystalline structure of the silver nanowires, which lead to less reducing scattering effects compared to the polycrystalline structure with grains of the thin platinum films. The determination of the absolute Seebeck coefficient of the thin platinum films is important beyond the comparison between silver and platinum because it is necessary in order to determine the correct absolute Seebeck coefficient of the silver nanowires. Taking the wrong reference values for the Seebeck coefficient can, for example, lead to a significant increase of the Seebeck coefficient of the silver nanowires at low bath temperatures compared to bulk silver. Even small deviations of the Seebeck coefficient of the reference material can lead to a misinterpretation of the measurement results.

Chapter 9

Structural and thermoelectric properties of individual bismuth-based core/shell nanowires

In this chapter, a special measurement platform was used in to order to investigate the temperature-dependent thermoelectric transport properties of individual Bi-based nanowires. The influence of different shell materials on the electrical conductivity, the absolute Seebeck coefficient and the thermal conductivity is investigated.

9.1 Sample preparation

The bismuth-based core/shell nanowires consist of a bismuth (Bi) core and a tellurium (Te) or titanium dioxide (TiO_2) shell, respectively. The single crystalline Bi core was prepared by means of the on-film formation of nanowires (OFFON) method, see Fig. 9.1. Bi thin films were deposited by radio frequency sputtering on SiO_2/Si substrates. The sputtering system was evacuated to 10^{-7} Torr before the deposition [61]. The vacuum was maintained during the sputtering under a 2-mTorr Ar environment at a temperature of 300 K [61]. After the deposition process, a heat treatment of the Bi thin films was conducted for several hours at 523 K in a vacuum of 10^{-7} Torr [61]. A compressive thermal stress in the Bi film is induced due to the mismatch of the thermal expansion coefficients of the Bi thin film and the SiO_2/Si substrate [152]. This leads to the growth of the Bi nanowires. Radio frequency sputtering was then used to deposit the Te shell onto the Bi core. Atomic layer deposition was used to deposit TiO_2 as a shell material. All processes were performed in a high vacuum environment to prevent the formation of an oxidation layer between the core and the shell material. The Bi-based core/shell nanowires were prepared by Hongjae Moon, Dr. Jeongmin Kim and Prof. Dr. Wooyoung Lee at the Yonsei University in Korea.

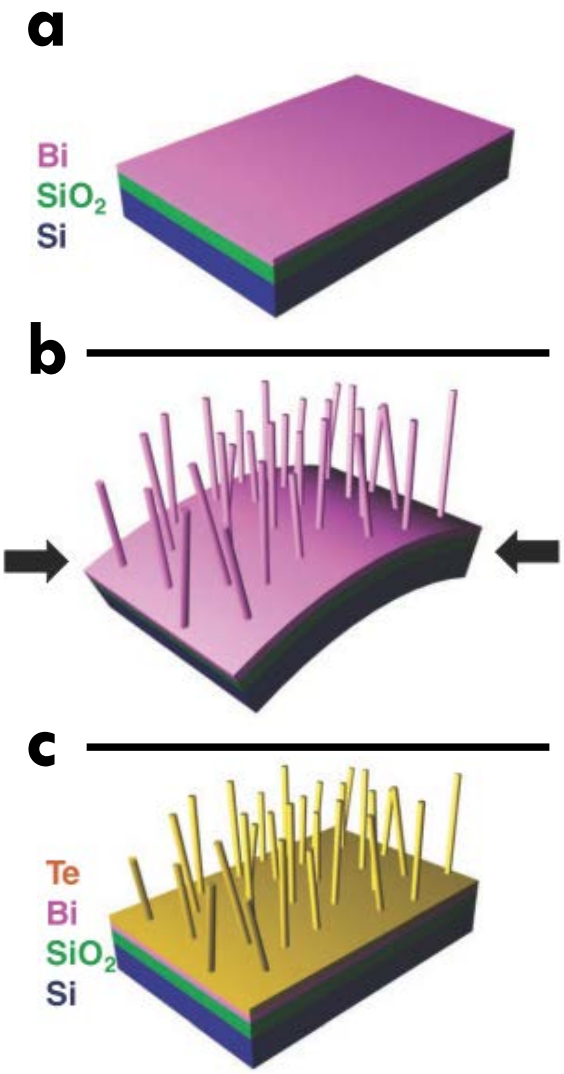

Figure 9.1: **Sample preparation of Bi-based nanowires.** **a**, Deposition of a 40 nm Bi thin film onto an oxidized Si substrate by sputtering. **b**, Heat treatment of the Bi thin films is conducted for several hours at 523 K in a vacuum. The compressive thermal stress in the Bi film is induced due to the mismatch of the thermal expansion coefficients of the Bi thin film and the SiO_2/Si substrate. **c**, Radio frequency sputtering can be used to deposit a shell material, e.g. Te, onto the Bi core. Figures were taken from Ref. [59].

Sample	Diameter d (nm)	Length l (μm)	Shell thickness t (nm)
Bi 1	170 ± 5	15.0 ± 0.6	–
Bi 2	210 ± 5	15.4 ± 0.7	–
Bi 3	550 ± 10	11.3 ± 0.7	–
Bi/Te 1	370 ± 5	21.7 ± 0.4	$10 - 30$
Bi/Te 2	490 ± 20	12.9 ± 0.8	$10 - 30$
Bi/Te 3	490 ± 10	12.9 ± 0.6	$10 - 30$
Bi/TiO_2 1	155 ± 5	17.1 ± 1.8	30
Bi/TiO_2 2	470 ± 10	15.4 ± 1.1	30
Bi/TiO_2 3	590 ± 10	15.5 ± 1.3	30

Table 9.1: **Geometry parameters.** Overview of entire diameter d, length l and shell thickness t of bismuth (Bi), bismuth/tellurium (Bi/Te) and bismuth/titanium oxide Bi/TiO_2 nanowires, respectively. Bi nanowires have a native oxide layer of 5 nm to 10 nm. Bi/Te nanowires are coated with a non-uniform Te-shell with a thickness of $10-30$ nm by radio frequency sputtering. Bi/TiO_2 nanowires are coated with a uniform TiO_2-shell with a thickness of 30 nm. The geometry parameters have been determined by scanning and transmission electron microscopy.

9.2 Experimental Details

The thermoelectric nanowire characterization platform (TNCP B), see Fig. 9.2, was used to perform a full analysis of the transport properties of individual Bi-based core/shell nanowires. TNCP B was developed and fabricated at the Laboratory for Design of Microsystems (IMTEK) of the University of Freiburg by Dr. S. Hoda Moosavi, Dr. Michael Kroener and Prof. Dr. Peter Woias.

Individual Bi-based nanowires were picked up from the growth substrate and placed on the measurement zone of the TNCP by a micromanipulation system with a thin tungsten tip. Electron beam-induced deposition (EBID) of platinum-based or tungsten-based precursor contacts was conducted in order to prepare a mechanical and electrical connection between the nanowire and the TNCP. For Bi and Bi/Te nanowires, the EBID contacts were applied directly on the shell material. The EBID process of the Bi/Te nanowires was assisted by Dr. Danny Kojda (Humboldt-Universität zu Berlin) and Dr. Martin Albrecht (Leibniz Institute for Crystal Growth (IKZ), Berlin). For Bi/TiO_2 core/shell nanowires, the shell was removed selectively by means of focused ion beam milling before the deposition of the EBID contacts, see Fig. 9.3 b. This process was done by Hongjae Moon, Dr. Jeongmin Kim and Prof. Dr. Wooyoung Lee at the Yonsei University in Korea.

A four-terminal configuration of the platinum electrodes E_c, E_h, T_c and T_h was used to measure the resistance R of Bi-based nanowires. Scanning electron microscopy was performed to determine the length and the diameter of the nanowires. These geometry parameters were used to calculate the electrical conductivity σ.

In order to determine the relative Seebeck coefficient of the nanowires, the thermovoltage U_S was measured by applying a heating current at one of the micro heaters. The resulting temperature difference δT along the nanowires was determined by the two resistance thermometers T_c and T_h at certain stabilized bath temperatures T.

The thermal conductivity λ of the Bi-based core/shell nanowires was determined by the increase of the resistance of the nanowires due to self-heating [92]. Therefore,

a gradually increasing current was applied at the outer electrodes E_c and E_h.

In the experiments, the four-terminal resistance of the nanowires was measured by a Keithley 6221 AC and DC Current Source and a Keithley 2182A Nanovoltmeter. For Seebeck measurements, the micro heater power was controlled by a Keithley SourceMeter 2401. The thermometer resistances were determined by four-terminal measurements performed by Keithley 6221 and 2182A devices. The thermovoltage was measured by a Keithley 2182A Nanovoltmeter. The measurement configurations were changed by a Keithley 7001 switch matrix system.

The transport experiments of the Bi/Te and Bi/TiO_2 core/shell nanowires were performed in a flow cryostat in helium atmosphere at ambient pressure for the electrical and Seebeck measurements and in vacuum for the thermal conductivity measurements, respectively. All transport experiments of the Bi nanowires were performed in a closed cycle cryocooler in vacuum.

Scanning (SEM) and transmission electron microscopy (TEM) as well as energy-dispersive X-ray spectroscopy (EDX) were performed to investigate the structure and chemical composition of the Bi-based core/shell nanowires. Dr. Anna Mogilatenko conducted the structural investigations of the Bi-based nanowires using TEM at the Humboldt-Universität zu Berlin.

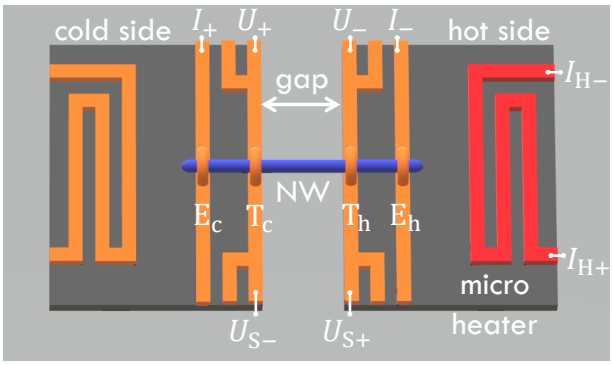

Figure 9.2: **Thermoelectric nanowire characterization platform (TNCP B).** Sketch of the measurement area of the platform. An electron transparent gap divides the measurement area into two sides. The determination of the four-terminal resistance of a nanowire (NW) (blue) can be performed by applying a current I at the outer platinum conduction lines E_c and E_h (orange) and measuring the voltage U at inner conduction lines. The thermovoltage U_S of a nanowire relative to the platinum conduction lines can be measured by applying a heating current I_H at the micro heater (red). This creates a temperature difference along the nanowire that can be calculated by four-terminal resistance thermometers T_c and T_h (orange) for the cold and hot side, respectively.

9.3 Transmission and scanning electron microscopy investigations

For structural investigations, a nanowire is placed over the electron transparent gap of the TNCP. The gap is situated in the measurement area in the middle of the platform. A sketch of this area is given in Fig. 9.2. Fig. 9.3 a shows a Bi nanowire bridging the platform gap and attached with EBID contacts to four

platinum conduction lines. The electrical and mechanical contacts were prepared by electron beam-induced deposition (EBID). Fig. 9.3 b shows a SEM image of Bi/TiO_2 core/shell nanowire before the contact preparation. The shell was removed selectively by focused ion beam milling because of the electrical insulating behavior of TiO_2. The distinct interface between the tellurium (Te) shell and the bismuth (Bi) core of Bi/Te nanowire (Bi/Te 1 (370 nm)) can been seen in the conventional transmission electron microscopy image in Fig. 9.3 c. Elemental line scan obtained across the Bi/Te nanowire by energy dispersive X-ray (EDX) spectroscopy is given in Fig. 9.3 d.

The tellurium shell distribution of the Bi/Te core/shell nanowire (Bi/Te 1 (370 nm)) is not uniform. This is indicated by the different Te shell thickness on both sides of the nanowire (also see the image obtained by scanning transmission electron microscopy below the EDX line scan). A non-uniform shell can be achieved when the nanowire is not completely perpendicular to the growth substrate during the sputtering process of the shell. In this case, the nanowire shadowing effect leads to the formation of a shell with a non-uniform thickness. The influence of the non-uniform shell on the thermoelectric transport properties is discussed later.

Fig. 9.3 e shows an image of a Bi/TiO_2 nanowire with a uniform shell prepared by atomic layer deposition. A scanning transmission electron microscopy image (Fig. 9.3 f) of a Bi/TiO_2 nanowire placed on a carbon film exhibits the growth direction. Fig. 9.3 g depicts the selected area electron diffraction pattern of the Bi/TiO_2 nanowire proving its single crystallinity. Indexing the electron diffraction spots confirms the rhombohedral crystal structure of the Bi core (see the structural model in the inset of Fig. 9.3 g).

Several Bi nanowires were placed on lacey carbon film in order to investigate the structural properties by transmission electron microscopy. Annular dark-field images of Bi nanowires are given in Fig. 9.4. Fig. 9.4 a shows a thick (diameter $d \approx 460\,\text{nm}$) Bi nanowire with a rough surface and with deep indentations (up to 170 nm deep). In contrast, Fig. 9.4 b shows a thin ($d \approx 225\,\text{nm}$) Bi nanowire with a smooth surface without indentations. Both surface properties can be observed on the same Bi nanowire in Fig. 9.4 c. The thick area shows a rough surface with indentations. The diameter of this nanowire changes from thick to thin after several hundred nanometers. Along with this change in diameter, the surface becomes smoother. The process that leads to the rough surface with indentations of the Bi nanowires may be explained by the different thermal compressive stress between the substrate and the nanowire during the growth process. The geometry parameters of the Bi-based nanowires are given in Tab. 9.1.

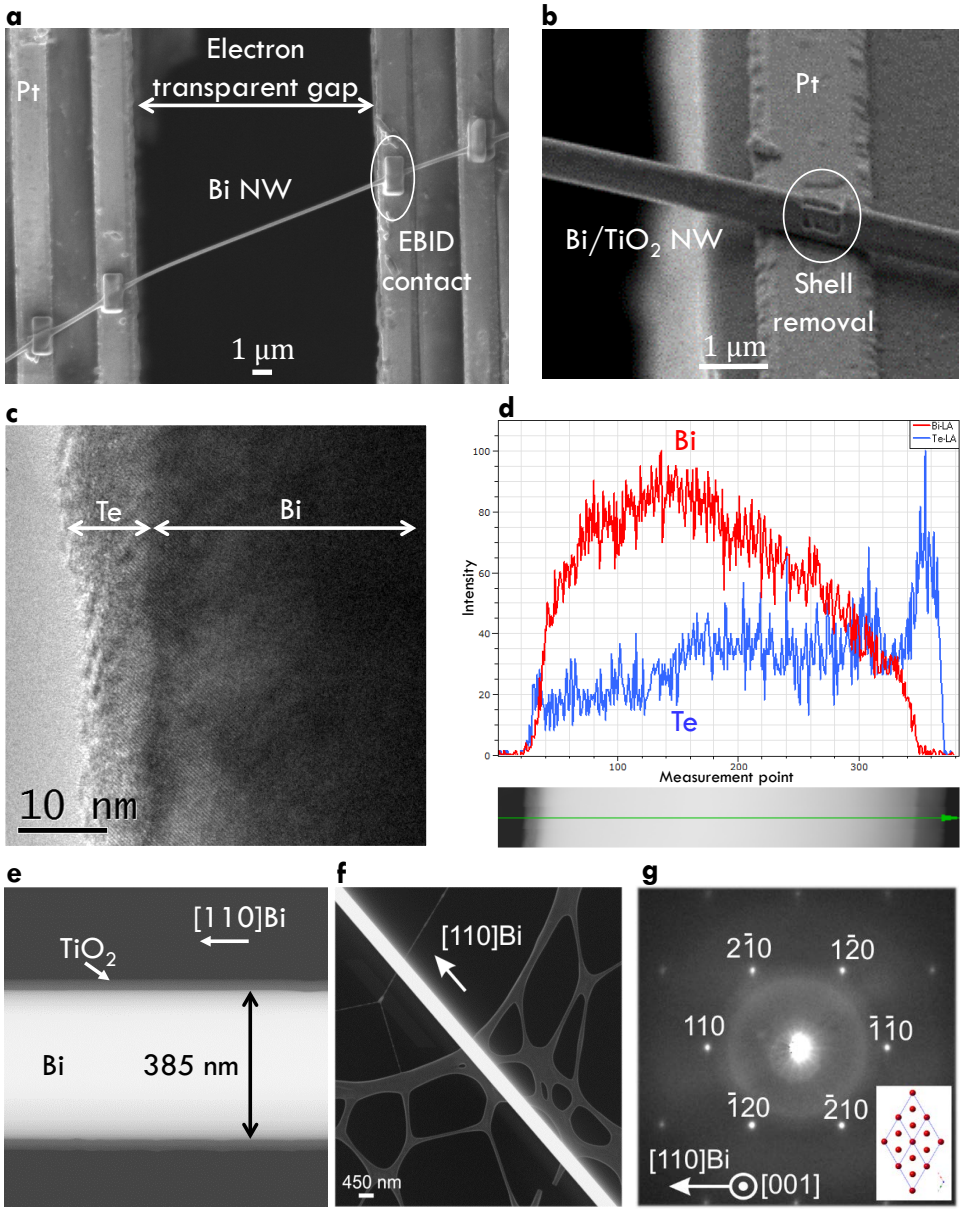

Figure 9.3: **Structural properties of the Bi-based core/shell nanowires. a**, Scanning electron microscopy image of a Bi nanowire (Bi 1) placed on the thermoelectric nanowire characterization platform. Electrical and mechanical connection between the nanowire and the measurement platform was prepared by electron beam-induced deposition (EBID). **b**, Scanning electron microscopy image of a Bi/TiO_2 nanowire after a selected area shell removal in order to prepare EBID contacts directly at the Bi core. **c**, Conventional transmission electron microscopy image that shows a section of the Bi/Te nanowire (Bi/Te 1 (370 nm)). **d**, Energy dispersive X-ray spectroscopy presenting the tellurium shell distribution of the Bi/Te core/shell nanowire (Bi/Te 1 (370 nm)). **e**, Scanning transmission electron microscopy image of a Bi/TiO_2 showing the uniform shell thickness. **f**, Scanning transmission electron microscopy image of a Bi/TiO_2 nanowire placed on a carbon film showing the nanowire growth direction. **g**, Selected area electron diffraction confirms the single crystalline crystal structure of the Bi core of a Bi/TiO_2 nanowire.

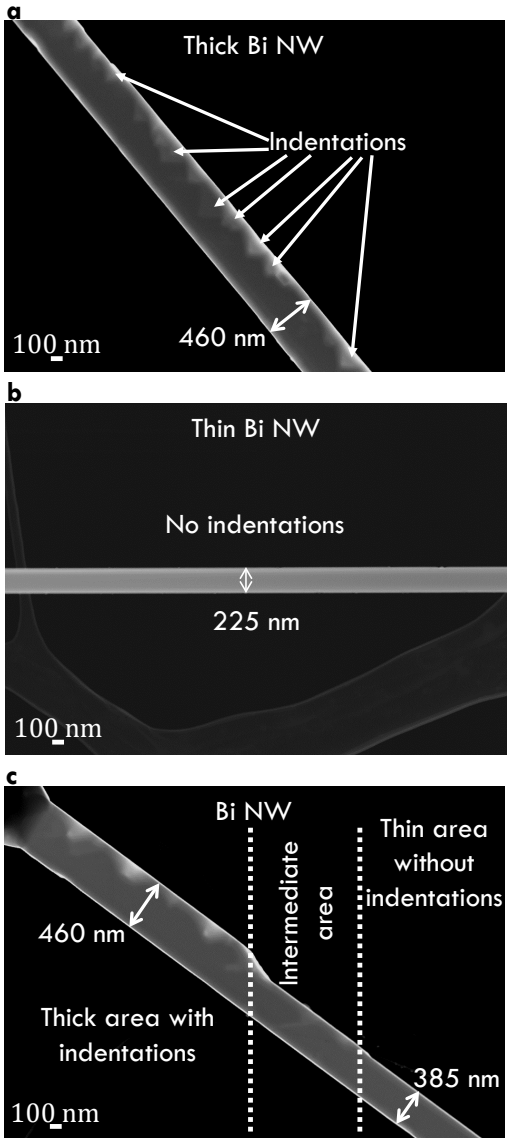

Figure 9.4: **Annular dark-field transmission electron microscopy images of Bi nanowires. a**, Thick nanowire with a rough surface and indentations. **b**, Thin nanowire with a smooth surface and no indentations. **c**, Bi nanowire with changing diameter. The thick area exhibits several indentations while the thin area is without indentation.

9.4 Electric transport properties

A four-terminal configuration of the platinum electrodes is depicted as E_c, E_h, T_c and T_h in Fig. 9.2. It was used to measure the resistance R of the Bi-based nanowires. The electrical conductivity σ of Bi-based nanowires can be determined under the assumption that the cross-sectional area of the nanowires is circular by

$$\sigma = \frac{4l}{R\pi d_e^2}, \tag{9.1}$$

where R is the four-terminal resistance of the nanowire, l is the length and d_e is the effective diameter. The effective diameter ($d_e = d - 2 \cdot t_{\text{shell}}$, t_{shell} is the shell thickness) is smaller than the entire diameter d due to the electrical insulating native oxide layer of the Bi nanowires and the electrical insulating TiO_2 shell of the Bi/TiO_2 nanowires. However, the entire diameter d for the Bi/Te nanowires has to be taken into account.

The uncertainty of the electrical conductivity σ mainly comes from the determination of the geometry parameters. The diameter was measured by scanning electron microscopy (SEM) at several points along each nanowire. The uncertainty of the diameter results from the resolution limitation of the SEM investigations and from the diameter variation of the nanowires and is between 5 nm and 20 nm. The length l was also measured by SEM. The uncertainty of l mainly comes from the size of the contact area that is defined by the electron beam-induced deposition contacts and varies between 0.4 μm and 1.8 μm. The four-terminal resistance R was determined by linear fits of corresponding linear I-U curves, see Fig. 9.5, and its relative uncertainty is less than 1 %. All geometry parameters are given in Tab. 9.1.

Fig. 9.6 a shows the four-terminal resistance of the Bi-based nanowires as a function of the bath temperature T. The Bi nanowires (Bi 1 (170 nm), Bi 2 (210 nm) and Bi 3 (550 nm)) and Bi/Te nanowires (Bi/Te 1 (370 nm), Bi/Te 2 (490 nm) and Bi/Te 3 (490 nm)) exhibit a semimetallic-like temperature dependence of the resistance. A linear representation of the pronounced temperature dependence of R of Bi 3 (550 nm) is given in Fig. 9.6 b. The Bi/TiO_2 core/shell nanowires show an increase of the resistance with decreasing bath temperatures.

Fig. 9.9 a shows the temperature-dependent electrical conductivity σ of all Bi and Bi/TiO_2 nanowires. Fig. 9.10 a shows σ of the Bi/Te nanowires as a function of the bath temperature T. Moreover, σ_{bulk} (perpendicular to the trigonal axis) from Ref. [53] is added to the diagrams. The electrical conductivity of all nanowires is reduced compared to the bulk material. Bi/TiO_2 nanowires exhibit a clearly reduced electrical conductivity compared to the Bi nanowires and a semiconducting temperature dependence of the electrical conductivity.

9.5 Determination of Seebeck coefficient

The temperature-dependent thermovoltage $U_{\text{S-Bi-based,Pt}}$, see Fig. 9.7, of individual Bi-based nanowires relative to 200 nm thick platinum conduction lines was measured between bath temperatures of 10 K and 350 K. The temperature difference δT between the hot and the cold side of the nanowires was calculated by the change of four-terminal-resistance thermometers due to the variation of the power of the micro heater on the TNCP by increasing the applied heating current I_H from zero to $-I_{H,\max}$ and from zero to $+I_{H,\max}$ stepwise in equidistant steps. The slope of

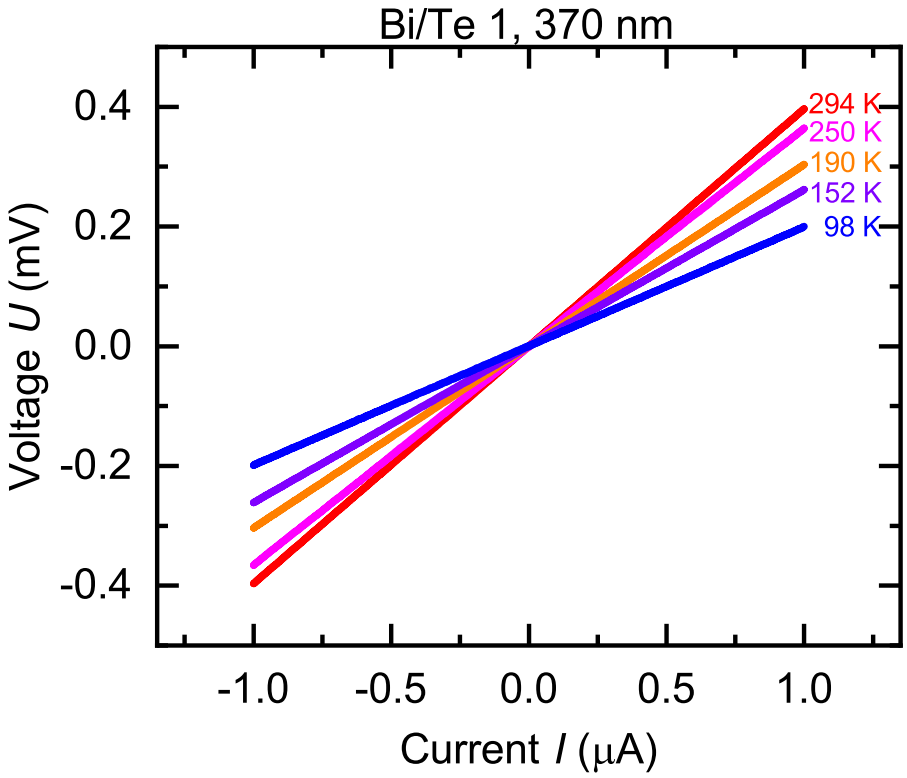

Figure 9.5: **Exemplary four-terminal I-U curves of Bi/Te 1, 370 nm at different bath temperatures.** Offset corrected voltage U as a function of the current I.

the function $U_{\text{S-Bi-based,Pt}}(\delta T)$ gives the relative Seebeck coefficient $S_{\text{Bi-based,Pt}}$ of the Bi-based nanowires with respect to the platinum conduction lines

$$S_{\text{Bi-based,Pt}} = S_{\text{Bi-based}} - S_{\text{Pt}} = -\frac{\mathrm{d}U_{\text{S-Bi-based,Pt}}}{\mathrm{d}\delta T}. \tag{9.2}$$

The absolute Seebeck coefficient of a Bi-based nanowire is given by

$$S = S_{\text{Bi-based}} = S_{\text{Bi-based,Pt}} + S_{\text{Pt}}, \tag{9.3}$$

where S_{Pt} is the absolute Seebeck coefficient of the platinum conduction line. For bath temperatures between $T = 10\,\text{K}$ and $T = 300\,\text{K}$, S_{Pt} was taken from a thin platinum film with a thickness of 197 nm with heat treatment as determined in Ch. 7. For bath temperatures above $T = 300\,\text{K}$, S_{Pt} was taken from bulk platinum [28, 41]. This is reasonable because the difference between S_{bulk} and S_{film} is within the measurement limit. The uncertainty of the thermovoltage is given by the confidence interval of the thermovoltage which was measured ten times at each step of the applied heating current and then arithmetically averaged. The uncertainty of the relative Seebeck coefficient is determined by the modulus of the largest deviation of the mean value of different fit lines due to applied heating current I_{H} that was varied from zero to $-I_{\text{H,max}}$ and from zero to $+I_{\text{H,max}}$. The uncertainty of the absolute Seebeck coefficient was determined by error propagation.

Fig. 9.9 b shows the temperature-dependent absolute Seebeck coefficient S of all Bi and Bi/TiO_2 nanowires. Fig. 9.10 b shows S of the Bi/Te nanowires as a function of the bath temperature T. S_{bulk} (perpendicular to the trigonal axis) from Ref. [53] is added to the diagrams. The absolute Seebeck coefficients of all Bi

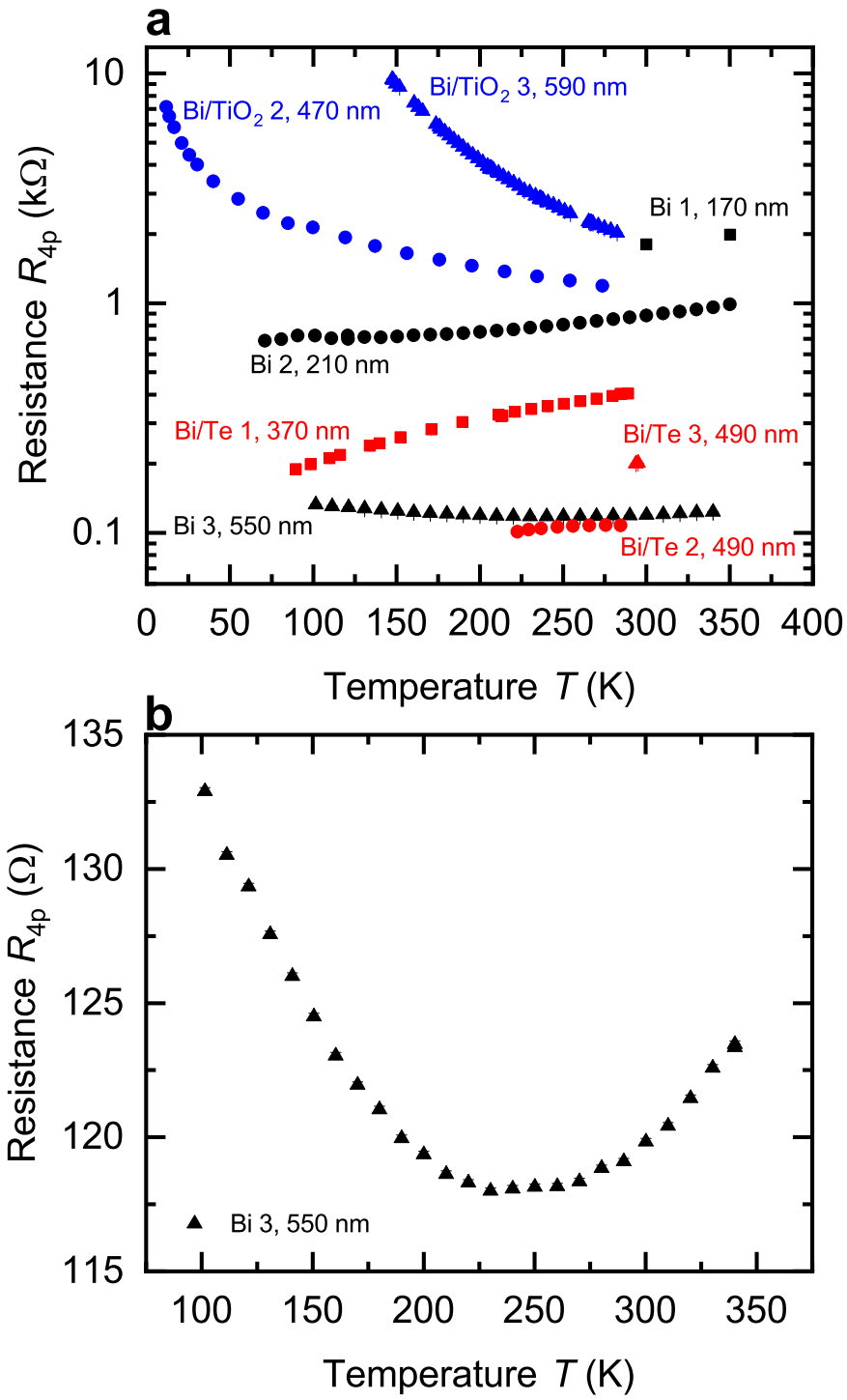

Figure 9.6: **Resistance of the Bi-based core/shell nanowires. a**, Four-terminal resistance R_{4p} of the Bi-based core/shell nanowires as a function of the bath temperature T. Bi nanowires exhibit a semimetallic temperature dependence. Bi/TiO_2 nanowires show a semiconducting behavior of the resistance. **b**, Four-terminal resistance R_{4p} of Bi 3 (550 nm) as a function of the bath temperature T in a linear representation of $R(T)$. The resistance is decreasing with decreasing bath temperatures from $T = 340\,\mathrm{K}$ down to $T = 270\,\mathrm{K}$. Below $T = 230\,\mathrm{K}$, the resistance is increasing with decreasing temperatures.

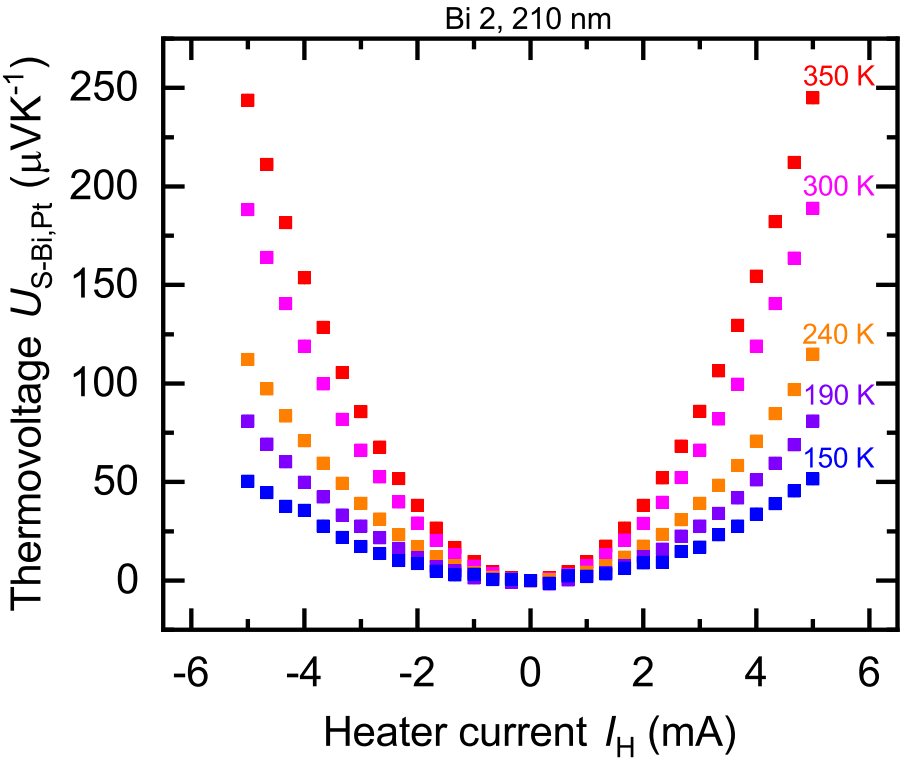

Figure 9.7: **Exemplary thermovoltage as a function of the heater current of Bi 2, 210 nm at different bath temperatures.** Offset corrected thermovoltage $U_{\text{S-Bi,Pt}}$ of Bi 2, 210 nm as a function of the heater current I_{H}.

nanowires are comparable with the bulk material in terms of both magnitude and temperature dependence. S of the Bi/Te core/shell nanowires is larger than that of Bi bulk. The absolute Seebeck coefficient of Bi/Te 1 (370 nm) is increased by 27 % compared to the bulk material at $T = 290$ K. S of Bi/TiO_2 1 (155 nm) is reduced by 27 % compared to the bulk material at $T = 300$ K.

9.6 Thermal transport properties

The temperature-dependent thermal conductivity λ of individual Bi-based nanowires was determined by the change of the resistance of the nanowires due to self-heating [92]. A current was applied at the outer electrodes E_c and E_h, see Fig. 9.2, and gradually increased. The thermal conductivity λ is given by

$$\lambda = \frac{1}{12}\frac{\alpha l R}{A}\frac{\mathrm{d}P}{\mathrm{d}r(P)}. \tag{9.4}$$

α is the temperature coefficient of the resistance of the nanowire, R is the four-terminal resistance, l is the length, A is the cross-sectional area of the nanowire, P is the resulting power in the nanowire based on the voltage drop due to the applied current and r is the resistance of the nanowire at a certain power. Contributions to the uncertainty of the thermal conductivity are coming from the determination of the nanowire length, the resistance increase and the temperature coefficient of the resistance. The uncertainty of the thermal conductivity due to the different shell materials depends on the thermal conductivity of the shell material and the cross-sectional area occupied by the shell and will be discussed later.

Fig. 9.8 shows the resistance r of Bi 2 (210 nm) as a function of the power P in the nanowire due to the applied current at 300 K. The slope of the corresponding curves yields the relation between r and P that is necessary in order to determine the thermal conductivity.

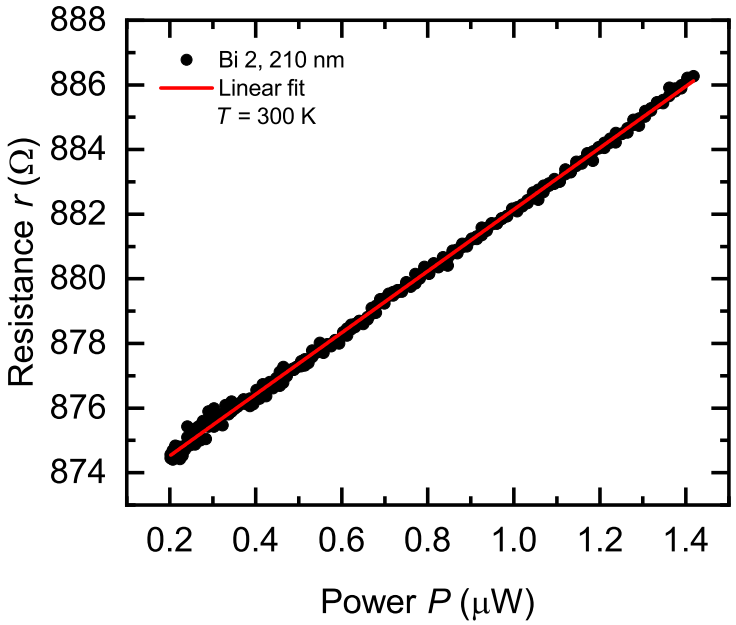

Figure 9.8: **Resistance change of a Bi nanowire due to self-heating. a**, Four-terminal resistance r of Bi 2 (210 nm) as a function of the power P in the nanowire due to the applied current at $T = 300$ K. The slope of the red line (linear fit) yields the relation between r and P that is used to determine the thermal conductivity.

Fig. 9.14 a shows the thermal conductivity of the Bi and Bi/TiO_2 nanowires. Fig. 9.10 c shows λ of the Bi/Te nanowires as a function of the bath temperature T. Moreover, λ_{bulk} (perpendicular to the trigonal axis) from Ref. [53] is added to the diagrams. The thermal conductivity of all nanowires is reduced compared to the bulk material. The Bi-based nanowires exhibit a monotonic decrease in λ with decreasing bath temperature while Bi bulk shows a monotonic increase of the thermal conductivity.

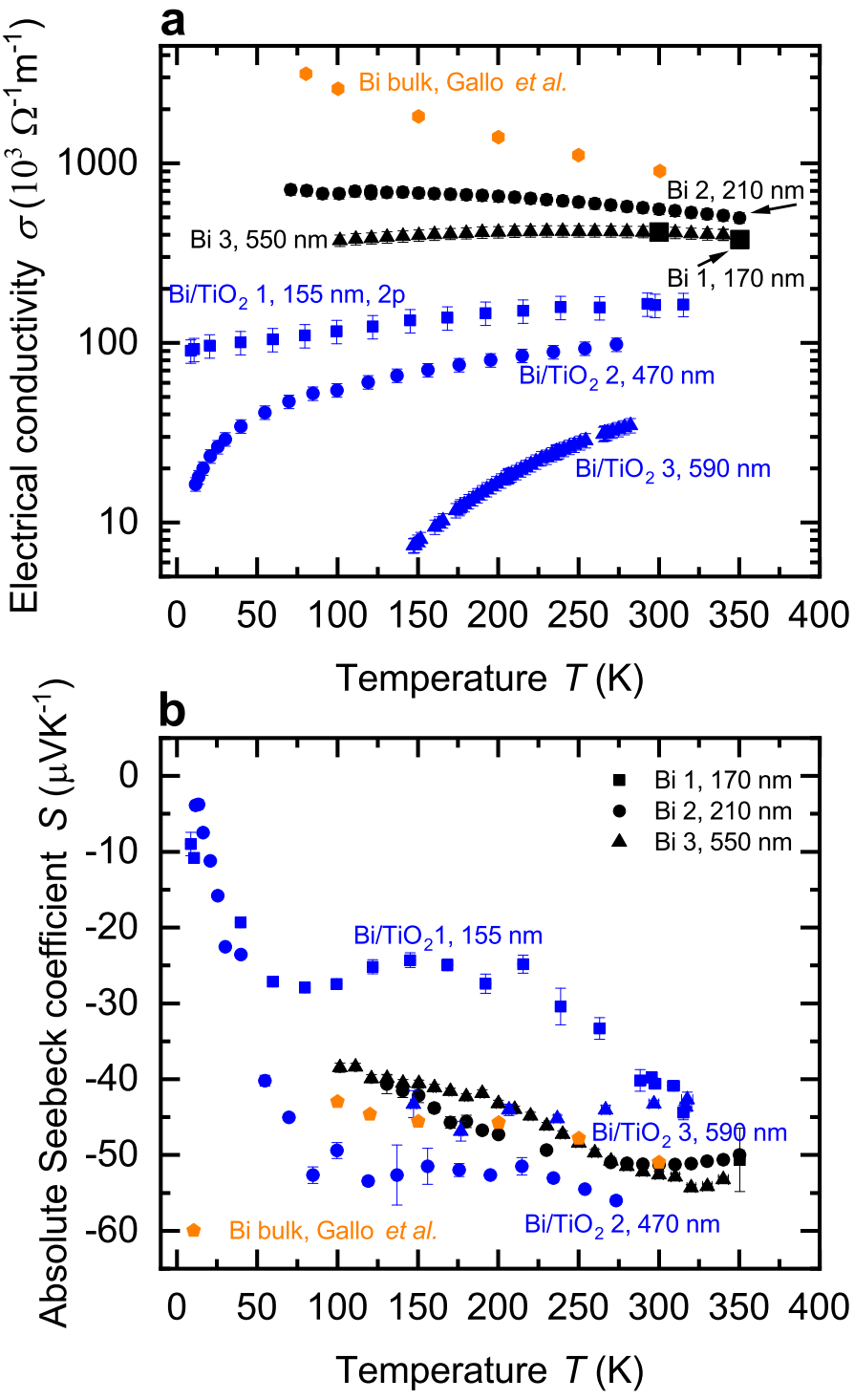

Figure 9.9: **Electrical conductivity and absolute Seebeck coefficient of the Bi-based core/shell nanowires.** **a**, Electrical conductivity σ of the Bi-based core/shell nanowires as a function of the bath temperature T. Bi nanowires exhibit a semimetallic-like electrical conductivity whereas the Bi/TiO_2 nanowires show a semimetallic or seminconducting trend. In addition, the electrical conductivity of Bi bulk (perpendicular to the trigonal axis) from Ref. [53] is added. **b**, Absolute Seebeck coefficient S of the Bi-based core/shell nanowires as a function of the bath temperature T. The absolute Seebeck coefficient of bulk Bi (perpendicular to the trigonal axis) from Ref. [53] is added.

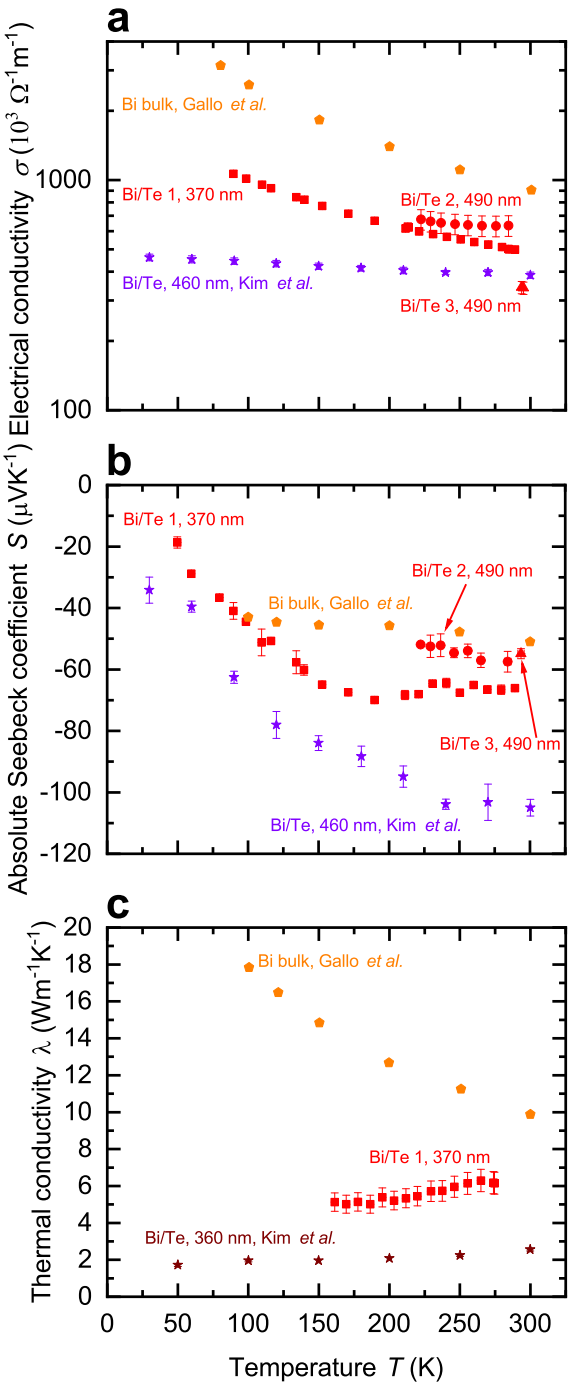

Figure 9.10: **Electrical conductivity, absolute Seebeck coefficient and thermal conductivity of the Bi/Te core/shell nanowires with non-uniform Te shell.** **a**, The electrical conductivity σ is reduced compared to the bulk material but increased compared to a Bi/Te nanowire with a uniform Te shell. This can be attributed to a reduced influence of the Te shell on the Bi core. **b**, The absolute Seebeck coefficient S is increased compared to the bulk material but decreased compared to a Bi/Te nanowire with a uniform Te shell. This can be attributed to the reduced compressive strain effect due to the non-uniform shell. **c**, The thermal conductivity λ is reduced compared to the bulk material and exhibits an opposite temperature dependence. The transport properties of Bi bulk (perpendicular to the trigonal axis) from Ref. [53] and of Bi/Te nanowires with a uniform shell from Ref. [61] are added to the corresponding diagram. The Seebeck coefficient of the of Bi/Te nanowire from Ref. [61] was corrected by the absolute Seebeck coefficient of the reference material.

9.7 Discussion: Influence of different shell materials on the thermoelectric transport properties

Electrical characterization

The temperature dependence of the electrical conductivity of the bulk Bi semimetal can be explained by the competing influence of carrier concentration and mobility [53, 55, 56, 103, 153, 154]. Bi bulk has a small carrier concentration varying between $2.7 \cdot 10^{17}\,\mathrm{cm}^{-3} - 3.0 \cdot 10^{18}\,\mathrm{cm}^{-3}$ at temperatures between $2\,\mathrm{K} - 300\,\mathrm{K}$ [53, 55, 56, 103]. The change of mobility μ of Bi bulk exceeds the change of the carrier concentration by more than one order of magnitude in the temperature range from $77\,\mathrm{K} - 300\,\mathrm{K}$ [53, 55, 56].

All Bi nanowires show semimetallic behavior and have a reduced electrical conductivity compared to that of bulk. This can be attributed to enhanced surface scattering due to a higher surface-area-to-volume ratio in nanowires. Hence, σ of Bi 1 (170 nm) is reduced compared to that of Bi 2 (210 nm). A smaller diameter leads to increased surface scattering, which will reduce the electrical conductivity, because the mean free path of the charge carriers becomes restricted by the nanowire diameter. This is consistent with Ref. [102, 103, 154].

However, σ of Bi 3 (550 nm) is reduced compared to that of Bi 2 (210 nm) despite the larger diameter. The temperature dependence of the electrical conductivity of Bi 3 (550 nm) can be attributed to a change of the dominant scattering mechanism from surface scattering (Bi 1 (170 nm) and Bi 2 (210 nm)) to scattering at indentations (Bi 3 (550 nm)). Additional scattering at indentations arises preferably in nanowires with larger diameters as shown in Fig. 9.4.

According to Matthiessen's rule, the total scattering rate, which is given by $\tau_{\mathrm{tot}}^{-1} = \tau_{\mathrm{bulk}}^{-1} + \tau_{\mathrm{sc}}^{-1} + \tau_{\mathrm{ind}}^{-1}$, leads to a reduction of the charge carrier mean free path. $\tau_{\mathrm{bulk}}^{-1}$ characterizes the inverse lifetime in the bulk material and its temperature dependence can be described by the Bloch-Grüneisen relation. τ_{sc}^{-1} is the surface scattering rate which depends on the nanowire diameter. τ_{ind}^{-1} is the indentation scattering rate which depends on the density and depth of the indentations.

Like for the Bi nanowires, the Bi/Te core/shell nanowires show also a reduced electrical conductivity compared to the bulk. Moreover, the shell material can have an additional influence on the electrical conductivity. Kim *et al.* showed that the electrical conductivity of Bi/Te nanowires can be further reduced compared to Bi nanowires and to the bulk material due the compressive strain effect of Te shell on the Bi core [60, 61]. This was observed for Bi/Te nanowires with a uniform Te shell thickness. However, the Bi/Te nanowires with a non-uniform shell thickness, which were investigated in this work, showed a reduction of the electrical conductivity compared to the bulk material that is in general not as large as for the Bi/Te nanowires with a uniform Te shell. This can be attributed to the strain effect of the shell on the core that will be larger for a uniform shell thickness than for a non-uniform shell. Furthermore, bismuth and tellurium are both conductive materials. As a result, the electrical conductivity has to be considered as parallel conduction in both materials. The total electrical conductivity of such a combination can be written as

$$\sigma_{\mathrm{tot}} = \frac{A_{\mathrm{Bi}}\sigma_{\mathrm{Bi}} + A_{\mathrm{Te}}\sigma_{\mathrm{Te}}}{A_{\mathrm{Bi}} + A_{\mathrm{Te}}}. \tag{9.5}$$

A_{Bi} and A_{Te} are the cross-sectional areas of Bi and Te, respectively. σ_{Bi} and σ_{Te} are the partial conductivities of Bi and Te, respectively. The influence of the Te shell thickness on the reduction of the total electrical conductivity σ_{tot} is illustrated in the following example. Taking Eq. 9.5 and the electrical conductivity of Bi bulk $\sigma_{\mathrm{Bi,bulk}} = 901600\,\Omega^{-1}\mathrm{m}^{-1}$ [53] and Te bulk $\sigma_{\mathrm{Te,bulk}} = 185\,\Omega^{-1}\mathrm{m}^{-1}$ [112] and assuming the cross-sectional area of a nanowire with a total diameter of 300 nm results in a reduction of σ_{tot} by 13% compared to $\sigma_{\mathrm{Bi,bulk}}$ if the Te shell thickness is 10 nm or in a reduction of σ_{tot} by 36% if the Te shell thickness is 30 nm. As a result, a uniform Te shell will lead to a larger reduction of σ compared to the bulk than a non-uniform shell.

For Bi/TiO_2 core/shell nanowires, an electrical conduction in the shell material can be neglected due to the electrical insulating TiO_2. All Bi/TiO_2 nanowires show a decreasing electrical conductivity with decreasing bath temperature. Bi/TiO_2 core/shell nanowires show an increasing electrical conductivity with decreasing diameter and exhibit a diameter-dependent transition from the semiconducting to the semimetallic state.

The effect of strain on the electrical conductivity can be observed for the Bi/TiO_2 nanowires. However, there are some different manifestations of the strain influence and the resulting change of the electrical conductivity. The effect of the so-called elastic strain of the TiO_2 shell on the Bi core can be observed for Bi/TiO_2 3 (590 nm) in Fig. 9.9 a. The electrical conductivity of Bi/TiO_2 3 (590 nm) is 25 times smaller than that of the bulk material and nearly 15 times smaller compared to the Bi nanowires at room temperature. The strain effect leads to an opening of a band gap. This is illustrated in Fig. 9.11 that shows the natural logarithm of the electrical conductivity of the Bi/TiO_2 nanowires as a function of the inverse bath temperature. The Arrhenius equation

$$\sigma = A \exp\left(-\frac{E_{\mathrm{A}}}{k_{\mathrm{B}}T}\right) \tag{9.6}$$

can be used to determine the activation energy E_{A}. σ is the electrical conductivity, A is a constant, k_{B} is the Boltzmann constant and T is the bath temperature. An activation energy of $|41.3 \pm 0.2|$ meV in the temperature range from 140 K to 310 K was determined for Bi/TiO_2 3 (590 nm). For Bi/TiO_2 2 (470 nm), a reduced activation energy of $|9.3 \pm 0.5|$ meV compared to Bi/TiO_2 3 (590 nm) was determined.

This reduction is accompanied by an increase of the electrical conductivity. This may be attributed to a partly lattice relaxation which leads to the beginning of the recovery of the semimetallic state induced by the semiconducting to semimetallic transition. For this reason, the electrical conductivity of Bi/TiO_2 2 (470 nm) is larger than that of Bi/TiO_2 3 (590 nm) despite the smaller core diameter.

The lattice relaxation process can be understood in a way that the influence of the shell on the core exceeds the elastic limit and as a result, the Bi core relaxes spontaneously. The probability that this relaxation process occurs is higher for nanowires with smaller diameter because the compressive strain has the largest influence at the interface between the core and the shell and decreases with some distance from the interface as shown in Ref. [60, 61] for Bi/Te core/shell nanowires.

For this reason, the largest electrical conductivity can be observed for Bi/TiO_2 1 (155 nm) due to the fully relaxed, non-elastic influence of the strain effect. The electrical conductivity of this nanowire could only be determined from two-terminal (2p) resistance measurements. Hence, the values in Fig. 9.9 a denote only a lower limit of the electrical conductivity. This is determined by the contact resistance. However, the tendency of the recovery of the semimetallic state is clearly visible.

In addition, the lattice relaxation process was observed for Bi/TiO_2 3 (590 nm). An irreversible increase of the electrical conductivity occurred during the measurement, see Fig. 9.13 a. This change of the electrical conductivity occurred at a bath temperature of 147 K. Two *I-U* curves of this nanowire were taken at this bath temperature which are given in Fig. 9.12. The resulting four-terminal resistance R of the second measurement is 19 times smaller than the resistance of the first measurement. Three minutes elapsed between both measurements. However, the measurement setup was not changed before, during or after the resistance change. As a result of the lattice relaxation, the semiconducting behavior of the electrical conductivity, which was induced by the strain effect of the shell, changed back to the semimetallic state, the original state of the Bi nanowires without a shell. This semiconducting to semimetallic transition also leads to a reduction of the absolute Seebeck coefficient, see Fig. 9.13 b. This was also observed for the Bi/Te nanowires.

The strain release can be attributed to the different thermal expansion coefficients of Bi ($\alpha_{\text{Bi,c-axis}} \approx 17.4 \cdot 10^{-6}\,\text{K}^{-1}$) at room temperature [155] and of TiO_2 ($\alpha_{\text{TiO}_2\text{,c-axis}} = 8.4 \cdot 10^{-6}\,\text{K}^{-1}$ up to $\alpha_{\text{TiO}_2\text{,c-axis}} = 9.4 \cdot 10^{-6}\,\text{K}^{-1}$) at room temperature [156]. As a result, the contraction of the Bi core is estimated to $\Delta d \approx 2.5$ nm at 147 K compared to the original diameter during the manufacturing process. This could lead to the irreversible lattice relaxation.

Thermoelectric characterization

The temperature-dependent absolute Seebeck coefficient S of all Bi and Bi/TiO_2 nanowires is shown in Fig. 9.9 b. S_{bulk} (perpendicular to the trigonal axis) from Ref. [53] is added to the diagrams. The absolute Seebeck coefficients of all Bi nanowires are comparable with the bulk material in terms of both magnitude and temperature dependence. However, S of Bi/TiO_2 1 (155 nm) is reduced by 27 % compared to the bulk material at $T = 300$ K.

As the absolute Seebeck coefficient S of Bi bulk and of all Bi-based nanowires is negative, electrons are identified as the dominant charge carriers. In general, the total Seebeck coefficient S_{tot} is determined by the partial contribution of holes and electrons and it is given by

$$S_{\text{tot}} = \frac{\sigma_{\text{e}} S_{\text{e}} + \sigma_{\text{h}} S_{\text{h}}}{\sigma_{\text{e}} + \sigma_{\text{h}}}. \tag{9.7}$$

Here, σ_{e} and σ_{h} are the partial electrical conductivities of the electrons and holes, respectively and S_{e} and S_{h} are the partial Seebeck coefficients of the electrons and holes, respectively. Theoretical studies revealed that each partial Seebeck coefficient can be larger than S_{tot} [58, 103] but due to the opposite sign of both contributions, they cancel each other out. This results in a saturation regime with a weak temperature dependence between bath temperatures of $T = 100$ K and $T = 300$ K of S_{bulk} and in general also for the Bi-based nanowires. With decreasing bath temperatures, the absolute Seebeck coefficient is expected to tend linear to zero below

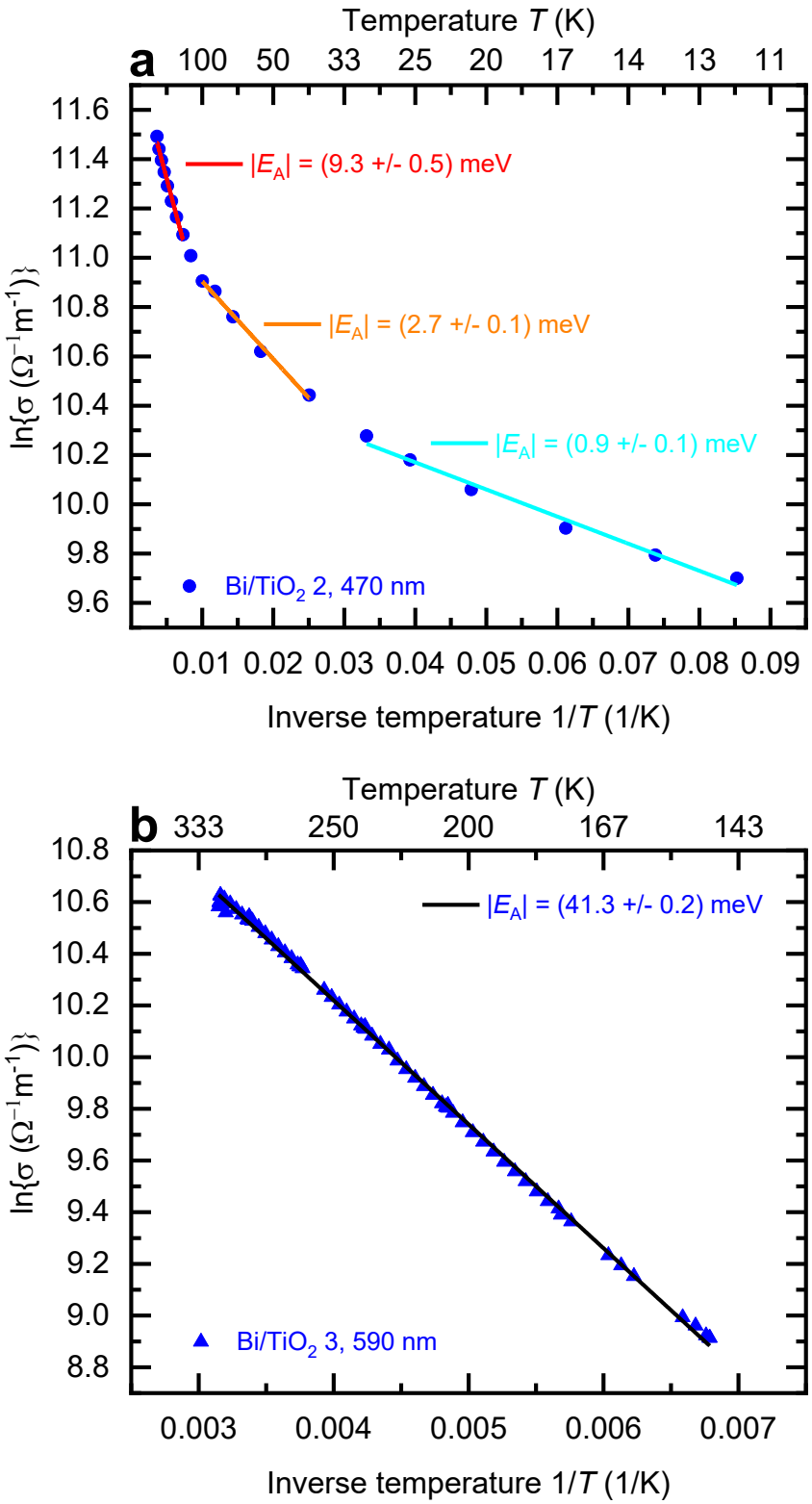

Figure 9.11: **Activation energy of Bi/TiO_2 core/shell nanowires.** **a**, Natural logarithm of the electrical conductivity of Bi/TiO_2 2 (470 nm) as a function of the inverse bath temperature T^{-1}. The modulus of the activation energy $|E_A|$ can be determined in three distinct temperature ranges from 10 K to 30 K, from 40 K to 120 K and from 140 K to 270 K. Increasing the bath temperature also increases the activation energy. Bi/TiO_2 2 (470 nm) shows a semimetallic-like behavior. **b**, Natural logarithm of the electrical conductivity of Bi/TiO_2 3 (590 nm) as a function of the inverse bath temperature T^{-1}. The activation energy $|E_A|$ can only be determined in the temperature range from 140 K to 310 K. Bi/TiO_2 3 (590 nm) shows a semiconducting behavior.

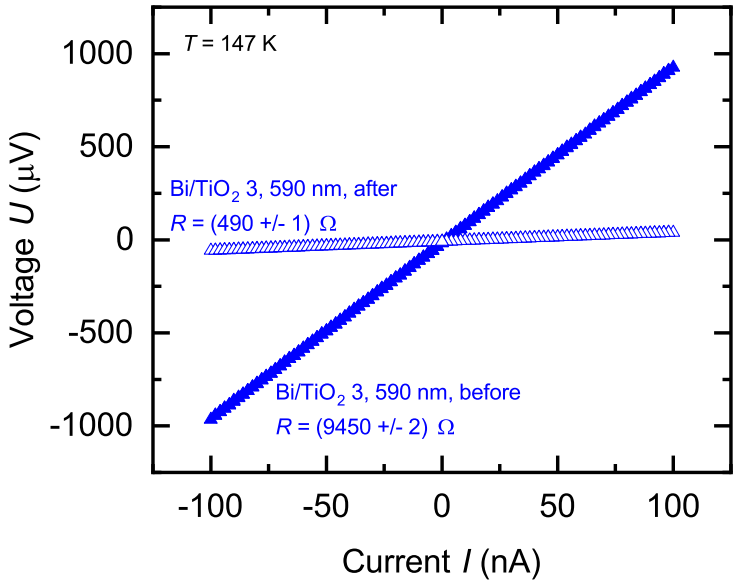

Figure 9.12: **Resistance change of Bi/TiO_2 3 (590,nm) due to lattice relaxation.** Measured voltage U of the nanowire before and after the lattice relaxation as a function of the applied current I. The four-terminal resistance R of the nanowire is after the lattice relaxation 19 times smaller than before.

$T = 100\,\mathrm{K}$ due to the decrease of the thermodiffusion contribution. This temperature dependence of S is expected for all investigated Bi-based nanowires as observed for Bi/TiO_2 2 (470 nm).

The temperature dependence and absolute value of S of the Bi nanowires are comparable with that of bulk [53]. Theoretical studies showed that Bi nanowires exhibit only a small change of S along the binary axis for diameters between $d = 100\,\mathrm{nm}$ and $d = 500\,\mathrm{nm}$ [122]. A significant change of S of the Bi nanowires is expected only for diameters below 60 nm due to a change of the density of states [103].

For Bi/Te core/shell nanowires the direct influence of the Te shell on the total Seebeck coefficient as part of a parallel conduction model can be neglected due to the larger cross-sectional area of the Bi core compared to the Te shell. For this reason, the thermoelectric transport is dominated by the Bi core. S of the Bi/Te core/shell nanowires is larger than that of Bi bulk. The absolute Seebeck coefficient of Bi/Te 1 (370 nm) is increased by 27 % compared to the bulk material at $T = 290\,\mathrm{K}$ and it has the largest S of all investigated Bi-based nanowires in this work. This can be attributed to the compressive strain effect of the Te shell on the Bi core as previously reported in Ref. [60, 61]. However, S is smaller compared to the data given in Ref. [60, 61]. This can be explained by the non-uniform shell of the Bi/Te nanowires, as shown in Fig. 9.3 c, d, and the resulting lower compressive strain effect of the Te shell on the Bi core compared to Bi/Te nanowires with a uniform shell.

For Bi/TiO_2 core/shell nanowires, a contribution of the shell to the total absolute Seebeck can be neglected due to the electrical insulating TiO_2. Bi/TiO_2 1 (155 nm) has the smallest Seebeck coefficient over a wide temperature regime of all investigated Bi-based nanowires. Furthermore, a larger change of S with decreasing bath temperatures compared to Bi bulk and the other Bi-based nanowires can be observed between $T = 100\,\mathrm{K}$ and $T = 300\,\mathrm{K}$. This can be attributed to the small

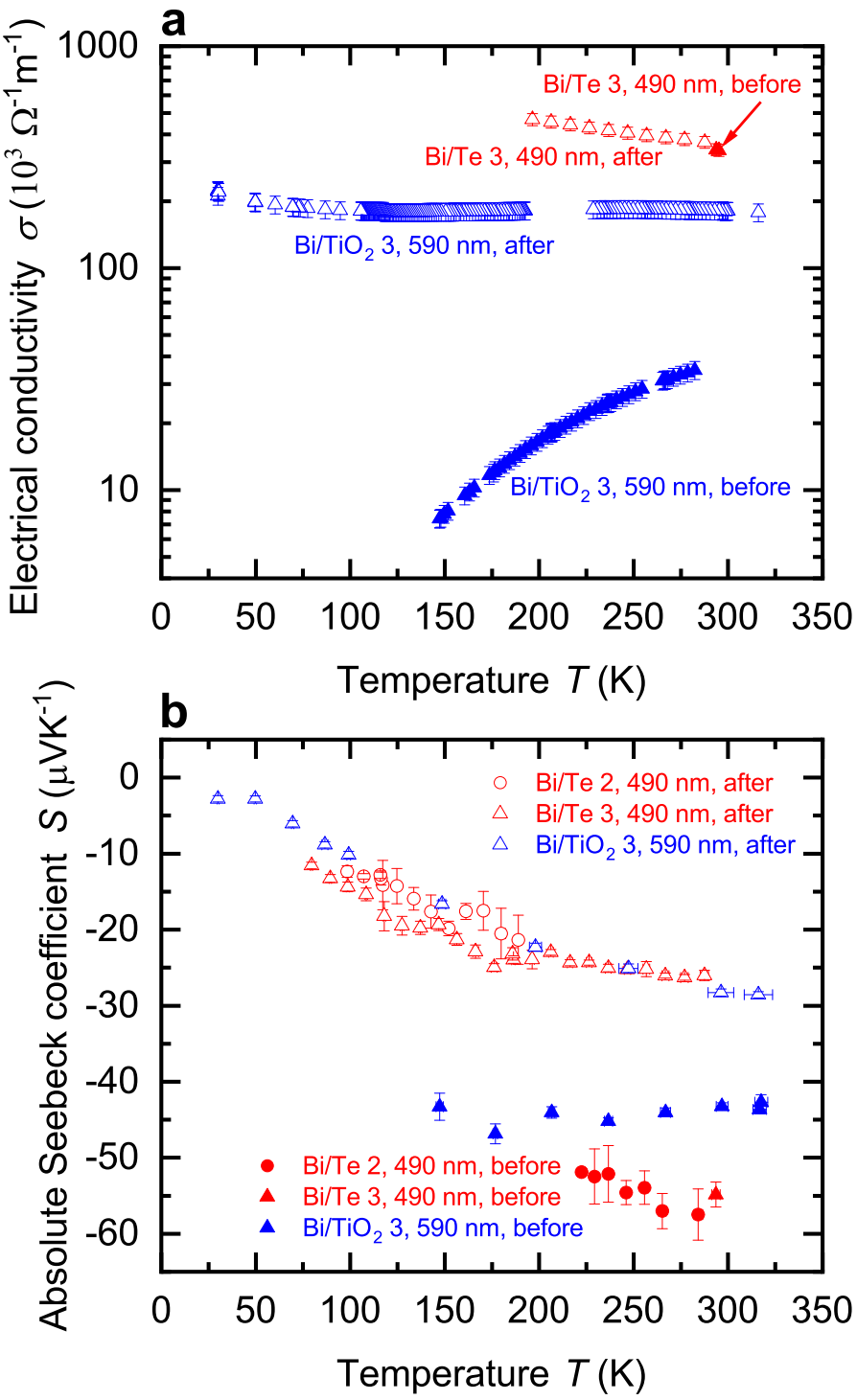

Figure 9.13: **Influence of lattice relaxation on the electrical conductivity and the absolute Seebeck coefficient of the Bi-based core/shell nanowires.** *Before*, indicates the corresponding transport properties before relaxation. *After*, indicates the corresponding transport properties relaxation. **a**, Electrical conductivity σ of the Bi-based core/shell nanowires as a function of the bath temperature T. The relaxation process of the core/shell structure of Bi/TiO_2 2 (470 nm) leads to a change of the temperature dependence of the electrical conductivity from semiconducting to semimetallic. A small change of σ can also be observed for Bi/Te 3 (490 nm). **b**, Absolute Seebeck coefficient S of the Bi-based core/shell nanowires as a function of the bath temperature T. The relaxation process induces a significant change of the absolute Seebeck coefficient of the Bi-based core/shell nanowires. The changes in the transport properties after the relaxation process indicate that the shell had a significant compressive strain effect on the Bi core.

diameter of the Bi core that is only 95 nm without the shell. The spatial limitation leads to more surface scattering, a reduced charge carrier mean free path and as a result to a reduction of the thermodiffusion contribution (from both electrons and holes) to the absolute Seebeck coefficient [1, 2]. Furthermore, the slightly increase of S at around $T = 100\,\mathrm{K}$ may be attributed to the influence of phonon drag.

For Bi/TiO_2 nanowires with a larger diameter, like Bi/TiO_2 2 (470 nm) and Bi/TiO_2 3 (590 nm), the absolute Seebeck coefficient is comparable with that of the Bi nanowires. The slight increase of the Seebeck coefficient of Bi/TiO_2 2 (470 nm) compared to that of the Bi nanowires and Bi bulk may be attributed to the influence of the compressive strain effect of the TiO_2 shell on the Bi core which results in the transition of the semimetallic to semiconducting behavior of the electrical conductivity. The accompanied band opening may reduce the partial hole contribution of the bipolar transport to the total Seebeck coefficient, see Eq. 9.7. The further band opening of Bi/TiO_2 3 (590 nm) do not lead to an increase of the Seebeck coefficient. However, the electrical conductivity of this nanowire is significantly reduced compared to the electrical conductivity of the other Bi/TiO_2 nanowires. For this reason, the further pronounced reduction of the weighting factor σ_e and σ_h, see Eq. 9.7, limit the actual amount of the Seebeck coefficient.

The relaxation process of the Bi core, which changes the electrical conductivity of Bi/TiO_2 3 (590 nm), also leads to a significant and irreversible reduction of the Seebeck coefficient, see Fig. 9.13 b. As the degree of band energy overlap increases a transition from semiconducting to semimetallic behavior is induced. This is also observed for the Bi/Te nanowires.

Thermal characterization

In contrast to the electrical conductivity, all shell materials contribute to the thermal conductivity λ. Thus, the entire diameter d, as given in Tab. 9.1, of the nanowires is required to determine λ. Fig. 9.14 a shows the thermal conductivity of the Bi and Bi/TiO_2 nanowires and λ_{bulk} (perpendicular to the trigonal axis) from Ref. [53]. The thermal conductivity of all nanowires is reduced compared to the bulk and exhibits a monotonic decrease in λ with decreasing bath temperature while Bi bulk shows a monotonic increase. In general, λ depends on partial contributions from different heat carrier sources and the electronic contribution can be estimated by the Wiedemann-Franz relation [157, 158]. For Bi bulk it has been shown, that phonons are the dominant heat carrier source at low temperatures [53, 104]. As the bath temperatures rises, the charge carrier contribution becomes the dominant part [53, 104]. At $T = 300\,\mathrm{K}$, nearly 70 % of the total thermal conductivity can be attributed to the charge carrier contribution. For Bi-based nanowires, the increased surface-area-to-volume ratio acts both on the charge carrier and lattice scattering which leads to a reduction of the thermal conductivity.

For core/shell nanowires, the shell material has to be taken into account in order to determine the total thermal conductivity λ_{tot} as given by

$$\lambda_{tot} = \frac{\lambda_{Bi} A_{Bi} + \lambda_{shell} A_{shell}}{\lambda_{Bi} + \lambda_{shell}}. \tag{9.8}$$

λ_{Bi} and λ_{shell} are the partial thermal conductivities of the Bi core and of the shell material, respectively. A_{Bi} and A_{shell} are the partial cross-sectional areas of the Bi core and of the shell material, respectively. An upper limit of the thermal

conductivity for bismuth oxide is $2.2\,\mathrm{Wm^{-1}K^{-1}}$ [159]. λ of titanium dioxide films is $1.3\,\mathrm{Wm^{-1}K^{-1}}$ [160]. The thermal conductivity of the shell yields to a relative uncertainty of the thermal conductivity of the complete nanowires ranging from $< 1\,\%$ for Bi 3 (550 nm) due to large cross-sectional area of the Bi core compared to the small cross-sectional area of the bismuth oxide shell to 14 % for Bi/TiO_2 1 (155 nm) due to the larger cross-sectional area of the TiO_2 shell. The dominant contribution to the thermal conductivity comes from the Bi core. This applies for all core/shell nanowires investigated in this work.

The thermal conductivity of Bi 2 (210 nm) is comparable with other Bi nanowires reported in Ref. [102, 103]. The reduction of λ and the change of the temperature dependence can be attributed to the spatial confinement of the nanowires and the resulting increased phonon surface and charge carrier surface scattering [102, 103]. The dominant contribution to the thermal conductivity comes from charge carriers, even when the bath temperatures decreases.

Bi 3 (550 nm) has the smallest λ of all Bi-based nanowires investigated in this work. Scattering at the rough surface and at indentations, see Fig. 9.4 a, lead to a strong reduction of the thermal conductivity. This reduction can mainly be attributed to a reduction of the lattice thermal conductivity. For this reason, λ of Bi 3 (550 nm) is smaller than that of Bi/TiO_2 2 (470 nm) despite the larger electrical conductivity of Bi 3 (550 nm).

For the Bi/Te nanowires it was shown, that the rough interface between the Bi core and Te shell can lead to a reduction of the thermal conductivity as reported in Ref. [59–61]. However, the thermal conductivity of Bi/Te 1 (370 nm) is larger compared to other Bi/Te core/shell nanowires reported in Ref. [59–61]. This can be attributed to the non-uniform Te shell as shown in Fig. 9.3 c, d. As a result, the compressive strain effect is lower compared to Bi/Te nanowires with a uniform shell. This will lead to a larger charge carrier contribution to the thermal conductivity increasing the overall thermal conductivity.

The thermal conductivity of Bi/TiO_2 2 (470 nm) is reduced compared to the bulk material and to that of Bi 2 (210 nm). The reduction of λ of Bi/TiO_2 2 (470 nm) can be attributed to an increase of charge carrier and phonon interface scattering comparable to the effect of the Te shell on the thermal conductivity of Bi/Te core/shell nanowires [59–61]. The compressive strain effect of the shell, which leads to a reduction of the electrical conductivity, will also lead to a reduction of the charge carrier contribution to the total thermal conductivity.

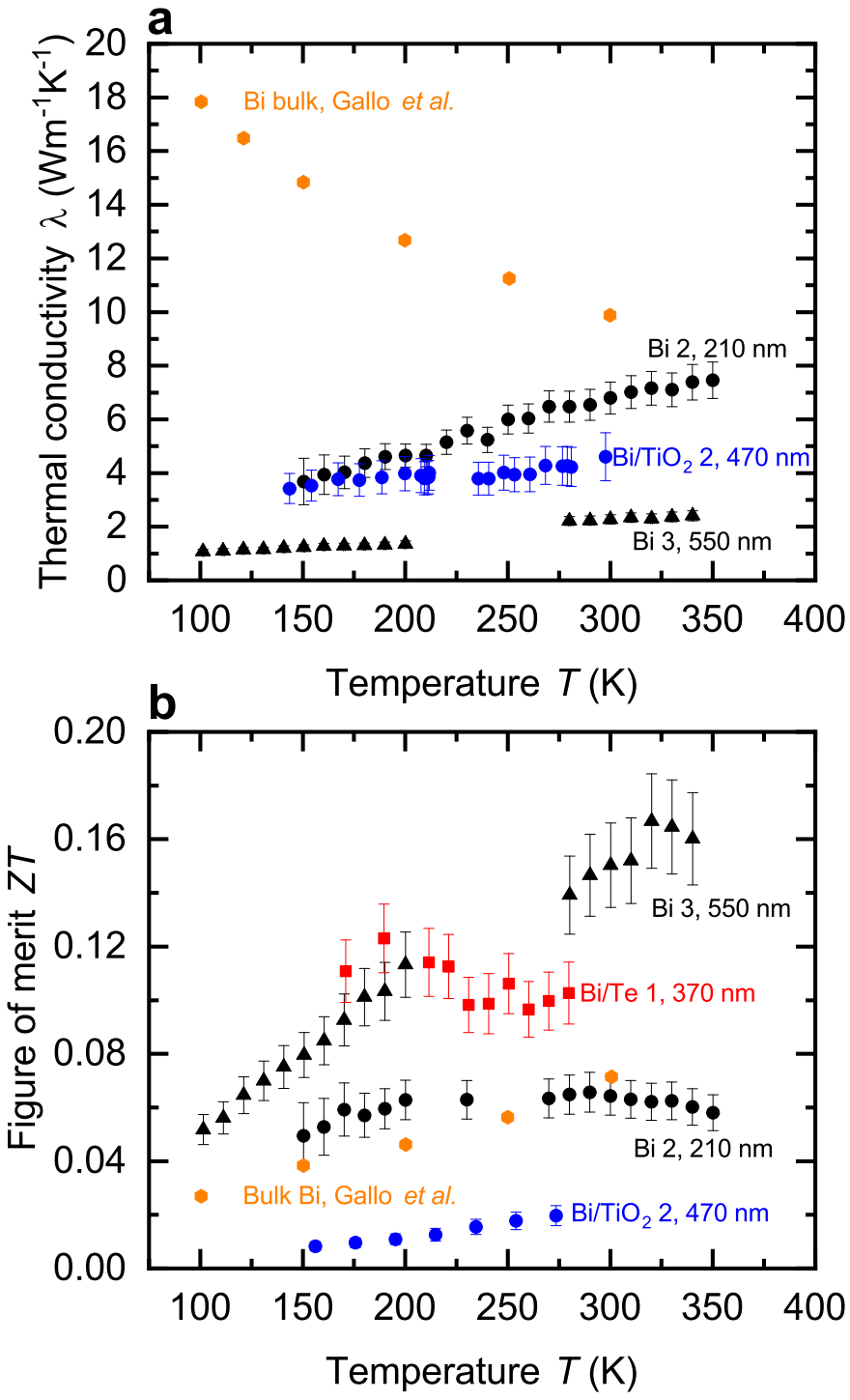

Figure 9.14: **Thermal conductivity and figure of merit of the Bi-based core/shell nanowires.** **a**, Thermal conductivity λ of the Bi-based core/shell nanowires as a function of the bath temperature T. The thermal conductivity of Bi bulk (perpendicular to the trigonal axis) from Ref. [53] is added. λ of the Bi-based core/shell nanowires is reduced compared to the bulk material. **b**, Figure of merit ZT of the Bi-based core/shell nanowires as a function of the bath temperature T. The figure of merit of Bi bulk (perpendicular to the trigonal axis) from Ref. [53] is added.

Figure of merit

The thermoelectric figure of merit ZT at a given bath temperature T is determined by

$$ZT = \frac{\sigma S^2}{\lambda} T \tag{9.9}$$

and depicted for the Bi-based nanowires in Fig. 9.14b. For comparison, the figure of merit of bulk Bi is $ZT = 0.07$ at room temperature [53]. This is comparable with ZT of Bi 2 (210 nm).

Bi 3 (550 nm) has the highest figure of merit $ZT = 0.15$ at room temperature. This can be attributed to the strong reduction of the thermal conductivity that is a result of scattering effects at the rough surface and in addition at indentations. The thermoelectric properties are tunable over a wide range by the choice of the shell material and the nanowire diameter. For a high figure of merit, it is necessary that the Seebeck coefficient is large enough. The Seebeck coefficient can be increased by shifting the Fermi energy and opening a band gap. Bi/TiO_2 nanowires show a rather low figure of merit. This can be attributed to the significantly reduced electrical conductivity compared to the Bi/Te nanowire due to the influence of the TiO_2 shell on the Bi core.

Short summary

The transport properties of the Bi-based core/shell nanowires are tunable over a wide range depending on the applied shell material. The electrical conductivity of all Bi-based nanowires is reduced compared to the bulk due to size effects. This is consistent with the results of the thin platinum film and silver nanowire measurements. The electrical conductivity of the Bi-based nanowires can be further reduced by a sufficient compressive strain induced by the shell (e.g. TiO_2 shell). The strain effect can increase the absolute Seebeck coefficient by band opening (e.g. Te shell). The absolute Seebeck coefficient of the Bi-based nanowires is less sensitive to size effects compared to the Seebeck coefficient of the silver nanowires and thin platinum films. This can be attributed to the single crystalline structure and the semimetallic behavior of the Bi-based nanowires. A significant reduction of the Seebeck coefficient is only observed for a Bi core with a diameter less than 100 nm. The thermal conductivity of the Bi-based nanowires is reduced compared to the Bi bulk due to size effects and additional scattering events at the core/shell interface. The thermoelectric transport properties of the Bi-based nanowires are less sensitive to size effects compared to the silver nanowires and thin platinum films. This can be attributed to the single crystalline structure of the Bi-based nanowires

Chapter 10

Summary

Key aspects of this work are the investigations of size effects and structural properties on the thermoelectric transport properties of micro- and nanopatterned

- platinum (thin films)
- silver (nanowires)
- bismuth (Bi-based core/shell nanowires).

Another key aspect is the modeling of the absolute Seebeck coefficient of micro- and nanopatterned platinum and silver with regard to the

- distinction between thermodiffusion and phonon drag contribution
- influence of electron-phonon and phonon-phonon interaction.

Furthermore, aspects of metrology and technology were discussed in this work. In particular, thin platinum films were established as a new Seebeck reference standard for micro and nanostructures. These reference values can now be used to determine the absolute Seebeck coefficient of other micro- and nanopatterned materials. Such values are important because even small deviations of the Seebeck coefficient of the reference material can lead to misinterpretations of the measurement results.

In addition, a measurement platform was developed which enables the standardized determination of the thermoelectric transport properties of a thin film. The functionality and reliability was demonstrated with thin platinum films.

Moreover, this work proves that the thermoelectric nanowire characterization platform (TNCP A) is suitable to examine the thermoelectric properties of very fine individual silver nanowires. In combination with the thermoelectric investigations of the thin platinum films, it was possible to determine the absolute Seebeck coefficient of the silver nanowires. It was shown that they can be used as a model systems to investigate the influence of micro- and nanopatterning on the transport properties and that they are suitable to be used as reference material for metrology at the micro and nano level.

Furthermore, this work shows that it is possible to produce metallic interconnects in such a way that the resulting relative Seebeck coefficient can be zero in order to prevent parasitic thermovoltages by tailoring the absolute Seebeck coefficient through size effects.

In this thesis, a full temperature-dependent thermoelectric and structural characterization of individual Bi-based nanowires was performed. It turned out that

the core/shell system shows a way beyond miniaturization to make it possible to change the transport properties of a strainable material on purpose by the choice of a specific shell material. The main results are subsequently described in more detail.

Thermeoelectric characterization platforms

Three different thermeoelectric characterization platforms were used to investigate the transport properties of the materials in this thesis. A measurement platform, the thermoelectric micro lab (TML), was developed that enables the determination of the absolute Seebeck coefficient of a thin film. The functionality and reliability was demonstrated with thin platinum films. The design of the platform allows other materials to be examined thermoelectrically. Materials that have a very small Seebeck coefficient can also be investigated with the TML, because it is constructed in such a way that parasitic thermovoltages can be neglected.

Furthermore, two versions of the thermoelectric nanowire characterization platform (TNCP A and TNCP B) were used to determine the transport properties of individual nanowires. It was shown that the electrical conductivity, the Seebeck coefficient and the thermal conductivity and in addition structural investigations can be determined successfully with these measurements platforms. However, there are differences between TNCP A and TNCP B from a thermoelectrical point of view that were discussed. For this comparison, silver nanowires were selected as reference material due to the high purity, single crystalline structure and very small absolute Seebeck coefficient. It was shown that there is a difference of $\Delta S \approx 2\,\mu\mathrm{VK}^{-1}$ between the relative Seebeck coefficients of the silver nanowires on both TNCPs at room temperature due to parasitic Seebeck coefficients on TNCP B. As a result, both TNCPs are suitable for carrying out thermoelectric measurements. However, if materials are examined that have a very small absolute Seebeck coefficient, for example metals, then TNCP A is preferable over TNCP B because no parasitic Seebeck coefficients occur on TNCP A due to the absent of an additional temperature difference at bond pads.

Electron beam-induced deposition

A procedure in order to prepare electron beam-induced deposition contacts on nanowires with a Raith Pioneer Two electron microscope was established. The electrical properties of two EBID precursor materials (platinum-based $C_9H_{16}P_6$ and tungsten-based $W(CO)_6$) were characterized. The electrical characterization showed that the resistivity of the tungsten-based precursor is about 8 times larger at room temperature than the resistivity of the platinum-based precursor. This difference increases to a factor of approximately 108 at a temperature of $T = 130\,\mathrm{K}$. The difference of the resistivity between the two materials can be attributed to the composition of the precursor material. The platinum-based precursor contains a much larger amount of carbon than the tungsten-based precursor. As a result, the tungsten-based EBID contacts should be preferred because they have a lower resistivity.

Furthermore, it was examined how EBID contacts, which are based on platinum, can be improved. The influence of the dwell time during the EBID process, the influence of the electron beam power and the influence of a subsequent heat treatment

on the EBID contacts were investigated. The quality of the EBID contacts was partly improved. However, the used methods can have a negative impact on the measurement object itself, e.g. strong electron beam irradiation and halo effects.

Preparatory measurements of metallic microwires

The characterization of the transport properties of individual nanowires can be very challenging. Great care has to be taken while performing these measurements. The transport properties of three metallic (platinum, gold, aluminum/silicon) microwires were determined in order to test the measurement setup and lay the foundation for the measurements of the thin films and nanowires. It was shown that the electrical conductivity, the absolute Seebeck coefficient and the thermal conductivity of the microwires are in total agreement with the corresponding literature values proving the reliability of the measurement principles.

Thin platinum films

In this work, thermoelectric and structural characterizations of thin sputtered platinum films with a thickness of 22 nm, 134 nm and 197 nm were performed. The influence of heat treatment and film thickness on the electrical conductivity and the absolute Seebeck coefficient were investigated. Additional heat treatment with a maximum temperature of 400 °C and a larger film thickness increased the crystal quality of the platinum films.

Furthermore, the electrical conductivity and the absolute Seebeck coefficient were reduced compared to the bulk due to size effects like surface and boundary scattering. The electrical conductivity σ decreased at room temperature from $\sigma_{\mathrm{bulk}} = (9.6 \pm 0.5) \cdot 10^6\,\Omega^{-1}\mathrm{m}^{-1}$ to $\sigma_{\mathrm{film}} = (3.0 \pm 0.3) \cdot 10^6\,\Omega^{-1}\mathrm{m}^{-1}$ for a thin film with a thickness of 22 nm. The absolute Seebeck coefficient S changed from $S_{\mathrm{bulk}} = (-5.0 \pm 0.2)\,\mu\mathrm{VK}^{-1}$ to $S_{\mathrm{film}} = (0.8 \pm 0.1)\,\mu\mathrm{VK}^{-1}$.

It was found that structural properties like the average crystallographic grain size and the film thickness, which limit the electron mean free path, influence the absolute Seebeck coefficient. For the phonon drag part of the absolute Seebeck coefficient, the electron-phonon interaction compared to the phonon-phonon interaction plays a more dominant role in thin films than in bulk. If the mean free path of thin metallic films is in the order of the film thickness, the absolute Seebeck coefficient of bulk is no more valid. This has to be taken into account, when using thin platinum films as a reference material for the determination of the absolute Seebeck coefficient. Due to the influence of the microstructure, metallic interconnects can be tailored in a way, that the relative Seebeck coefficient can be reduced to zero which is interesting for low-noise applications.

Silver nanowires

A method to determine the absolute Seebeck coefficient of individual metallic nanowires is demonstrated in this thesis. Furthermore, a model that describes the temperature dependence of the absolute Seebeck coefficient of a metal was introduced. This model allows an estimation of the thermodiffusion and phonon drag contributions to the absolute Seebeck coefficient. The detailed analysis showed that both contributions to the absolute Seebeck coefficient of individual single crystalline silver nanowires are

reduced compared to bulk silver. In particular, the factor that scales the thermodiffusion part (from $F_{\mathrm{diff,bulk}} = (1.0 \pm 0.1)\,\mu\mathrm{VK}^{-1}$ to $F_{\mathrm{diff,NWs}} = (0.3 \pm 0.1)\,\mu\mathrm{VK}^{-1}$) is reduced more than the phonon drag part (from $F_{\mathrm{ph,bulk}} = (12 \pm 2)\,\mu\mathrm{VK}^{-1}$ to $F_{\mathrm{ph,NWs}} = (5.2 \pm 0.4)\,\mu\mathrm{VK}^{-1}$).

The reason for this reduction can be attributed to size effects like surface scattering that lead to an electron mean free path that is comparable to the nanowire diameter. The ratio of the electron-phonon to phonon-phonon interaction, which is described by the γ-factor, is larger in the silver nanowires than in the bulk material.

As a consequence of the small diameter of the nanowires, a channeling effect may restrict the phonon-phonon interaction perpendicular to the nanowire growth direction. For this reason, the electron-phonon interaction of the silver nanowires is significant at room temperature. The possibility of suppressing the absolute Seebeck coefficient (below $S = 1\,\mu\mathrm{VK}^{-1}$ at room temperature) by design of nanopatterned metallic interconnects may become important for low-noise applications.

Bismuth-based core/shell nanowires

In this thesis, a full temperature-dependent thermoelectric characterization of individual Bi-based core/shell nanowires was performed. The thermoelectric properties were related to the structural properties. The influence of the shell material on the electrical conductivity, the absolute Seebeck coefficient and the thermal conductivity was investigated. The findings reveal that different shell materials and spatial dimensions can influence the transport properties in various directions. The Bi-based nanowires can show a semimetallic or semiconducting behavior of the electrical conductivity accompanied with a band gap opening of the Bi core depending on the intensity of the compressive strain effect induced by the shell. Scattering of charge carriers at surfaces, grain boundaries and core/shell interfaces lead to a reduction of the electrical as well as the thermal conductivity. In particular, the thermal conductivity was reduced up to a quarter of the bulk value at room temperature. Moreover, all Bi-based nanowires showed an opposite temperature dependence of the thermal conductivity (decreasing λ with decreasing T) compared to Bi bulk.

The influence of the shell can lead to a compressive strain on the Bi core that can improve the Seebeck coefficient to $S_{\mathrm{max}} = (-69.9 \pm 0.6)\,\mu\mathrm{VK}^{-1}$. However, if the strain exceeds the elastic limits, then a relaxation process will change the transport properties irreversible. This will lead to a transition from a semiconducting to semimetallic behavior. For the Bi/Te core/shell nanowires, the influence of a non-uniform tellurium shell on the Bi core was investigated. It was shown that the thermoelectric properties are less improved compared to Bi/Te nanowires with a uniform shell. This can be attributed to a reduction of the compressive strain effect on the Bi core. The new shell material TiO_2 for Bi nanowires leads to a rather small figure of merit which is mainly a result of the low electrical conductivity of the Bi/TiO_2 nanowires. $\sigma_{\mathrm{Bi/TiO_2}}$ is reduced by a factor of 30 compared to Bi bulk near room temperature.

The findings reveal that different shell materials can influence the transport properties in various directions. This demonstrates the importance of a full thermoelectric characterization of an individual nanowire. As a consequence of the results, Bi-based nanowires can be tailored by a shell in a way that the transport properties are tunable over a wide range in order to allow the adaption to different application scenarios.

Chapter 11

Outlook

The thermoelectric mirco lab (TML) developed in this thesis was used to determine the thermoelectric properties of thin platinum films. This is of interest because platinum is an important Seebeck reference material. Another important Seebeck reference material is gold. For this reason, the TML should be used in order to determine the absolute Seebeck coefficient of thin gold films. The temperature dependence of the absolute Seebeck coefficient of thin platinum films up to a bath temperature of 300 K was determined in this work. Next, the absolute Seebeck coefficient for temperatures above 300 K should be determined as they can be used as reference values. In addition, further confinement effects can be investigated when the film thickness is sufficiently small (e.g. below 5 nm).

The silver nanowires examined in this work showed a minimum of the absolute Seebeck coefficient at room temperature. The Seebeck model predicts that the Seebeck coefficient will rise again for increasing temperatures above room temperature. This has to be confirmed experimentally because the single crystalline silver nanowires are perfectly suitable to benchmark the model not only in the low and room temperature regime but also in the high temperature region.

The preparation of electrical contacts for nanomaterials continues to be a challenge for metrology and technology. For bismuth-based (Bi-based) nanowires, the shell should be selectively removed for an optimal contact. In combination with the thermoelectric nanowire characterization platform (TNCP), this has so far only been possible using focused ion beam milling. Further methods should be developed that enable the removal of the shell, for example with an etching mask. Furthermore, it was shown that a non-uniform shell has a negative effect on the figure of merit increase. For this reason, a method should be used that produces a uniform shell, such as atomic layer deposition. So far, the influence of a shell with a thickness of 30 nm or less has been investigated. Subsequent work should investigate the influence of a thicker shell on the transport properties.

Individual nanowires are interesting from a scientific point of view. However, ensembles made of nanowires are required for commercial applications. Bi-based core/shell nanowires with a uniform tellurium (Te) shell with a thickness of 30 nm and with a Bi core diameter of about 400 nm are particularly suitable for thermoelectric applications. Thus, nanowire ensemble measurements could be one of the next steps in the field of core/shell materials.

Appendix A - Instructions for contacting via electron beam-induced deposition

- These instructions apply for the scanning electron microscope (SEM) with gas injection system (GIS) Pioneer Two from Raith.
- Put the sample with the chip carrier on a mount on the sample holder, see Fig. 11.1.
- Use carbon tape to fix the chip carrier on the mount.

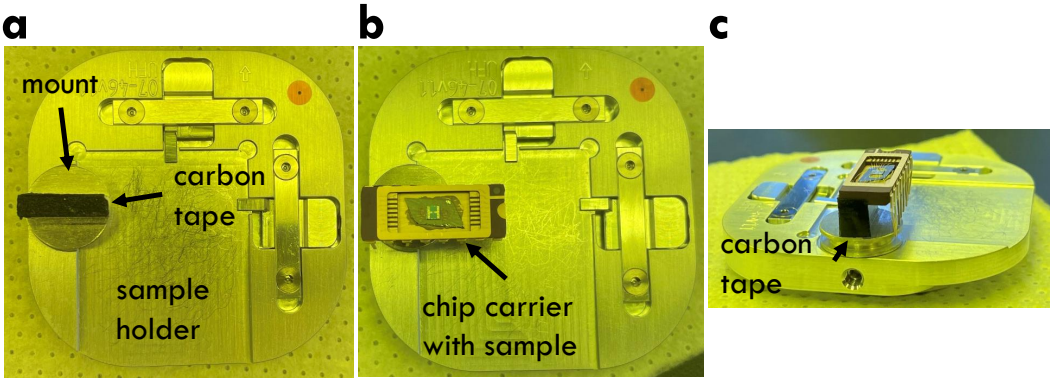

Figure 11.1: **Electron beam-induced deposition (EBID) - Sample installment.** **a**, Put the mount with the carbon tape on the sample holder. **b**, Put the sample on the mount. **c**, Put the carbon tape on the side of the sample and the mount.

- Load sample into the SEM.
- As soon as the sample has been loaded successfully, the outgas process must be started.
- Activate the side menu → click on *Airlock* → click on *Close Column Chamber Valve*, see Fig. 11.2 a.
- Activate *Outgas* in the *Gas Flow Control*, see Fig. 11.2 b.
- Click on *Open Column Chamber Valve* after the outgas process.
- Activate *Reservoir Heating* and *Capillary Heating* in the *Gas Flow Control*, see Fig. 11.2 b.

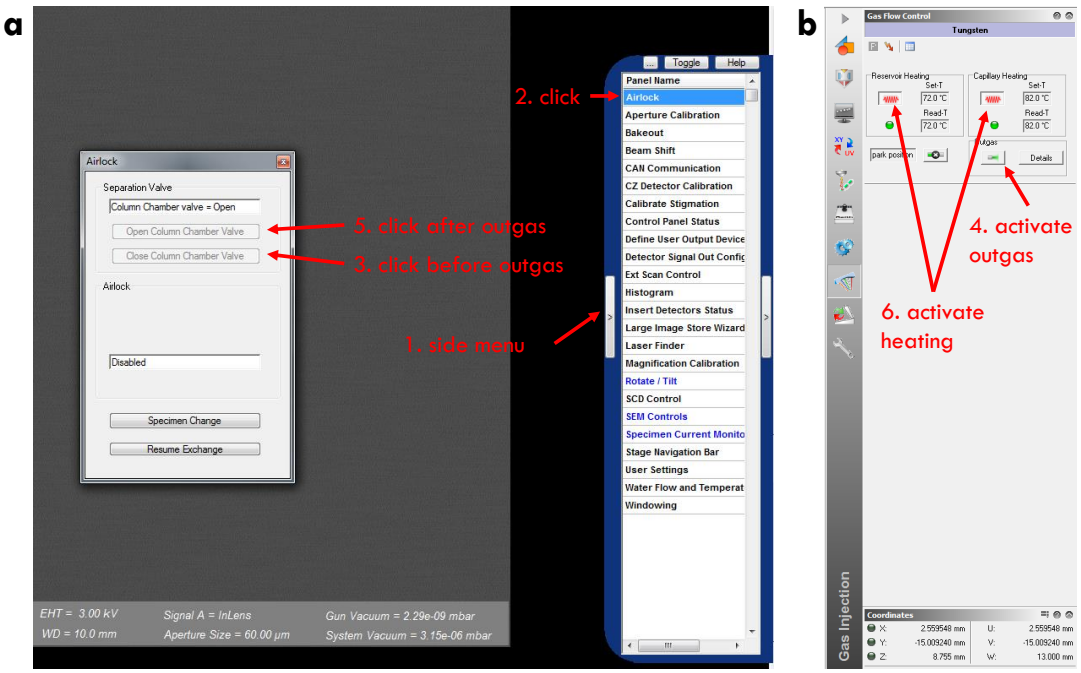

Figure 11.2: **Electron beam-induced deposition (EBID) - Preparation. a**, Close the airlock valve for the outgas process. After that, open it again. **b**, Start and stop the outgas process and activate the heating.

- Activate EHT (3 kV) and use an aperture of 60 μm.
- Drive to the sample and do a coarse focus adjustment.
- The working distance should now be 10 mm.
- Do a beam current measurement.
- The beam current should be in order of 0.5 nA up to 0.6 nA with EHT (3 kV) and an aperture of 60 μm.
- Go back to the sample.
- Drive the stage control to $W = 13$ mm. This is the safety distance for the GIS, see Fig. 11.3 a.
- Activate the GIS. It will go in the working position, see Fig. 11.3 c.
- Slowly drive back to $W = 10$ mm with the joystick.
- Do a fine focus adjustment.

- Click on *New Image Window* → click on *Scan Image*, see Fig. 11.4.
- Draw a structure (the EBID contact) with the *GDSII Editor* in the scanned image.
- Click on the structure and open the *Patterning Attributes* with the key *A* of the keyboard.

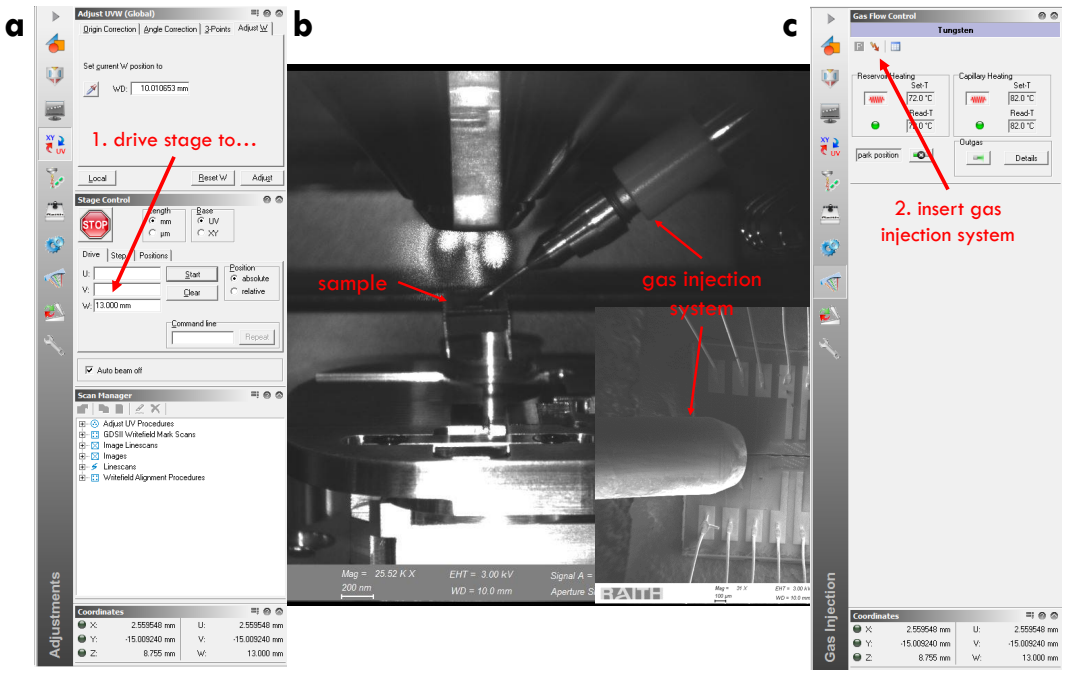

Figure 11.3: **Electron beam-induced deposition (EBID) - Gas injection system (GIS). a**, Drive the stage control to $W = 13\,\text{mm}$. This is the safety distance for the GIS. **b**, GIS is in the working position. **c**, Lighting bolt symbol drives the GIS in the working position.

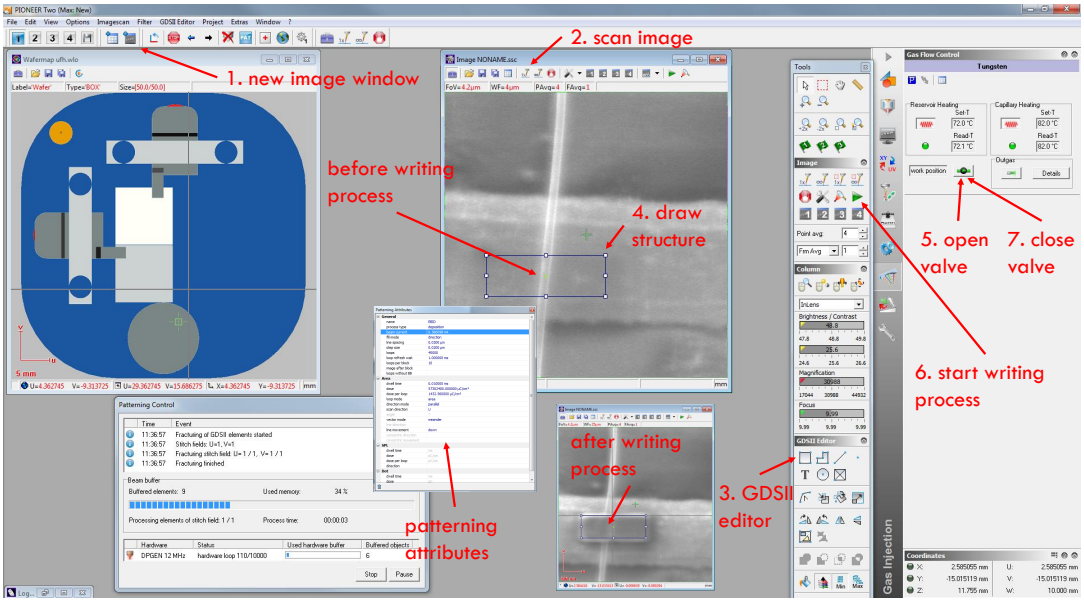

Figure 11.4: **Electron beam-induced deposition (EBID) - Structure.** An image of the area where the EBID contact will be prepared has to be scanned. Now, a structure for the contact can be drawn. The patterning attributes have to updated. The valve of the gas injection system can be opened. Then, the writing process can be started. The valve has to be closed after the writing process.

- The *Patterning Attributes* can be seen in Fig. 11.5.
- Some parameters have to be updated every time a new sample is loaded in the SEM.
- The beam current was measured some steps prior. The actual value of the current has to be updated in the *Patterning Attributes*.
- Click on the value of the *beam current* in the *Patterning Attributes*, see Fig. 11.5 a.
- A new window will open. Don't click on the pipette, just click *OK*, see Fig. 11.5 b.
- The amount of *loops* can be changed.
- If the *beam current* and/or the *loops* have changed, then the *dose* and *dose per loop* have to be updated.
- Click on the value of *dose* in the *Patterning Attributes*, see Fig. 11.5 a.
- A new window, *Patterning Attributes Calculator*, will open.
- All lights should be green. If not, at first click on the right calculator symbol at *dose per loop*. Then, click on the left calculator symbol. At last, click on the calculator symbol at *dose*, see Fig. 11.5 c.

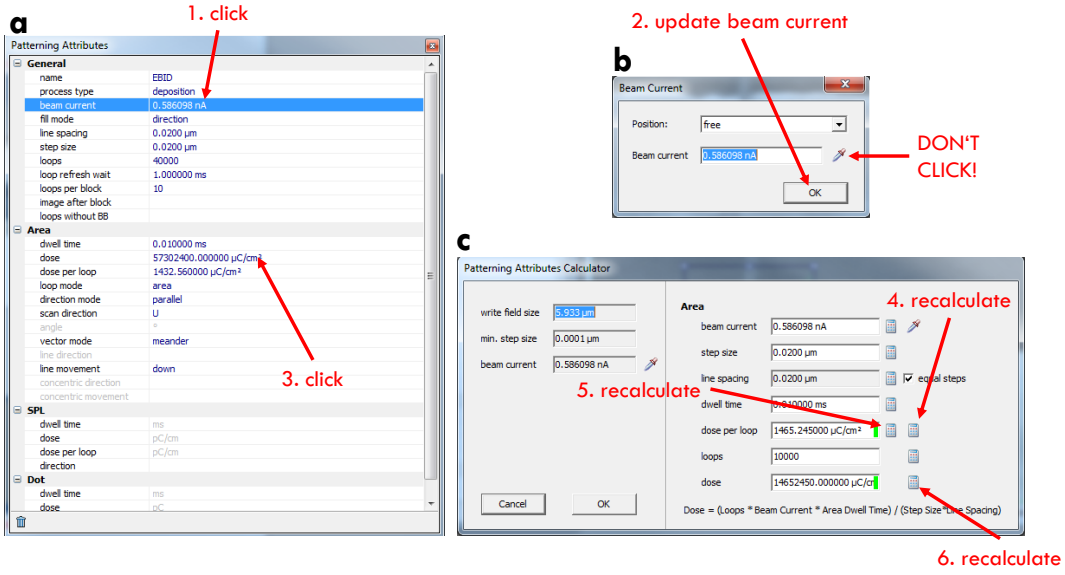

Figure 11.5: **Electron beam-induced deposition (EBID) - Patterning attributes. a**, Overview of all patterning attributes. Click on the beam current. **b**, Update the beam current by clicking *OK*. Don't click on the pipette. **c**, All lights should be green. If not, at first click on the right calculator symbol at *dose per loop*. Then, click on the left calculator symbol. At last, click on the calculator symbol at *dose*.

- Open the valve of the GIS in the *Gas Flow Control*, see Fig. 11.4.

- Wait approx. one minute until the gas flow is stabilized.
- Start the writing process, see Fig. 11.4.
- Close the valve of the GIS after the writing process.
- Wait several minutes until the residual gas of the GIS have been removed before a new image is scanned.
- Additional information about the EBID process is given in the main text.

Appendix B - Assembly and measurement of a nanowire sample

- These instructions apply for measurements (in particular for nanowire measurements) in the ARS DE-202A-DMX-20 closed cycled cryostat.
- Start all measurement devices and make some test measurements with the software but without a sample.
- Put on the strap for the grounding, see Fig. 11.6 a.
- Prepare all connections with BNC cables and grounding plugs, see Fig. 11.6 b.
- Install the sample flat on the copper holder for a good thermal contact, see Fig. 11.6 c.
- Install the sample upside down in the cryostat, see Fig. 11.6 d.
- Connect the cryostat connections with corresponding sample holder connections.
- Insert both sealing heads (thin and thick) into the cryostat.
- Open the He bottle and open the wall valve.
- Open the cooling water for the compressor.
- Start the turbo pump and pump the vacuum.
- Perform the rinsing process. To do this, set the table valve to 0.08 bar $\rightarrow$ check the safety valve $\rightarrow$ set the table valve to 0.04 bar $\rightarrow$ open and close the green valve. Repeat this three to five times.
- Start the compressor.
- Remove the grounding plugs when all machines are running.
- Start the nanowire measurement. The following applies to all nanowire measurements: Start with a very small current, for example 10 nA.
- The circuit diagram of the electrical conductivity and thermal conductivity measurements is given in Fig. 11.7 a.
- The circuit diagram of the Seebeck coefficient measurements is given in Fig. 11.7 b.

- Additional information about the measurement process is given in the main text.

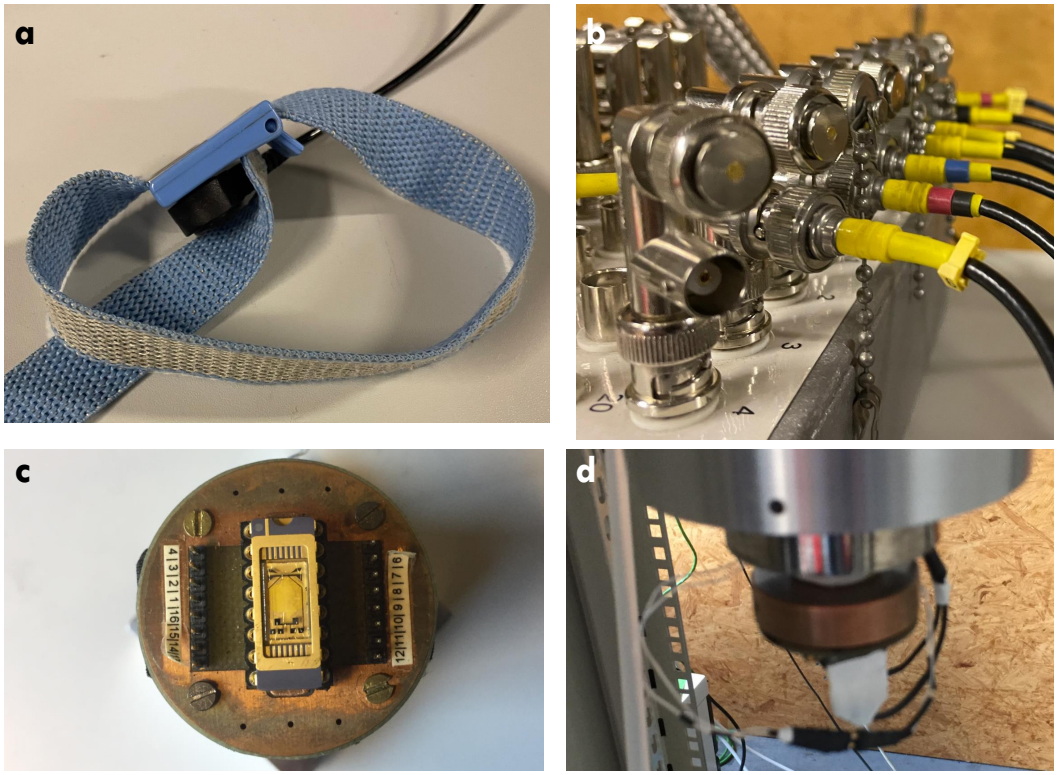

Figure 11.6: **Nanowire measurement - Preparation.** **a**, Arm strap for the grounding. **b**, Connections with BNC cables and grounding plugs. **c**, Chip carrier installed on the copper holder. **d**, Sample installed upside down in the cryostat.

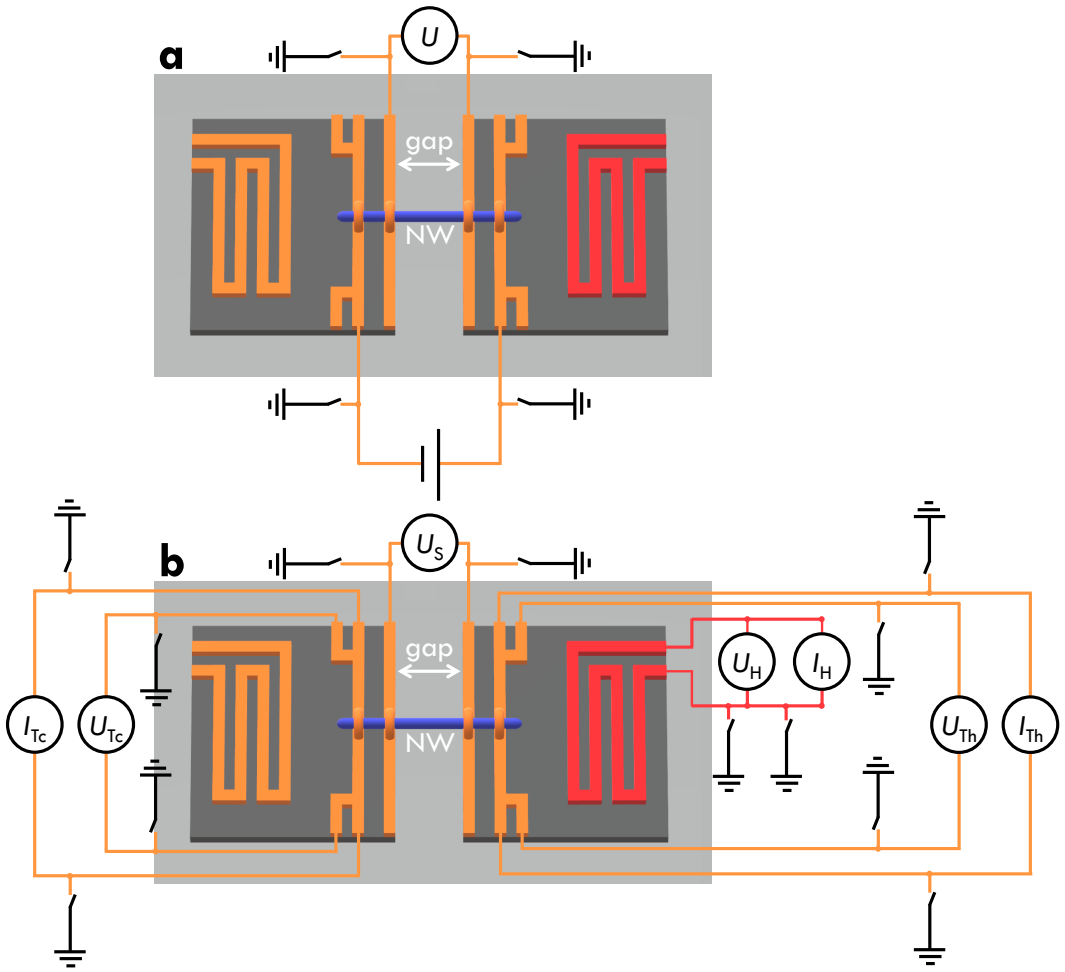

Figure 11.7: **Nanowire measurement - Circuit diagram and sketch of the measurement area of the thermoelectric nanowire characterization platform (TNCP B). a**, A current I is applied at outer contacts in order to perform a four-terminal resistance measurement. The voltage drop U is measured at the inner contacts. The same connections are used for the thermal conductivity measurements. **b**, The micro heater (red) is used to create a temperature difference between the two sides of the platform. The temperature difference is determined by the resistance thermometers on the hot (I_{Th}, U_{Th}) and cold side (I_{Tc}, U_{Tc}), respectively. The cold thermometer is identified with the low potential of the thermovoltage U_{S}.

Bibliography

[1] M. Kockert, R. Mitdank, A. Zykov, S. Kowarik, and S. F. Fischer. Absolute Seebeck coefficient of thin platinum films. *Journal of Applied Physics*, **126**(10):105106, (2019).

[2] M. Kockert, D. Kojda, R. Mitdank, A. Mogilatenko, Z. Wang, J. Ruhhammer, M. Kroener, P. Woias, and S. F. Fischer. Nanometrology: Absolute Seebeck coefficient of individual silver nanowires. *Scientific Reports*, **9**(20265):1, (2019).

[3] M. Kockert, R. Mitdank, H. Moon, J. Kim, A. Mogilatenko, S. H. Moosavi, M. Kroener, P. Woias, W. Lee, and S. F. Fischer. Semimetal to semiconductor transition in Bi/TiO_2 core/shell nanowires. *Nanoscale Advances*, **3**(1):263–271, (2021).

[4] G. E. Moore. Cramming more components onto integrated circuits. *Electronics*, **38**(8):114–117, (1965).

[5] G. E. Moore. Progress In Digital Integrated Electronics. *International Electron Devices Meeting, IEEE*, pages 11–13, (1975).

[6] J.-P. Niemela, G. Marin, and M. Karppinen. Titanium dioxide thin films by atomic layer deposition: a review. *Semiconductor Science and Technology*, **32**(9):093005, (2017).

[7] G. Qiu, S. Huang, M. Segovia, P. K. Venuthurumilli, Y. Wang, W. Wu, X. Xu, and P. D. Ye. Thermoelectric Performance of 2D Tellurium with Accumulation Contacts. *Nano Letters*, **19**(3):1955–1962, (2019).

[8] S. M. George. Atomic Layer Deposition: An Overview. *Chemical Reviews*, **110**(1):111–131, (2010).

[9] F. Völklein. Review of the Thermoelectric Efficiency of Bulk and Thin-Film Materials. *Sensors and Materials*, **8**(6):389–408, (1996).

[10] G.-S. Kim, M.-R. Lee, S.-Y. Lee, J.-H. Hyung, N.-W. Park, E. S. Lee, and S.-K. Lee. Reduction in thermal conductivity of Bi thin films with high-density ordered nanoscopic pores. *Nanoscale Research Letters*, **8**(371):1–7, (2013).

[11] A. I. Hochbaum, R. Chen, R. D. Delgado, W. Liang, E. C. Garnett, M. Najarian, A. Majumdar, and P. Yang. Enhanced thermoelectric perfomance of rough silicon nanowires. *Nature*, **451**(7175):163–167, 2008.

[12] W.-J. Kwak, H.-G. Jung, S.-H. Lee, J.-B. Park, D. Aurbach, and Y.-K. Sun. Silver nanowires as catalytic cathodes for stabilizing lithium-oxygen batteries. *Journal of Power Sources*, **311**:49–56, (2016).

[13] W. Kim. Thermal transport in individual thermoelectric nanowires: a review. *Materials Research Innovations*, **15**(6):375–385, (2011).

[14] S. Bäßler, T. Böhnert, J. Gooth, C. Schumacher, E. Pippel, and K. Nielsch. Thermoelectric power factor of ternary single-crystalline Sb_2Te_3- and Bi_2Te_3-based nanowires. *Nanotechnology*, **24**(49):495402, (2013).

[15] A. I. Boukai, Y. Bunimovich, J. Tahir-Kheli, J.-K. Yu, W. A. Goddard III, and J. R. Heath. Silicon nanowires as efficient thermoelctric materials. *Nature*, **451**(7175):168–171, (2008).

[16] Z. Li, Y. Chen, X. Li, T. I. Kamins, K. Nauka, and R. S. Williams. Sequence-Specific Label-Free DNA Sensors Based on Silicon Nanowires. *Nano Letters*, **4**(2):245–247, (2004).

[17] Y. Cui, Z. Zhong, D. Wang, W. U. Wang, and C. M. Lieber. High Performance Silicon Nanowire Field Effect Transistors. *Nano Letters*, **3**(2):149–152, (2003).

[18] Y. Engel, R. Elnathan, A. Pevzner, G. Davidi, E. Flaxer, and F. Patolsky. Supersensitive Detection of Explosives by Silicon-Nanowire Arrays. *Angewandte Chemie*, **122**(38):6982–6987, (2010).

[19] J. Machin, D. Tucker, and J. V. Pearce. A comprehensive survey of thermoelectric homogeneity of commonly used thermocouples types. *Measurement Science and Technology*, **29**(6):067002, (2018).

[20] D. Kojda, R. Mitdank, A. Mogilatenko, W. Töllner, Z. Wang, M. Kröner, P. Woias, K. Nielsch, and S. F. Fischer. The effect of a distinct diameter variation on the thermoelectric properties of individual $Bi_{0.39}Te_{0.61}$ nanowires. *Semiconductor*, **29**(12):124006, (2014).

[21] D. Kojda, R. Mitdank, M. Handwerg, A. Mogilatenko, M. Albrecht, Z. Wang, J. Ruhhammer, M. Kroener, P. Woias, and S. F. Fischer. Temperature-dependent thermoelectric properties of individual silver nanowires. *Physical Review B*, **91**(2):024302, (2015).

[22] A. I. Hochbaum, R. Chen, R. D. Delgado, W. Liang, E. C. Garnaett, M. Najarian, A. Majumdar, and P. Yang. Enhanced thermoelectric performance of rough silicon nanowires. *Nature*, **451**(7175):163–167, (2008).

[23] J. Kim, G. Kim, J.-H. Bahk, J. S. Noh, and W. Lee. Enhanced thermoelectric properties in Bi/Te core/shell heterostructure nanowires through strain and interface engineering. *Nano Energy*, **32**:520–525, (2017).

[24] Z. Wang, S. S. Adhikari, M. Kroener, D. Kojda, R. Mitdank, S. F. Fischer, W. Toellner, K. Nielsch, and P. Woias. Electrical conductivity and seebeck coefficient measurements of single nanowires by utilizing a microfabricated thermoelectric nanowire characterization platform. In *2013 IEEE 26th International Conference on Micro Electro Mechanical Systems (MEMS)*, pages 508–511. IEEE, (2013).

[25] S. H. Moosavi, D. Kojda, M. Kockert, S. F. Fischer, M. Kroener, and P. Woias. The Effect of the MEMS Measurement Platform Design on the Seebeck Coefficient Measurement of a Single Nanowire. *Nanomaterials*, **8**(219):1–14, (2018).

[26] V. Linseis, F. Völklein, H. Reith, P. Woias, and K. Nielsch. Platform for in-plane ZT measurement and Hall coefficient determination of thin films in a temperature range from 120 K up to 450 K. *Journal of Materials Research*, **31**(20):3196–3204, (2016).

[27] G. Brändli and J. L. Olsen. Size Effects in Electron Transport in Metals. *Materials Science and Engineering*, **4**(2-3):61–83, (1969).

[28] R. P. Huebener. Size effect on phonon drag in platinum. *Physical Review*, **140**(5A):A1834, (1965).

[29] R. P. Huebener. Thermoelectric Size Effect in Pure Gold. *Physical Review*, **136**(6A):A1740, (1964).

[30] W. F. Leonard and H.-Y. Yu. Thermoelectric power of thin copper films. *Journal of Applied Physics*, **44**(12):5320–5323, (1973).

[31] H.-Y. Yu and W. F. Leonard. Thermoelectric power of thin silver films. *Journal of Applied Physics*, **44**(12):5324–5327, (1973).

[32] V. D. Das and N. Soundararajan. Size and temperature effects on the Seebeck coefficient of thin bismuth films. *Physical Review B*, **35**(12):5990, (1987).

[33] B. Wiley, Y. Sun, and Y. Xia. Synthesis of silver nanostructures with controlled shapes and properties. *Accounts of Chemical Research*, **40**(10):1067–1076, (2007).

[34] N. Cusack and P. Kendall. The absolute scale of thermoelectric power at high temperature. *Proceedings of the Physical Society*, **72**:898–901, (1958).

[35] W. B. Pearson. Survey of thermoelectric studies of the group I metals at low temperatures carried out at NRL, Ottawa. *Soviet Physics - Solid State*, **3**:1024–1033, (1961).

[36] C. C. Lee and P. A. Schroeder. Phonon drag thermopower in silver alloys. *Philosophical Magazine*, **25**(5):1161–1168, (1972).

[37] V. V. R. N. Rao, S. Mohan, and P. J. Reddy. The size effect in the thermoelectric power of silver films. *Thin Solid Films*, **42**(3):283–289, (1977).

[38] D. R. Smith and F. R. Fickett. Low-temperature properties of silver. *Journal of Research of the National Institute of Standards and Technology*, **100**(2):119, (1995).

[39] M. Cann *et al.* High performance transparent multi-touch sensors based on silver nanowires. *Materials Today Communications*, **7**:42–50, (2016).

[40] L. Yang *et al.* Solution-processed flexible polymer solar cells with silver nanowire electrodes. *ACS Appl. Mater. Interfaces*, **3**(10):4075–4084, (2011).

[41] R. P. Huebener. Phonon scattering by lattice vacancies in platinum. *Physical Review*, **146**(2):490, (1966).

[42] X. F. Zhu, H. F. Zhang, J. S. Williams, R. P. Wang, L.D. Zhang, and X. J. Wu. Low-temperature thermopower in nanostructured silver. *Applied Physics Letters*, **75**(1):136–138, (1999).

[43] H. Y. Yu and W. F. Leonard. Thermoelectric power of thin silver films. *Journal of Applied Physics*, **44**(12):5324–5327, (1973).

[44] S. F. Lin and W. F. Leonard. Thermoelectric Power of Thins Gold Films. *Journal of Applied Physics*, **42**(9):3634–3639, (1971).

[45] R. P. Huebener. Thermoelectric Power of Lattice Vacancies in Gold. *Physical Review*, **135**(5A):A1281, (1964).

[46] E. Shapira, A. Tsukernik, and Y. Selzer. Thermopower measurements on individual 30 nm nickel nanowires. *Nanotechnology*, **18**(48):485703, (2007).

[47] D. Kojda *et al.* Surface effects on thermoelectric properties of metallic and semiconducting nanowires. *physica status solidi A*, **213**(3):557–570, (2016).

[48] Z. Cheng, L. Liu, S. Xu, and M. Lu. Temperature dependence of electrical and thermal conduction in single silver nanowires. *Scientific Reports*, **5**:10718, (2015).

[49] F. Völklein, H. Reith, T. W. Cornelius, M. Rauber, and R. Neumann. The experimental investigation of thermal conductivity and the Wiedemann-Franz law for single metallic nanowires. *Nanotechnology*, **20**(32):325706, (2009).

[50] David Keith Chalmers MacDonald. *Thermoelectricity: an introduction to the principles*. Courier Corporation, (2006).

[51] M. Cutler and N. F. Mott. Observation of Anderson Localization in an Electron Gas. *Physical Review*, **181**(3):1336, (1969).

[52] M. Bailyn. The phonon drag component of the thermoelectric power of the alkali metals at low temperatures. *Philosophical Magazine*, **5**(58):1059–1085, (1960).

[53] C. F. Gallo, B. S. Chandrasekhar, and P. H. Sutter. Transport Properties of Bismuth Single Crystals. *Journal of Applied Physics*, **34**(1 oder issue):144–152, (1963).

[54] K. Liu, C. L. Chien, and P. C. Searson. Finite-size effects in bismuth nanowires. *Physical Review B*, **58**(22):R14681, (1998).

[55] Z. Zhang, X. Sun, M. S. Dresselhaus, J. Y. Ying, and J. Heremans. Electronic transport properties of single-crystal bismuth nanowire arrays. *Physical Review B*, **61**(7):4850, (2000).

[56] J. Heremans, C. M. Thrush, Y.-M. Lin, S. Cronin, Z. Zhang, M. S. Dresselhaus, and J. F. Mansfield. Bismuth nanowire arrays: Synthesis and galvanomagnetic properties. *Physical Review B*, **61**(4):2921, (2000).

[57] S. Lee, J. Ham, K. Jeon, J.-S Noh, and W. Lee. Direct observation of the semimetal-to-semiconductor transition of individual single-crystal bismuth nanowires grown by on-film formation of nanowires. *Nanotechnology*, **21**(40):405701, (2010).

[58] M. S. Dresselhaus, G. Dresselhaus, X. Sun, Z. Zhang, S. B. Cronin, and T. Koga. Low-dimensional thermoelectric materials. *Physics of the Solid State*, **41**(5):679–682, (1999).

[59] J. Kang, J. W. Roh, W. Shim, J. Ham, J.-S. Noh, and W. Lee. Reduction of Lattice Thermal Conductivity in Single Bi-Te Core/Shell Nanowires with Rough Interface. *Advanced Materials*, **23**(30):3414–3419, (2011).

[60] J. Kim, G. Kim, J.-H. Bahk, J.-S. Noh, and W. Lee. Enhanced thermoelectric properties in Bi/Te core/shell heterostructure nanowires through strain and interface engineering. *Nano Energy*, **32**:520–525, (2017).

[61] J. Kim, M.-W. Oh, G. Kim, J.-H. Bahk, J. Y. Song, S. G. Jeon, D. W. Chun, J.-H. Bae, W. Shim, and W. Lee. Strain-engineered allotrope-like bismuth nanowires for enhanced thermoelectric performance. *Acta Materialia*, **144**:145–153, (2018).

[62] H. Moon, J. Kim, D. W. Chun, S. Hong, Y. S. Yoon, and W. Lee. Radial heterostructure and interface effects on thermoelectric transport properties of Bi/Sn and Bi/Sb core/shell nanowires. *Current Applied Physics*, **20**(1):43–48, (2020).

[63] R. Gross and A. Marx. *Festkörperphysik*. De Gruyter, Berlin/Boston, 3 edition, (2018).

[64] H. Ibach and H. Lüth. *Festkörperphysik: Einführung in die Grundlagen*. Springer-Verlag, Berlin Heidelberg, 7 edition, (2009).

[65] R. B. Belser and W. H. Hicklin. Temperature Coefficients of Resistance of Metallic Films in the Temperature range 25° to 600°C. *Journal of Applied Physics*, **30**(3):313–322, (1959).

[66] W. F. Leonard and R. L. Ramey. Temperature Coefficient of Resistance in Thin Metal Films. *Journal of Applied Physics*, **37**(9):3634–3635, (1966).

[67] M. Krishnan, E. Valderrama, B. Bures, K. Wilson-Elliott, X. Zhao, L. Phillips, A.-M. Valente-Feliciano, J. Spradlin, C. Reece, and K. Seo. Very high residual resistivity ratios of heteroepitaxial superconducting niobium films on MgO substrates. *Superconductor Science and Technology*, **24**(11):115002, (2011).

[68] B. D. Hennings, D. G. Naugle, and P. C. Canfield. Thermal transport of the single-crystal rare-earth nickel borocarbides $R\mathrm{Ni_2B_2C}$. *Physical Review B*, **66**(21):214512, (2002).

[69] P. K. Das and A. Thamizhavel. Crystal growth and magnetic properties of equiatomic CeAl. *Journal of Physics: Conference Series*, **592**:012009, (2015).

[70] H. Ibach and H. Lüth. *Solid-State Physics: An Introduction to Principles of Materials Science*. Springer-Verlag, Berlin Heidelberg, **4** edition, (2009).

[71] C. Kittel. *Introduction to Solid State Physics*. Wiley, 1 edition, (1953).

[72] T. M. Tritt. *Thermoelectrics Handbook: Macro to Nano, Electrical and Thermal Transport Measurement Techniques for Evaluation of the Figure-of-Merit of Bulk Thermoelectric Materials*. CRC Press, (2005).

[73] R. P. Huebener. Thermoelectricity in metals and alloys. *Solid State Physics*, **27**:63–134, (1972).

[74] T. J. Seebeck. Ueber die magnetische Polarisation der Metalle und Erze durch Temperaturdifferenz. *Annalen der Physik*, **82**(3):253–286, (1826).

[75] J. C. A. Peltier. Nouvelles expériences sur la caloricite des courans électriques. *Annales de Chimie et de Physique*, **56**:371–386, (1834).

[76] C. L. Foiles. *Landolt-Börnstein: Electrical Resistivity, Thermoelectrical Power and Optical Properties - Thermopower of pure metals and dilute alloys*. Springer Materials, New York, 15b edition, (1985).

[77] L. Onsager. Reciprocal Relations in Irreversible Processes. I. *Physical Review*, **37**(4):405–426, (1931).

[78] R. Pelster, R. Pieper, and I. Hüttl. Thermospannungen - viel genutzt und fast immer falsch erklärt! *Physik und Didaktik in Schule und Hochschule*, **1**(4):10–22, (2005).

[79] Y. Amagai, T. Shimazaki, K. Okawa, H. Fujiki, T. Kawae, and N.-H. Kaneko. Precise measurement of absolute seebeck coefficient from Thomson effect using ac-dc technique. *AIP Advances*, **9**(6):065312, (2019).

[80] J. W. Christian, J. p. Jan, W. B. Pearson, and I. M. Templeton. Thermoelectricity at low temperatures. VI. A redetermination of the absolute scale of thermo-electric power of lead. *Proceedings Of The Royal Society A*, **245**(1241):213–221, (1958).

[81] N. F. Mott. The Resistance and Thermoelectric Properties of the Transition Metals. *Proceedings Of The Royal Society A*, **156**(888):368–382, (1936).

[82] C. T. Walker and R. o. Pohl. Phonon scattering by point defects. *Physical Review*, **131**(4):1433, (1963).

[83] R. P. Huebener. Thermoelectric Power of Aluminum and Dilute Aluminum Alloys. *Physical Review*, **171**(3):634–641, (1968).

[84] F. J. Blatt. Thermoelectric power of noble metals. *Physics Letters*, **8**(4):235–237, (1964).

[85] J. E. Robinson. Thermoelectric Power in the Nearly-Free-Electron Model. *Physical Review*, **161**(3):533–539, (1967).

[86] R. Fletcher and D. Greig. The low temperature thermoelectric power of some palladium and platinum alloys. *The Philosophical Magazine: A Journal of Theoretical Experimental and Applied Physics*, **17**(145):21–35, (1968).

[87] G. J. Snyder and A. H. Snyder. Figure of merit ZT of a thermoelectric device defined from materials properties. *Energy Environmental Science*, **10**(11):2280–2283, (2017).

[88] NOMAD Encyclopedia. Crystal structure of platinum. https://encyclopedia.nomad-coe.eu/gui/#/material/17221, 16.04.2020, 18:20 Uhr.

[89] N. Stojanovic, D. H. S. Maithripala, J. M. Berg, and M. Holtz. Thermal conductivity in metallic nanostructures at high temperature: Electrons, phonons, and the Wiedemann-Franz law. *Physical Review B*, **82**(7):075418, (2010).

[90] J. W. Arblaster. Selected Electrical Resistivity Values for the Platinum Group of Metals Part I: Palladium and Platinum. *Johnson Matthey Technology Review*, **59**(3):174–181, (2015).

[91] Y. S. Touloukian, R. W. Powell, C. Y. Ho, and P. G. Klemens. Thermophysical Properties of Matter - The TPRC Data Series - Vol. 1. Thermal Conductivity - Metallic Elements and Alloys. *Thermophysical Properties Research Center*, **1**:1–1595, (1970).

[92] F. Völklein, H. Reith. T. W. Cornelius, M. Rauber, and R. Neumann. The experimental investigation of thermal conductivity and the Wiedemann-Franz law for single metallic nanowires. *Nanotechnology*, **20**(32):325706, (2009).

[93] G. Fischer, H. Hoffmann, and J. Vancea. Mean free path and density of conductance electrons in platinum determined by the size effect in extremely thin films. *Physical Review B*, **22**(12):6065–6073, (1980).

[94] Q. G. Zhang, B. Y. Cao, X. Zhang, M. Fujii, and K. Takahashi. Size effects on the thermal conductivity of polycrystalline platinum nanofilms. *Journal of Physics: Condensed Matter*, **18**(34):7937–7950, (2006).

[95] X. Zhang, H. Xie, M. Fujii, H. Ago, K. Takahashi, T. Ikuta, H. Abe, and T. Shimizu. Thermal and electrical conductivity of a suspended platinum nanofilm. *Journal of Applied Physics*, **86**(17):171912, (2005).

[96] M. C. Salvadori, A. R. Vaz, F. S. Teixeira, M. Cattani, and I. G. Brown. Thermoelectric effect in very thin film Pt/Au thermocouples. *Applied Physics Letters*, **88**(13):133106, (2006).

[97] NOMAD Encyclopedia. Crystal structure of silver. https://encyclopedia.nomad-coe.eu/gui/#/material/10219, 16.04.2020, 18:25 Uhr.

[98] R. S. Seth and S. B. Woods. Electrical Resistivity and Deviations from Matthiessen's Rule in Dilute Alloys of Aluminum, Cadmium, Silver, and Magnesium. *Physical Review B*, **2**(8):2961, (1970).

[99] A. A. Abrikosov and L. A. Fal'kovskiĭ. Theory of semimetals - Original. *Zhurnal Éksperimental'noĭ i Teoreticheskoĭ Fiziki*, **43**:1089, (1962).

[100] A. A. Abrikosov and L. A. Fal'kovskiĭ. Theory of semimetals - Translation. *Soviet Physics JETP*, **16**:769, (1963).

[101] V. S. Édel'man. Electrons in bismuth. *Advances in Physics*, **25**(6):555–613, (1976).

[102] J. Kim, W. Shim, and W. Lee. Bismuth nanowire thermoelectrics. *Journal of Materials Chemistry C*, **3**(46):11999–12013, (2015).

[103] J. Kim, S. Lee, Y. M. Brovman, P. Kim, and W. Lee. Diameter-dependent thermoelectric figure of merit in single-crystalline Bi nanowires. *Nanoscale*, **7**(11):5053–5059, (2015).

[104] C. Uher and H. J. Goldsmid. Separation of the Electronic and Lattice Thermal Conductivities in Bismuth Crystals. *physica status solidi b*, **65**(2):765–772, (1974).

[105] M. S. Dresselhaus, G. Chen, M. Y. Tang, H. Lee R. Yang, D. Wang, Z. Ren, J.-P. Fleurial, and P. Gogna. New Directions for Low-Dimensional Thermoelectric Materials. *Advanced Materials*, **19**(8):1043–1053, (2007).

[106] L. D. Hicks and M. S. Dresselhaus. Effect of quantum-well structures on the thermoelectric figure of merit. *Physical Review B*, **47**(19):12727–12731, (1993).

[107] L. D. Hicks and M. S. Dresselhaus. Thermoelectric figure of merit of a one-dimensional conductor. *Physical Review B*, **47**(24):16631–16634, (1993).

[108] X. Sun, Z. Zhang, and M. S. Dresselhaus. Theoretical modeling of thermoelectricity in Bi nanowires. *Applied Physics Letters*, **74**(26):4005–4007, (1999).

[109] A. Nikolaeva, D. Gitsu, L. Konopko, M. J. Graf, and T. E. Huber. Quantum interference of surface states in bismuth nanowires probed by the Aharonov-Bohm oscillatory behavior of the magnetoresistance. *Physical Review B*, **77**(7):075332, (2008).

[110] T. E. Huber, A. Adeyeye, A. Nikolaeva, L. Konopko, R. C. Johnson, and M. J. Graf. Surface state band mobility and thermopower in semiconducting bismuth nanowires. *Physical Review B*, **83**(23):235414, (2011).

[111] P. Grosse. *Die Festkörpereigenschaften von Tellur*. Springer Series in Optical Sciences. Springer-Verlag, (1969).

[112] A. Nussbaum. Electrical Properties of Pure Tellurium and Tellurium-Selenium Alloys. *Physical Review*, **94**(2):337, (1954).

[113] S. Lin, W. Li, Z. Chen, J. Shen, B. Ge, and Y. Pei. Tellurium as a high-performance elemental thermoelectric. *Nature Communications*, **7**(10287):1–6, (2016).

[114] H. Peng, N. Kioussis, and G. J. Snyder. Elemental tellurium as a chiral p-type thermoelectric material. *Physical Review B*, **89**(19):195206, (2014).

[115] B. S. Chandrasekhar. The seebeck coefficient of bismuth single crystals. *Journal of Physics and Chemistry of Solids*, **11**(3-4):268–273, (1959).

[116] S. B. Cronin, Y.-M. Lin, O. Rabin, M. R. Black, J. Y. Ying, M. S. Dresselhaus, P. L. Gai, J.-P. Minet, and J.-P. Issi. Making electrical contacts to nanowires with a thick oxide coating. *Nanotechnology*, **13**(5):653–658, (2002).

[117] V. P. Duggal and R. Rup. Thickness-Dependent Oscillatory Behavior of Resistivity and Hall Coefficient in Thin Single-Crystal Bismuth Films. *Journal of Applied Physics*, **40**(2):492–495, (1969).

[118] T. W. Cornelius and M. E. Toimil-Molares. *Nanowires - Finite- and Quantum-size Effects of Bismuth Nanowires*. IntechOpen, (2010).

[119] J. Heremans and C. M. Thrush. Thermoelectric power of bismuth nanowires. *Physical Review B*, **59**(19):12579–12583, (1999).

[120] J. Ham, W. Shim, D. H. Kim, S. Lee, J. Roh, S. W. Sohn, K. H. Oh, P. W. Voorhees, and W. Lee. Direct Growth of Compound Semiconductor Nanowires by On-Film Formation of Nanowires: Bismuth Telluride. *Nano Letters*, **9**(8):2867–2872, (2009).

[121] J. W. Roh, K. Hippalgaonkar, J. H. Ham, R. Chen, M. Z. Li, P. Ercius, A. Majumdar, W. Kim, and W. Lee. Observation of Anisotropy in Thermal Conductivity of Individual Single-Crystalline Bismuth Nanowires. *ACS Nano*, **5**(5):3954–3960, (2011).

[122] M. Murata, A. Yamamoto, Y. Hasegawa, T. Komine, and A. Endo. Theoretical modeling of electrical resistivity and Seebeck coefficient of bismuth nanowires by considering carrier mean free path limitation. *Journal of Applied Physics*, **121**(1):014303, (2017).

[123] H. J. Levinson. *Principles of Lithography*. Springer Series in Optical Sciences. SPIE, 3 edition, (2010).

[124] I. Utke, P. Hoffmann, and J. Melngailis. Gas-assisted focused electron beam and ion beam processing and fabrication. *Journal of Vacuum Science & Technology B: Microelectronics and Nanometer Structures Processing, Measurement, and Phenomena*, **26**(4):1197–1276, (2008).

[125] A. Botmana, M. Hesselberth, and J. J. L. Mulders. Improving the conductivity of platinum containing nano structures created by electron-beam-induced deposition. *Microelectronic Engineering*, **85**(5-6):1139–1142, (2008).

[126] D. Brunel, D. Troadec, D. Hourlier, D. Deresmes, M. Zdrojek, and T. Mélin. Characterization of ion/electron beam induced deposition of electrical contacts at the sub-μm scale. *Microelectronic Engineering*, **88**(7):1569–1572, 2011.

[127] N. Jalili and K. Laxminarayana. A review of atomic force microscopy imaging systems: application to molecular metrology and biological sciences. *Mechatronics*, **14**(8):907–945, (2004).

[128] U. Kilian. *Lexikon der Physik: Mi bis Sb. 4*. Spektrum, Akademischer Verlag, Berlin Heidelberg, (1999).

[129] W. Demtröder. *Experimentalphysik 2: Elektrizität und Optik*. Springer-Verlag, Berlin Heidelberg, 3 edition, (2004).

[130] L. Reimer. *Scanning Electron Microscopy: Physics of Image-Formation and Microanalysis*. Springer-Verlag, Heidelberg, 2 edition, (1998).

[131] D. D. Williams and C. B. Carter. *Transmission Electron Microscopy - Part 1: Basics*. Springer-Verlag, 2 edition, (2009).

[132] P. Scherrer. Bestimmung der Groesse und der inneren Struktur von Kolloidteilchen mittels Röntgenstrahlen. *Nachrichten von der Königlichen Gesellschaft der Wissenschaften zu Göttingen*, **2**:98–100, (1918).

[133] C. Weber, L. Pithan, A. Zykov, S. Bommel, F. Carla, R. Felici, C. Knie, D. Bleger, and S. Kowarik. Multiple timescales in the photoswitching kinetics of crystalline thin films of azobenzene-trimers. *Journal of Physics: Condensed Matter*, **29**(43):434001, (2017).

[134] M. Kockert. Preparation and characterisation of silicon nanowires for thermoelectrical measurements. Master's thesis, Humboldt-Universität zu Berlin, (2015).

[135] Z. Wang. *Structural and Thermoelectric Characterization of Individual Single Crystalline Nanowires*. PhD thesis, Albert-Ludwigs-Universität Freiburg, (2014).

[136] S. H. Moosavi. *Design and Fabrication of a Thermoelectric Nanowire Characterization Platform*. PhD thesis, Albert-Ludwigs-Universität Freiburg, (2018).

[137] P. A. Smith, C. D. Nordquist, T. N. Jackson, T. S. Mayer, B. R. Martin, J. Mbindyo, and T. E. Mallouk. Electric-field assisted assembly and alignment of metallic nanowires. *Applied Physics Letters*, **77**(9):1399–1401, (2000).

[138] P. Kim and C. M. Lieber. Nanotube Nanotweezers. *Science*, **286**(5447):2148–2150, (1999).

[139] K. Flöhr, M. Liebmann, K. Sladek, H. Y. Günel, R. Frielinghaus, F. Haas, C. Meyer, H. Hardtdegen, T. Schäpers, D. Grützmacher, and M. Morgenstern. Manipulating InAs nanowires with submicrometer precision. *Review of Scientific Instruments*, **82**(11):113705, (2011).

[140] J. J. L. Mulders, L. M. Belova, and A. Riazanova. Electron beam induced deposition at elevated temperatures: compositional changes and purity improvement. *Nanotechnology*, **22**(5):055302, (2010).

[141] A. Botman, J. J. L. Mulders, R. Weemaes, and S. Mentink. Purification of platinum and gold structures after electron-beam-induced deposition. *Nanotechnology*, **17**(15):3779–3785, (2006).

[142] J. J. L. Mulders. Purity and resistivity improvements for electron-beam-induced deposition of Pt. *Applied Physics A*, **117**(4):1697–1704, (2014).

[143] X. Zhang, H. Xie, M. Fujii, and H. Ago. Thermal and electrical conductivity of a suspended platinum nanofilm. *Applied Physics Letters*, **86**(17):171912, (2005).

[144] R. A. Matula. Electrical resistivity of copper, gold, palladium, and silver. *Journal of Physical and Chemical Reference Data*, **8**(4):1147–1298, 1979.

[145] R. Brandt and G. Neuer. Electrical Resistivity and Thermal Conductivity of Pure Aluminum and Aluminum Alloys up to and above the Melting Temperature. *International Journal of Thermophysics*, **28**(5):1429–1446, (2007).

[146] R. W. G. Wyckoff. *Crystal Structures*. Interscience Publisher, (1963).

[147] L. L. Kazmerski, D. M. Racine, and M. S. Ayyagari. Temperature coefficient of resistance in ultrathin metal films. *Journal of Applied Physics*, **46**(6):2658–2661, (1975).

[148] M. C. Salvadori, L. L. Melo, A. R. Vaz, R. S. Wiederkehr, F. S. Teixeira, and M. Cattani. Platinum and gold thin films deposited by filtered vacuum arc: morphological and crystallographic grain sizes. *Surface & Coatings Technology*, **200**(9):2965–2969, (2006).

[149] M. C. Salvadori, L. L. Melo, A. R. Vaz, R. S. Wiederkehr, F. S. Teixeira, and M. Cattani. Grain Sizes and Surface Rougness in Platinum and Gold Thin Films. *Journal of Metastable and Nanocrystalline Materials*, **20-21**:623–628, (2004).

[150] J. S. Agustsson, U. B. Arnalds, A. S. Ingason, K. B. Gylfason, K. Johnsen, S. Olafsson, and J. T. Gudmundsson. Electrical resistivity and morphology of ultra thin Pt films grown by dc magnetron sputtering on SiO_2. *Journal of Physics: Conference Series*, **100**(8):082006, (2008).

[151] M. Bailyn. Phonon-Drag Part of the Thermoelectric Power in Metals. *Physical Review*, **157**(3):480, (1967).

[152] W. Shim, J. Ham, K. i. Lee, W. Y. Jeung, M. Johnson, and W. Lee. On-Film Formation of Bi Nanowires with Extraordinary Electron Mobility. *Nano Letters*, **9**(1):18–22, (2009).

[153] T. E. Huber, A. Nikolaeva, D. Gitsu, L. Konopko, C. A. Foss, and M. J. Graf. Confinement effects and surface-induced charge carriers in Bi quantum wires. *Applied Physics Letters*, **84**(8):1326–1328, (2004).

[154] A. Nikolaeva, T. E. Huber, D. Gitsu, , and L. Konopko. Diameter-dependent thermopower of bismuth nanowires. *Physical Review B*, **77**(3):035422, (2008).

[155] E. F. Cave and L. V. Holroyd. Thermal Expansion Coefficients of Bismuth. *Journal of Applied Physics*, **31**(8):1357–1358, (1960).

[156] D. R. Hummer, P. J. Heaney, and J. E. Post. Thermal expansion of anatase and rutile between 300 and 575 K using synchrotron powder X-ray diffraction. *Powder Diffraction*, **22**(4):352–357, (2007).

[157] R. Franz and G. Wiedemann. Ueber die Wärme-Leitungsfähigkeit der Metalle. *Annalen der Physik*, **165**(8):497–531, (1853).

[158] A. H. Wilson. The Theory of Metals. *Cambridge University Press*, (1954).

[159] N.I. Anisimova, G.A. Bordovsky, V.A. Bordovsky, and V.I. Seldayev. Electrical and thermal properties of Bi_2O_3, Pbo and mixed oxides of Bi_2O_3-Pbo system. *Proceedings of the 2004 IEEE International Conference on Solid Dielectrics*, **1**:141–142, (2004).

[160] S. Ali, T. Juntunen, S. Sintonen, O. M. E. Ylivaara, R. L. Puurunen, H. Lipsanen, I. Tittonen, and S.-P. Hannula. Thermal conductivity of amorphous Al_2O_3/TiO_2 nanolaminates deposited by atomic layer deposition. *Nanotechnology*, **27**(44):445704, (2016).

List of Figures

List of Tables

List of scientific contributions

Publications

- **M. Kockert**, R. Mitdank, H. Moon, J. Kim, A. Mogilatenko, S. H. Moosavi, M. Kroener, P. Woias, W. Lee and S. F. Fischer. "Semimetallic to semiconductor transition in Bi/TiO_2 core/shell nanowires." *Nanoscale Advances*, **3**(1):263-271, (2020).

- **M. Kockert**, D. Kojda, R. Mitdank, A. Mogilatenko, Z. Wang, J. Ruhhammer, M. Kroener, P. Woias and S. F. Fischer. "Nanometrology: Absolute Seebeck coefficient of individual silver nanowires." *Scientific Reports*, **9**(1):20265, (2019).

- **M. Kockert**, R. Mitdank, A. Zykov, S. Kowarik and S. F. Fischer. "Absolute Seebeck coefficient of thin platinum films." *Journal of Applied Physics*, **126**(10):105106, (2019).

- S. H. Moosavi, D. Kojda, **M. Kockert**, S. F. Fischer, M. Kroener and P. Woias. "The Effect of the MEMS Measurement Platform Design on the Seebeck Coefficient Measurement of a Single Nanowire." *Nanomaterials*, **8**(219), (2018).

- S. H. Moosavi, D. Kojda, **M. Kockert**, P. Schoenherr, T. Hesjedal, S. F. Fischer, M. Kroener and P. Woias. "Thermoelectric Measurement of a Single TiO_2-Catalyzed Bi_2Te_3 Nanowire." *Proceedings of Eurosensors Paris 2017*, **1**(311), (2017).

- S. Weidemann, **M. Kockert**, D. Wallacher, M. Ramsteiner, A. Mogilatenko, K. Rademann and S. F. Fischer. "Controlled Pore Formation on Mesoporous Single Crystalline Silicon Nanowires: Threshold and Mechanisms." *Journal of Nanomaterials*, **2015**:672305, (2015).

Talks and posters

- **M. Kockert**, R. Mitdank, H. Moon, J. Kim, A. Mogilatenko, S. H. Moosavi, M. Kroener, P. Woias, W. Lee and S. F. Fischer. Poster: "Influence of strain on the thermoelectric properties of Bi/TiO_2 core/shell nanowires." *CMD2020GEFES online - Condensed Matter Division*, Online, (09/2020).

- **M. Kockert**, R. Mitdank, A. Zykov, S. Kowarik and S. F. Fischer. Talk: "Influence of size effects on the absolute Seebeck coefficient of platinum." *17th European Conference on Thermoelectrics*, Limassol (Cyprus), (09/2019).

- **M. Kockert**, R. Mitdank, A. Zykov, S. Kowarik and S. F. Fischer, presented by S. F. Fischer. Talk: "How size matters: Influence of size effects on the absolute Seebeck coefficient of platinum." *38th International Conference on Thermoelectrics*, Gyeongju (South Korea), (07/2019).

- **M. Kockert**, D. Kojda, R. Mitdank, A. Zykov, S. Kowarik, J. Ruhhammer, Z. Wang, M. Kroener, P. Woias, T. Markurt and S. F. Fischer. Talk: "Absolute Seebeck coefficient of thin platinum films and individual silver nanowires." *Spring meeting 2019 - Deutsche Physikalische Gesellschaft*, Regensburg (Germany), (04/2019).

- **M. Kockert**, D. Kojda, R. Mitdank, A. Mogilatenko, J. Kim, H. Moon, W. Lee, S. H. Moosavi, M. Kroener, P. Woias and S. F. Fischer. Talk: "Bi-based Core-Shell Nanowires: Thermoelectric Properties." *International Workshop on Thermoelectric Nanomaterials*, Berlin (Germany), (06/2018).

- **M. Kockert**, D. Kojda, R. Mitdank, A. Mogilatenko, T. Markurt, M. Albrecht, Z. Wang, J. Ruhhammer, M. Kroener, P. Woias and S. F. Fischer. Poster: "Determination of the absolute Seebeck coefficient of thin films and individual nanowires." *667. WE-Heraeus-Seminar on System-oriented approach to thermoelectrics Materials - Interfaces*, Bad Honnef (Germany), (04/2018).

- **M. Kockert**, D. Kojda, R. Mitdank, J. Ruhhammer, Z. Wang, M. Kroener, P. Woias, T. Markurt and S. F. Fischer. Talk: "Absolute Seebeck coefficient of individual silver nanowires." *Spring meeting 2018 - Deutsche Physikalische Gesellschaft*, Berlin (Germany), (03/2018).

- **M. Kockert**, D. Kojda, R. Mitdank, J. Ruhhammer, Z. Wang, M. Kroener, P. Woias, T. Markurt and S. F. Fischer. Poster: "Temperature-dependent Seebeck coefficient of silver nanowires." *Spring meeting 2017 - Deutsche Physikalische Gesellschaft*, Berlin (Germany), (03/2017).

- **M. Kockert**, D. Kojda, R. Mitdank, A. Mogilatenko, T. Markurt, M. Albrecht, Z. Wang, J. Ruhhammer, M. Kroener, P. Woias and S. F. Fischer. Poster: "Thermoelectric Characterization Of Bismuth/Tellurium Core/Shell Nanowires And Silver Nanowires." *Thermoelectrics Colloquium - Helmholtz-Zentrum Berlin für Materialien und Energie*, Berlin (Germany), (11/2016).

- **M. Kockert**, S. Weidemann, D. Kojda, Z. Wang, M. Kroener, P. Woias, K. Rademann, M. Albrecht and S. F. Fischer. Poster: "The influence of nanopatterning on the electrical conductivity of boron-doped silicon nanowires." *Spring meeting 2016 - Deutsche Physikalische Gesellschaft*, Regensburg (Germany), (03/2016).

Awards

- **M. Kockert**, D. Kojda, R. Mitdank, A. Mogilatenko, Z. Wang, J. Ruhhammer, M. Kroener, P. Woias and S. F. Fischer. "Präzisionsmessungen in der angewandten Messtechnik." *Helmholtz-Preis 2020.*

Acknowledgment

First and foremost, I would like to thank all members of the Novel Materials group at Humboldt-Universität zu Berlin for the pleasant teamwork over the past years.

I would like to express my gratitude to my supervisor Prof. Dr. Saskia F. Fischer who gave me the opportunity to do my PhD research in her fabulous team. She fully supported me on this path.

I would like to thank my thesis committee and examination board: Prof. Dr. Thorsten Kamps, Prof. Christoph T. Koch, PhD, Prof. Dr. Kornelius Nielsch and Prof. Dr. Jürgen P. Rabe for agreeing to dedicate their valuable time to judge my work.

I would particularly like to thank Dr. Rüdiger Mitdank for his long-term scientific support. His support did not end with his retirement.

A big thank goes out to Dr. Danny Kojda who has introduced me to the wonderful world of nanowire investigations.

The entire nanowire measurements would not have been possible without the TNCP. Therefore, a great thanks to Dr. Zhi Wang, Dr. S. Hoda Moosavi, Dr. Michael Kroener and Prof. Dr. Peter Woias from the Laboratory for Design of Microsystem (IMTEK) of the University of Freiburg.

I would like to thank my Korean cooperation partners Hongjae Moon, Dr. Jeongmin Kim and Prof. Dr. Wooyoung Lee from the Department of Material Science and Engineering of the Yonsei University (Seoul) for providing the Bi-based core/shell nanowires and the pleasant hospitality when visiting Korea.

I would like to thank Dr. Anna Mogilatenko from the Ferdinand-Braun-Institut (FBI), Leibniz-Institut für Höchstfrequenztechnik in Berlin for the transmission electron microscopy investigations of the nanowires and the corresponding insight into the structural properties.

Furthermore, I would like to thank Dr. Anton Zykov and Prof. Dr. Stefan Kowarik for conducting the X-ray investigations of the thin platinum films.

Moreover, I would like to thank Dr. Olivio Chiatti for the time-consuming maintenance of the scanning electron microscope. The EBID contacting would not have been possible without the SEM.

I would like to thank Dr. Johannes Bourbon (neé Ruhhammer) from the Laboratory for Design of Microsystem (IMTEK) of the University of Freiburg for providing the silver nanowires.

Great thanks also go out to my Bachelor, Master, research students and fans, Jie Chen, Birkan Düzel, Michal Góra, Mahni Müller and Max Pfeifer for their active support in the laboratory.

I would like to thank Jürgen Sölle for providing the many glass substrates in order to test the TML.

I would like to thank Dr. Toni Markurt and Dr. Martin Albrecht for giving me the opportunity to take my first steps in EBID contacting at the Leibniz Institute for Crystal Growth (IKZ) in Berlin.

Furthermore, I would like to thank, German Science Foundation (No. DFG-SPP1386), the Bundesministerium für Bildung und Forschung (BMBF grant 01DR17012), the Humboldt-Universität zu Berlin, the Humboldt-Innovation GmbH and the Yonsei University (Korea) for the financial support.

Special thanks go out to Andreas, Christian, Christine, Corinna and Martin for the non-solid-state physics activities in the leisure time.

I would like to thank from the bottom of my heart my friends and family especially my grandparents and my mother, who supported me throughout my studies.

A special thank you goes to my wife Corinna, who has supported me all along and who has shown the necessary understanding for this time-consuming engagement.

Finally, I would like to thank my daughter Elli. She was born in June 2020 and accompanied me on the last part of my journey. She always put a smile on my face after a hard day at work.

Elli and Corinna, I love you both.

Statement of authorship / Selbstständigkeitserklärung

Ich erkläre, dass ich die Dissertation selbstständig und nur unter Verwendung der von mir gemäß § 7 Abs. 3 der Promotionsordnung der Mathematisch-Naturwissenschaftlichen Fakultät, veröffentlicht im Amtlichen Mitteilungsblatt der Humboldt-Universität zu Berlin Nr. 42/2018 am 11.07.2018 angegebenen Hilfsmittel angefertigt habe.

Berlin, den 03.03.2021

Maximilian Kockert